Compressibility effects in near-wall turbulence

Hasan, A.M.

DOI
10.4233/uuid:1f220c99-b4c4-48e9-939e-043a9056d591

Publication date
2025

Document Version
Final published version

Citation (APA)
Hasan, A. M. (2025). *Compressibility effects in near-wall turbulence*. [Dissertation (TU Delft), Delft University of Technology]. https://doi.org/10.4233/uuid:1f220c99-b4c4-48e9-939e-043a9056d591

COMPRESSIBILITY EFFECTS IN NEAR-WALL TURBULENCE

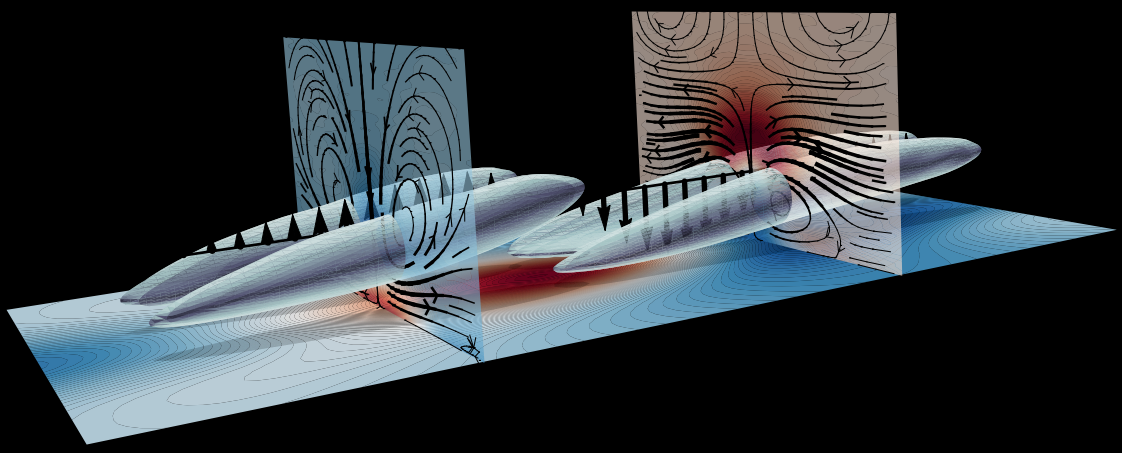

Cover Image: Opposition of vortices by fluid expansions and contractions (chapter 3)

Asif Manzoor Hasan

COMPRESSIBILITY EFFECTS IN NEAR-WALL TURBULENCE

COMPRESSIBILITY EFFECTS IN NEAR-WALL TURBULENCE

Dissertation

for the purpose of obtaining the degree of doctor
at Delft University of Technology,
by the authority of the Rector Magnificus, prof. dr. ir. T.H.J.J. van der Hagen,
chair of the Board for Doctorates,
to be publicly defended on Wednesday 8 October 2025 at 17:30 o'clock

by

Asif Manzoor HASAN

Master of Science in Mechanical Engineering,
Delft University of Technology, The Netherlands,
born in Mumbai, India.

This dissertation has been approved by the promotors.
Composition of the doctoral committee:

Rector Magnificus,	chairperson
Prof. dr. R. Pecnik	Delft University of Technology, promotor
Dr. P. Costa	Delft University of Technology, copromotor
Independent members:	
Prof. dr. ir. S.K. Lele	Stanford University, United States of America
Prof. dr. ir. S. Hickel	Delft University of Technology
Prof. dr. ir. P. Cinnella	Sorbonne University, France
Prof. dr. ir. H. Foysi	University of Siegen, Germany
Dr. ir. W.P. Breugem	Delft University of Technology
Prof. dr. ir. C. Poelma	Delft University of Technology, reserve member

This work was performed at Delft University of Technology and was supported by the European Research Council grant no. ERC-2019-CoG335 864660, Critical.

Keywords:	Compressible turbulence, Turbulent boundary layer, Turbulence modeling
Cover:	Opposition of vortices by fluid expansions and contractions (chapter 3).
Printed by:	Ridderprint | `www.ridderprint.nl`

ISBN 978-94-6522-738-2
An electronic version of this dissertation is available at
`http://repository.tudelft.nl/`

Dedicated to my father

Manzoor Mohammed Hasan

CONTENTS

SUMMARY

It is difficult to envision an industrial application where turbulent flows interacting with solid walls do not play a critical role. While understanding these flows at low speeds is already challenging, the complexity increases significantly when the flow speed exceeds the speed of sound or when heat transfer through the walls is intense. These so-called compressible flows are at the core of many engineering applications including aerospace vehicles, combustors, high-speed propulsion systems, gas turbines and other power-generating technologies. Understanding the physics governing these flows is essential for developing accurate predictive models, which in turn enable the improved design of engineering systems.

Compressible wall-bounded turbulent flows involve two distinct effects: those related to heat transfer, commonly referred to as variable-property effects, and those arising from density changes of fluid elements in response to changes in pressure, termed intrinsic compressibility (IC) effects. While the former can occur across all flow speeds, the latter becomes significant only at high Mach numbers. In the past, variable-property effects have been extensively studied; in contrast, the influence of intrinsic compressibility has received limited attention. This gap is largely attributed to Morkovin's hypothesis, which asserts that IC effects can be neglected in wall-bounded flows under certain conditions.

The present work revisits this assumption and directly addresses the question posed by Otto Zeman in 1993: *"are the (intrinsic) compressibility effects significant in reality, and can they be isolated in experiments and verified?"* To isolate such effects, we perform direct numerical simulations (DNS) of fully developed high-Mach-number channel flows, in which the energy equation is augmented with an external heat source to maintain approximately constant mean thermophysical properties, thereby eliminating variable-property effects.

This thesis is divided in two parts. The first part uses these tailored flow cases to investigate the **physics associated with IC effects**. We demonstrate that IC effects significantly influence various turbulence statistics—an influence previously misattributed to variable-property effects. The underlying mechanism is as follows: pressure-induced expansions and contractions of the near-wall fluid oppose sweeps and ejections, leading to a weakening of quasi-streamwise vortices. The weakened vortices reduce the energy transferred from the streamwise to the wall-normal velocity components, thereby modulating turbulence statistics.

The second part builds on these insights to develop **scaling laws and predictive models** applicable to a wide range of channel flows and zero-pressure-gradient boundary layers. Specifically, we derive scaling laws for wall pressure fluctuations, the peak of streamwise turbulent stress, and the mean velocity profile—accounting for both variable-property and intrinsic compressibility effects. The mean velocity scaling is then further exploited to derive predictive models that estimate skin friction and heat transfer coefficients, and to propose compressibility corrections for Reynolds-averaged Navier-Stokes (RANS) turbulence models. These corrected models demonstrate significantly

improved accuracy over the state-of-the-art and hold strong potential for enhancing the modeling of complex, real-world engineering systems.

SAMENVATTING

Het is moeilijk om een industriële toepassing voor te stellen waarbij turbulente stromingen die in contact staan met vaste wanden geen cruciale rol spelen. Hoewel het uitdagend is om deze stroming bij lage snelheden te beschrijven, neemt de complexiteit aanzienlijk toe wanneer de stroomsnelheid de geluidssnelheid overschrijdt of wanneer warmteoverdracht door de wanden intens is. Zulke comprimeerbare stromingen vormen de kern van vele technische toepassingen, waaronder lucht- en ruimtevaartuigen, verbrandingskamers, hogesnelheidsaandrijfsystemen, gasturbines en andere energieopwekkende technologieën. Inzicht in de fysica die deze stromingen beheerst is essentieel voor het ontwikkelen van nauwkeurige voorspellende modellen, die op hun beurt een verbeterd ontwerp van technische systemen mogelijk maken.

Comprimeerbare wandgebonden turbulente stromingen bevatten twee afzonderlijke effecten: effecten gerelateerd aan warmteoverdracht, algemeen aangeduid als variabele-eigenschappen effecten, en effecten die voortkomen uit dichtheidsveranderingen van fluidelementen als reactie op drukveranderingen, aangeduid als intrinsieke comprimeerbaarheidseffecten (IC effecten). Terwijl het eerste effect bij alle stroomsnelheden kan optreden, wordt het tweede effect significant alleen bij hoge Mach-getallen. In het verleden zijn variabele-eigenschappen effecten uitgebreid bestudeerd; daarentegen heeft de invloed van intrinsieke comprimeerbaarheid tot nu toe beperkte aandacht gekregen. Deze kloof wordt grotendeels toegeschreven aan de hypothese van Morkovin, die stelt dat IC effecten onder bepaalde omstandigheden kunnen worden verwaarloosd in wandgebonden stromingen.

Dit werk heroverweegt deze veronderstelling en behandelt direct de vraag die Otto Zeman in 1993 stelde: *"are the (intrinsic) compressibility effects significant in reality, and can they be isolated in experiments and verified?"* (Vertaalt: Zijn de (intrinsieke) comprimeerbaarheidseffecten in werkelijkheid significant, en kunnen ze geïsoleerd en geverifieerd worden met experimenten?) Om dergelijke effecten te isoleren, voeren we directe numerieke simulaties (DNS) uit van volledig ontwikkelde kanaalstromingen bij hoge Mach-getallen, waarbij de energievergelijking wordt uitgebreid met een externe warmtebron om de gemiddelde thermofysische eigenschappen ongeveer constant te houden, waardoor variabele-eigenschappen effecten worden geëlimineerd.

Dit proefschrift is opgedeeld in twee delen. Het eerste deel maakt gebruik van deze speciaal aangepaste stromingsgevallen om de **fysica gerelateerd aan IC effecten** te onderzoeken. We tonen aan dat IC effecten de turbulentiestatistieken significant beïnvloeden—een invloed die eerder ten onrechte werd toegeschreven aan variabele-eigenschappen effecten. Het onderliggende mechanisme is als volgt: drukgeïnduceerde uitzettingen en contracties van het vlakbij-de-wand fluïdum werken in tegen sweeps en ejections, waardoor quasi-stroomgerichte wervelstructuren verzwakken. De verzwakte vortexen verminderen de energieoverdracht van de stroomlijnrichting naar de wandnormale snelheidscomponenten, waardoor de turbulentiestatistieken worden veranderd.

Het tweede deel bouwt voort op deze inzichten om **schaalwetten en voorspellende modellen** te ontwikkelen die toepasbaar zijn op een breed scala aan kanaalstromingen en grenslagen zonder drukgradiënt. We leiden de schaalwetten af voor wanddruk-fluctuaties, de piek van de turbulente spanning in stroomrichting, en het gemiddelde snelheidsprofiel—rekening houdend met zowel variabele-eigenschappen als intrinsieke comprimeerbaarheids effecten. De schaal van het gemiddelde snelheidsprofiel wordt vervolgens verder benut om voorspellende modellen af te leiden die wrijvingscoëfficiënten en warmteoverdrachtscoëfficiënten schatten, en om compressiecorrecties voor Reynolds-averaged Navier-Stokes (RANS) turbulentie-modellen voor te stellen. Deze gecorrigeerde modellen tonen aanzienlijk verbeterde nauwkeurigheid ten opzichte van de huidige stand van de techniek en bieden een sterk potentieel voor de verbetering van de modellering van complexe, realistische technische systemen.

1

INTRODUCTION

"...it is precisely the ability of numerical techniques to simulate 'impossible' physics that makes them a tool of choice in unravelling the physics of complex systems."

— Javier Jiménez and Alfredo Pinelli

1

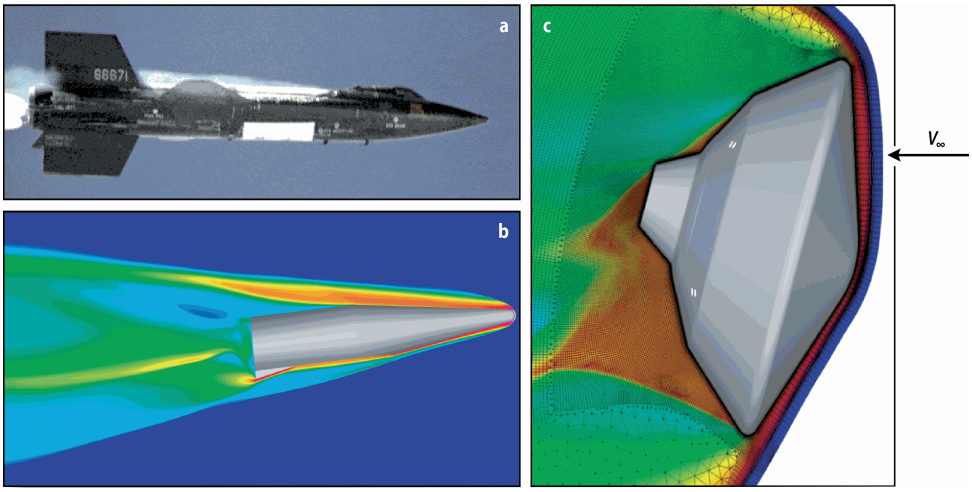

Figure 1.1: Visualizations of three hypersonic flows from Candler (2019): (a) the NASA X-15 rocket plane, (b) a generic lifting hypersonic body, and (c) the Mars Science Laboratory (MSL) capsule at Mars entry conditions.

Compressible wall-bounded turbulent flows[1,2,3] are at the core of many engineering applications such as aerospace vehicles, combustion processes, high-speed propulsion systems, applications involving supercritical[4] flows, gas turbines and other power-generating systems.

Figure 1.1 illustrates three hypersonic[5] flows from Candler (2019). Subfigure (a) shows the piloted hypersonic X-15 plane developed by NASA and its collaborators in the 1960s, which holds the unofficial speed record of about 2 km/s (Mach 6.7) (Jenkins, 2000). Shortly after achieving this milestone, the X-15 crashed due to extreme thermal loads that led to partial melting of its surface—highlighting the complexities and risks

[1]Compressible flows are traditionally defined as those in which the fluid density varies due to changes in pressure (compression or expansion) and/or temperature (heating or cooling). Such flows may occur at both low as well as high Mach numbers, where the Mach number is defined as $Ma = \mathscr{U}/c$, with $\mathscr{U}$ representing a characteristic flow velocity and c the characteristic speed of sound. A detailed classification of the effects associated with compressible flows is shown in figure 1.3.

[2]Wall-bounded flows are those that occur in the vicinity of solid walls. Internal flows, such as those in pipes or ducts (channels), and external flows, such as those over flat plates, can all be identified as wall-bounded flows.

[3]Turbulent flows are those in which fluid elements undergo random and irregular motions, which makes a deterministic approach to the problem impossible, thereby relying on statictical methods (Tennekes and Lumley, 1972) . This flow regime typically occurs at high Reynolds numbers, defined as $Re = \mathscr{U}\mathscr{L}/\nu$, where $\mathscr{U}$ and $\mathscr{L}$ are characteristic velocity and length scales, and ν is the kinematic viscosity of the fluid. For a more detailed discussion on turbulence, the reader is referred to Pope (2001) or Tennekes and Lumley (1972), among many other textbooks on this subject.

[4]Supercritical flows are those that occur at high temperatures and pressures, above the critical point of the fluid. In this thermodynamic region, the fluid undergoes a smooth transition from a liquid-like to a gas-like behaviour, thereby depicting strong changes in its thermophysical properties.

[5]Flows with speeds greater than five times the speed of sound (Mach number > 5) are classified as 'hypersonic' flows. Those with Mach number below 5 and above 1 are termed 'supersonic', and those below 1 are labelled 'subsonic'.

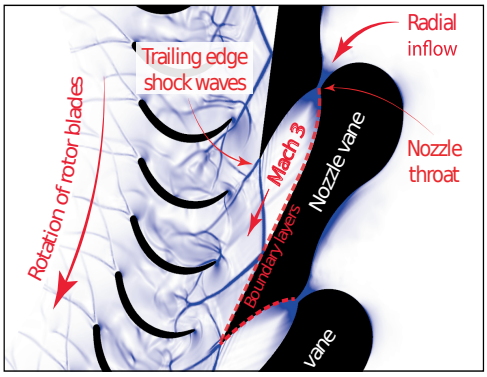

Figure 1.2: A Reynolds-averaged Navier-Stokes (RANS) simulation of a radial inflow turbine operating with an organic fluid at Mach 3 (reproduced from Pecnik and Hasan (2026), originally adapted from Otero Rodriguez et al. (2021)) .

involved in such flights. Subfigure (b) shows a generic lifting hypersonic body, while subfigure (c) shows the space exploration vehicle 'MSL' (Mars Science Laboratory) flying at a hypersonic speed of 6 km/s (Candler, 2019), which was designed to carry a large rover (> 800 kg) to the surface of Mars (Edquist et al., 2007). Subfigures (b) and (c) correspond to computational fluid dynamics (CFD) simulations, and the contours therein represent the temperature field at the symmetry plane. In the past few decades, with the advent of sophisticated numerical and innovative measuring techniques, substantial progress has been made in understanding hypersonic flows. However, many key aspects still remain elusive, such as shock-boundary layer interactions, high-temperature dissociation effects, laminar to turbulent transition, turbulence modeling, and ablation of surfaces (Leyva, 2017). Understanding these aspects is essential in making routine hypersonic flights within and beyond Earth's atmosphere an achievable reality.

Figure 1.2 illustrates another application where compressible flows play a key role—turbines—specifically, a radial turbine designed for an organic Rankine cycle (ORC) system (Otero Rodriguez et al., 2021). ORC systems are power generation units operating on the Rankine cycle but with an organic fluid (e.g. alkanes, alcohols, hydrofluorocarbons, etc.) as the working medium instead of steam. The working fluid can be selected based on the heat source temperature and other factors, making ORC systems possibly the most flexible in terms of capacity and operating temperature (Colonna et al., 2015). This flexibility enables them to effectively harness low-grade heat sources such as geothermal reservoirs, biomass combustion, solar energy, waste heat from industrial processes and so on. While the selection of working fluid adds flexibility, it also influences the design of the turbomachines used in an ORC system. For instance, expanding organic vapors in turbines can attain very high supersonic Mach numbers due to low values of the sound speed, and thus, special care is required in their fluid-dynamic design (Colonna et al., 2015). These challenges become even more pronounced when the working fluid operates in the supercritical region, where thermophysical properties can vary significantly.

In these applications, one of the key phenomena that is not yet fully understood is the behavior of fully developed turbulence near solid walls at high Mach numbers and

under strong heat transfer conditions. Turbulence in the near-wall region plays a central role in determining the viscous drag and surface heating experienced by such systems, thereby directly influencing their performance and efficiency. To predict these quantities accurately, our objective is to develop novel scaling laws and turbulence modeling techniques. However, in order to achieve this goal, it is first necessary to understand the underlying physics.

1.1. CLASSIFICATION OF COMPRESSIBILITY EFFECTS

Turbulence in compressible flows involves effects related to heat transfer—also termed as variable-property effects—and intrinsic compressibility (hereby IC) effects—also termed as 'true' compressibility effects (Smits and Dussauge, 2006), 'genuine' compressibility effects (Yu et al., 2019), or simply 'compressibility' effects (Lele, 1994). These effects are summarized in figure 1.3.

Heat transfer is in turn responsible for two main effects. First, it is associated with mean temperature variations, and hence variations in the mean density and viscosity. Second, it can cause fluctuations in fluid volume (or density) as a result of a change in entropy (Livescu, 2020). Mean property variations further influence the traditional definitions of the friction velocity and viscous length scales (discussed later), and they are also responsible for the property fluctuations generated as a result of solenoidal passive mixing. On the other hand, intrinsic compressibility effects are associated with changes in fluid volume in response to changes in pressure (Lele, 1994). While variable-property effects can be relevant at any (even zero) Mach number, IC effects only become important at high Mach numbers.

To better understand these effects, let us note the thermodynamic identity relating density (ρ), pressure (p) and entropy (s) for **ideal gas** flows (Gatski and Bonnet, 2013):

$$-\frac{1}{\rho}d\rho = \frac{1}{c_p}ds - \frac{1}{\rho c^2}dp, \tag{1.1}$$

where c_p is the specific heat capacity at constant pressure, and $c = \sqrt{(\partial p/\partial \rho)_s}$ is the definition of the speed of sound, which is equal to $\sqrt{\gamma RT}$ for ideal gases, where T is the temperature, R the specific gas constant and γ the ratio of specific heat capacities. Note that for ideal gases $\rho c^2 = \gamma p$.

This thermodynamic relation generalized for a fluid in motion reads (Lele, 1994; Gatski and Bonnet, 2013)

$$-\frac{1}{\rho}\frac{D\rho}{Dt} = \frac{1}{c_p}\frac{Ds}{Dt} - \frac{1}{\rho c^2}\frac{Dp}{Dt}, \tag{1.2}$$

where $D/Dt = \partial/\partial t + u_j \partial/\partial x_j$ represents material derivative, the left hand side represents changes in volume ($v = 1/\rho$) per unit volume of a fluid material element, and the right hand side represents the sources responsible for this change—entropy and pressure[6]. Note that the left hand side of this equation—also referred to as the dilatation 'd'—is equal to the divergence of velocity

$$d = -\frac{1}{\rho}\frac{D\rho}{Dt} = \frac{\partial u_i}{\partial x_i}, \tag{1.3}$$

[6]Interestingly, these entropic and isentropic volume changes are analogous to the entropic and acoustic modes, as per Kovasznay's decomposition (Kovasznay, 1953).

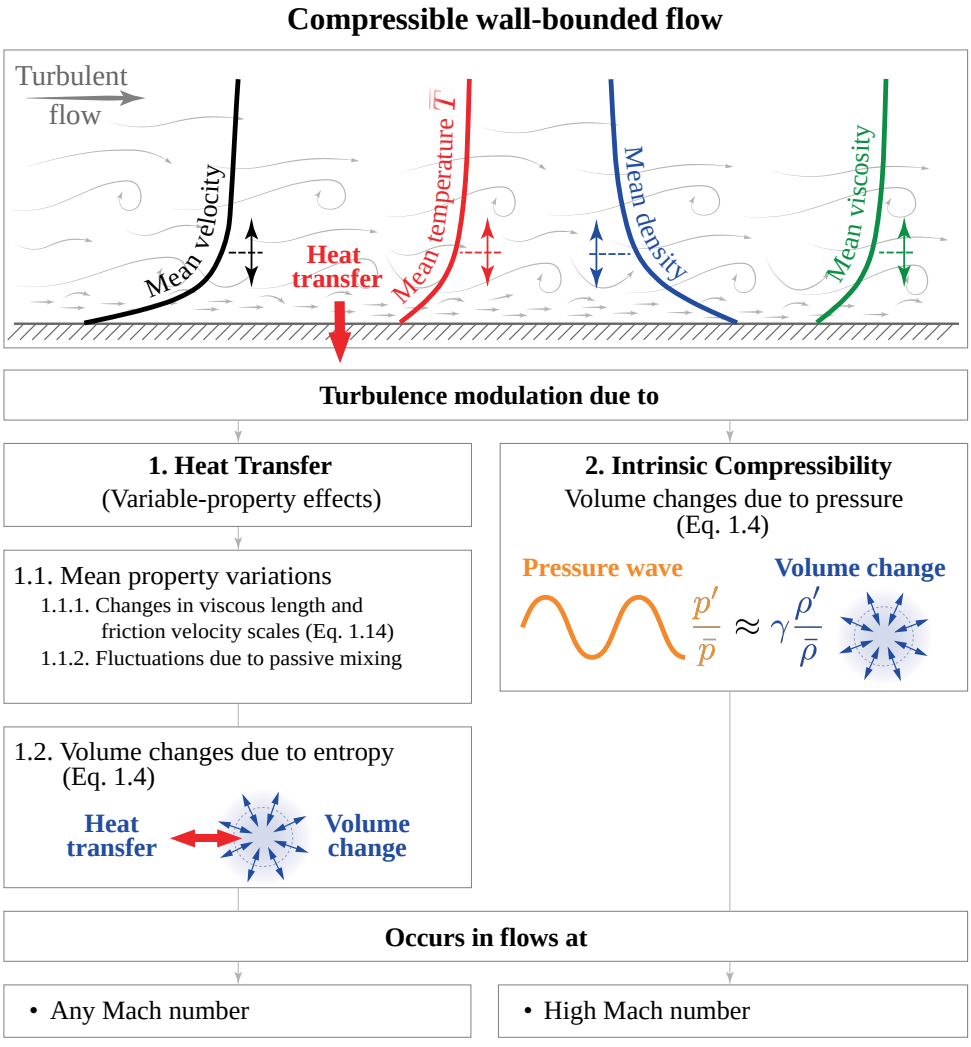

Figure 1.3: Schematic overview of compressibility effects in wall-bounded turbulence (adapted from Pecnik and Hasan (2026)).

as per the continuity equation.

Rewriting the first term on the right-hand-side of equation (1.2) in the form of the mechanisms through which entropy of a fluid element can change—i.e., heat conduction and viscous dissipation (and other externally added heat sources, if present)—, we get

$$-\frac{1}{\rho}\frac{D\rho}{Dt} = \underbrace{\frac{1}{\rho c_p T}\left(\Phi - \frac{\partial q_j}{\partial x_j}\right)}_{\text{block 1.2 in Fig. 1.3}} - \underbrace{\frac{1}{\rho c^2}\frac{Dp}{Dt}}_{\text{block 2 in Fig. 1.3}} \quad , \tag{1.4}$$

where Φ represents the heat sources in the domain, and $q_j = -\lambda \partial T/\partial x_j$ represents Fourier's heat conduction formula, where λ is the thermal conductivity coefficient.

Equation (1.4) mathematically represents the following picture: imagine a fluid parcel moving through a domain. In its journey it receives heat from the surrounding, or rejects heat to it. In this process, the entropy of the parcel changes, causing its volume to change. Similarly, in its journey if it encounters a change in pressure, its volume changes. Such volume changes would influence the flow field around the parcel, thereby influencing the flow dynamics, leading to effects highlighted in blocks 1.2 and 2 of figure 1.3. In fact, in chapter 3, we present such a mechanistic picture in which the pressure-induced volume change of a fluid parcel modifies the flow field in such a way that it weakens the vortical structures.

In 1962, Morkovin postulated that, for non-hypersonic flows, the effects associated with the volume changes of fluid material elements (blocks 1.2 and 2 in figure 1.3; equation 1.2), are small, such that only mean property variations and its influence on the velocity and length scales (item 1.1.1 in block 1 of figure 1.3) remain important. This hypothesis is commonly referred to as **Morkovin's hypothesis** (Morkovin, 1962; Bradshaw, 1977; Coleman et al., 1995; Smits and Dussauge, 2006)—a cornerstone in the theory of compressible turbulence. Some years later, Bradshaw (1977) performed a detailed study on this hypothesis and provided an engineering estimate as to when the hypothesis should hold. According to Bradshaw, Morkovin's postulate may be true in flows where the root-mean-square (r.m.s.) of the density fluctuation is below 10% of the mean density ($\rho_{rms}/\bar{\rho} < 0.1$).

To better understand this condition, let us represent density fluctuations in wall-bounded flows in terms of entropy and pressure based on the ideal gas equation of state as (Lele, 1994)

$$\frac{\rho'}{\bar{\rho}} = \underbrace{-\frac{s'}{c_p}}_{\rho'^s} + \underbrace{\frac{p'}{\bar{\rho}\bar{c}^2}}_{\rho'^{is}} + \ldots, \tag{1.5}$$

where overbar signifies mean quantities, primes represent fluctuations, and the superscripts 's' and 'is' indicate entropic and isentropic fluctuations, respectively. (The three dots on the right hand side signify other higher order terms resulting from the non-linearity of the equation of state.) The term $-s'/c_p$ represents density fluctuations arising from two distinct mechanisms: (1) fluctuations generated when a fluid material element undergoes a change in volume due to entropy change (equation 1.2); and (2) fluctuations induced when a fluid material element moves in the wall-normal direction across mean density and entropy gradients (i.e., passive mixing). The latter are related to the mean gradients as $\rho' \sim \eta \partial\bar{\rho}/\partial y$ and $s' \sim \eta \partial\bar{s}/\partial y$ (Lele, 1994), where η is the

Lagrangian displacement in the wall-normal direction—also referred to as the 'mixing length'. On the other hand, $p'/(\bar{\rho}\bar{c}^2)$ mainly represents density fluctuations that are generated when a fluid material element undergoes a volume change due to change in pressure (equation 1.2); the contribution by passive mixing being negligible in boundary layers, where $\bar{p}$ is approximately constant.

In compressible wall-bounded flows, passive mixing—embedded in the term s'/c_p—generates the majority of the total density fluctuations (Lele, 1994; Coleman et al., 1995). In other words, the density r.m.s.—as proposed by Bradshaw—is not a rigorous measure of density fluctuations that are generated when a fluid parcel undergoes a change in its volume due to change in entropy or pressure. Consequently, it is not an appropriate indicator of the effects assumed to be small according to Morkovin's conjecture (Coleman et al., 1995), namely blocks 1.2 and 2 in figure 1.3. The effects related to passive mixing (item 1.1.2 in block 1 of figure 1.3) are implicitly neglected in Morkovin's hypothesis (Coleman et al., 1995), since it does not account for the spatial gradients of mean properties (Bradshaw, 1977) that are necessary in the passive mixing mechanism.

As just noted, $p'/(\bar{\rho}\bar{c}^2)$ quantifies changes in volume of fluid material elements in response to changes in pressure. Thus, it is a direct measure of intrinsic compressibility effects (block 2). In light of this, Coleman et al. (1995) suggested that, consistent with the original conjecture, $p_{rms}/(\bar{\rho}\bar{c}^2)$ (or $p_{rms}/\bar{p}$), along with the total temperature r.m.s. scaled by its mean[7], would be a better evaluator of Morkovin's hypothesis, than Bradshaw's $\rho_{rms}/\bar{\rho}$. To our knowledge, there is no engineering estimate for these fluctuations such as the one for density.

1.1.1. VARIABLE-PROPERTY EFFECTS

If Morkovin's hypothesis holds, then only mean property variations are needed to describe turbulence dynamics. Although this assertion is rather vague (Smits and Dussauge, 2006), it leads to a powerful implication: the same scaling laws[8] and models developed for incompressible flows could be applied to compressible flows, provided that mean property variations are appropriately accounted for. Before proceeding with this idea, let us first review the state-of-the-art in scaling incompressible flows.

THE CLASSICAL SCALING FRAMEWORK

In incompressible flows, the 'classical' scaling framework—based on the friction velocity and viscous length scales, defined as

$$u_\tau = \sqrt{\frac{\tau_w}{\rho_w}}, \quad \delta_\nu = \frac{\mu_w}{\rho_w u_\tau}, \tag{1.6}$$

where τ_w is the wall shear stress, and ρ_w, μ_w represent the fluid density and viscosity at the wall (the subscript w indicates wall values)—is popularly utilized to develop scaling laws. To follow the subsequent discussion better, refer to the structure of a turbulent boundary layer in figure 1.4.

[7] The reasoning behind why the total temperature r.m.s. serves as an indicator for the validity of the hypothesis remains unclear (Lele, 1994).

[8] Scaling laws describe how a turbulence quantity should be non-dimensonalized such that it collapses onto one master curve, independent of the flow conditions.

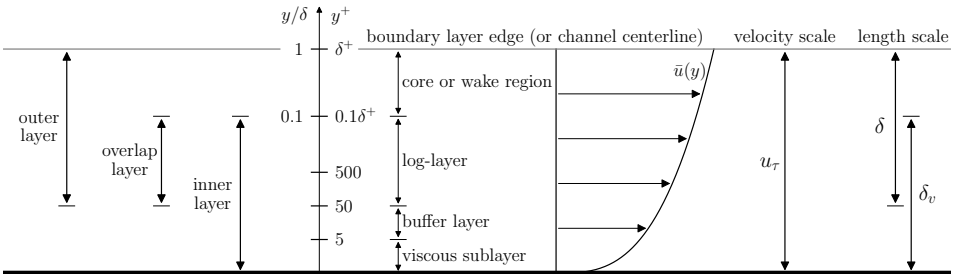

Figure 1.4: A schematic showing the different regions and the appropriate velocity and length scales in an incompressible turbulent boundary layer (adapted from Larsson and Pirozzoli (2026)). A similar schematic for compressible flows is shown in chapter 6 (figure 6.1). Here, $y^+ = y/\delta_v$ and $\delta^+ = \delta/\delta_v$, where y represents the wall-normal coordinate and δ is the boundary layer thickness. $\bar{u}$ denotes the mean velocity in the streamwise direction. Note that both the y/δ and y^+ axes are logarithmic.

The classical paradigm advocates the use of δ_v as the characteristic length scale in the inner layer of a boundary layer, and the use of δ—defined as the thickness of the boundary layer[9]—as the appropriate scale in the outer layer. Consequently, in the overlap region, the two length scales are equivalent, meaning either of the two can be used there. The inner and outer layers share a common velocity scale u_τ, leading to a logarithmic region between them (Marusic et al., 2010). These scales and their regions of validity are schematically depicted in figure 1.4. In the past, various turbulent quantities have been scaled following the classical framework, with varying degree of success in achieving a consistent collapse. See table 7.1 for some examples. Note that classical scaling will be denoted using a superscript '+' for the inner layer and '⊕' for the outer layer.

Among all, the best collapse is achieved for mean velocity profiles. Specifically, the mean velocity $\bar{u}$ scaled by u_τ (i.e., $\bar{u}^+ = u/u_\tau$), when plotted as a function of the wall-normal distance y normalized by δ_v (i.e., $y^+ = y/\delta_v$), results in a universal collapse in the inner layer, independent of the Reynolds number (Lee and Moser, 2015). This scaling of the mean velocity in the inner layer is commonly referred to as **the law of the wall**—a cornerstone in the theory of fluid dynamics (Bradshaw and Huang, 1995).

The law of the wall has played a significant role in shaping the field of turbulence modeling. From the simplest mixing-length models to the more complex ones, where transport equations need to be solved (such as the k-ϵ and k-ω family of models), essentially all models are calibrated to reproduce this law. These turbulence models then drive Reynolds-averaged Navier-Stokes (**RANS**) simulations[10]—an indispensable predictive tool for industries. Beyond RANS, these turbulence models are also at the core of high-fidelity numerical simulations, namely, wall-modeled large eddy simulations (**WMLES**), in which the viscous sublayer and buffer layer are solved using a RANS simulation that provides the wall shear stress and heat flux as an input to the LES (Larsson et al., 2016; Bose and Park, 2018). With rapid advances in computational resources and numerical techniques, WMLES has made major leaps in the CFD domain.

[9]The thickness of the boundary layer is arbitrarily defined to be the distance from the wall where the mean flow velocity is equal to 99% of the free-stream velocity (Pope, 2001).

[10]The reader is referred to the textbook by Wilcox et al. (2006) for the fundamentals on RANS modeling.

For instance, recently, this tool was applied to simulate a landing aircraft at an affordable cost (Goc et al., 2021), marking the readiness of WMLES for industrial deployment.

Moreover, even experimentalists have benefitted from this law, particularly, in estimating wall shear stress without needing to measure extremely close to the wall.

Unlike mean velocity, classical scaling applied to other statistical quantities in the inner layer, such as the streamwise Reynolds stress, does not lead to a collapse, but rather depicts a Reynolds number dependence. For instance, the inner-scaled peak of the streamwise Reynolds stress increases as a logarithmic (Marusic et al., 2017; Samie et al., 2018) or a power-law (Chen and Sreenivasan, 2021, 2022; Monkewitz, 2022) function of the Reynolds number, due to interactions between the inner and outer layers.

THE SEMI-LOCAL SCALING FRAMEWORK

In the past, several scaling laws have been proposed for compressible flows, by simply accounting for mean property variations in the incompressible scaling laws (Morkovin's hypothesis). The first key contribution in accounting for variable-property effects is attributed to Van Driest (1951), who incorporated mean density variations in the mean shear formulation such that

$$\frac{d\bar{u}}{dy} = \frac{\sqrt{\tau_w/\bar{\rho}}}{\kappa y}, \tag{1.7}$$

where u is the streamwise velocity, τ_w the wall shear stress, ρ the fluid density, and κ the von Kármán constant. Equation (1.7) led to two major outcomes: (1) the Van Driest mean velocity transformation[11] (Van Driest, 1956a; Danberg, 1964) given as

$$\bar{U}^+_{VD} = \int_0^{\bar{u}^+} \sqrt{\frac{\bar{\rho}}{\rho_w}}\, d\bar{u}^+, \tag{1.8}$$

and (2) the Van Driest skin-friction theory (Van Driest, 1956b; Hopkins and Inouye, 1971). These scaling breakthroughs are still widely used, despite their known shortcomings (Bradshaw, 1977; Huang and Coleman, 1994; Trettel and Larsson, 2016; Patel et al., 2016a; Griffin et al., 2021; Kumar and Larsson, 2022; Hasan et al., 2024b).

Another key contribution is attributed to Morkovin (1962) who proposed scaling the turbulent shear stress with $\bar{\rho}/\rho_w$ such that

$$\widetilde{u''v''}^* = \frac{\bar{\rho}}{\rho_w}\frac{\widetilde{u''v''}}{u_\tau^2} \tag{1.9}$$

collapses with the incompressible distributions. Here, the tilde denotes density-weighted (Favre) averaging, and the double primes denote fluctuations from Favre average. The contributions of Van Driest and Morkovin can be consolidated by interpreting their corrections as if they were to change the definition of the friction velocity scale from u_τ to $u^*_\tau = \sqrt{\tau_w/\bar{\rho}}$ (termed 'semi-local' friction velocity scale[12]), such that equations (1.7), (1.8), and (1.9) can be rewritten as

$$\frac{d\bar{u}}{dy} = \frac{u^*_\tau}{\kappa y}, \quad \bar{U}^+_{VD} = \int_0^{\bar{u}} \frac{1}{u^*_\tau}\, d\bar{u}, \quad \widetilde{u''v''}^* = \frac{\widetilde{u''v''}}{u^{*2}_\tau}. \tag{1.10}$$

[11] A mean velocity transformation is a scaling law which, when plotted as a function of an appropriately scaled wall distance, collapses onto the incompressible law of the wall.

[12] The friction velocity scale is termed 'semi-local' instead of 'local' because the total shear stress in its definition is still taken at the wall.

Similarly, efforts to account for mean density and viscosity variations in the definition of the viscous length scale were made since the 1950s (Lobb et al., 1955), giving rise to the well-known semi-local wall-normal coordinate $y^* = y/\delta_\nu^*$ (where $\delta_\nu^* = \bar{\mu}/(\bar{\rho}u_\tau^*)$ is the semi-local viscous length scale). Much later, the companion papers by Huang et al. (1995) and Coleman et al. (1995) performed a comprehensive analysis where they showed that turbulence quantities show a much better collapse when reported as a function of y^* rather than y^+. Another major consequence of using the semi-local wall coordinate is reflected in mean velocity scaling. The 'semi-local' velocity transformation, derived independently by Trettel and Larsson (2016) using high-Mach-number channel flows and by Patel et al. (2016a) using low-Mach-number variable-property flows, extends the Van Driest transformation by accounting for variations in the semi-local viscous length scale. This transformation (also known as the TL transformation) can be written as

$$\bar{u}^* = \bar{U}_{TL}^+ = \int_0^{\bar{u}} \left(1 - \frac{y}{\delta_\nu^*}\frac{d\delta_\nu^*}{dy}\right) \underbrace{\frac{1}{u_\tau^*} d\bar{u}}_{d\bar{U}_{VD}^+}. \tag{1.11}$$

As we will see in chapter 5, because this transformation accounts only for variable-property effects, it is strictly applicable to low-Mach-number flows—such as those considered by Patel et al. (2016a).

These studies form the basis of the semi-local scaling framework, according to which, the friction velocity and viscous length scales are defined using mean properties as

$$u_\tau^* = \sqrt{\frac{\tau_w}{\bar{\rho}}}, \quad \delta_\nu^* = \frac{\bar{\mu}}{\bar{\rho}u_\tau^*}. \tag{1.12}$$

Analogous to incompressible flows, in chapter 6, we find that compressible flows are also governed by two distinct length scales: δ_ν^* in the inner layer and δ in the outer layer. These two layers share a common velocity scale u_τ^*, leading to a logarithmic region between them (figure 6.1). Some examples of inner- and outer-layer semi-locally scaled quantities are provided in table 7.1. Note that semi-local scaling in the outer layer, namely using u_τ^* and δ as characteristics scales, is also referred to as **Van Driest** scaling. Also note that semi-local scaling will be denoted using a superscript '$*$' for the inner layer and '$\circledast$' for the outer layer.

As outlined above, the law of the wall for incompressible flows plays a foundational role in turbulence modeling. Thus, considerable effort has been devoted to establishing an analogous law for compressible flows (Zhang et al., 2012), which would then directly benefit both mixing-length models (chapter 6) and transport-equation-based turbulence models (chapter 7).

Several mean velocity scalings in compressible flows have been derived based on the semi-local scaling framework—for instance, the Van Driest and the semi-local transformations just discussed. The Van Driest transformation has proven to be effective in adiabatic flows, however, its accuracy reduces in flows with heat transfer at the wall (Bradshaw, 1977; Huang and Coleman, 1994; Trettel and Larsson, 2016; Patel et al., 2016a; Griffin et al., 2021). This is also clear from figure 1.5(a), which plots the Van Driest transformed profiles as a function of $y^+ = y/\delta_\nu$ for a wide range of channel flow and boundary layer cases described in the caption (and also in table 2.3). As seen, the

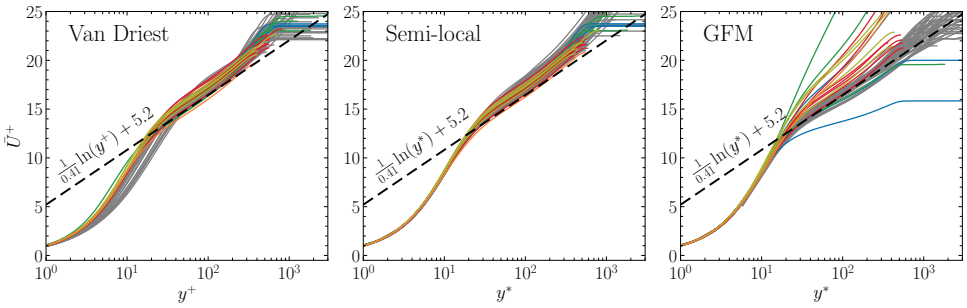

Figure 1.5: The mean velocity profiles after (a) Van Driest (VD), (b) semi-local (TL), and (c) GFM transformations for the channel flow and boundary layer cases described later in table 2.3. These cases include adiabatic and diabatic air-like ideal-gas channels and boundary layers, as well as ideal-gas channels and boundary layers with non-air-like viscosity behaviour—where the dynamic viscosity does not follow air-like laws such as a power-law, $\tilde{\mu}/\mu_w = (\tilde{T}/T_w)^{0.75}$, or Sutherland's law, but instead follows a non-conventional behavior, for e.g., $\tilde{\mu}/\mu_w = (\tilde{T}/T_w)^{-0.5}$—, and non-ideal-fluid cases such as supercritical flows. The conventional air-like cases are denoted using gray lines, and the remaining non-conventional cases are represented using colored lines, where the line color corresponds to the color of the symbols associated with each respective author; see table 2.3. The dashed black lines correspond to the incompressible law of the wall.

collapse is poor, especially in the viscous sublayer and the buffer layer. This is because the Van Driest transformation does not account for changes in the viscous length scale (δ_ν^*), which can vary significantly, especially in diabatic flows. In fact, since viscosity (or δ_ν^*) variations are not accounted for, Van Driest's transformation is best applied in the outer layer as a function of y/δ (Fernholz and Finley, 1980); see also chapter 6.

The semi-local velocity transformation ($\bar{u}^*$) extends the Van Driest transformation by accounting for δ_ν^* variations. When plotted as a function of the semi-locally scaled wall-normal coordinate $y^* = y/\delta_\nu^*$, $\bar{u}^*$ collapses onto the incompressible law of the wall for low-Mach number (Patel et al., 2016a) and high-Mach number (Trettel and Larsson, 2016) channel flows. However, this transformation loses accuracy for high-Mach number boundary layers (Patel et al., 2016a; Trettel and Larsson, 2016; Griffin et al., 2021). Figure 1.5(b) plots this transformation for a range of channel flow and boundary layer cases described in the caption. While we see an improvement with respect to the VD transformation in the viscous sublayer and buffer layer—since δ_ν^* variations are accounted for—the profiles in the log-layer are still inaccurate depicting an upward shift with respect to the incompressible law of the wall.

Zhang et al. (2018) suspected this shift in the semi-local profiles to be an effect caused by the wake region on the inner layer. This naturally leads to the question of why a similar wake effect is absent in incompressible flows. On the other hand, Griffin et al. (2021) argued that, in the region where the semi-local transformation fails, i.e. the log-layer, the viscous shear stress (whose integration leads to the semi-local velocity profiles, i.e., $\bar{u}^* = \int_0^{y^*} (\bar{\mu} d\bar{u}/dy)/\tau_w dy^*$) is close to zero, such that even small differences in the absolute stress values can lead to unbounded percent errors. In other words, high relative errors in the viscous shear stress might explain why the velocity profiles do not collapse. However, such an argument related to high relative error questions the robustness of the incompressible law of the wall itself, which is

also based on the universality of the viscous shear stress in the entire inner layer, i.e., $\bar{u}^+ = \int_0^{y^+} (\mu_w d\bar{u}/dy)/\tau_w dy^+$ (Bradshaw and Huang, 1995).

Several other mean velocity transformations have been proposed in the literature, to further improve the Van Driest (Zhang et al., 2012) and semi-local transformations (Volpiani et al., 2020b; Griffin et al., 2021; Lee et al., 2023). Of these, the one proposed by Griffin et al. (2021) (hereafter GFM) is widely used and has shown promising results for ideal gas air flows. Figure 1.5(c) presents the GFM transformation for a range of channel flow and boundary layer cases described in the caption (see also table 2.3). While the results improve for the air-like ideal-gas conventional cases (gray lines), they deteriorate for ideal-gas cases with a non-air-like viscosity behavior and for non-ideal-gas cases such as those involving supercritical fluids (colored lines). A similar behavior for non-ideal-gas flows was observed by Bai et al. (2022). The reader is referred to chapter 5 for further details on the reduced accuracy of GFM scaling in non-conventional flows.

Among the various transformations listed above, the semi-local transformation shows a better overall performance over a wide range of cases (figure 1.5b; see also Bai et al. (2022) for comparisons with other transformations not shown in figure 1.5). Yet, a convincing explanation for why it fails in the logarithmic region of high-Mach-number flows is missing.

Similar shortcoming in achieving a universal collapse under the semi-local framework is also observed for other turbulence quantities—for instance, the streamwise Reynolds stress. Specifically, it has been reported in the literature that the peak of semi-locally-scaled streamwise Reynolds stress is higher in compressible flows than in incompressible flows, despite having similar Reynolds numbers (Gatski and Erlebacher, 2002; Pirozzoli et al., 2004; Foysi et al., 2004; Duan et al., 2010; Modesti and Pirozzoli, 2016; Zhang et al., 2018; Cogo et al., 2022, 2023).

Therefore, an important question arises: **could such failures in achieving a universal collapse be due to effects that are consistently neglected under Morkovin's hypothesis—most importantly, intrinsic compressibility effects?** In order to address this question, it is first necessary to review the literature on IC effects.

1.1.2. INTRINSIC COMPRESSIBILITY EFFECTS

Compared to the vast literature available on variable-property effects in low-Mach (Patel et al., 2015, 2016a, 2017; Pecnik and Patel, 2017; Modesti and Pirozzoli, 2024) and high-Mach number flows (Van Driest, 1951; Morkovin, 1962; Huang et al., 1995; Coleman et al., 1995; Maeder et al., 2001; Morinishi et al., 2004; Foysi et al., 2004; Duan et al., 2010, 2011; Modesti and Pirozzoli, 2016; Zhang et al., 2018; Cogo et al., 2022; Zhang et al., 2022; Wenzel et al., 2022; Cogo et al., 2023), less studies have focused on intrinsic compressibility effects, possibly due to the belief that Morkovin's hypothesis holds even for hypersonic flows (Duan et al., 2011; Zhang et al., 2018).

Recently, significant progress has been made towards understanding IC effects, particularly attributed to the series of publications by Yu and co-workers (Yu et al., 2019, 2020; Yu and Xu, 2021), who analysed these effects in channel flows through direct numerical simulations (DNS). They performed a Helmholtz decomposition of the velocity field (see Appendix A) and mainly focused on dilatational motions and their direct contribution to several turbulence statistics. Their main observations were: (1) intrinsic compressibility effects, if present, are likely concentrated in the near-wall region, where

the wall-normal dilatational velocity field exceeds the solenoidal counterpart; (2) the correlation between the solenoidal streamwise and the dilatational wall normal velocity is negative and can constitute up to 10% of the total shear stress; (3) this negative correlation was attributed to the opposition of sweeps near the wall by dilatational motions; and (4) the dilatation field (and thus the dilatational velocity) exhibits a travelling wave-packet-like structure, whose origin is yet unknown (see also Tang et al., 2020; Gerolymos and Vallet, 2023; Yu et al., 2024).

The aforementioned studies mainly focus on the direct IC effects—those that are reflected directly in the dilatational component of velocity. However, it is so far unclear how important are the indirect IC effects—those that are observed in the solenoidal (vortical) component of velocity. This is particularly important to study, since any IC effect on the mean velocity or the streamwise Reynolds stress (as noted above), which are largely solenoidal[13], must be an indirect effect.

Studying indirect IC effects on the solenoidal component of velocity is challenging, since variable-property effects mainly reside in this component. Thus, it would be impossible to differentiate whether an effect on the vortical velocity field is a variable-property effect or an intrinsic compressibility one. In order to study these effects without any variable-property influence, we would need to perform tailored "unphysical" simulations that would in principle isolate IC effects. There are two ways prescribed in the literature to achieve this. One, attributed to Lele (1994), who advocates simulating low-Mach-number flows having similar mean property distributions as in a high-Mach-number flow. Upon comparing the two flows, one can isolate effects that occur only at high Mach numbers, i.e. IC effects. Another method is attributed to Coleman et al. (1995) who advocate nullifying variable-property effects, such that IC effects are isolated. They introduce a source term in their DNS of channel flows, which balances the heat generated due to viscous heating, thereby achieving flows at high Mach numbers but with approximately constant mean properties. Here, we follow the latter approach which is simpler compared to Lele's, since achieving a low-Mach flow with properties matching a high-Mach one is challenging[14]. We will discuss Coleman's approach further in chapter 2.

1.2. OBJECTIVES

In this work, we aim to study intrinsic compressibility (IC) effects whose impact has often been overlooked or incorrectly attributed to mean property variations. The primary challenge in investigating these effects lies in distinguishing them from variable-property effects. In this thesis, we simulate tailored cases at high Mach numbers, with approximately constant mean properties, whereby IC effects are isolated. Having isolated these effects, the **first part** of this thesis focuses on understanding the physics associated with IC effects. Building upon the physical insights gained from the tailored, non-physical cases, the **second part** of this thesis develops novel scaling laws and turbulence model corrections that are applicable to a wide range of conventional cases reported in the literature. Specifically, our objectives are:

[13] The Reynolds stresses are mainly contributed by solenoidal velocity fluctuations (Yu et al., 2019).

[14] One would need to prescribe heat sources in the energy equation of a low-Mach-number flow which results in mean property distributions as in a high-Mach-number flow. The procedure described in section 2.2 could be used to generate such heat source distributions.

1. To perform tailored direct numerical simulations that isolate IC effects (chapter 2).
2. To study the influence of IC effects on the mean velocity profiles, and to explain the observed influence using various turbulence statistics (chapter 3).
3. To investigate the physical mechanism through which these effects modulate the near-wall vortical dynamics (chapter 3).
4. To account for IC and variable-property effects in the scaling of turbulence statistics such as the wall-pressure r.m.s. and the peak of streamwise Reynolds stress (chapter 4).
5. To derive a mean velocity scaling (transformation) incorporating these effects (chapter 5).
6. To improve the existing turbulence modeling techniques based on the proposed mean velocity scaling. Specifically:
   (a) To predict full mean velocity and temperature profiles, and skin-friction and heat transfer coefficients in turbulent boundary layers (chapter 6).
   (b) To derive compressibility corrections for turbulence models accounting for both variable-property and IC effects (chapter 7).

Objectives 2 and 3 are addressed in the first part of this thesis, whereas objectives 4 to 6 are addressed in the second part.

1.3. OUTLINE

Following this introduction, the thesis is structured as follows.

Chapter 2 presents the setup used for simulating high-Mach-number constant-property (CP) channel flows, along with specific non-conventional variable-property cases. It also lists several zero-pressure-gradient boundary layer and channel flow cases from the literature, which are used to test the scaling laws and models developed in this work.

Part I: Theory

Chapter 3, using the CP cases described in chapter 2, analyzes the influence of IC effects on the mean velocity profiles. It then examines key turbulence statistics—such as turbulent stresses, pressure-strain correlation, and coherent structures—and attributes the changes in mean velocity profiles to the weakening of quasi-streamwise vortices. Finally, based on the insights from incompressible turbulence, it explains the physical mechanism responsible for this weakening.

Part II: Scaling laws and predictive models

Chapter 4 presents a framework for incorporating IC effects, alongside variable-property effects, into the development of scaling laws for turbulence statistics such as the wall-pressure r.m.s. and the streamwise Reynolds stress peak.

Chapter 5, based on the CP cases, assesses whether the log-law shift observed in the semi-local transformation (figure 1.5b) is due to IC effects. Consequently, it proposes a velocity transformation which accounts for these effects, in addition to variable-property effects.

The following two chapters build upon the proposed velocity transformation to improve the state-of-the-art turbulence predictive techniques. Specifically:

Chapter 6 utilizes a mixing-length eddy-viscosity model, together with an outer-layer wake function to derive a mean shear equation that is valid in the entire boundary layer. This equation—coupled with a temperature-velocity relation—predicts full mean velocity and temperature profiles, and skin-friction and heat transfer coefficients in high-speed turbulent boundary layers.

Chapter 7 proposes a novel approach to derive compressibility corrections through which any incompressible turbulence model can be extended for compressible flows.

Chapter 8 provides concluding remarks and an outlook for future studies.

2

COMPUTATIONAL APPROACH AND CASE DESCRIPTION

Parts of this chapter have been published as:
Hasan, A. M., Costa, P., Larsson, J., Pirozzoli, S., and Pecnik, R. (2025). Intrinsic compressibility effects in near-wall turbulence. *Journal of Fluid Mechanics*, 1006:A14.

In order to investigate turbulence in high-speed wall-bounded flows, we perform direct numerical simulations (DNS) by solving the compressible Navier-Stokes equations in conservative form, given as

$$\begin{aligned} \frac{\partial \rho}{\partial t} + \frac{\partial \rho u_i}{\partial x_i} &= 0, \\ \frac{\partial \rho u_i}{\partial t} + \frac{\partial \rho u_i u_j}{\partial x_j} &= -\frac{\partial p}{\partial x_i} + \frac{\partial \tau_{ij}}{\partial x_j} + f\delta_{i1}, \\ \frac{\partial \rho E}{\partial t} + \frac{\partial \rho u_j E}{\partial x_j} &= -\frac{\partial p u_j}{\partial x_j} - \frac{\partial q_j}{\partial x_j} + \frac{\partial \tau_{ij} u_i}{\partial x_j} + f u_1 + \Phi. \end{aligned} \tag{2.1}$$

The viscous stress tensor and the heat flux vector are given as

$$\tau_{ij} = \mu\left(\frac{\partial u_i}{\partial x_j} + \frac{\partial u_j}{\partial x_i} - \frac{2}{3}\frac{\partial u_k}{\partial x_k}\delta_{ij}\right), \; q_j = -\lambda\frac{\partial T}{\partial x_j}, \tag{2.2}$$

where u_i is the velocity component in the i^{th} direction, and where $i = 1,2,3$ corresponds to the streamwise (x), wall-normal (y) and spanwise (z) directions, respectively. ρ is the density, p the pressure, $E = c_v T + u_i u_i/2$ the total energy per unit mass, μ the viscosity, λ the thermal conductivity and $Pr = \mu c_p/\lambda$ the Prandtl number. c_p and c_v indicate specific heats at constant pressure and constant volume, respectively. f is a uniform body force that is adjusted in time to maintain a constant total mass flux in periodic flows (e.g., a fully developed turbulent channel or pipe). Φ is a source term that can be adjusted to achieve desired variations in mean temperature and fluid properties.

We perform DNS of fully developed channel flows by solving (2.1) using a high-order finite-difference code `STREAmS` (Bernardini et al., 2021). The domain is periodic in the streamwise and spanwise directions, while at the walls an isothermal boundary condition is used for temperature, and a zero normal gradient is specified for pressure.

The fluid used in the simulations is modeled as a calorically perfect ideal gas (constant specific heat capacities, c_p and c_v) with the specific heat ratio, $\gamma = c_p/c_v$ of 1.4. The fluid is assumed to have an air-like Prandtl number of 0.7 which is constant in the domain, and the viscosity is assumed to either follow an air-like (Sutherland, or exponential $(\tilde{T}/T_w)^{0.75}$) or a non-air-like (exponential $(\tilde{T}/T_w)^{-0.5}$) behaviour.

2.1. CONSTANT-PROPERTY CASES

As outlined in chapter 1, herein we attempt to remove mean property gradients to isolate intrinsic compressibility effects. For that purpose, we follow the approach presented by Coleman et al. (1995), whereby the energy equation is augmented with a source term

$$\Phi = -\tau_{ij}\frac{\partial u_i}{\partial x_j} \tag{2.3}$$

that counteracts the effects of viscous dissipation. Consequently, the mean internal energy remains approximately uniform across the entire domain. For an ideal gas, this implies that the mean temperature is also approximately constant, which, when combined with a uniform mean pressure, leads to a nearly uniform mean density. Furthermore, the mean dynamic viscosity and mean thermal conductivity are also

Case name	M_b	M_{cl}	M_τ	Re_τ	Re_{τ_c}	Line colour
Mach 0.3	0.3	0.34	0.0162	556	556	
Mach 2.28	2.28	2.59	0.1185	546	539	
Mach 3	3.0	3.37	0.1526	547	527	
Mach 4	4.0	4.47	0.1968	544	513	

Table 2.1: Description of the constant-property high-Mach-number cases simulated in this thesis. $M_b = U_b/\sqrt{\gamma R T_w}$ is the bulk Mach number, $M_{cl} = U_c/\sqrt{\gamma R T_c}$ is the channel centreline Mach number and $M_\tau = u_\tau/\sqrt{\gamma R T_w}$ is the wall friction Mach number. $Re_\tau = \rho_w u_\tau h/\mu_w$ is the friction Reynolds number based on the channel half-height h and Re_{τ_c} corresponds to the value of the semi-local friction Reynolds number ($Re^*_\tau = \bar{\rho} u^*_\tau h/\bar{\mu}$) at the channel centre.

uniform. However, it is important to note that the simulations still permit fluctuations of these properties—primarily along isentropes, as we will see below.

Using this approach, four cases with increasing Mach numbers are simulated, as presented in table 2.1. These simulations are performed using an air-like power law for viscosity with an exponent of 0.75. Since the four cases have similar Re_τ values, we use the same grid for all simulations. The computational grid consists of $n_x = 1280$, $n_y = 480$ and $n_z = 384$ points for a domain of size $L_x = 10h$, $L_y = 2h$ and $L_z = 3h$, where h is the channel half-height. This gives a near-wall resolution of $\Delta x^+ = 4.3$ and $\Delta z^+ = 4.3$. The grid in the wall-normal direction is stretched in such a way that $y^+ \leq 1$ is achieved for the first grid point.

Figure 2.1 shows the mean density, viscosity, and semi-local Reynolds number profiles for the four cases introduced in table 2.1. The figure also shows the profiles of a conventional boundary layer at a free-stream Mach number of 14, taken from Zhang et al. (2018). Compared to the conventional $M_\infty = 14$ boundary layer case, our cases show little to no variation in mean properties. This implies that mean heat transfer effects are indeed negligible in the present cases.

To determine whether other heat transfer effects associated with changes in fluid volume as a result of changes in entropy are important, we compute density fluctuations using the isentropic relation

$$\frac{\rho^{is}_{rms}}{\bar{\rho}} \approx \frac{1}{\gamma}\frac{p_{rms}}{\bar{p}}, \tag{2.4}$$

and compare it with the density fluctuations obtained from DNS in figure 2.2(a). With the exception of the viscous sublayer, the two distributions appear to collapse, which implies that other heat transfer effects are also negligible in the present cases. Hence, any deviations from incompressible flows observed in these cases should be attributed to intrinsic compressibility effects.

Figure 2.2(a) also shows the total and isentropic density fluctuations for the $M_\infty = 14$ flow case computed by Zhang et al. (2018). As can be seen, the total density fluctuations are much higher than the isentropic ones in the buffer layer and beyond. This suggests that a significant portion of the density fluctuations is also caused by heat transfer effects, such as passive mixing across mean density gradients or heat-induced volume changes, corroborating that both heat transfer and intrinsic compressibility effects are important for the $M_\infty = 14$ case. Interestingly, our highest Mach number case (Mach 4) and Zhang's $M_\infty = 14$ boundary layer have similar isentropic density r.m.s. (or similar pressure r.m.s.). Given that the pressure r.m.s. scaled by mean pressure is an effective

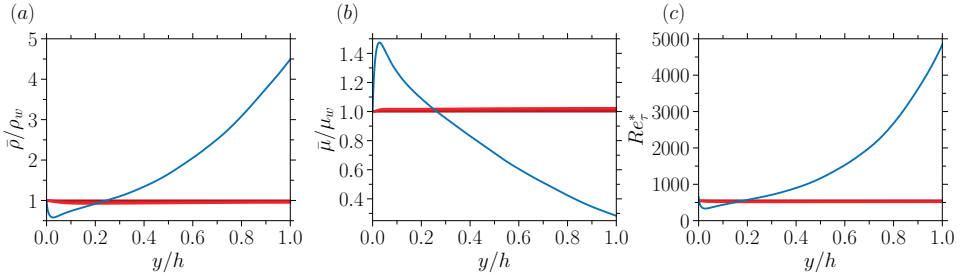

Figure 2.1: Wall-normal distributions of (a) density $\overline{\rho}$, (b) viscosity $\overline{\mu}$, and (c) the semi-local friction Reynolds number $Re^*_\tau = \bar{\rho} u^*_\tau h/\bar{\mu}$ for the cases described in table 2.1. The blue lines represent the $M_\infty = 14$ case of Zhang et al. (2018). These quantities are plotted as a function of the wall-normal coordinate scaled by the channel half-height for the channel flow cases, and by the boundary layer thickness (δ) for the $M_\infty = 14$ boundary layer case.

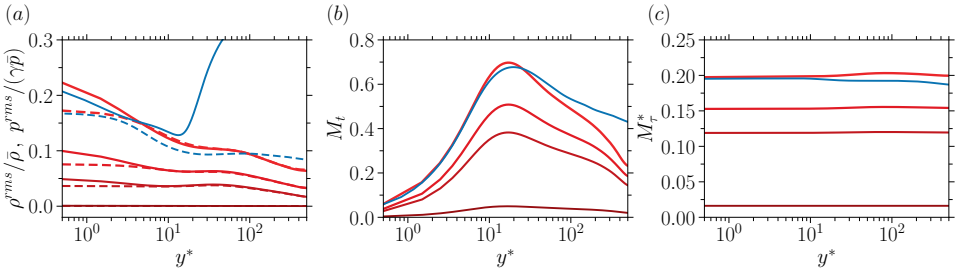

Figure 2.2: Wall-normal distributions of (a) the root-mean-square (r.m.s.) of the total (solid) and isentropic (dashed) density fluctuations (equation 2.4); (b) the turbulence Mach number $M_t = \sqrt{2k}/\sqrt{\gamma R \bar{T}}$; and (c) the semi-local friction Mach number $M^*_\tau = u^*_\tau/\sqrt{\gamma R \bar{T}}$ for the cases described in table 2.1. The blue lines represent the $M_\infty = 14$ case of Zhang et al. (2018).

measure of intrinsic compressibility effects (Coleman et al., 1995, see also chapter 1), we can expect that these effects are of comparable magnitude for our Mach 4 case and the conventional $M_\infty = 14$ boundary layer.

In addition to the pressure r.m.s., intrinsic compressibility effects can also be quantified in terms of Mach numbers. Figure 2.2(b) shows the turbulence Mach number, defined as $M_t = (\widetilde{u''_i u''_i}/\gamma R \bar{T})^{1/2}$, where the denominator is the local speed of sound for ideal gases. Three out of four cases are above the threshold of $M_t = 0.3$, above which intrinsic compressibility effects are considered important (Smits and Dussauge, 2006). Due to the inhomogeneous nature of wall-bounded flows, M_t is not constant throughout the domain, becoming zero at the wall where the pressure and density r.m.s. are the strongest as shown in figure 2.2(a).

Other parameters have been proposed in the literature as a better measure of intrinsic compressibility effects in wall-bounded flows, most prominently the friction Mach number $M_\tau = u_\tau/\sqrt{\gamma R T_w}$ (Bradshaw, 1977; Smits and Dussauge, 2006, also refer to chapter 5). When defined in terms of local properties, one obtains the semi-local friction Mach number

$$M^*_\tau = u^*_\tau/\sqrt{\gamma R \bar{T}}. \tag{2.5}$$

Case name	M_b	M_{cl}	M_τ	Re_τ	Re_{τ_c}	Line type
BL-like	1.73	2.8	0.100	495	1285	– – – –
Mach 2.28 non-air-like	2.28	1.8	0.111	559	558	·····
Mach 4 non-air-like	4	3.1	0.185	567	562	— — —
Mach 2.28 heat-source	2.28	1.88	0.104	801	360	———

Table 2.2: Description of the variable-property cases simulated in this thesis. Details corresponding to each column are provided in table 2.1.

Figure 2.2(c) shows the distribution of M_τ^* for the four CP cases and the Mach 14 case of Zhang et al. (2018). In contrast to M_t, the distribution of M_τ^* is nearly constant and equal to the wall value, M_τ, for both constant- and variable-property flows. This constant distribution is because in these flows $\bar{T}/T_w \approx \rho_w/\bar{\rho}$ (ideal gas assumption) such that

$$M_\tau^* = \frac{u_\tau^*}{\sqrt{\gamma R \bar{T}}} = \frac{u_\tau \sqrt{\rho_w/\bar{\rho}}}{\sqrt{\gamma R \bar{T}}} \approx \frac{u_\tau \sqrt{\bar{T}/T_w}}{\sqrt{\gamma R \bar{T}}} = \frac{u_\tau}{\sqrt{\gamma R T_w}} = M_\tau. \tag{2.6}$$

Since M_τ^* is uniform, its wall value M_τ can be directly used in developing scaling laws (see chapters 5 and 4)

It is interesting to note from figure 2.2(b) and (c) that the profiles of M_t and M_τ^* are equivalent for both the Mach 4 CP case and the conventional $M_\infty = 14$ case, similar to the isentropic density r.m.s. shown in figure 2.2(a).

2.2. VARIABLE-PROPERTY CASES

In addition to the constant-property compressible cases, we have also simulated three types of variable-property cases as presented in table 2.2. Similar to the CP cases, these cases are non-conventional or tailored, since they are simulated with external heat sources with an intention to achieve desired mean property profiles.

The first case is termed 'BL-like' since in this case, the heat source added is such that the mean property profiles in a channel flow resembles that of a boundary layer. The appropriate heat source to simulate such a case is obtained as follows:

1. Select a boundary layer whose property profiles are to be replicated.

2. Interpolate the mean property profiles of this case on to a channel flow mesh ($y/\delta \rightarrow y/h$).

3. Using these interpolated property profiles, solve the semi-locally scaled RANS equations in a channel flow (see chapter 7) to obtain the eddy viscosity μ_t.

4. Using this μ_t along with the turbulent Prandtl number $Pr_t = 0.9$, compute a heat source Ψ as

$$\Psi = \frac{d}{dy}\left[\left(\frac{\bar{\mu} c_p}{Pr} + \frac{\mu_t c_p}{Pr_t}\right)\frac{d\bar{T}}{dy}\right],$$

   where the thermophysical properties ($\bar{\mu}$, c_p, Pr) and the mean temperature ($\bar{T}$) are taken from the DNS of the boundary layer to be replicated.

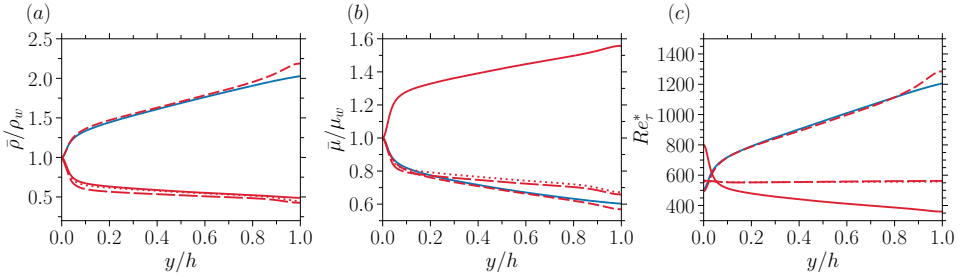

Figure 2.3: Wall-normal distributions of (a) density $\overline{\rho}$, (b) viscosity $\overline{\mu}$, and (c) the semi-local friction Reynolds number $Re^*_\tau = \bar{\rho} u^*_\tau h/\bar{\mu}$ for the cases described in table 2.2. The blue lines represent the $M_\infty = 2.5$ case of Zhang et al. (2018). These quantities are plotted as a function of the wall-normal coordinate scaled by the channel half-height for the channel flow cases, and by boundary layer thickness (δ) for the $M_\infty = 2.5$ boundary layer case.

5. Set up a DNS simulation with $\Phi = \Psi - \tau_{ij}\partial u_i/\partial x_j$ as the extenal heat source in the energy equation. Subtracting the aerodynamic heating term is important to get the desired temperature profile.

Using this procedure, we replicated the $M_\infty = 2.5$ air-like case of Zhang et al. (2018). The property profiles for the tailored channel case, along with the boundary layer case are plotted in figure 2.3. As seen, the profiles in the channel flow case (short-dashed red lines) closely follow those in the boundary layer (solid blue lines), thereby validating our approach.

The primary motivation for simulating this case was to test the hypothesis that the log-law shift observed under the semi-local transformation in boundary layers (figure 1.5b) arises from the influence of the wake region (Zhang et al., 2018)—an effect typically absent in channel flows. However, our findings show that the velocity profile of the BL-like channel flow case depicts a similar log-law shift as the replicated boundary layer (not shown), thereby disproving this hypothesis (see also chapter 5).

In the second set of cases (non-air-like), the viscosity law is adjusted such that the local Reynolds number (Re^*_τ) is approximately constant in the domain (Patel et al., 2015). Specifically, instead of following the air-like viscosity law of $(\bar{T}/T_w)^{0.75}$, these cases follow $(\bar{T}/T_w)^{-0.5}$. Figure 2.3 shows the corresponding property profiles for these cases (see dotted and long-dashed red lines). As seen from subfigure (c), the semi-local Reynolds number is almost uniform for these cases.

The primary objective of simulating these cases is to assess the robustness of the mean velocity scaling developed in chapter 5 with respect to variations in the viscosity law. Specifically, the aim is to verify that the proposed scaling remains valid irrespective of the underlying viscosity-temperature relationship—a criterion not satisfied by several state-of-the-art velocity transformations (Volpiani et al., 2020a; Griffin et al., 2021).

The final case in table 2.2 corresponds to an ideal-gas flow with an air-like viscosity law, but with arbitrary heat sources added to the energy equation. The resulting property profiles are shown in figure 2.3 (solid red lines). The primary objective of this case is to demonstrate the robustness of the mean velocity scaling with respect to non-physical, arbitrarily imposed heat sources.

In addition to the cases presented above, this thesis will also utilize the data provided

by several authors in the literature. Table 2.3 provides an overview of all the cases referenced in this thesis, along with the chapters in which they are used. A visual summary of these cases is presented in figure 2.4.

Source	# of cases	Chapter #	Type	Re_τ	M_∞, M_b	M_τ	T_w/T_r	Symbol
Boundary layer								
Bernardini and Pirozzoli (2011)	9	1, 4, 5, 6, 7	Conventional	205-1113	2-4	0.065-0.105	1	☆
Zhang et al. (2018)	3	1, 4, 5, 6, 7	Conventional	450-646	2.5-13.64	0.085-0.195	0.18-1	✚
Hirai et al. (2021)	3	1, 5	Non-air-like	504-641	2.28	0.065-0.089	0.5-2	○
Ceci et al. (2022)	6	1, 4, 5, 6, 7	Conventional	500-1000	5.84	0.149-0.167	0.25	◇
Huang et al. (2022)	2	1, 4, 5, 6, 7	Conventional	775, 1172	10.9	0.167, 0.182	0.2	✚
Cogo et al. (2022)	4	1, 4, 5, 6, 7	Conventional	453, 1947	2, 5.86	0.066-0.132	0.76	✖
Cogo et al. (2023)	12	1, 4, 5, 7	Conventional	443	2-6	0.075-0.159	0.35-1	✖
A. Ceci (Private Comm.)	2	1, 4, 5, 6, 7	Conventional	450, 475	5.84, 7.87	0.129, 0.152	0.48, 0.76	△
J. Larsson (Private Comm.)	3	1, 5	Non-air-like	473-710	2.28	0.078-0.100	0.3, 1	○
J. Larsson (Private Comm.)	2	1, 5	Conventional	469, 816	2.28	0.079, 0.096	0.3, 1	☆
Channel								
Trettel and Larsson (2016)	9	1, 4, 5, 7	Conventional	322-1876	0.7-4	0.036-0.118	-	▽
Sciacovelli et al. (2017)	4	1, 4, 5	Dense-gas	402-692	1.5-3	0.08-0.15	-	▲
Patel et al. (2016a)	1	7	Low-Mach	395	0	0	-	▽
Pecnik and Patel (2017)	1	7	Low-Mach	950	0	0	-	▽
Yu et al. (2019)	6	1, 5	T_b-controlled	494-528	0.77-2.52	0.042-0.135	-	□
Yu and Xu (2021)	2	1, 5	T_b-controlled	450, 504	2.52, 3.58	0.146, 0.178	-	□
Toki et al. (2020)	1	1, 5	Supercritical	384	≈ 0	≈ 0	-	△
Modesti and Pirozzoli (2024)	13	4	Low-Mach	356-3202	≈ 0	≈ 0	-	△
Present	4	1, 3, 4, 5	CP	544-556	0.3-4	0.016-0.197	-	★
Present	1	1, 5	BL-like	495	1.73	0.100	-	✚
Present	2	1, 5	Non-air-like	559, 567	2.28, 4	0.111, 0.185	-	○
Present	1	1, 5	Heat-source	801	2.28	0.104	-	◇

Table 2.3: Description of the cases that will be analysed in this thesis. The chapter(s) where they appear are shown in the third column. The fourth column depicts the type of cases. 'Conventional' corresponds to the ideal-gas air-like boundary layers and channel flows commonly found in the literature. 'Non-air-like' signifies ideal-gas cases with a non-air-like viscosity law. 'Dense-gas' and 'Supercritical' corresponds to the non-ideal-fluid cases close to the critical point. 'Low-Mach' corresponds to the variable-property cases at zero or approximately zero Mach numbers. 'T_b-controlled' corresponds to the cases in which external heat sources are added so as to achieve a desired and constant bulk temperature. 'CP' corresponds to the constant-property cases discussed in table 2.1. 'BL-like' represents channel flow cases where external heat sources are added to reproduce property profiles of a boundary layer (see table 2.2). Finally, 'Heat-source' represents a case with arbitrary heat sources. $Re_\tau = \rho_w u_\tau h/\mu_w$ is the friction Reynolds number based on the boundary layer thickness δ or the channel half-height h. $M_\infty = U_\infty/\sqrt{\gamma R T_\infty}$ is the free-stream Mach number (for boundary layers), $M_b = U_b/\sqrt{\gamma R T_w}$ is the bulk Mach number (for channel flows), and $M_\tau = u_\tau/\sqrt{\gamma R T_w}$ is the wall friction Mach number. T_w/T_r is the wall-cooling parameter, with T_r being the adiabatic temperature. These cases are visually represented in figure 2.4.

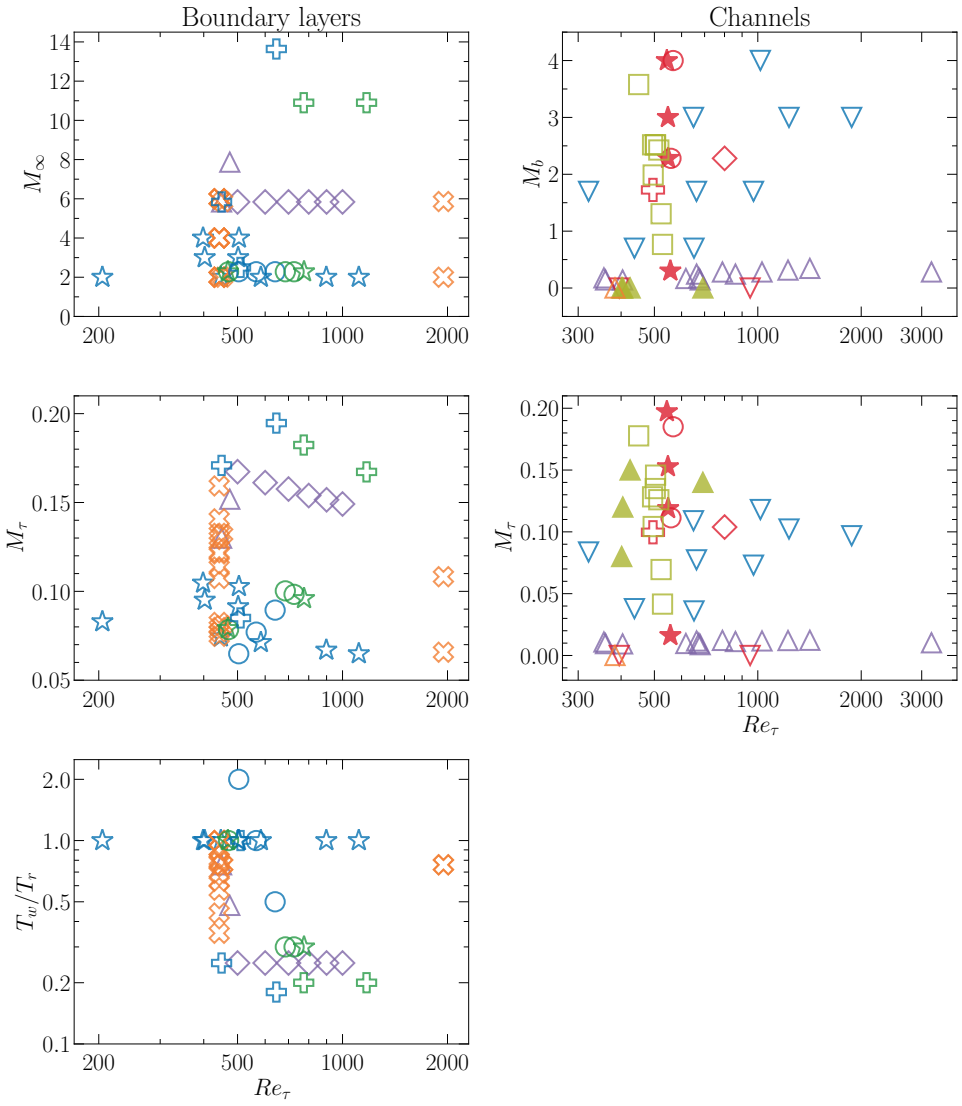

Figure 2.4: A visual representation of the cases described in table 2.3.

3

IC EFFECTS IN NEAR-WALL TURBULENCE: PHYSICAL MECHANISM

In this chapter, we assess intrinsic compressibility (IC) effects using constant-property compressible (CP) cases that are specifically designed to isolate such effects. These cases reveal that IC effects yield a significant upward shift in the logarithmic mean velocity profile (similar to that observed in figure 1.5b) that can be attributed to the reduction in the turbulent shear stress. This reduction stems from the weakening of the near-wall quasi-streamwise vortices. We in turn attribute this weakening to the spontaneous opposition of sweeps and ejections from the near-wall expansions and contractions of the fluid, and provide a theoretical explanation for this mechanism. Our results also demonstrate that intrinsic compressibility effects play a crucial role in the increase in inner-scaled streamwise turbulence intensity in compressible flows, as compared to incompressible flows, which was previously regarded to be an effect of mean property variations alone.

The contents of this chapter have been published as:
Hasan, A. M., Costa, P., Larsson, J., Pirozzoli, S., and Pecnik, R. (2025). Intrinsic compressibility effects in near-wall turbulence. *Journal of Fluid Mechanics*, 1006:A14.

3.1. INTRODUCTION

Understanding the impact of compressibility effects on turbulent flow is crucial for a wide range of engineering applications, as it influences the performance and efficiency of aerospace vehicles, gas turbines, combustion processes, and high-speed propulsion systems. As outlined in chapter 1, compressibility effects in wall-bounded turbulent flows can be classified into two main branches. The first involves effects related to heat transfer, often referred to as variable-property effects. The second branch is associated with changes in fluid volume in response to changes in pressure, also termed intrinsic compressibility (IC) effects. While variable-property effects can be significant at any, or even at zero, Mach number, intrinsic compressibility effects become important only at high Mach numbers.

In 1962, Morkovin postulated that intrinsic compressibility effects (among other effects; see chapter 1) are insignificant, and that only mean fluid property variations matter for compressible flows. If this hypothesis holds, then turbulence statistics in compressible flows can be collapsed onto their incompressible counterparts by simply accounting for mean property variations. This powerful implication of the hypothesis has led many compressible flow studies to focus mainly on variable-property effects (Van Driest, 1951; Morkovin, 1962; Huang et al., 1995; Coleman et al., 1995; Maeder et al., 2001; Morinishi et al., 2004; Foysi et al., 2004; Duan et al., 2010, 2011; Patel et al., 2015, 2016a; Modesti and Pirozzoli, 2016; Patel et al., 2017; Pecnik and Patel, 2017; Zhang et al., 2018; Cogo et al., 2022; Zhang et al., 2022; Wenzel et al., 2022; Cogo et al., 2023; Modesti and Pirozzoli, 2024). Compared to the vast literature on variable-property effects, the studies focused on IC effects are limited, possibly due to the belief that Morkovin's hypothesis holds even in the hypersonic regime (Duan et al., 2011; Zhang et al., 2018).

Recently, evidence on the importance of intrinsic (or 'genuine') compressibility effects in wall-bounded flows has been provided in a series of publications by Yu and co-workers (Yu et al., 2019, 2020; Yu and Xu, 2021), who analysed these effects in channel flows through direct numerical simulations (DNS). They performed a Helmholtz decomposition of the velocity field and mainly focused on dilatational motions and their direct contribution to several turbulence statistics. Their key findings (summarized in chapter 1, but reiterated here for convenience) are: (1) intrinsic compressibility effects, if present, are likely concentrated in the near-wall region, where the wall-normal dilatational velocity field exceeds the solenoidal counterpart; (2) the correlation between the solenoidal streamwise and the dilatational wall normal velocity is negative and can constitute up to 10% of the total shear stress; (3) this negative correlation was attributed to the opposition of sweeps near the wall by dilatational motions; and (4) the dilatation field (and thus the dilatational velocity) exhibits a travelling wave-packet-like structure, whose origin is yet unknown (see also Tang et al., 2020; Gerolymos and Vallet, 2023; Yu et al., 2024).

These studies mainly focus on the direct IC effects—those that are reflected directly in the dilatational component of velocity. However, the significance of the indirect IC effects—those observed in the solenoidal (vortical) component—remains unclear. It is important to quantify these effects to determine whether the log-law shift in the mean velocity profiles (figure 1.5b), and the higher peak of streamwise Reynolds stress in compressible flows compared to incompressible flows—discussed in chapter 1—are

caused by IC effects. Any such influence must be indirect, since both quantities are mainly constituted by the solenoidal component of velocity[1].

In this chapter, we will focus mainly on the indirect effects of intrinsic compressibility. We use our tailored constant-property cases (CP) described in table 2.1, whereby IC effects are isolated. With these cases, we first analyse the influence of these effects on the mean velocity profiles. Then, we look into various fundamental statistics of turbulence such as turbulent stresses, pressure-strain correlation, and into coherent structures, eventually tracing back the change in mean velocity profiles to the weakening of quasi-streamwise vortices. Subsequently, with the help of what is known from the incompressible turbulence literature, we provide a theoretical explanation as to why the vortices weaken.

3.2. INTRINSIC COMPRESSIBILITY EFFECTS ON TURBULENCE STATISTICS

In this section, we first present IC effects on the mean velocity profiles. Next, we relate the IC-induced changes in mean velocity to corresponding variations in turbulent shear stress and wall-normal turbulent stress. Finally, we explain the variations in wall-normal stress by analyzing the energy transfer from the streamwise to the other components. Unless otherwise stated, all quantities will be presented in their semi-locally scaled form. Nevertheless, since the CP cases have approximately constant mean properties, there is no major difference between the classical wall scaling (denoted by the superscript '+') and the semi-local scaling (denoted by the superscript '$*$').

3.2.1. LOG-LAW SHIFT IN THE MEAN VELOCITY PROFILES

Figure 3.1(a) shows the mean velocity profiles for the four CP cases. The velocity profile for the low-Mach number case ($M_b = 0.3$) collapses with the incompressible law of the wall. However, as the Mach number increases, a clear increase in the log-law intercept is observed. Due to roughly constant mean properties and negligible fluctuations generated by heat transfer (as discussed in chapter 2), the log-law shift can be solely attributed to intrinsic compressibility effects, which contradicts Morkovin's hypothesis.

Interestingly, a similar log-law shift was also oberved in the semi-locally transformed mean velocity profiles of the variable property cases (figure 1.5b). Analyzing whether the shift in those cases is also due to IC effects is the focus of chapter 5. Here, we continue to discuss the physics behind the observed log-law shift in figure 3.1(a).

3.2.2. OUTWARD SHIFT IN VISCOUS AND TURBULENT SHEAR STRESSES

In the inner layer of parallel (or quasi-parallel) shear flows, integration of the mean streamwise momentum equation implies that the sum of viscous and turbulent shear stresses is equal to the total shear stress, given as

$$\overline{\mu\left(\frac{\partial u}{\partial y}+\frac{\partial v}{\partial x}\right)}-\overline{\rho u'' v''}=\tau_{tot}, \tag{3.1}$$

[1]The mean velocity is largely solenoidal since the mean dilatation is negligible in wall-bounded flows. The streamwise Reynolds stress is also mainly contributed by the solenoidal velocity fluctuations (Yu et al., 2019), as also seen in section 3.2.6.

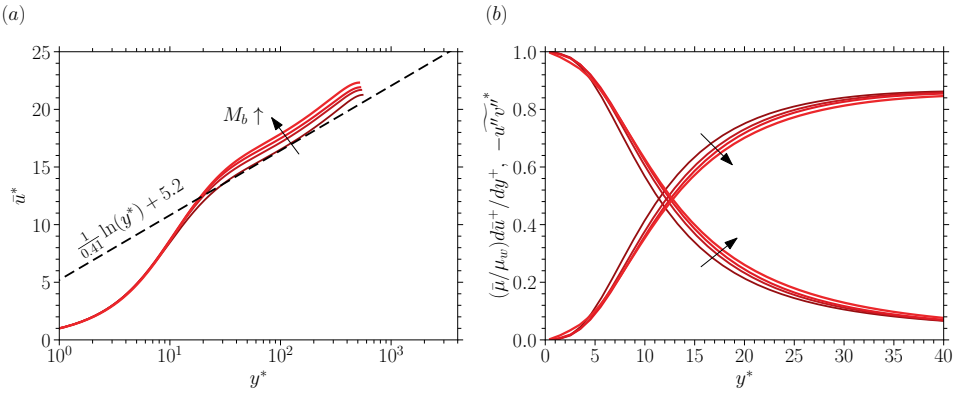

Figure 3.1: (a) The semi-locally-transformed mean velocity profiles (equations 1.11, 3.3), and (b) the viscous and turbulent shear stresses for the CP cases described in table 2.1. Since property variations are absent in these cases, the transformed velocity is equivalent to $\bar{u}^+$.

where $\tau_{tot} \approx \tau_w$ in zero-pressure-gradient boundary layers, whereas it decreases linearly with the wall distance in channel flows. Neglecting terms due to viscosity fluctuations and normalizing equation (3.1) by τ_w, we get for the latter case

$$\frac{\bar{\mu}}{\mu_w}\frac{d\bar{u}^+}{dy^+} - \widetilde{u''v''}^* \approx 1 - \frac{y}{h}, \tag{3.2}$$

where h is the channel half-height.

Integrating the viscous shear stress yields the semi-locally-transformed mean velocity profile (Trettel and Larsson, 2016; Patel et al., 2016a) as

$$\bar{u}^* = \int_0^{y^*} \frac{\bar{\mu}}{\mu_w}\frac{d\bar{u}^+}{dy^+}dy^*. \tag{3.3}$$

Based on equation (3.3), an upward shift in the mean velocity profile (figure 3.1a) corresponds to an equivalent upward shift (or increase) in the viscous shear stress. This is evident from figure 3.1(b). Since the total shear stress is universal for the four flow cases under inspection, an increase in the viscous shear stress directly implies a decrease in the turbulent shear stress. Indeed, figure 3.1(b) shows that the turbulent shear stress reduces with increasing Mach number. In other words, the log-law shift observed in figure 3.1(a) is a consequence of the modified damping of the turbulent shear stress.

3.2.3. OUTWARD SHIFT IN WALL-NORMAL REYNOLDS STRESS: CHANGE IN TURBULENCE ANISOTROPY

The outward shift in the turbulent shear stress corresponds to an outward shift in the wall-normal turbulent stress, because wall-normal motions directly contribute to turbulent shear stress by transporting momentum across the mean shear (Townsend, 1961; Deshpande et al., 2021). This is also reflected in the turbulent shear stress budget, whose production is controlled by the wall-normal turbulent stress (Pope, 2001).

Figure 3.2(b) shows profiles of the wall-normal turbulent stress. A clear outward shift is evident, which is consistent with the observed outward shift in the turbulent shear

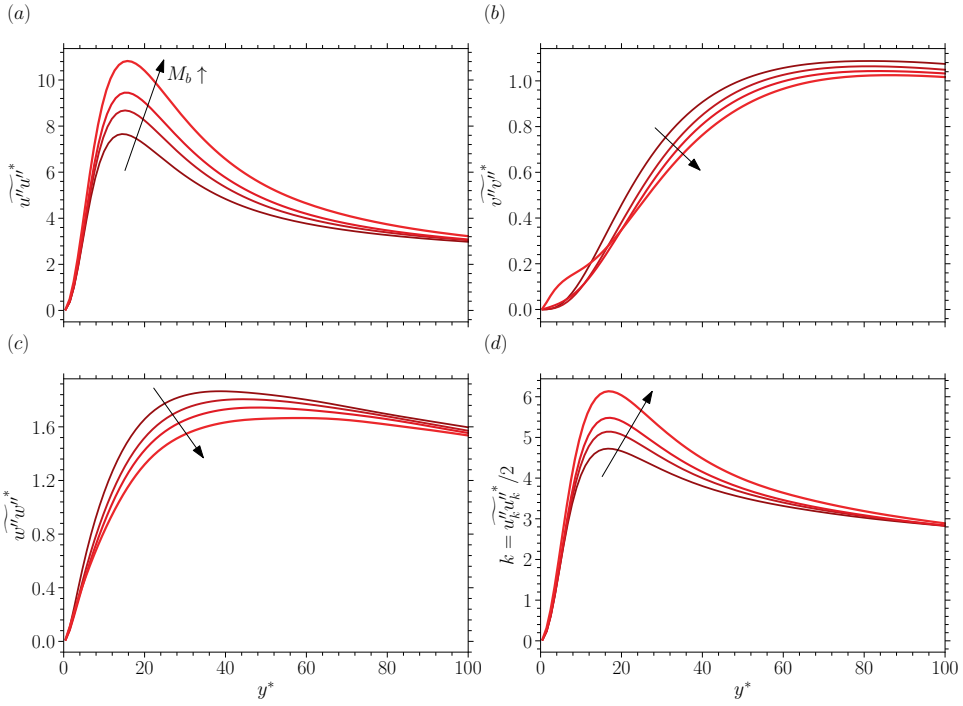

Figure 3.2: Wall-normal distributions of (a) streamwise, (b) wall-normal and (c) spanwise turbulent stresses, and (d) the turbulent kinetic energy (TKE) for the cases described in table 2.1.

stress. Now, the decrease in the wall-normal stress can either be due to less energy being received from the streamwise component (inter-component energy transfer), or due to an overall reduction of the turbulent kinetic energy (TKE). In order to clarify this, we report the streamwise and the spanwise turbulent stresses, along with the turbulent kinetic energy in panels (a), (c) and (d) of figure 3.2, respectively.

Figure 3.2(a) shows that the streamwise turbulent stress becomes stronger with increasing Mach number. The increase in the peak streamwise turbulence intensity in compressible flows, compared to incompressible flows at similar Reynolds numbers, has also been observed in several other studies (Gatski and Erlebacher, 2002; Pirozzoli et al., 2004; Foysi et al., 2004; Duan et al., 2010; Modesti and Pirozzoli, 2016; Zhang et al., 2018; Trettel, 2019; Cogo et al., 2022, 2023). However, these studies did not explicitly assess whether intrinsic compressibility effects play a role in peak strengthening. In fact, the higher peak observed in the $M_\infty = 14$ boundary layer was attributed to variable-property effects by Zhang et al. (2018). Our results instead demonstrate unambiguously that intrinsic compressibility effects play a central role in the strengthening of streamwise turbulence intensity, since our flow cases are essentially free of variable-property effects. Refer to chapter 4 for more details on the scaling of the peak streamwise turbulence intensity.

Similar to the wall-normal stress, the spanwise turbulent stress also decreases with increasing Mach number, shown in figure 3.2(c). The increase in the streamwise stress and the decrease in the wall-normal and spanwise stresses imply suppression of inter-component energy transfer with increasing Mach number. However, before discussing this in more detail in subsection 3.2.5, we take a slight detour and note that the increase in the streamwise turbulent stress is much more pronounced than the decrease in the other two components, which essentially results in an increase in the turbulent kinetic energy with Mach number as shown in figure 3.2(d). This suggests that, in addition to the change in intercomponent energy transfer, there is also a change in the production of $\widetilde{u''u''}^*$. We discuss this in more detail in the next subsection, where we present the budget of the streamwise turbulent stress, and provide a phenomenological explanation for the increase in $\widetilde{u''u''}^*$.

3.2.4. INCREASE IN THE STREAMWISE TURBULENCE INTENSITY

In order to explain the increase in the streamwise turbulent stress and hence in the turbulent kinetic energy, we consider the streamwise turbulent stress budget for a fully-developed compressible channel flow:

$$P_{11} + \epsilon_{11} + T^{\nu}_{11} + T^{u}_{11} + \Pi_{11} + C_{11} = 0, \tag{3.4}$$

where

$$\begin{aligned} P_{11} &= -2\overline{\rho u'' v''}\frac{\partial \widetilde{u}}{\partial y},\ \epsilon_{11} = -2\overline{\tau'_{1j}\frac{\partial u''}{\partial x_j}}, \\ T^{\nu}_{11} &= 2\frac{\partial}{\partial y}\left(\overline{\tau'_{12}u''}\right),\ T^{u}_{11} = -\frac{\partial}{\partial y}\left(\overline{\rho u'' u'' v''}\right), \\ \Pi_{11} &= 2\overline{p'\frac{\partial u'}{\partial x}},\ C_{11} = 2\overline{u''}\frac{\partial \bar{\tau}_{12}}{\partial y}. \end{aligned} \tag{3.5}$$

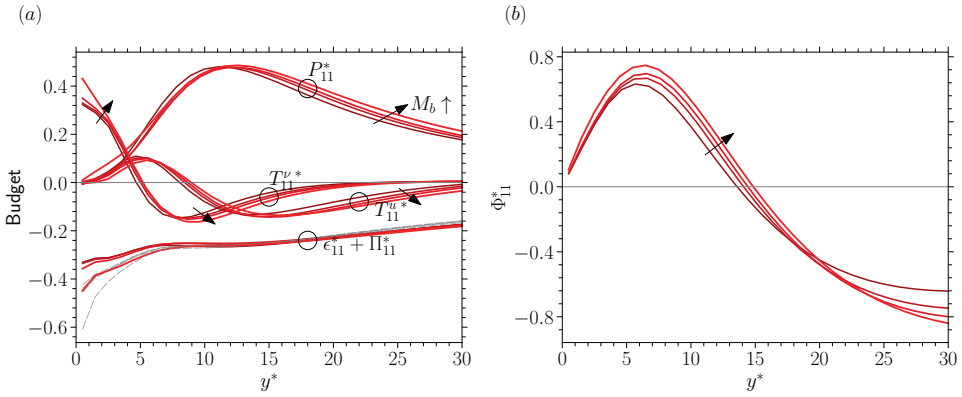

Figure 3.3: Wall-normal distributions of (a) the streamwise turbulent stress budget (see equation 3.4) scaled in semi-local units, and (b) the sum of viscous and turbulent fluxes obtained upon integrating the semi-locally scaled viscous and turbulent diffusion terms (see equation 3.8), for the cases described in table 2.1.

The distributions of the production, viscous and turbulent diffusion terms, and the sum of dissipation and pressure-strain correlation, are shown in figure 3.3, scaled by $\bar{\rho} u_\tau^{*3}/\bar{\mu}$. The compressibility term C_{11} is omitted because of its negligible magnitude.

Three observations can be made. First, there is an outward shift in P_{11}^* with increasing Mach number. Since the production term in scaled form is simply the product of the turbulent and viscous shear stresses, its outward shift is explained by the corresponding shift in the shear stresses in figure 3.1(b) as follows. Assuming that the total stress is approximately equal to τ_w, such that the sum of the scaled stresses is unity, one can substitute the viscous shear by the turbulent shear stress in P_{11} to obtain (Pope, 2001)

$$P_{11}^* \approx -2\widetilde{u''v''}^* \left(1 + \widetilde{u''v''}^*\right) = 2\left(-\widetilde{u''v''}^*\right) - 2\left(-\widetilde{u''v''}^*\right)^2. \tag{3.6}$$

Taking the derivative of P_{11}^* with respect to the turbulent shear stress yields

$$\frac{dP_{11}^*}{d\left(-\widetilde{u''v''}^*\right)} \approx 2 - 4\left(-\widetilde{u''v''}^*\right). \tag{3.7}$$

Between the wall and the location where $-\widetilde{u''v''}^*$ is equal to 0.5 the derivative is positive, while it is negative above this location. On the other hand, from figure 3.1(b), we observe that the rate of change of the turbulent shear stress with the Mach number, i.e. $\partial(-\widetilde{u''v''}^*)/\partial M_b$, at a fixed y^* is negative. Combining these two observations, we can conclude that the rate of change of production of the streamwise turbulent stress with the Mach number, i.e. $\partial P_{11}^*/\partial M_b$, is negative close to the wall and becomes positive away from it, resulting in an effective outward shift.

Second, except very close to the wall, the sum of the two sink terms in the budget of the streamwise turbulent stress (3.4), namely ϵ_{11}^* and Π_{11}^*, show a weak Mach number dependence. Interestingly, the TKE dissipation ($2\epsilon_k^* = \epsilon_{11}^* + \epsilon_{22}^* + \epsilon_{33}^*$), reported with grey dashed lines in figure 3.3, also shows marginal dependence on the Mach number. This

is consistent with the observation made in chapter 5 regarding the universality of the local Kolmogorov length scale. The universality of $\epsilon^*_{11}+\Pi^*_{11}$ and ϵ^*_k are related as follows. Any Mach-number-dependent reduction in Π^*_{11} would imply that less energy is being received by the lateral turbulent stresses, and hence, less TKE is being dissipated through the terms $\epsilon^*_{22}+\epsilon^*_{33}$. This suggests that the Mach-number-dependence of Π^*_{11} and $\epsilon^*_{22}+\epsilon^*_{33}$ is linked, such that the universality of $\epsilon^*_{11}+\Pi^*_{11}$ is connected with the universality of the TKE dissipation.

Third, above $y^*\approx 12$, the production term is higher at higher Mach numbers, which combined with the observation that the total sink $\epsilon^*_{11}+\Pi^*_{11}$ is universal, implies more negative values of the diffusion term. This means that the surplus production is transported away from the buffer layer towards the wall. For further insight, figure 3.3(b) shows the sum of the viscous and turbulent fluxes obtained by integrating the transport terms as

$$\Phi^*_{11}=\int_0^{y^*}\left(T^{\nu*}_{11}+T^{u*}_{11}\right)dy^*, \tag{3.8}$$

such that positive values signify that energy is transported towards the wall, and negative values signify the opposite. As one can observe, the flux is positive close to the wall and increases with the Mach number. This implies that more energy is being carried towards the wall at higher Mach numbers. Between the wall and the peak location of the streamwise turbulence intensity, the total flux is mainly controlled by the viscous flux, which can be approximated as $d\widetilde{u''u''}^*/dy^*$. Thus, a higher positive flux at increasing Mach numbers implies a higher gradient of the streamwise turbulent stress, which results in a higher peak value upon integration.

The strengthening of the streamwise velocity fluctuations can also be explained based on a phenomenological mixing-length model. The semi-locally scaled streamwise stress can be written as

$$\left(\overline{u'u'}^*\right)^{1/2}\sim \ell^*\frac{d\bar{u}^*}{dy^*}, \tag{3.9}$$

where ℓ^* is the mixing length scaled by δ^*_v, and $d\bar{u}^*/dy^*$ is the semi-locally scaled mean velocity gradient. Note that the streamwise stress is written in the Reynolds averaged form, since we observe that the peak of both Reynolds and Favre averaged stresses increases alike (not shown), and therefore the error incurred by excluding density fluctuations from equation (3.9) is small. The mixing length is determined as $\ell^*\sim\sqrt{\overline{v'v'}^*}\,\mathcal{T}$ (Durbin, 1991), where $\mathcal{T}\sim k^*/\epsilon^*$. For the present cases this definition of mixing length yields universal distributions across the Mach number range (not shown). This is because the velocity with which a fluid parcel travels reduces with increasing Mach number. However, the time scale over which it retains its streamwise momentum increases with the Mach number (due to higher TKE and almost universal dissipation), thus effectively travelling the same distance. Due to the universality of the mixing length, equation (3.9) implies that the increase in mean shear observed in figure 3.1 is directly responsible for an increase in the peak streamwise turbulence intensity. Interestingly, an increase in the mean shear was also found to be responsible for higher production in the buffer layer (see figure 3.3) that formed the basis of our explanation above, making the phenomenological model consistent.

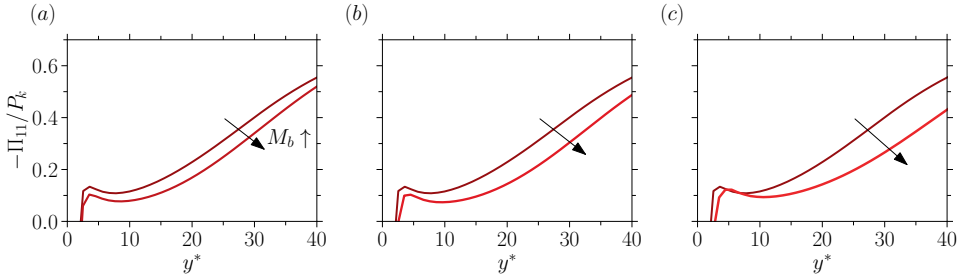

Figure 3.4: Wall-normal distributions of the streamwise pressure-strain correlation ($-\Pi_{11}$) scaled by the production term (P_{11}) for (a) Mach 2.28, (b) Mach 3 and (c) Mach 4 cases described in table 2.1, compared to the Mach 0.3 case.

3.2.5. REDUCED INTER-COMPONENT ENERGY TRANSFER

The strengthening of the streamwise turbulent stress and the weakening of the other two components, as observed in figures 3.2(a) - (c), imply an increase in turbulence anisotropy, which was also previously observed in several studies on compressible wall-bounded flows (Foysi et al., 2004; Duan et al., 2010; Zhang et al., 2018; Cogo et al., 2022, 2023), mainly regarded as a variable-property effect.

From turbulence theory, one can argue that the change in turbulence anisotropy is due to reduced inter-component energy transfer. Since the negative of the streamwise pressure-strain correlation ($-\Pi_{11} = -2\,\overline{p'\partial u''/\partial x}$) is a measure of the energy transferred from the streamwise turbulent stress to the cross-stream components, we expect it to decrease with increasing Mach number for our cases. To verify this, figure 3.4 shows $-\Pi_{11}$ scaled by the TKE production (Duan et al., 2010; Patel et al., 2015; Cogo et al., 2023), for (a) Mach 2.28, (b) Mach 3 and (c) Mach 4 cases, compared to the Mach 0.3 case. The figure clearly corroborates our claims. We further note that Π_{11} scaled by semi-local units ($\bar{\rho}u_\tau^{*3}/\delta_\nu^*$) also reduces for the three high-Mach-number cases compared to the Mach 0.3 case (not shown).

3.2.6. IDENTIFYING DIRECT AND INDIRECT EFFECTS OF INTRINSIC COMPRESSIBILITY

So far we have observed strong intrinsic compressibility effects on various turbulence statistics. Are these strong effects due to a direct contribution from the dilatational motions or due to IC effects on the solenoidal motions? To answer this, we apply Helmholtz decomposition to the velocity field obtained from DNS to isolate the solenoidal (divergence-free) and dilatational (curl-free) parts, namely

$$u_i'' = u_i^{s''} + u_i^{d''}. \tag{3.10}$$

Appendix A reports details on how the decomposition is actually performed. Following Yu et al. (2019), the turbulent stresses are then split as

$$\widetilde{u_i'' u_j''}^* = \widetilde{u_i^{s''} u_j^{s''}}^* + \widetilde{u_i^{d''} u_j^{s''}}^* + \widetilde{u_j^{s''} u_j^{d''}}^* + \widetilde{u_i^{d''} u_j^{d''}}^*. \tag{3.11}$$

The terms involving dilatational motions are absent in incompressible flows, and thus any contribution from them is regarded as a *direct* effect. However, the first term

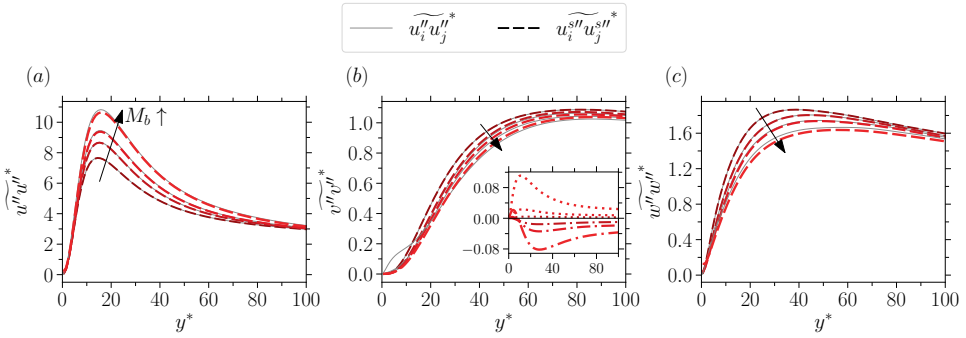

Figure 3.5: Wall-normal distributions of the total and solenoidal (a) streamwise, (b) wall-normal and (c) spanwise turbulent stresses as per equation (3.11), for the cases described in table 2.1. *Inset:* profiles of the terms $\widetilde{v^{d''}v^{d''}}^*$ (dotted) and $2\,\widetilde{v^{s''}v^{d''}}^*$ (dash-dotted).

on the right-hand side is also present in incompressible flows. Thus, any effect of compressibility on this term will be regarded as an *indirect* effect.

Figure 3.5 shows the first term on the right-hand side of equation (3.11), associated with solenoidal velocity fluctuations, for the normal turbulent stresses. They are seen to almost overlap with the total turbulent stresses, which is shown in grey. This implies that any change in the total stresses as a function of the Mach number is reflected in their respective solenoidal components, and thus intrinsic compressibility effects on turbulence statistics are mainly indirect. The collapse of the total and solenoidal stresses also implies that the correlations involving $u_i^{d''}$ are small. However, there are some exceptions, particularly the terms $\widetilde{v^{d''}v^{d''}}^*$ and $\widetilde{v^{s''}v^{d''}}^*$, that can have large contributions in the near-wall region as shown in the inset of figure 3.5(b). Negative values of $\widetilde{v^{s''}v^{d''}}^*$ physically represent opposition of solenoidal motions (sweeps/ejections) from dilatational wall-normal velocity. This opposition was first observed by Yu et al. (2019), and plays a key role in the forthcoming discussion.

3.3. WEAKENING OF THE QUASI-STREAMWISE VORTICES

Quasi-streamwise vortices play an important role in transferring energy from the streamwise to the wall-normal and spanwise components (Jeong et al., 1997). Thus, any reduction in this inter-component energy transfer (see figure 3.4), and hence any weakening of the wall-normal and spanwise velocity fluctuations (see figure 3.2) is directly related to the weakening of those vortices. To verify this claim, the root-mean-square of the streamwise vorticity is shown in figure 3.6(a). This quantity indeed decreases with increasing Mach number, implying weakening of the quasi-streamwise vortices. Note that the decrease in the root-mean-square of the streamwise vorticity could also be associated with a reduced population of the quasi-streamwise vortices, rather than their reduced strength. By visualizing them using the normalized swirling strength parameter (Wu and Christensen, 2006), it becomes clear that the population of these vortices at any given instant is similar across all Mach numbers (not shown). In contrast to the streamwise vorticity, the root-mean-square of the wall-normal and spanwise vorticity

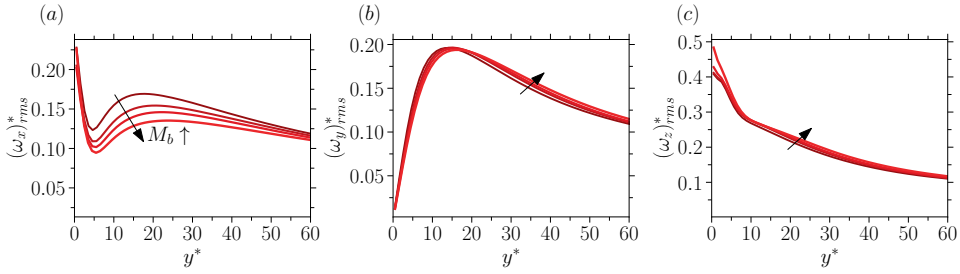

Figure 3.6: Wall-normal distributions of the root-mean-square of (a) streamwise, (b) wall-normal, and (c) spanwise vorticity fluctuations, scaled by u^*_τ/δ^*_ν, for the cases described in table 2.1.

shows a weak Mach number dependence, as seen in figure 3.6(b) and (c).

Choi et al. (1994) showed that active opposition of sweeps and ejections is effective in weakening the quasi-streamwise vortices. As noted in §3.2.6, a similar opposition also occurs spontaneously in compressible flows, in which solenoidal motions like sweeps and ejections are opposed by wall-normal dilatational motions.

To explain the physical origin of near-wall opposition of sweeps and ejections, and hence the weakening of the quasi-streamwise vortices, we perform a conditional averaging procedure that identifies shear layers. Shear layers are in fact inherently associated with quasi-streamwise vortices, being formed as a consequence of sweeps and ejections initiated by those vortical structures (Jeong et al., 1997). To educe shear layers, we rely on the variable interval space averaging (VISA) technique introduced by Kim (1985), which is the spatial counterpart of the variable interval time averaging (VITA) technique developed by Blackwelder and Kaplan (1976). Since only the solenoidal motions carry the imprint of incompressible turbulent structures, like shear layers, the VISA detection criterion is directly applied to the solenoidal velocity field.

3.3.1. STEPS TO PERFORM VARIABLE INTERVAL SPACE AVERAGING

In this conditional average technique, strong sweep and ejection events resulting in a shear layer are said to occur when the short-space variance, given by

$$\mathrm{var}(x,z,t) = \frac{1}{L}\int_{-\frac{L}{2}}^{\frac{L}{2}} [u^{s\prime\prime}(x+s,y_{ref},z,t)]^2\,\mathrm{d}s - \left(\frac{1}{L}\int_{-\frac{L}{2}}^{\frac{L}{2}} u^{s\prime\prime}(x+s,y_{ref},z,t)\,\mathrm{d}s\right)^2, \qquad (3.12)$$

exceeds $K[u^s_{rms}(y_{ref})]^2$, where K is the threshold level. Here, y_{ref} is the location of the reference $x-z$ plane where the detection criteria is applied, and L is the size of the averaging window, representative of the length scale of the shear layer identified by this technique (Johansson et al., 1987). Following Johansson et al. (1991), we take $K=1$, $y^*_{ref}\approx 15$, and $L^*\approx 200$. To analyse the sensitivity of the results with respect to these parameters, we varied each one individually and assessed its impact on the correlation shown in figure 3.12(a) (not presented here). The correlation remains almost unaffected when K is increased from 1 to 1.2 or when L^* is increased from 200 to 240. However, when y^*_{ref} is increased from 15 to 20, we observe that the peak of the correlation shifts outward, and there is a slight increase in the peak value. Despite these differences, the results remain qualitatively similar and the conclusions made from them still hold.

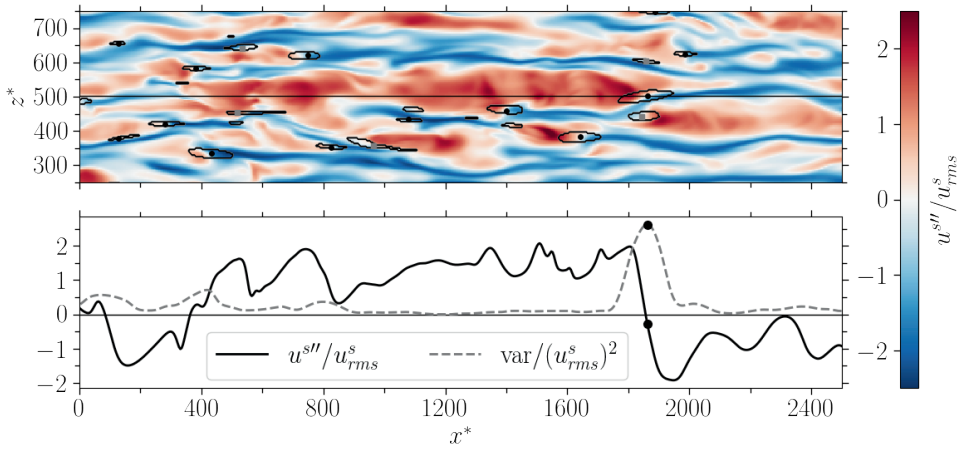

Figure 3.7: (Top) $x^* - z^*$ contour plot of the instantaneous solenoidal streamwise velocity fluctuations at $y^*_{ref} \approx 15$ for the Mach 2.28 case. Boundaries of patches where the short-space variance exceeds the Reynolds averaged value (see equation 3.13) are overlaid on the contour plot. Additionally, the location inside each patch where the short-space variance is locally maximum is also displayed by a black circle or a grey square for acceleration and deceleration events, respectively. (Bottom) Instantaneous solenoidal streamwise velocity fluctuation along the horizontal line indicated in the top plot. The black circle is the same point as in the top plot. The short-space variance (equation 3.12) is also shown using a grey dashed line.

Having computed the short-space variance at the reference plane, a condition variable C is set to non-zero values in regions where the variance exceeds the threshold, and zero otherwise. The assigned non-zero value is 1 for acceleration events and -1 for deceleration events. Mathematically, this is written as

$$\mathrm{C}(x,z,t) = \begin{cases} 1, & \text{for } \mathrm{var} > K[u^s_{rms}(y_{ref})]^2 \text{ and } \dfrac{\partial u^{s\prime\prime}}{\partial x} < 0 \\ -1, & \text{for } \mathrm{var} > K[u^s_{rms}(y_{ref})]^2 \text{ and } \dfrac{\partial u^{s\prime\prime}}{\partial x} > 0 \\ 0, & \text{otherwise,} \end{cases} \tag{3.13}$$

where $\partial u^{s\prime\prime}/\partial x < 0$ implies $\partial u^{s\prime\prime}/\partial t > 0$ and vice-versa, as per Taylor's hypothesis. This will result in patches on the reference $x - z$ plane with values of 1 and -1 as shown in figure 3.7. Within these patches, the location where the short-space variance is locally maximum is also shown. Let the coordinates of these locations be denoted by (x_o, z_o). These coordinates, detected at $y^* \approx 15$, will form the basis around which conditional averaging is performed at all wall-normal locations.

With the detected VISA locations, the conditional average of any variable Ψ is then given as:

$$\langle \Psi \rangle (\xi, y, \zeta) = \frac{1}{N} \sum_{f=1}^{N_f} \sum_{n=1}^{N_e} \Psi(x^n_o + \xi, y, z^n_o + \zeta, t^f), \tag{3.14}$$

where ξ and ζ are the streamwise and spanwise displacements with respect to the reference or detected locations (x_o, z_o), and they vary from $-L_x/2$ to $L_x/2$ and $-L_z/2$ to $L_z/2$, respectively. The inner sum is over the number of detected events (N_e) in a particular snapshot f (at time instant t^f), whereas the outer sum is over the number of snapshots (N_f), such that the global sum of the detected events over all the snapshots is N.

Note that equation (3.14) leads to a conditional average from which phase jitter is yet to be removed (Johansson et al., 1987). The concept of phase-jitter is explained with an example as follows. It is known that an acceleration VISA event detected at the location $(x_o, y^+ \approx 15, z_o)$ corresponds to a wall pressure peak directly underneath, i.e. at $(x_o, y^+ \approx 0, z_o)$. However, there can be a small and random phase lag or lead. This means that in reality, the pressure peak may occur at a location that is randomly shifted in the streamwise-spanwise direction with respect to the detected location, i.e. it may occur at $(x_o + \Delta_x, y^+ \approx 0, z_o + \Delta_z)$. This misalignment leads to a reduction in the magnitude of the pressure peak obtained after conditional averaging.

To fix this issue, we employ a cross-correlation technique (Johansson et al., 1987) that is described using the above example as follows. We first compute the conditional average of wall pressure as usual without fixing the phase-jitter issue. We then cross-correlate this conditionally averaged wall pressure plane with the instantaneous wall pressure plane using the Fourier transform. Having done this, we should obtain a $x-z$ plane of correlation coefficients on the wall that displays a local maximum close to but not necessarily at the point of detection, i.e. (x_o, z_o). This maximum implies that the conditionally averaged wall pressure profile has its imprint in the instantaneous plane around the detection location. The shift between the detection location (x_o, z_o) and the local maximum around (x_o, z_o) gives the amount of phase lag or lead in the streamwise and spanwise directions, i.e. Δ_x and Δ_y discussed above. In order to remove the phase lag or lead, we compute a new conditional average by shifting the instantaneous planes by this Δ_x and Δ_y around the detection points, thereby aligning them. Mathematically, equation (3.14) is modified for wall pressure as

$$\langle p' \rangle (\xi, 0, \zeta) = \frac{1}{N} \sum_{f=1}^{N_f} \sum_{n=1}^{N_e} p'(x_o^n + \Delta_x^n + \xi, 0, z_o^n + \Delta_z^n + \zeta, t^f). \tag{3.15}$$

Now, the same procedure described for pressure at the wall can be repeated for pressure at any wall-normal location. Doing this results in Δ_x and Δ_y that depend on y for each detected event. With this, equation (3.15) can be rewritten for the entire pressure field as

$$\langle p' \rangle (\xi, y, \zeta) = \frac{1}{N} \sum_{f=1}^{N_f} \sum_{n=1}^{N_e} p'(x_o^n + \Delta_x^n(y) + \xi, y, z_o^n + \Delta_z^n(y) + \zeta, t^f). \tag{3.16}$$

Although this gives more control on the alignment of three-dimensional conditionally averaged structures, it may result in a conditionally averaged profile that may not be very smooth in the wall-normal direction, such that layering is observed (some layering can be seen in figure 3.9).

In the phase-jitter removal procedure, events for which the required shift is greater than approximately 40 viscous lengths in the streamwise or spanwise directions are

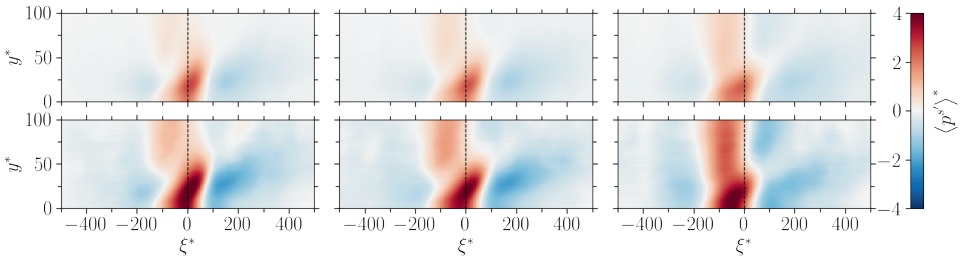

Figure 3.8: Contours of the solenoidal pressure along the $\xi^* - y^*$ plane at $\zeta^* = 0$ after (top row) equation (3.14) (no alignment), and after (bottom row) equation (3.16) (first alignment iteration). The left, middle and right columns correspond to the Mach 2.28, 3 and 4 cases in table 2.1, respectively.

excluded from the averaging procedure, and the total number of detected events (N) is reduced accordingly. Since the applied shifts are wall-normal dependent, the excluded number of events would also be wall-normal dependent.

Figure 3.8 shows the $\xi^* - y^*$ pressure contours taken at the centre of the shear layer, i.e. at $\zeta^* = 0$, after no alignment (equation 3.14) and after one iteration of alignment (equation 3.16). As seen, the pressure contours remain qualitatively similar in both the cases, however, the magnitude after one iteration of alignment has increased substantially.

The conditionally averaged profile obtained from equation (3.16) can be cross-correlated again with the instantaneous field, and the procedure above can be repeated to further improve the alignment. However, as noted in Johansson et al. (1987), and also verified for our cases, the maximum jitter is eliminated in the first iteration. Thus, the results presented next are obtained after one iteration.

3.3.2. RESULTS FROM THE VARIABLE INTERVAL SPACE AVERAGING TECHNIQUE

Figure 3.9 shows the conditionally averaged $\xi^* - y^*$ planes, at $\zeta^* = 0$, of various quantities for the Mach 2.28, 3 and 4 cases, only considering acceleration events. A similar plot with deceleration events is not shown since they are much less frequent (Johansson et al., 1987).

The first row in figure 3.9 shows the contours of the conditionally averaged solenoidal streamwise velocity fluctuations $\langle u^{s\prime\prime}\rangle^*$, which clearly represent a shear layer. The second row of the plot shows the contours of the conditionally averaged solenoidal wall-normal velocity fluctuations $\langle v^{s\prime\prime}\rangle^*$. Positive streamwise velocity fluctuations are associated with negative wall-normal fluctuations, resulting in a sweep event. Similarly, negative streamwise fluctuations are associated with positive wall-normal velocity, resulting in an ejection event. For greater clarity, we also show streamlines constructed using $\langle u^{s\prime\prime}\rangle^*$ and $\langle v^{s\prime\prime}\rangle^*$, with their thickness being proportional to the local magnitude of $\langle v^{s\prime\prime}\rangle^*$.

Similar to the velocity field, we also split pressure into solenoidal and dilatational parts, namely

$$p' = p^{s\prime} + p^{d\prime}. \tag{3.17}$$

Unlike the Helmholtz decomposition for velocities, this splitting is not unique. In this work, we adhere to the definition of solenoidal pressure given for homogeneous flows by Ristorcelli (1997); Jagannathan and Donzis (2016); Wang et al. (2017), which we extend

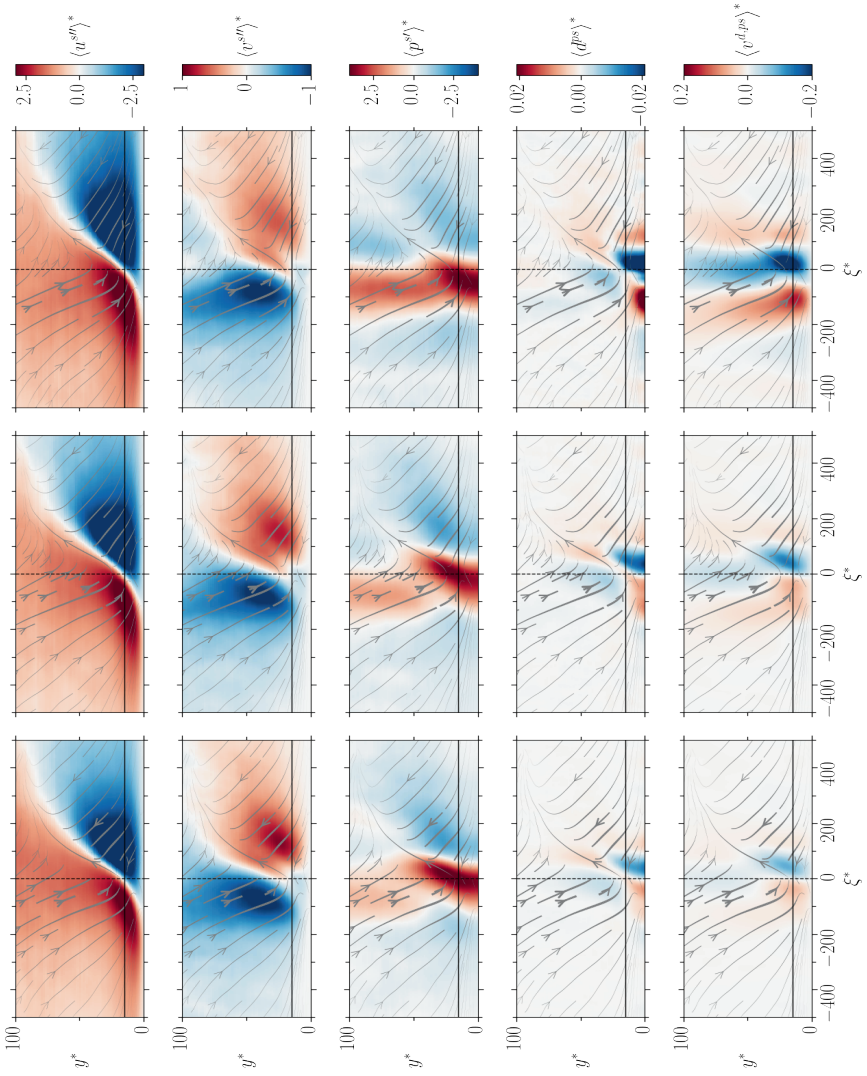

Figure 3.9: Conditionally averaged quantities, based on VISA applied to streamwise velocity fluctuations at $y^* \approx 15$, for the Mach 2.28 (left column), Mach 3 (centre column), and Mach 4 (right column) cases in table 2.1. The $\xi^* - y^*$ planes are taken at the centre of the shear layer ($\zeta^* = 0$). The velocity contours (first, second and fifth rows) are scaled by the semi-local friction velocity u_τ^*, the pressure contours (third row) are scaled by τ_w, and the dilatation contours (fourth row) are scaled by u_τ^*/δ_v^*. The overlaying streamlines are constructed using $\langle u^{s\prime\prime}\rangle^*$ and $\langle v^{s\prime\prime}\rangle^*$, and their thickness is scaled by the magnitude of $\langle v^{s\prime\prime}\rangle^*$. The solid black line indicates $y^* \approx 15$ and the dashed black line indicates $\xi^* = 0$.

to inhomogeneous flows as follows:

$$\frac{\partial^2 p^{s\prime}}{\partial x_i \partial x_i} = -\frac{\partial(\overline{\rho} u_i^{s\prime\prime} u_j^{s\prime\prime} - \overline{\rho}\,\overline{u_i^{s\prime\prime} u_j^{s\prime\prime}})}{\partial x_i \partial x_j} - 2\overline{\rho}\frac{d\widetilde{u}}{dy}\frac{\partial v^{s\prime\prime}}{\partial x}. \tag{3.18}$$

This part of the pressure field is also referred to as pseudo-pressure (Ristorcelli, 1997), as it propagates with the flow speed. Looking at the source terms on the right-hand side of equation (3.18), the solenoidal pressure can be interpreted as being generated from vortices and shear layers, similar to incompressible flows (Bradshaw and Koh, 1981).

The third row of figure 3.9 shows the conditionally averaged solenoidal pressure as per equation (3.18). Clearly, the pressure maxima occur approximately in between the high-velocity regions, which suggests a phase shift between velocity and pressure. To shed further light on this point, in figure 3.10 we plot the wall-normal velocity at $y^* \approx 15$, and the solenoidal pressure at the wall as a function of the streamwise coordinate (ξ^*). Since the wall pressure is mainly contributed by the buffer-layer eddies (Kim, 1989; Johansson et al., 1987; Kim and Hussain, 1993; Luhar et al., 2014), its convection velocity is comparable with the speed of the buffer-layer coherent structures (Kim and Hussain, 1993). Using this information and Taylor's hypothesis, one can transform the spatial axis in figure 3.10 to a temporal axis (τ) by taking the mean velocity at $y^* \approx 15$ as the propagation velocity. Reading figure 3.10 using the temporal axis (axis on the top), we note that the high negative sweep velocity corresponds to a high negative rate of change of the wall pressure, and likewise for the ejection velocity, i.e.,

$$\frac{\partial \langle p_w^{s\,\prime} \rangle^*}{\partial \tau^*} \sim \langle v^{s\prime\prime} \rangle^*. \tag{3.19}$$

Similar observations were made by Johansson et al. (1987), using the VITA technique, and by Luhar et al. (2014), using the resolvent analysis. Other interesting observations can be made from figure 3.10. First, the magnitude of the conditionally averaged streamwise fluctuations increases, whereas the magnitude of the conditionally averaged wall-normal fluctuations decreases with increasing Mach number, as also seen in the first two rows of figure 3.9. This is consistent with the strengthening of the streamwise and weakening of the wall-normal turbulent stresses observed in figure 3.5. Second, the wall pressure maximum shifts upstream with increasing Mach number, as also seen in the third row of figure 3.9. While we know that such shift is attributed to the Mach number dependence of the solenoidal motions that contribute to the source terms in equation (3.18), at the moment we cannot provide a detailed explanation for this and leave it for future studies.

After establishing the relation between the solenoidal wall-normal velocity and the rate of change of the solenoidal pressure in equation (3.19), we continue in our attempt to relate the solenoidal and the dilatational velocity fields. For that purpose, we first isolate the dilatation generated from the solenoidal pressure—also referred to as 'pseudo-sound' dilatation (superscript ps) in the literature (Ristorcelli, 1997; Wang et al., 2017)—, as follows

$$d^{ps} \approx \frac{-1}{\gamma \bar{p}}\left(\frac{\partial p^{s\prime}}{\partial t} + u_j \frac{\partial p^{s\prime}}{\partial x_j}\right). \tag{3.20}$$

Pseudo-sound dilatation represents the volume changes of fluid elements caused by pressure changes associated with solenoidal turbulent structures such as vortices and

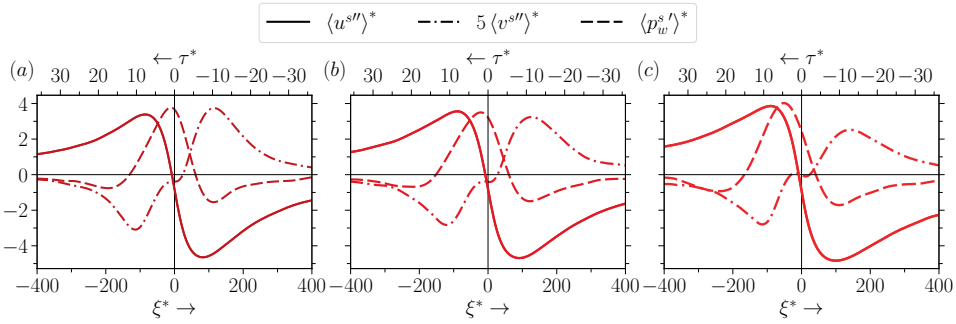

Figure 3.10: Conditionally averaged profiles of solenoidal streamwise and wall-normal velocities at $y^* \approx 15$, and wall pressure as a function of space (ξ^*, at ζ^*=0; bottom-axis) and time ($\tau^* = \tau/(u_\tau^*/\delta_v^*)$; top-axis), for (a) Mach 2.28, (b) Mach 3 and (c) Mach 4 cases in table 2.1.

Case name	M_{b_w}	M_τ	$(d_w^{ps})^*_{rms}$	$(v_p^d)^*_{rms}$	$(v_p^{d,ps})^*_{rms}$	$(v_p^{d,nps})^*_{rms}$
Mach 2.28	2.28	0.1185	0.0096	0.066	0.047	0.059
Mach 3	3	0.1526	0.0160	0.153	0.078	0.140
Mach 4	4	0.1968	0.0311	0.332	0.150	0.323
		b	2.42	3.1	2.37	3.3

Table 3.1: Root-mean-square (r.m.s.) of the pseudo-sound dilatation at the wall and the peak r.m.s. value of the total, pseudo-sound and non-pseudo-sound wall-normal dilatational velocities. 'b' is the exponent obtained from power-law fitting (aM_τ^b) of the data.

shear layers. Normalization by the wall shear stress yields

$$d^{ps} \approx \frac{-\tau_w}{\gamma \bar{p}} \left(\frac{\partial p^{s\prime *}}{\partial t} + u_j \frac{\partial p^{s\prime *}}{\partial x_j} \right), \tag{3.21}$$

where the factor $\tau_w/(\gamma\bar{p})$ is equal to the square of the semi-local friction Mach number for ideal gas flows. Using $M_\tau^* \approx M_\tau$ (see equation (2.6) and figure 2.2), we then rewrite equation (3.21) as

$$d^{ps} \approx -M_\tau^2 \left(\frac{\partial p^{s\prime *}}{\partial t} + u_j \frac{\partial p^{s\prime *}}{\partial x_j} \right). \tag{3.22}$$

According to the pseudo-sound theory (Ristorcelli, 1997), the inner-scaled solenoidal pressure is assumed to be unaffected by compressibility effects. Thus, from equation (3.22), one would expect d^{ps} to increase with the square of the friction Mach number. However, as noted in the discussion following figure 3.10, the solenoidal motions change as a function of the Mach number, thereby affecting the solenoidal pressure as per equation (3.18). This suggests that d^{ps} could increase with an exponent that is close to two but not necessarily equal to two. To assess the correct scaling, in table 3.1 we report the root-mean-square of d^{ps} at the wall. Data fitting yields $d^{ps} \sim M_\tau^{2.42}$, hence close to what was suggested by equation (3.22).

Continuing on our path to relate solenoidal and dilatational motions, close to the wall we can write

$$d_w^{ps*} \approx -M_\tau^2 \frac{\partial p_w^{s\prime *}}{\partial t^*}, \tag{3.23}$$

where $d_w^{ps*} = d_w^{ps}/(u_\tau^*/\delta_v^*)$. This equation, when conditionally averaged and combined with equation (3.19), leads to

$$\langle d_w^{ps} \rangle^* \sim -M_\tau^2 \langle v^{s\prime\prime} \rangle^* . \tag{3.24}$$

Using this result, we expect positive dilatation events (expansions) to be mainly associated with sweeps and negative dilatation events (compressions) to be associated with ejections. The fourth row in figure 3.9 shows the contours of conditionally averaged pseudo-sound dilatation defined in equation (3.22). Consistent with our expectation, positive dilatation is indeed found to be associated with sweeps and negative dilatation with ejections, and its magnitude increases with the Mach number.

Having related the pseudo-sound dilatation and the solenoidal velocity in equation (3.24), the next step is to introduce the pseudo-sound dilatational velocity as

$$\begin{aligned} \frac{\partial^2 \phi^{ps}}{\partial x_j \partial x_j} &= d^{ps}, \\ v^{d,ps} &= \frac{\partial \phi^{ps}}{\partial y}, \end{aligned} \tag{3.25}$$

where ϕ^{ps} is the scalar potential. Note that this equation is similar to equations (A.2) and (A.3) used to solve for the total dilatational velocity, as reported in Appendix A. Based on equation (3.25), one would expect $v^{d,ps}$ to increase with the Mach number at a similar rate as d^{ps}. Power-law fitting of the data reported in table 3.1 indeed yields $v^{d,ps} \sim M_\tau^{2.37}$, hence close to what was found for d^{ps}.

Equation (3.25) stipulates that the conditionally averaged pseudo-sound dilatational velocity in the buffer layer should be proportional to and in phase with the dilatation at the wall. Thus, we can write

$$\langle v^{d,ps} \rangle^* \sim \langle d_w^{ps} \rangle^* . \tag{3.26}$$

Using equation (3.26) and (3.24) we can finally develop a relation between the solenoidal and the pseudo-sound dilatational velocity, namely

$$\langle v^{d,ps} \rangle^* \sim -M_\tau^2 \langle v^{s\prime\prime} \rangle^* . \tag{3.27}$$

In our opinion, this relation is quite meaningful as it theoretically supports near-wall opposition of sweeps and ejections by dilatational motions. Moreover, it suggests that the opposition effect should approximately increase with the square of M_τ.

In order to verify this, the final row in figure 3.9 reports the conditionally averaged contours of the pseudo-sound wall-normal dilatational velocity given in equation (3.25). As suggested from equation (3.26), the contours of $v^{d,ps}$ appear to be in phase with those of d^{ps}. Thus, consistent with the observations made for the pseudo-sound dilatation, the wall-normal dilatational velocity is positive during sweeps and negative during ejections, and its magnitude increases with the Mach number. This opposition is also clearly seen in figure 3.11, which shows the conditionally averaged profiles of $v^{s\prime\prime}$ and $v^{d,ps}$ at $y^* \approx 15$. Additionally, in figures 3.9 and 3.11 we note that the pseudo-sound dilatational velocity contour (or profile) shifts upstream (leftward) with increasing Mach number. This is due to the upstream shift in the pressure contour mentioned above. Interestingly (as also pointed out by a reviewer), if the $v^{d,ps}$ profile continues to shift upstream with increasing Mach number, then at sufficiently high Mach numbers the dilatational velocity could become approximately in-phase with the solenoidal velocity, thereby assisting sweeps

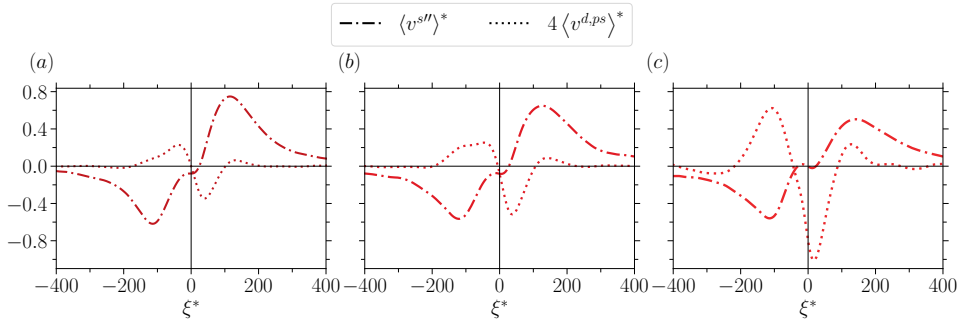

Figure 3.11: Conditionally averaged profiles of solenoidal and pseudo-sound dilatational wall-normal velocities at $y^* \approx 15$ as a function of ξ^* (at ζ^*=0) for (a) Mach 2.28, (b) Mach 3 and (c) Mach 4 cases in table 2.1.

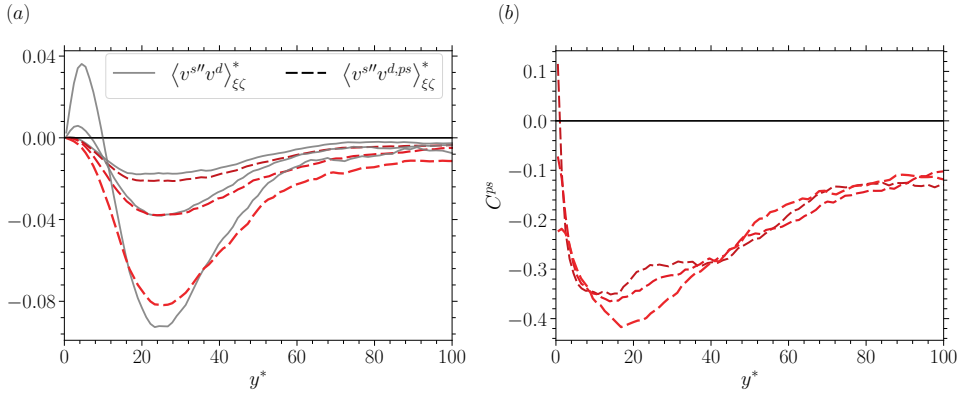

Figure 3.12: (a) Conditionally averaged and integrated (equation 3.28) correlations between solenoidal and dilatational velocities. (b) Conditionally averaged pseudo-sound correlation coefficient (C^{ps}) as defined in equation (3.29).

and ejections rather than opposing them. Investigating whether this trend persists at higher Mach numbers is beyond the scope of this work and is left for future studies.

To further quantify the opposition effect, we analyse the conditionally averaged correlation between solenoidal and pseudo-sound dilatational wall-normal velocity, i.e. $\langle v^{s''}v^{d,ps}\rangle$. The correlation is integrated over a window of 300 viscous units in the streamwise direction and 40 viscous units in the spanwise direction (Johansson et al., 1991), at each wall-normal location as

$$\langle v^{s''}v^{d,ps}\rangle_{\xi\zeta}(y^*) = \int_{\zeta^*=-20}^{20}\int_{\xi^*=-150}^{150} \langle v^{s''}v^{d,ps}\rangle(\xi^*, y^*, \zeta^*)\, d\xi^*\, d\zeta^*. \tag{3.28}$$

The integrated correlation, scaled by the squared semi-local friction velocity, is reported in figure 3.12(a) with dashed lines. Figure 3.12(b) shows the pseudo-sound correlation coefficient defined as

$$C^{ps} = \frac{\langle v^{s''}v^{d,ps}\rangle_{\xi\zeta}}{\sqrt{\langle v^{s''}v^{s''}\rangle_{\xi\zeta}\,\langle v^{d,ps}v^{d,ps}\rangle_{\xi\zeta}}}. \tag{3.29}$$

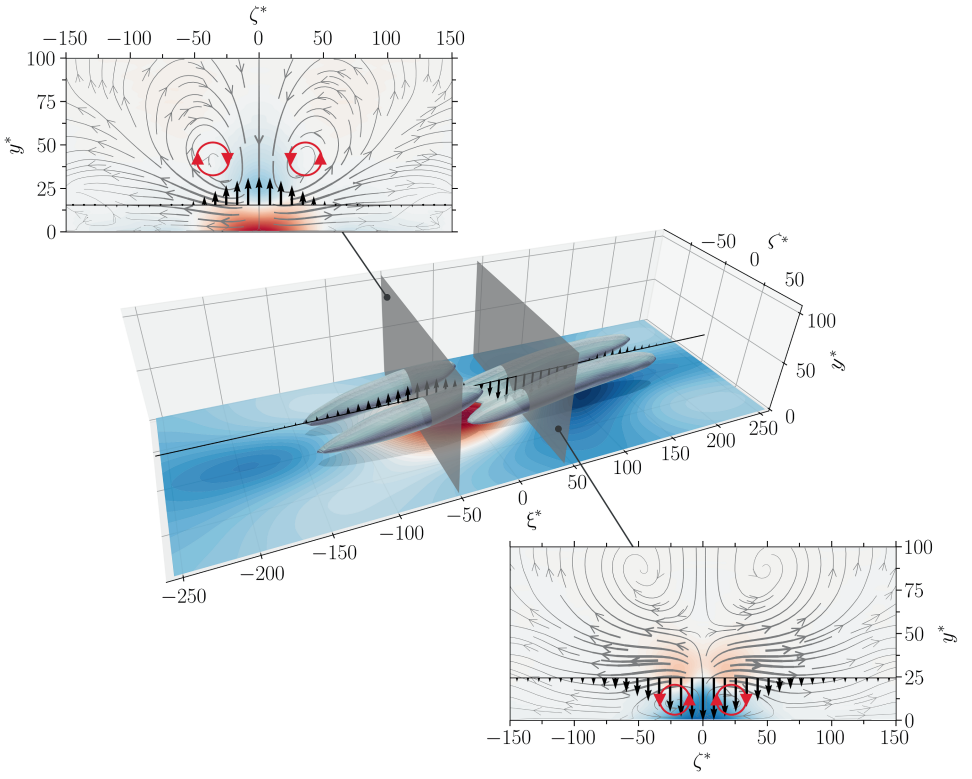

Figure 3.13: Opposition of sweeps and ejections by wall-normal pseudo-sound dilatational velocity in the context of quasi-streamwise vortices. The shaded three-dimensional isosurfaces represent quasi-streamwise vortices identified by applying the Q-criterion to the conditionally averaged velocity field. Their shadows are also plotted on the wall below, showing that the vortices are inclined and tilted. Underneath the vortices, the contours of solenoidal wall pressure are shown. The transparent planes mark regions of high rate of change of wall pressure and hence high wall-normal pseudo-sound dilatational velocity $\langle v^{d,ps} \rangle^*$ (see discussion related to equations 3.19 - 3.27). The arrows between the vortices indicate $\langle v^{d,ps} \rangle^*$ as a function of ξ^* at $\zeta^* = 0$ and $y^* \approx 20$. Note that the line along which the arrows are plotted is slightly shifted away from the wall for better visibility. *Insets:* contours of pseudo-sound dilatation $\langle d^{ps} \rangle^*$ along the transparent planes, overlaid with the streamlines generated by quasi-streamwise vortices. These streamlines are constructed using the wall-normal and spanwise solenoidal velocities, i.e. $\langle v^s \rangle^*$ and $\langle w^s \rangle^*$, with their thickness being proportional to the magnitude of the local planar velocity. $\langle v^{d,ps} \rangle^*$ at $y^* \approx 15$ and $y^* \approx 25$ is also shown using arrows in the left and right planes, respectively. These wall-normal locations correspond to the maximum value of $\langle v^{d,ps} \rangle^*$ in those planes. The red and blue colours in the contour plots indicate positive and negative values, respectively. An interactive version of this figure can be accessed here.

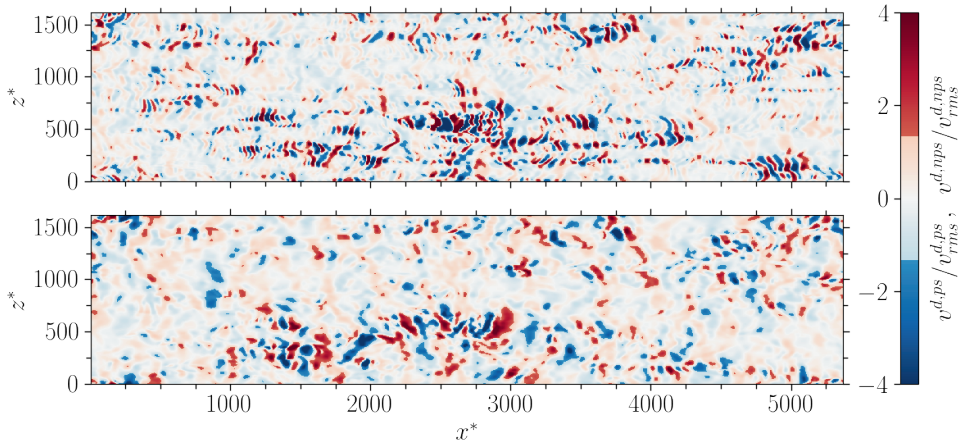

Figure 3.14: Instantaneous $x^* - z^*$ planes at $y^* \approx 11$ of (top) the non-pseudo-sound and (bottom) the pseudo-sound wall-normal dilatational velocities (see the text for definitions) scaled by their respective root-mean-squares for the Mach 3 case in table 2.1. Note that, for clarity, the colour bar is adjusted such that structures stronger than 1.33 times the root-mean-square value are highlighted.

The correlation and its coefficient are negative as expected. The magnitude of the correlation increases approximately with the square of Mach number, as expected. However, the correlation coefficient almost collapses across all Mach numbers.

The association of the opposition effect with the quasi-streamwise vortices is visualised in figure 3.13 for the Mach 2.28 case, all other cases being qualitatively similar. Indeed, the figure insets illustrate that sweeps and ejections initiated by quasi-streamwise vortices are opposed by the near-wall pseudo-sound dilatational velocity, thereby resulting in their weakening.

3.3.3. ROLE OF NON-PSEUDO-SOUND DILATATIONAL VELOCITY IN NEAR-WALL OPPOSITION

So far we have looked into the pseudo-sound dilatational velocity and provided an explanation for why they are out-of-phase with respect to the solenoidal motions. However, from table 3.1, we see that the peak root-mean-square value of $v^{d,ps}$ is much smaller than that of the total dilatational velocity. Hence, a large portion of the dilatational velocity and its correlation (if any) with the solenoidal velocity is still unexplained. To address this point, figure 3.12(a) shows the integrated correlation between solenoidal and total dilatational velocities, i.e. $\langle v^{s\prime\prime} v^d \rangle^*_{\xi\zeta}$, denoted by solid grey lines. Except very close to the wall, the total and pseudo-sound correlations almost overlap. This implies that the contribution from the remaining portion of the dilatational velocity, referred to as the 'non-pseudo-sound' component and given by

$$v^{d,nps} = v^d - v^{d,ps}, \tag{3.30}$$

is small. In other words, despite being stronger in magnitude than the pseudo-sound component, the non-pseudo-sound dilatational velocity does not play an important role in opposing sweeps and ejections.

Before concluding, we would like to comment on the travelling wave-packet-like structures, first identified by Yu et al. (2019) and later studied in Yu et al. (2020); Yu and Xu (2021); Tang et al. (2020); Gerolymos and Vallet (2023); Yu et al. (2024). Figure 3.14 shows the $x^* - z^*$ plane with the instantaneous contours of the pseudo-sound and non-pseudo-sound dilatational velocity at $y^* \approx 11$, for the Mach 3 case in table 2.1. The wave-packet structures are predominantly present in the non-pseudo-sound component, whereas the pseudo-sound component shows a spotty structure similar to that observed for the streamwise gradient of wall pressure in incompressible flows (Kim, 1989). Combining the observation above that the non-pseudo-sound component hardly contributes to the opposition effect, and that the wave-packet-like structures are present mainly in this component, one can argue that these structures do not play an important role in opposing sweeps and ejections.

3.4. SUMMARY

In this chapter, we have attempted to provide an explanation for the underlying mechanism through which intrinsic compressibility effects modulate the near-wall dynamics of turbulence. To rigorously assess these effects, we analyse four DNS cases of fully developed high-Mach-number channel flows with approximately constant mean properties, whereby intrinsic compressibility effects are isolated. Our findings, sketched as a flow chart in figure 3.15, are summarised as follows.

First, we have decomposed the velocity field into solenoidal and dilatational parts and educed shear layers by applying conditional averaging to the solenoidal component. We have noticed that there exists a streamwise phase shift between the buffer-layer sweeps and ejections that form shear layers, and the associated 'solenoidal' wall pressure. Equivalent observations were made for incompressible flows by Johansson et al. (1987) and Luhar et al. (2014). By using Taylor's hypothesis, this streamwise shift in phase can be interpreted as a phase shift in time, such that regions of high positive rate of change of wall pressure correspond to regions of high positive wall-normal velocity. Similarly, regions of high negative rate of change of wall pressure correspond to the regions of high negative wall-normal velocity. Close to the wall, the high rate of change of the solenoidal pressure results in large dilatation values with an opposite sign (also referred to as pseudo-sound dilatation), which upon integration results in a wall-normal dilatational velocity that inherently opposes sweeps and ejections. Since sweeps and ejections are initiated by quasi-streamwise vortices, their opposition directly affects the evolution of those vortices, causing their weakening. This is schematically depicted in figure 3.13.

Interestingly, we also found that the remaining portion of the dilatational velocity (also referred to as the non-pseudo-sound component) does not play an important role in the opposition mechanism. Moreover, we have observed that the majority of the travelling wave-packet-like structures, recently discovered in the literature, are present in this non-pseudo-sound component.

The weakening of quasi-streamwise vortices directly hinders the energy transfer from the streamwise velocity component to the other two components, resulting in an outward shift (reduction) in the wall-normal turbulent stress with increasing Mach number. Since the wall-normal motions actively contribute to the transport of momentum across mean shear, thereby generating turbulent shear stress, the outward shift in the wall-normal turbulent stress results in a corresponding outward shift in the turbulent shear stress.

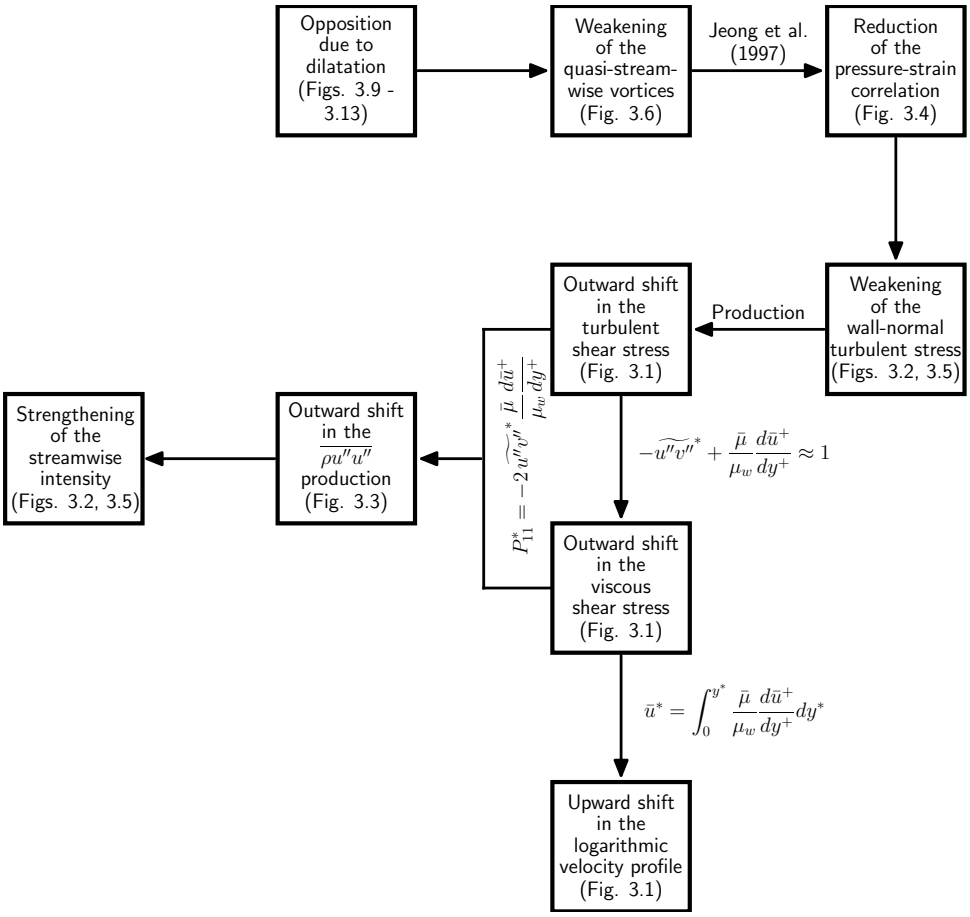

Figure 3.15: A graphical summary of the findings presented in this chapter. Note that the arrows are meant to indicate the chain of arguments made in this chapter, not relations of causality.

This reduction in the turbulent shear stress is in turn responsible for an upward shift in the logarithmic mean velocity profile.

A longstanding question in the compressible flow community is why the inner-scaled streamwise turbulent stress is higher in compressible flows than in incompressible flows, with similar Reynolds numbers. In this respect, our results suggest that intrinsic compressibility effects play a central role. Specifically, the increase in the peak value is a consequence of the outward shift in the turbulent and viscous shear stresses, since their product yields the production of the streamwise turbulent stress. This implies that the near-wall opposition mechanism outlined above is also responsible for the strengthening of the streamwise turbulence intensity. See chapter 4 for more details on the scaling of this quantity.

Some questions related to the findings made in this chapter remain unanswered as of yet. First, why do the solenoidal pressure maxima, and hence the pseudo-sound dilatational velocity contours, shift upstream with increasing Mach number (see figures 3.9 - 3.11), and would this trend continue at higher Mach numbers? Second, what is the Mach number scaling of the turbulence statistics presented in the chapter? Third, why is the dissipation of turbulent kinetic energy, and thus the small scales of turbulence, not affected by intrinsic compressibility effects (see section 3.2.4)? A spectral analysis of the velocity field could shed more light on this important issue.

4

SCALING OF WALL PRESSURE AND THE STREAMWISE TURBULENCE INTENSITY PEAK

Having verified that the contribution of intrinsic compressibility (IC) effects to various turbulence statistics is significant, this chapter proposes a framework for developing scaling laws for such statistics, accounting for both IC and variable-property effects. We particularly focus on the wall-pressure root-mean-square (r.m.s.) and the peak of streamwise turbulence intensity. To develop scaling laws for these quantities, we express them as an expansion series in powers of an appropriately defined Mach number. The leading-order term is represented using the scaling relations developed for incompressible flows, but with an effective Reynolds number. Higher-order terms capture IC effects and are modeled as constant coefficients, calibrated using flow cases specifically designed to isolate these effects (i.e., the 'CP' cases described in table 2.1). The resulting scaling relations are shown to be accurate for a wide range of turbulent channel flows and boundary layers.

The contents of this chapter are under review in *Journal of Fluid Mechanics* as:
Hasan, A. M., Costa, P., Larsson, J., and Pecnik, R. (2025). Scaling of wall pressure and the streamwise turbulence intensity peak in compressible wall flows. *arXiv preprint no. 2505.07407*.

4.1. INTRODUCTION

Wall-pressure fluctuations significantly impact the structural integrity of surfaces as well as the noise they emit (Bull, 1996). Their accurate prediction is vital for engineering applications, particularly in high-speed flows where such fluctuations become more intense and pose greater design challenges. As a result, the scaling behavior of wall-pressure fluctuations in compressible flows has been an active area of research for several decades (Laganelli et al., 1983; Bernardini and Pirozzoli, 2011; Ritos et al., 2019; Zhang et al., 2022; Gerolymos and Vallet, 2023; Wan et al., 2024).

Among the different Reynolds stresses, studying the scaling behavior of the streamwise turbulence intensity peak has garnered the most attention in the incompressible flow community (see, e.g., Marusic et al., 2017; Chen and Sreenivasan, 2021; Smits et al., 2021; Monkewitz, 2022). However, in contrast to wall pressure, relatively few studies have examined the scaling of the peak intensity in compressible flows.

In incompressible flows, both wall-pressure and the peak of streamwise intensity do not collapse under wall scaling (i.e., scaled using the friction velocity u_τ and the viscous length scale δ_v), but rather increase with the friction Reynolds number Re_τ. Recently, with high Reynolds number experimental and numerical data, various semi-empirical scaling laws have been proposed to capture this increase with Re_τ. There are particularly two schools of thought behind these scaling laws. One according to Townsend's attached eddy model, which advocates that the wall pressure and the peak streamwise turbulence intensity increase indefinitely as a logarithmic function of Re_τ (Marusic et al., 2017; Panton et al., 2017; Samie et al., 2018; Smits et al., 2021). As per this approach, scaling laws for wall-pressure r.m.s. (Panton et al., 2017) and the peak of streamwise turbulence intensity (Samie et al., 2018) are given as

$$\begin{aligned} p^+_{w,rms} &= \sqrt{-9.18 + 2.24\log(Re_\tau)} \quad \text{for channels and pipes,} \\ p^+_{w,rms} &= \sqrt{-8.96 + 2.42\log(Re_\tau)} \quad \text{for boundary layers,} \end{aligned} \tag{4.1}$$

and

$$\overline{u'u'}^+_p = 3.54 + 0.646\log(Re_\tau) \quad \text{for channels, pipes and boundary layers.} \tag{4.2}$$

The other approach corresponds to the power-law theory developed by Chen and Sreenivasan (2021) which argues that at infinitely high Re_τ, both wall pressure and the peak intensity (among other quantities) should asymptote to a constant value. Examples of scaling laws of wall-pressure r.m.s. and the peak intensity as per this theory are (Chen and Sreenivasan, 2022)

$$\begin{aligned} p^+_{w,rms} &= 4.4 - 10.5\,Re_\tau^{-1/4} \quad \text{for channels and pipes,} \\ p^+_{w,rms} &= 4.5 - 9.70\,Re_\tau^{-1/4} \quad \text{for boundary layers,} \end{aligned} \tag{4.3}$$

and

$$\overline{u'u'}^+_p = 11.5 - 19.3\,Re_\tau^{-1/4} \quad \text{for channels, pipes and boundary layers,} \tag{4.4}$$

respectively. The power-law increase of the peak intensity was recently supported by the high Reynolds number pipe flow DNS ($Re_\tau \approx 12000$) of Pirozzoli (2024). While the debate between these two theories is still ongoing, the focus of this chapter is to extend these scaling theories to variable-property and compressible flows, where other parameters

such as the free-stream Mach number M_∞ and the wall cooling ratio T_w/T_r[1] (where T_w and T_r correspond to the wall and adiabatic temperatures, respectively) also become important.

Kistler and Chen (1963) performed the first measurement of wall pressure fluctuations underneath supersonic (free-stream Mach number $M_\infty \leq 5$) boundary layers, followed by other experimental studies summarized in figure 1 of Beresh et al. (2011). Based on such experimental datasets, Laganelli et al. (1983) developed an engineering model for wall-pressure scaled with the free-stream dynamic pressure as

$$p_{rms,w}/q_\infty = \frac{(p_{rms,w}/q_\infty)_{inc}}{\left[0.5 + (T_w/T_r)\left(0.5 + 0.09M_\infty^2\right) + 0.04M_\infty^2\right]^\phi}, \tag{4.5}$$

where $q_\infty = 0.5\rho_\infty U_\infty^2$ (subscript '∞' implies free-stream values), $(p_{rms,w}/q_\infty)_{inc} = 0.006$ implies normalized pressure r.m.s. in incompressible boundary layers, and $\phi = 0.64$. The experimental measurements used to tune Laganelli's model were found to exhibit significant scatter, largely due to their high sensitivity to the measurement sensors (Beresh et al., 2011), thereby raising concerns about the model's accuracy. This high level of scatter also hindered the development of more accurate models (Beresh et al., 2011).

Bernardini and Pirozzoli (2011) reported one of the earliest wall-pressure r.m.s. data using direct numerical simulations (DNS). They found that for their supersonic adiabatic boundary layers (wall cooling ratio $T_w/T_r = 1$), $p_{w,rms}$ scaled by τ_w ($p^+_{w,rms}$) collapses for data at similar Re_τ. However, a strong Mach number effect was seen if $p_{w,rms}$ was scaled by q_∞, suggesting the inner layer scale (τ_w) to better characterize wall-pressure. Similarly, Duan et al. (2016) observed a weak Mach number effect on $p^+_{w,rms}$ for their quasi-adiabatic ($T_w/T_r = 0.76$) boundary layer at hypersonic Mach number ($M_\infty = 5.86$). However, Zhang et al. (2017) observed that at the same M_∞, $p^+_{w,rms}$ substantially increases when the wall is strongly cooled, i.e., $T_w/T_r = 0.25$. More recently, Zhang et al. (2022) observed that $p^+_{w,rms}$ decreases with wall cooling at sub- and supersonic Mach numbers, but increases with wall cooling at hypersonic Mach numbers $M_\infty > 5$. They subsequently re-tuned the constants in Laganelli's model, namely $(p_{rms,w}/q_\infty)_{inc} = 0.01$ and $\phi = 0.75$, to better fit their data. More recently, the same group (Wan et al., 2024) proposed another scaling model for $p^+_{w,rms}$ as a function of the free-stream Mach number for adiabatic boundary layers. However, this model does not account for changes in Re_τ and T_w/T_r.

Like boundary layers, several DNS studies were performed to study wall pressure and its scaling in fully developed channel flows. Yu et al. (2020) decomposed the pressure field into a rapid, slow, viscous and compressible part, and observed that the compressible pressure increases strongly with the bulk Mach number. This pressure component was associated with the travelling wave-packet-like structures, first observed in Yu et al. (2019), and later studied in (Tang et al., 2020; Zhang et al., 2022; Gerolymos and Vallet, 2023; Yu et al., 2024). Based on this increase in the compressible pressure, they proposed a scaling fit for the wall-pressure variance $(p^+_{rms,w})^2$ as

$$(p^+_{rms,w})^2(M_{b_b}) = (p^+_{rms,w})^2(0) + 0.143M_{b_b}^2, \tag{4.6}$$

[1]Note that other wall-cooling parameters—such as the diabatic parameter $\Theta = (T_w - T_\infty)/(T_r - T_\infty)$ (Zhang et al., 2014; Cogo et al., 2023), where T_∞ is the free-stream temperature, and the Eckert number $Ec = (\gamma - 1)M_\infty^2 T_\infty/(T_r - T_w)$ (Wenzel et al., 2022)—have been found to be more effective in quantifying wall-cooling effects than T_w/T_r.

where $M_{b_b} = U_b/c_b$ (where U_b is the bulk mean velocity and c_b is the speed of sound based on bulk temperature). However, this fit was proposed based on their dataset at similar Re_τ of 500, and thus it does not account for any Reynolds number effect. Yu et al. (2022) later modified this model to be a function of the friction Mach number M_τ. More recently, Gerolymos and Vallet (2023), using their comprehensive dataset of compressible channel flows with varying Reynolds number and centreline Mach number, proposed a scaling law for $p^+_{rms,w}$, which reads

$$p^+_{rms,w} = \left(4.4 - 10.5 Re_{\tau^\dagger}^{-1/4}\right)\left(\frac{1+0.020M_c^2}{1+0.011M_c^2}\right)\left(1+0.020\left(\frac{T_r}{T_w}-1\right)\right) \tag{4.7}$$

where $Re_{\tau^\dagger}$ is the minimum value of the semi-local friction Reynolds number Re^*_τ (defined as $\bar{\rho}u^*_\tau h/\bar{\mu}$, where $\bar{\rho}$ and $\bar{\mu}$ imply mean density and viscosity, and $u^*_\tau = \sqrt{\tau_w/\bar{\rho}}$ is the semi-local friction velocity) in the domain, and $M_c = U_c/c_c$ is the centreline Mach number (where U_c is the centreline mean velocity and c_c is the centreline speed of sound). Interestingly, the first factor on the right-hand-side is the same as the incompressible fit in (4.3), except that Re_τ is replaced with $Re_{\tau^\dagger}$.

The wall-pressure scaling laws proposed for boundary layers, like the ones in Laganelli et al. (1983) and Wan et al. (2024), have not been generalized to other class of flows, like channel and pipe flows. Moreover, the model of Gerolymos and Vallet (2023), which was originally tested for channel flows, when applied to boundary layers by modifying the first factor in (4.7) according to (4.3) and replacing M_c with M_∞ leads to significant errors at high Mach numbers (see section 4.3). Clearly, a universally applicable and accurate scaling law is lacking.

Compared to wall-pressure fluctuations, less work has been done to study the scaling behavior of peak streamwise turbulence intensity in compressible flows. For variable-property channel flow cases at zero Mach number, Patel et al. (2015) observed that the peak of inner-scaled streamwise turbulence intensity can be higher or lower than a corresponding incompresible flow at similar Re_τ, depending on the distribution of the semi-local Reynolds number Re^*_τ. Specifically, the peak intensity is higher if Re^*_τ decreases away from the wall and lower if it increases.

For flows at non-zero Mach numbers, the peak value is found to be higher than a corresponding incompressible flow at similar Re_τ, independent of the distribution of Re^*_τ (Gatski and Erlebacher, 2002; Pirozzoli et al., 2004; Foysi et al., 2004; Duan et al., 2010; Modesti and Pirozzoli, 2016; Zhang et al., 2018; Trettel, 2019; Cogo et al., 2022, 2023). In the previous chapter, we concluded that the higher value of the peak is due to intrinsic compressibility effects. However, a formal scaling law which accounts for these effects is missing.

In this chapter, we develop scaling laws for wall-pressure r.m.s. and the peak of streamwise turbulence intensity that account for compressibility effects—variable-property and intrinsic compressibility (see chapter 1)—and are applicable to both channel/pipe flows and boundary layers. To develop such scaling laws, we express wall-pressure r.m.s. and the peak intensity as an expansion series in powers of an appropriately defined Mach number (Ristorcelli, 1997). The leading-order term in this series accounts for Reynolds number and variable-property effects, and is represented by using the same scaling laws as developed for incompressible flows (Chen and Sreenivasan, 2022), however, with an effective value of the semi-local friction Reynolds

number, instead of the wall-based Re_τ. The higher-order terms mainly account for intrinsic compressibility effects, and are modeled using the constant-property high-Mach-number cases described in table 2.1, which are designed to isolate these effects.

4.2. APPROACH

For compressible homogeneous flows, Ristorcelli (1997) expressed the compressible flow quantities such as pressure, density, and velocity in the form of an expansion series as follows:

$$\begin{aligned}
\frac{p'}{\mathscr{P}} &= \epsilon^2 \left[\frac{p'_1}{\rho_\infty \mathscr{U}^2} + \epsilon^2 \frac{p'_2}{\rho_\infty \mathscr{U}^2} + \epsilon^4 \frac{p'_3}{\rho_\infty \mathscr{U}^2} + \ldots, \right. \\
\frac{\rho'}{\rho_\infty} &= \epsilon^2 \left[\frac{\rho'_1}{\rho_\infty} + \epsilon^2 \frac{\rho'_2}{\rho_\infty} + \epsilon^4 \frac{\rho'_3}{\rho_\infty} + \ldots, \right. \\
\frac{u'_i}{\mathscr{U}} &= \frac{u'_{0i}}{\mathscr{U}} + \epsilon^2 \left[\frac{u'_{1i}}{\mathscr{U}} + \epsilon^2 \frac{u'_{2i}}{\mathscr{U}} + \epsilon^4 \frac{u'_{3i}}{\mathscr{U}} + \ldots, \right.
\end{aligned} \tag{4.8}$$

where $\mathscr{P}$ is the thermodynamic scale of pressure, $\mathscr{U}$ is the velocity scale, ρ_∞ is the reference background density, $\epsilon^2 = \rho_\infty \mathscr{U}^2 / \mathscr{P}$ is the ratio of the hydrodynamic scale of pressure to the thermodynamic scale, and the subscripts '0, 1, 2, 3' signify the order of the variables. These expansions, when substituted in the Navier-Stokes equations and the terms with similar powers of ϵ are grouped, we get a set of zeroth order (proportional to ϵ^0), first order (proportional to ϵ^2) and higher order governing equations. The zeroth order set of equations solves for the incompressible velocity u'_{0i} and pressure p'_1 fields[2], whereas the higher order equations solve for the higher order fields.

It is worth noting that, in these expansions, Ristorcelli (1997) assumed the thermodynamic scale of pressure to be the reference background pressure P_∞, and the velocity scale to be $(2k/3)^{1/2}$, where k is the turbulent kinetic energy defined as $k = \overline{u'_i u'_i}/2$. This gives $\epsilon^2 = \rho_\infty (2k/3)/P_\infty$, which is equal to γM_t^2 for ideal gas flows, where γ is the ratio of specific heats and $M_t = (2k/3)^{1/2}/c_\infty$, with c_∞ being the reference speed of sound.

Let us now extend Ristorcelli's approach to compressible wall-bounded flows, however, with some notable differences. For homogeneous flows, Ristorcelli (1997) represented the compressible flow field as a sum of an incompressible field and higher order fields, with the latter capturing effects that arise only at finite Mach numbers. In the same spirit, we represent a compressible wall-bounded flow field as a sum of a variable-property zero-Mach-number field—having the same Reynolds number and mean property distributions as the compressible flow—and higher order fields representative of finite-Mach-number effects. Such an expansion ensures that the zeroth-order term in the expansion series comprises of variable-property and Reynolds number effects, such that the higher order terms primarily represent intrinsic compressibility effects which occur only at finite Mach numbers.

Some other differences are listed as follows. Since the base (zeroth order) state about which the expansion series is built, represents a zero-Mach-number flow with

[2]Note that since the pressure term in the Navier-Stokes equation, upon appropriate non-dimensionalization, is multiplied with ϵ^{-2}, a first order pressure p'_1 acts as the incompressible pressure to satisfy a meaningful balance between velocity and pressure terms (Ristorcelli, 1997).

mean property variations, the reference density ρ_∞ and c_∞ in Ristorcelli's work should be replaced with the mean density $\bar{\rho}$ and the mean speed of sound $\bar{c}$, respectively. Additionally, the semi-local friction velocity scale u_τ^* becomes the relevant scale in compressible wall-bounded flows, instead of $(2k/3)^{1/2}$. Lastly, we choose the thermodynamic pressure scale to be $\bar{\rho}\bar{c}^2$ rather than $\bar{p}$, for the following reason. The isentropic density fluctuations are related to pressure fluctuations through the relation (also see equation 2.4)

$$\frac{(\rho')^{is}}{\bar{\rho}} \approx \frac{p'}{\bar{\rho}\bar{c}^2}. \tag{4.9}$$

This implies that the density fluctuations depend on $\bar{\rho}\bar{c}^2$. Since intrinsic compressibility effects are, by definition, related to isentropic density fluctuations, it is natural that the parameter characterizing these effects—namely, ϵ—also depends on $\bar{\rho}\bar{c}^2$. Taking $\mathscr{P} = \bar{\rho}\bar{c}^2$, along with $\bar{\rho}u_\tau^{*2}$ as the hydrodynamic pressure scale, we get

$$\epsilon^2 = \frac{\bar{\rho}u_\tau^{*2}}{\bar{\rho}\bar{c}^2} = M_\tau^{*2}. \tag{4.10}$$

By accounting for these differences, we get the expansion series for pressure fluctuations in wall-bounded flows (analogous to equation 4.8 for homogeneous flows) as

$$\frac{p'}{\bar{\rho}\bar{c}^2} = M_\tau^{*2}\left[\frac{p_1'}{\bar{\rho}u_\tau^{*2}} + M_\tau^{*2}\frac{p_2'}{\bar{\rho}u_\tau^{*2}} + M_\tau^{*4}\frac{p_3'}{\bar{\rho}u_\tau^{*2}} + \ldots\right. \tag{4.11}$$

Now, noting that $\bar{\rho}u_\tau^{*2} = \tau_w$, we can write an equation for pressure fluctuations scaled by the hydrodynamic scale as

$$\frac{p'}{\tau_w} = \frac{p_1'}{\tau_w} + M_\tau^{*2}\frac{p_2'}{\tau_w} + M_\tau^{*4}\frac{p_3'}{\tau_w} + \ldots. \tag{4.12}$$

By writing this equation at the wall, squaring it, and averaging, we get the equation for wall-pressure variance, scaled by τ_w^2 as

$$\overline{p'p'}_w^+ = \overline{p_1'p_1'}_w^+ + M_\tau^{*2}\left[\overline{2p_1'p_2'}_w^+ + M_\tau^{*2}(\overline{p_2'p_2'}_w^+ + \overline{2p_1'p_3'}_w^+) + \ldots,\right. \tag{4.13}$$

where the first term on the right-hand-side signifies wall-pressure variance in a zero-Mach-number variable-property flow.

At this point, it is important to note that not only the leading-order correlation, but also other higher-order correlations on the right-hand side are mainly influenced by Reynolds number and variable-property effects. This is justified as follows. From the analysis of Ristorcelli (1997), we note that the first-order equations—governing the evolution of first-order velocity, second-order density, and second-order pressure (u_{i1}', ρ_2', and p_2')—depend explicitly on the leading-order (incompressible) variables: u_{i0}', ρ_1', and p_1'. For wall-bounded flows, this implies that these higher-order variables (u_{i1}', ρ_2', p_2') are indirectly affected by Reynolds number and variable-property effects, through their dependence on the incompressible solution. Similarly, even higher-order quantities, such as u_{i2}', ρ_3', p_3', are primarily influenced by these effects through their dependence on lower-order variables. These higher-order quantities are not explicitly affected by intrinsic compressibility effects since there is no Mach number or ϵ in the set

of governing equations (Ristorcelli, 1997, see equations (23)–(26) therein); instead, such effects are embedded in the parameter ϵ, by which these variables are multiplied in the expansion series.

Given this understanding, we model the correlations in equation (4.13) as a sum of a constant and a function which depends on Reynolds number and variable-property effects, inspired from the relations proposed for incompressible flows (4.3). For instance,

$$\overline{p_1' p_1'}^{+}_{w} = c_{0,p} + f_{0,p},$$

where $c_{0,p}$ is a constant, $f_{0,p}$ is an unknown function, and the subscript '$0,p$' signifies the leading order term for pressure. Representing all other higher order correlations also in a similar form and substituting them in equation (4.13), we get

$$\overline{p'p'}^{+}_{w} = \underbrace{c_{0,p} + f_{0,p}}_{Re\ \&\ \mathrm{VP}} + \underbrace{M_\tau^{*2} c_{1,p} + M_\tau^{*4} c_{2,p} + \ldots}_{\mathrm{IC}} + \underbrace{M_\tau^{*2} f_{1,p} + M_\tau^{*4} f_{2,p} + \ldots}_{\text{coupling } Re,\ \mathrm{VP},\ \mathrm{IC}}, \tag{4.14}$$

where 'Re' denotes contribution by Reynolds number effects, 'VP' variable-property effects and 'IC' intrinsic compressibility effects. The right-most expression under the brace highlights coupling between these effects.

Here, we postulate that the coupling effects are small, and can be neglected. We test this hypothesis aposteriori based on the available data. From this simplification, we get

$$\overline{p'p'}^{+}_{w} \approx \underbrace{c_{0,p} + f_{0,p}}_{Re\ \&\ \mathrm{VP}} + \underbrace{M_\tau^{*2} c_{1,p} + M_\tau^{*4} c_{2,p} + \ldots.}_{\mathrm{IC}} \tag{4.15}$$

Following a similar approach for the inner-scaled peak streamwise turbulence intensity, namely, $\widetilde{u''u''}^{*}_{p} = \overline{\rho u''u''}/\tau_w$, we get

$$\widetilde{u''u''}^{*}_{p} \approx \underbrace{c_{0,u} + f_{0,u}}_{Re\ \&\ \mathrm{VP}} + \underbrace{M_\tau^{*2} c_{1,u} + M_\tau^{*4} c_{2,u} + \ldots,}_{\mathrm{IC}} \tag{4.16}$$

where $c_{0,u}$, $c_{1,u}$, etc. are constants, analogous to $c_{0,p}$, $c_{1,p}$ for wall-pressure above. Here, $c_{0,u} + f_{0,u}$ represents the leading order correlation $\widetilde{u_0''u_0''}^{*}_{p}$.

Before proceding, we note that for ideal gas cases, the semi-local friction Mach number is approximately constant in the domain and equal to its wall value (see chapter 2). Also, for the non-ideal cases that will be analysed here (Sciacovelli et al., 2017), M_τ^* is approximately constant. This nature of M_τ^* makes it an even more appealing parameter for developing scaling laws. Hereafter, we assume

$$M_\tau^* \approx M_\tau. \tag{4.17}$$

In the following subsections, we will model the unknown functions $f_{0,p}$ and $f_{0,u}$, and determine the constants in equations (4.15) and (4.16).

4.2.1. VARIABLE-PROPERTY EFFECTS

Patel et al. (2015) showed that both semi-locally-scaled wall-pressure and the streamwise peak (along with other quantities) are similar for flows with similar distributions of Re_τ^*, independent of the distribution of $\bar{\rho}$ and $\bar{\mu}$. Through this they confirmed

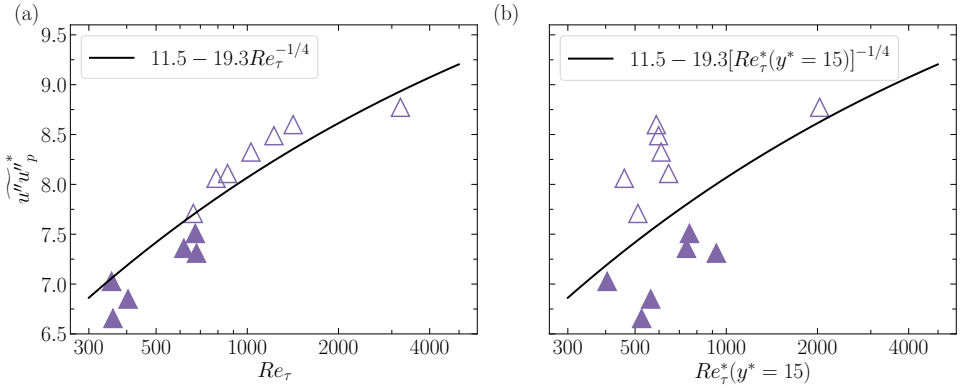

Figure 4.1: Semi-locally scaled streamwise turbulent peak intensity, i.e., $\widetilde{u''u''}^*_p = \widetilde{\rho u''u''}_p/\tau_w$ as a function of (a) Re_τ and (b) Re_τ^* taken at the peak location ($y^* = 15$), for the low-Mach-number variable-property cases of Modesti and Pirozzoli (2024) listed in table 2.3. The black curve corresponds to the fit proposed in Chen and Sreenivasan (2022) for incompressible flows. Filled symbols correspond to the cases with increasing Re_τ^* away from the wall, whereas unfilled symbols correspond to those with decreasing Re_τ^*.

that variable-property effects simply change the local Reynolds number of the flow, conjectured earlier in Morkovin (1962) and Spina et al. (1994). Consequently, a natural choice to model $\overline{p_1' p_1'}^+_w = c_{0,p} + f_{0,p}$ and $\widetilde{u_0'' u_0''}^*_p = c_{0,u} + f_{0,u}$ would be to use the scaling relations developed for incompressible flows, however, with an effective value of Re_τ^*, in place of Re_τ.

It is well established in the incompressible flow literature that the dominant contribution to wall pressure arises from the source terms in the buffer layer (Kim, 1989; Kim and Hussain, 1993). In light of this, we propose that Re_τ^* computed in the buffer layer, say at $y^* = 15$, should be used for scaling wall-pressure.

For the peak intensity, the choice is not as straightforward as it was for wall-pressure r.m.s. One obvious choice is to compute the Reynolds number at the peak location itself ($y^* \approx 15$). Another choice is to use the wall Re_τ. The motivation for the latter choice comes from the analysis of Bradshaw (1967), who argued that the increase in the peak intensity with Re_τ for incompressible flows is directly associated with the large-scale fluctuations in wall shear stress. This is also mathematically supported by the Taylor series expansion of $\overline{u'u'}^+$ at the wall (Chen and Sreenivasan, 2021; Smits et al., 2021), where the leading order term represents fluctuations in wall shear stress.

To assess the correct Reynolds number that accounts for variable-property effects on wall-shear-stress fluctuations, and hence, the peak intensity, we analyse the low-Mach-number variable-property cases of Modesti and Pirozzoli (2024). These cases are essentially free of intrinsic compressibility effects, and hence, they are ideal cases to quantify variable-property effects. For these cases, we have computed the wall shear stress fluctuations using the interpolation technique in Smits et al. (2021), and we observed that these fluctuations scale with Re_τ, and approximately follow the relation in Chen and Sreenivasan (2021), i.e., $0.25 - 0.42Re_\tau^{-1/4}$ (not shown). Following the discussion presented above, this implies that the peak intensity should also scale with Re_τ. This is verified in figure 4.1, which shows the semi-locally scaled peak intensity $\widetilde{u''u''}^*_p$ as a

Quantity ϕ	$c_{0,\phi}$	$f_{0,\phi}$	$c_{1,\phi}$	$c_{2,\phi}$
Channels and Pipes				
$\overline{p'p'}^+_w$	19.36	$-92.4\left[Re^*_\tau(y^*=15)\right]^{-1/4}+110.25\left[Re^*_\tau(y^*=15)\right]^{-1/2}$	2.4	8312.5
$\widetilde{u''u''}^*_p$	11.5	$-19.3Re_\tau^{-1/4}$	78.9	199.3
Boundary layers				
$\overline{p'p'}^+_w$	20.25	$-87.3\left[Re^*_\tau(y^*=15)\right]^{-1/4}+94.09\left[Re^*_\tau(y^*=15)\right]^{-1/2}$	2.4	8312.5
$\widetilde{u''u''}^*_p$	11.5	$-19.3Re_\tau^{-1/4}$	78.9	199.3

Table 4.1: The constants and functions in equations (4.15) and (4.16), i.e., $\phi = c_{0,\phi} + f_{0,\phi} + c_{1,\phi}M_\tau^2 + c_{2,\phi}M_\tau^4$ (neglecting higher order terms). The constant $c_{0,\phi}$ and the function $f_{0,\phi}$ are taken from equations (4.3) and (4.4) (Chen and Sreenivasan, 2022), as discussed in section 4.2.1. The constants $c_{1,\phi}$ and $c_{2,\phi}$ are calibrated based on the constant-property cases, as discussed in section 4.2.2.

function of (a) Re_τ and (b) Re^*_τ taken at the peak location, i.e., $Re^*_\tau(y^*=15)$. Clearly, the spread in the data with respect to the fit from Chen and Sreenivasan (2022) is lower for Re_τ than for $Re^*_\tau(y^*=15)$. Note that since these cases are at negligible Mach numbers, their peak intensity is a direct measure of the leading order term in the expansion series, i.e., $\widetilde{u''_0u''_0}^*_p$.

Even though Re_τ is a better choice than the Reynolds number at the peak location, there is still some spread in the data around the curve fit (see figure 4.1(a)). We denote the cases with increasing Re^*_τ away from the wall using filled symbols, and the ones with decreasing Re^*_τ using unfilled symbols. As seen, the cases with decreasing Re^*_τ away from the wall are shifted upwards with respect to the fit, the rightmost case (at $Re_\tau = 3200$) being the only exception. Whereas, the cases with increasing Re^*_τ are shifted downwards. This is consistent with the observations made in Patel et al. (2015), also outlined in the introduction. Such effects associated with the gradients in the Reynolds number are small for the cases considered, and will be neglected here.

Finally, with these choices of the Reynolds numbers, we model the leading order terms in equations (4.15) and (4.16) as described in table 4.1.

4.2.2. INTRINSIC COMPRESSIBILITY EFFECTS

In this section, we determine the higher order constants in equations (4.15) and (4.16) using our constant-property high-Mach-number cases reported in table 2.1.

Let us first focus on wall-pressure r.m.s. To obtain the constants, we first subtract the variable-property contribution ($c_{0,\phi} + f_{0,\phi}$; see table 4.1) from the total $\overline{p'p'}^+_w$ taken from the DNS. Next, we plot this difference—which signifes the contribution by intrinsic compressibility effects—as a function of the expansion parameter $\epsilon = M_\tau$ in figure 4.2(a) for the four constant-property cases (denoted by red stars). Fitting a curve of the form $M_\tau^2 c_{1,p} + M_\tau^4 c_{2,p}$ (neglecting higher order terms) to these cases, we obtain $c_{1,p} = 2.4$ and $c_{2,p} = 8312.5$; see figure 4.2(a) (black curve)

Figure 4.2(a) also plots the intrinsic compressibility contribution for several boundary layer and channel flow cases in the literature as listed in table 2.3. Despite the fact that these cases are at different Reynolds numbers, and possess different distributions of mean properties, majority of the cases follow the curve fit set by the constant property cases quite well. This corroborates the assumption we made regarding neglecting the coupling terms in section 4.2.

However, there are some exceptions. First, for the boundary layer cases of Huang

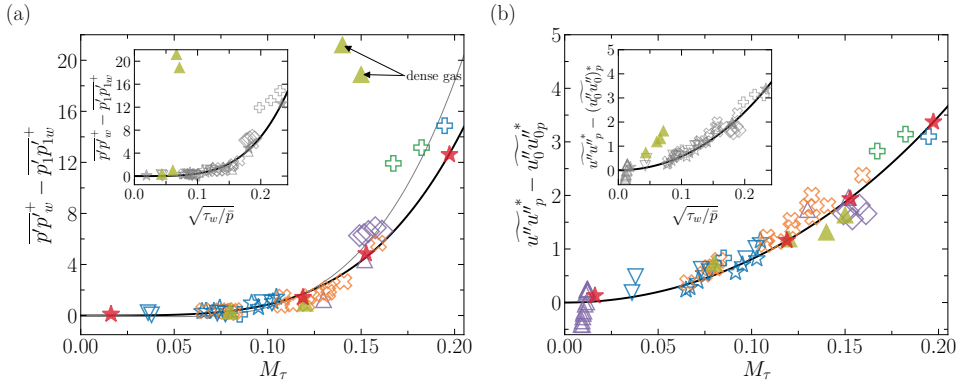

Figure 4.2: Contribution by intrinsic compressibility effects to (a) wall-pressure variance and (b) the peak streamwise turbulence intensity as a function of M_τ for the cases described in table 2.3. The black curve in (a) and (b) corresponds to $c_{1,\phi}M_\tau^2 + c_{2,\phi}M_\tau^4$, where $c_{1,\phi}$ and $c_{2,\phi}$ are reported in table 4.1, and ϕ represents wall-pressure r.m.s. or the peak intensity. These coefficients are calibrated using the constant-property cases in table 2.3 (red stars). The gray curve in (a) corresponds to $c_{1,p}M_\tau^2 + c_{2,p}M_\tau^4$, where the coefficients $c_{1,p} = -66.9$ and $c_{2,p} = 13148.7$ are obtained using the conventional turbulent boundary layer cases listed in table 2.3. (Insets) The insets report intrinsic compressibility contribution as a function of $\sqrt{\tau_w/\bar{\rho}}$. The gray symbols signify ideal gas air cases for which $\sqrt{\tau_w/\bar{\rho}} = \sqrt{1.4}M_\tau$, and the colored symbols represent the dense gas cases of Sciacovelli et al. (2017). Note that low-Reynolds-number cases (i.e., the cases where the semi-local Reynolds number Re_τ^* falls below 300 anywhere in the domain) are excluded.

et al. (2022), represented by green plus, the deviation from the curve fit is quite high. This could be possibly due to the simplifications we made in the analysis. It is also possible that the intrinsic compressibility contribution to wall-pressure r.m.s. differs in boundary layers compared to channels. Thus, the coefficients ($c_{1,p}$ and $c_{2,p}$) tuned based on the constant-property channels (CP) might not be accurate for boundary layers. Refining these coefficients for boundary layers would require constant-property high-Mach-number boundary-layer simulations, which is deferred to future work. Nevertheless, in figure 4.2(a), we show the gray curve obtained using the conventional turbulent boundary layer cases listed in table 2.3. As expected, this curve aligns more closely with the green plus symbols.

Second, the dense gas cases of Sciacovelli et al. (2017) at high Mach numbers depict extremely high wall-pressure fluctuations. This is due to the proximity of these cases to the Widom line (the curve that marks the maximum of the specific heat at constant pressure, above the critical point). In this region, small pressure fluctuations can cause large density fluctuations, which in turn intensify pressure fluctuations through the source terms. Such an effect is due to the complexity of the equation of state, and is thus not accounted for in the present scaling model.

Repeating the same analysis for the peak of streamwise turbulence intensity, we get $c_{1,u} = 78.9$ and $c_{2,u} = 199.3$. Figure 4.2(b) shows the intrinsic compressibility contribution towards the peak intensity for the constant- and variable-property cases listed in table 2.3, along with the curve fit with tuned constants. Clearly, majority of the cases follow the curve, corroborating that the coupling effects are small.

The insets in figure 4.2 show the intrinsic compressibility contributions to the

wall-pressure r.m.s. and the peak intensity as functions of $\sqrt{\tau_w/\bar{p}}$—the form that ϵ would take if $\bar{p}$ were chosen as the thermodynamic pressure scale. For the ideal gas air cases (shown in gray symbols), $\sqrt{\tau_w/\bar{p}}$ quantifies intrinsic compressibility effects as effectively as M_τ (main figure 4.2, discussed earlier), since $\sqrt{\tau_w/\bar{p}} \approx \gamma M_\tau$, with $\gamma = 1.4$ for these cases. However, for the dense gas cases of Sciacovelli et al. (2017) (shown in colored symbols), the characterization of intrinsic compressibility effects deteriorates for both wall-pressure and the peak when $\sqrt{\tau_w/\bar{p}}$ is used instead of M_τ. These observations support our choice made in section 4.2 of using $\bar{\rho}\bar{c}^2$ as the relevant thermodynamic scale of pressure rather than $\bar{p}$. This is further supported by the observation that, for the dense gas cases, the upward shift in the logarithmic mean velocity profiles due to intrinsic compressibility effects is well quantified in terms of M_τ (see ▲ in the inset of figure 5.1a), instead of $\sqrt{\tau_w/\bar{p}}$.

Finally, it is interesting to note that for wall pressure, most of the intrinsic compressibility contribution comes from the quartic term $M_\tau^4 c_{2,p}$, while the same for the peak intensity stems from the quadratic term $M_\tau^2 c_{1,u}$. This is evident in figure 4.2, where the fitted curve appears quartic in panel (a) and quadratic in panel (b).

For wall pressure, the increase with Mach number has been attributed to the presence of travelling wave-packet-like structures in the pressure field (Yu et al., 2022; Zhang et al., 2022). These structures have been extensively studied in the literature (Yu et al., 2019; Tang et al., 2020; Gerolymos and Vallet, 2023; Yu et al., 2024), although the physical mechanism underlying their genesis is still unclear. In chapter 3, we reported that the component of dilatational velocity (also termed non-pseudo-sound) associated with these wave-packet-like structures increases with $M_\tau^{3.3}$, close to a quartic dependence. This likely explains the quartic increase in wall pressure observed in figure 4.2(a).

For the streamwise turbulence intensity, chapter 3 concluded that the peak value increases due to the opposition of vortical motions by near-wall dilatational velocities. Specifically, this interaction modifies the turbulent shear stress, which in turn affects the production of streamwise turbulence intensity, thereby altering its peak value. This opposition mechanism scales with M_τ^2, thereby explaining the quadratic increase in the peak intensity.

4.3. THE FINAL SCALING RELATIONS

By combining the functions and constants obtained from sections 4.2.1 and 4.2.2, we get the final scaling relations for the wall-pressure r.m.s. and the peak streamwise turbulence intensity, as reported in table 4.1.

Using these relations, we estimate the wall-pressure r.m.s. and the peak intensity, and compare the estimation with respect to the DNS. The error in the estimation is defined as

$$\varepsilon_\phi = \frac{\phi^{DNS} - \phi^{model}}{\phi^{DNS}}, \tag{4.18}$$

where ϕ corresponds to wall-pressure r.m.s. or the peak intensity. We also compute the root-mean-square (RMS) error across all cases as

$$\text{RMS} = \sqrt{\frac{1}{N}\sum \varepsilon_\phi^2}, \tag{4.19}$$

where N is the total number of cases.

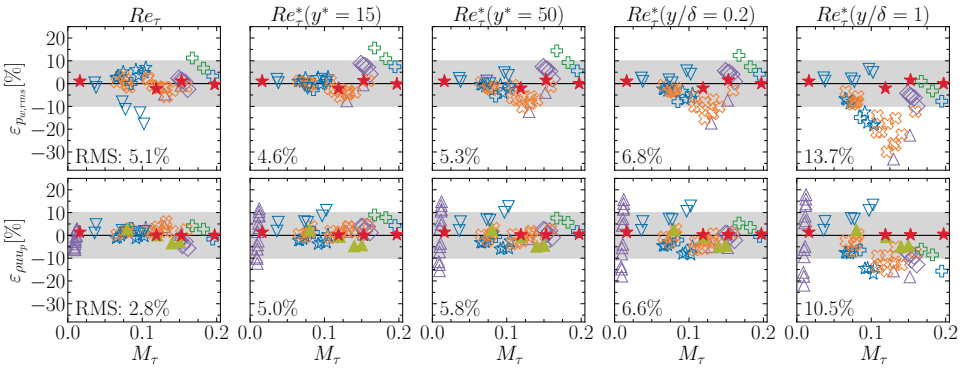

Figure 4.3: The error in the estimation of (top row) wall-pressure r.m.s. and (bottom row) the peak of streamwise turbulence intensity as a function of M_τ for the cases described in table 2.3. The errors are defined using equation (4.18). The different columns correspond to different Reynolds number definitions used while computing $f_{0,\phi}$ in table 4.1. The shaded areas represent an error margin of +/-10%. Note that low-Reynolds-number cases (i.e., the cases where the semi-local Reynolds number Re^*_τ falls below 300 anywhere in the domain) are excluded.

Figure 4.3 presents ε_ϕ for (top row) the wall-pressure r.m.s. and (bottom row) the peak streamwise turbulence intensity, for the cases listed in table 2.3. (Note that the dense-gas cases are excluded from wall-pressure error estimations, to maintain reasonable axis limits). The different columns correspond to different Reynolds number definitions used while computing $f_{0,\phi}$ in table 4.1. Clearly, the errors associated with the Reynolds number choices made in section 4.2.1—namely, $Re^*_\tau(y^* = 15)$ for wall-pressure fluctuations and Re_τ for the peak intensity—are relatively low when compared to those from other Reynolds number definitions, on average across all cases (compare their RMS values). Furthermore, with these Reynolds number choices, a majority of the cases lie within the +/-10% error band.

Comparison with existing models—Table 4.2 reports the maximum absolute error and the root-mean-square (RMS) error in predicting the wall-pressure r.m.s. using various models from the literature. The errors reported in table 4.2 are computed by applying each model to the type of flow (channel or boundary layer) for which it was originally developed. For example, the models by Laganelli et al. (1983); Ritos et al. (2019); Zhang et al. (2022); Wan et al. (2024) are applied exclusively to conventional air-like boundary layers. In contrast, the model by Gerolymos and Vallet (2023) is applied to both conventional channels and boundary layers, as listed in table 2.3. The present model is tested on a broader set of flows, including conventional channels and boundary layers, as well as the four constant-property cases reported in table 2.1.

As seen, the Laganelli family of models (Laganelli et al., 1983; Ritos et al., 2019; Zhang et al., 2022) yield relatively high error values, with an RMS error exceeding 12%. The model proposed by Wan et al. (2024) achieves better accuracy, with an RMS error of 9.4%, despite not explicitly accounting for Reynolds number or wall-cooling effects. Among the models available in the literature, the best performance is observed for the model by Gerolymos and Vallet (2023), which achieves an RMS error of 7.2%. However, this value is still high, primarily due to significant errors incurred in predicting

	Laganelli et al. (1983)†	Ritos et al. (2019)†	Zhang et al. (2022)†	G&V (2023)‡	Wan et al. (2024)†	Present⋆
Max abs error[%]	39	34.3	41.9	15.7	18.3	15.6
RMS[%]	29	12.4	13.3	6.9	9.5	4.6

Table 4.2: The maximum absolute error (L_∞ norm) and the RMS error (L_2 norm; equation 4.19) for various wall-pressure r.m.s. models available in the literature. The models marked with '†' have been applied exclusively to conventional (ideal-gas air) boundary layers reported in table 2.3, for which they were originally developed. The model marked with '‡' has been tested on both conventional channels and boundary layers. Finally, the present model marked by '⋆' has been applied to a broader set of flows, including conventional channels and boundary layers, as well as the four constant-property cases reported in table 2.1. Note that G&V stands for Gerolymos and Vallet (2023).

high-Mach-number boundary layers. The present model shows improved performance over existing approaches, with the lowest RMS error of 4.7%.

Finally, for the streamwise turbulence intensity peak, using the proposed relation results in a maximum absolute error of 6.8% and an RMS error of 2.8%. These values could not be compared to those obtained from other models in the literature, as, to the best of our knowledge, there are currently no models available that predict this quantity in compressible flows.

4.4. SUMMARY

In this chapter, we have proposed scaling models for the wall-pressure root-mean-square (r.m.s.) and the peak of streamwise turbulence intensity that are applicable to both channels and boundary layers. These models were developed by expressing the aforementioned quantities as an expansion series in terms of the friction Mach number, M_τ. The first term in this series accounts for Reynolds number and variable-property effects, whereas the higher-order terms primarily capture intrinsic compressibility effects.

To model the leading order term, we used the same expressions as proposed for incompressible flows, however, we replace Re_τ in them with an effective value of the semi-local Reynolds number which incorporates variable-property effects. For wall-pressure r.m.s., this value was found to be the Reynolds number defined in the buffer layer (at $y^* = 15$), whereas for the peak streamwise intensity, we found the effective value to be the wall Re_τ.

We model the higher-order correlations in the series as constants, whose values are found based on our constant-property high-Mach-number cases—described in table 2.1—representative of intrinsic compressibility effects. Modeling these correlations as simple constants implies that any coupling between Reynolds number, variable-property and intrinsic compressibility effects is small—an assumption which was verified aposteriori using the available data.

The final scaling models demonstrate high accuracy, with predictions for majority of the cases falling within a +/-10% error margin. The proposed model for wall-pressure r.m.s. outperforms those available in the literature. A similar comparative analysis could not be performed for the peak streamwise turbulence intensity, as no prior models exist for this quantity in compressible flows.

Finally, an additional key finding has been noted: based on the dense gas (non-ideal) cases of Sciacovelli et al. (2017), we confirm that $\bar{\rho}\tilde{c}^2$ is a more appropriate

thermodynamic pressure scale than the mean pressure $\bar{p}$, supporting the choice of expressing the expansion series in terms of M_τ. Future work should extend the proposed scaling approach to other turbulence quantities, and explore the role of higher-order terms and coupling effects relevant at Mach numbers beyond those considered here.

5

INCORPORATING IC EFFECTS IN VELOCITY TRANSFORMATIONS

In this chapter, by quantifying the log-law shift in terms of an appropriately defined Mach number, we assess whether the shift observed in the semi-local transformation for the variable-property cases (figure 1.5b) is also due to intrinsic compressibility (IC) effects—similar to the constant-property (CP) cases (figure 3.1a). Consequently, we derive a transformation that accounts for both variable-property and intrinsic compressibility effects, the latter being the key improvement over the current state-of-the-art. The importance of intrinsic compressibility effects contradicts the renowned Morkovin's hypothesis.

The contents of this chapter have been published as:
Hasan, A. M., Larsson, J., Pirozzoli, S., and Pecnik, R. (2023). Incorporating intrinsic compressibility effects in velocity transformations for wall-bounded turbulent flows. *Physical Review Fluids*, 8(11):L112601.

5.1. INTRODUCTION

The law of the wall for incompressible turbulent flows is one of the cornerstones of fluid dynamics (Bradshaw and Huang, 1995). Such a universal law is still missing for compressible flows, because the interplay of thermodynamics and hydrodynamics leads to significantly richer flow physics and even more intricate phenomena in turbulence. Efforts have long been devoted to find a transformation that reduces the mean velocity profile of compressible wall-bounded flows to that of incompressible, constant-property flows (Zhang et al., 2012). Such a transformation can assist in extending the incompressible modeling techniques to compressible flows, eventually enabling better flow and heat transfer predictions for a range of applications.

The history of velocity transformations dates back to the 1950s, when Van Driest (1951) (hereafter VD) proposed a correction to the incompressible law of the wall, accounting for mean density variations in the friction velocity scale. This transformation reads:

$$\bar{U}^+_{VD} = \int_0^{\bar{u}^+} \sqrt{\frac{\bar{\rho}}{\rho_w}}\, d\bar{u}^+, \tag{5.1}$$

where $u_\tau = \sqrt{\tau_w/\rho_w}$, $u^*_\tau = \sqrt{\tau_w/\bar{\rho}}$, ρ_w corresponds to density at the wall, and $\bar{\rho}$ signifies local mean density. Subsequently, Zhang et al. (2012) proposed a transformation that improves the collapse in the wake region of compressible boundary layers. However, both transformations were developed for adiabatic boundary layers, and as such, they fail for diabatic flows (see figure 1.5a).

In 2016, Trettel and Larsson (2016) formally derived an alternative to the VD transformation, suggesting that the semi-local wall coordinate, previously defined on intuitive grounds by Huang et al. (1995), is the correct scaling to account for changes in the viscous length scale. Their transformation reads:

$$\bar{U}^+_{TL} = \int_0^{\bar{u}^+} \sqrt{\frac{\bar{\rho}}{\rho_w}} \left[1 + \frac{1}{2}\frac{1}{\bar{\rho}}\frac{d\bar{\rho}}{dy} y - \frac{1}{\bar{\mu}}\frac{d\bar{\mu}}{dy} y \right] d\bar{u}^+, \tag{5.2}$$

where $\bar{\mu}$ is the mean viscosity.

Patel et al. (2016a), by studying the effect of variable density and viscosity on turbulence in channel flows at the zero Mach number limit, found that the primary influence of variable properties on the velocity transformation can be effectively characterized by the semi-local Reynolds number $Re^*_\tau = \bar{\rho} u^*_\tau h/\bar{\mu}$ (where h is the channel half-height). Consequently, they developed a velocity transformation, which is mathematically equivalent to $\bar{U}^+_{TL}$, as

$$\bar{u}^* = \int_0^{\bar{u}^+} \left(1 + \frac{y}{Re^*_\tau}\frac{dRe^*_\tau}{dy} \right) \sqrt{\frac{\bar{\rho}}{\rho_w}}\, d\bar{u}^+. \tag{5.3}$$

By noting that $Re^*_\tau = h/\delta^*_\nu$, where $\delta^*_\nu = \bar{\mu}/(\bar{\rho} u^*_\tau)$ is the semi-local viscous length scale, and $\sqrt{\bar{\rho}/\rho_w} = u_\tau/u^*_\tau$, we express this equation as

$$\bar{u}^* = \bar{U}^+_{TL} = \int_0^{\bar{u}^+} \left(1 - \frac{y}{\delta^*_\nu}\frac{d\delta^*_\nu}{dy} \right) \underbrace{\frac{u_\tau}{u^*_\tau} d\bar{u}^+}_{d\bar{U}^+_{VD}}. \tag{5.4}$$

Despite being accurate for channel flows, these transformations (also known as the 'TL' or 'semi-local' transformation) are inaccurate for high-speed boundary layers (Trettel and Larsson, 2016; Patel et al., 2016a; Zhang et al., 2018; Griffin et al., 2021; Hirai et al., 2021), typically yielding higher log-law intercept as compared to incompressible flows (see figure 1.5b).

Recently, Griffin et al. (2021) (hereafter GFM) derived a new transformation based on the universality of the ratio of production and dissipation, and a stress-based blending function. They argued that, in the log-layer, the ratio of TKE production—scaled using a mix of classical and semi-local frameworks, namely $P^{\ddagger} = \overline{\rho u'' v''}^{+} d\widetilde{u}^{+}/dy^{*}$—to the classically scaled dissipation ϵ^{+} (per unit volume[1]) is universal. Furthermore, assuming that $\epsilon^{+}/\bar{\mu}^{+}$ (where $\bar{\mu}^{+} = \bar{\mu}/\mu_w$) and $\overline{\rho u'' v''}^{+}$ are also universal in the log-layer of compressible flows, they proposed a universal mean shear formulation as

$$S_{eq} = \frac{P^{\ddagger}}{\epsilon^{+}} \frac{\epsilon^{+}}{\bar{\mu}^{+}} \frac{1}{\overline{\rho u'' v''}^{+}} = \frac{1}{\bar{\mu}^{+}} \frac{d\widetilde{u}^{+}}{dy^{*}} = \underbrace{\frac{1}{(\bar{\mu}^{+})^2} \frac{dy^{+}}{dy^{*}}}_{f_{GFM}} \underbrace{\bar{\mu}^{+} \frac{d\widetilde{u}^{+}}{dy^{+}}}_{d\widetilde{u}^{*}/dy^{*}}, \tag{5.5}$$

where $d\widetilde{u}^{*}/dy^{*}$ corresponds to the Favre-averaged semi-local mean shear whose integration would lead to $\widetilde{u}^{*}$ (similar to equation (5.4), except that the velocity is Favre-averaged), and f_{GFM} corresponds to the factor which primarily differentiates between the GFM and semi-local transformations. The final transformation is obtained by blending equation (5.5) in the log-layer with $d\widetilde{u}^{*}/dy^{*}$ in the viscous sublayer, using a suitable blending function. The GFM transformation improves the collapse of the velocity profile for air-like compressible boundary layers, however, it is inaccurate for ideal gas flows with non-air-like viscosity laws, and for flows with fluids at supercritical pressures (figure 1.5c; see also Bai et al., 2022).

Volpiani et al. (2020b) proposed a data-driven transformation which also improves the results for compressible boundary layers, although not rooted in physical principles. The lack of a universal, physics-driven compressibility transformation for turbulent wall-bounded flows sets up the motivation for this chapter.

All transformations outlined above rely on the implicit assumption that intrinsic compressibility effects are insignificant, and that only mean fluid property variations matter for this problem (Morkovin's hypothesis; see chapter 1). However, in chapter 3, we observed that IC effects can also play a key role in influencing the mean velocity profiles.

Objectives.—The first objective of this chapter is to assess whether the log-law shift observed in the semi-local transformation for high-speed boundary layers is an intrinsic compressibility effect, and the second objective is to derive a transformation that accounts for these effects.

5.2. INTRINSIC COMPRESSIBILITY EFFECTS ON MEAN VELOCITY

Figure 5.1(a), similar to figure 3.1(a), shows the mean velocity profiles for the four CP cases. It also shows the velocity profile for the incompressible case of Moser et al. (1999) at a similar Reynolds number. As we concluded in chapter 3, these cases depict

[1] $\epsilon^{+} = \epsilon/(\rho_w u_\tau^3/\delta_\nu)$, where u_τ and δ_ν are defined in equation (1.6).

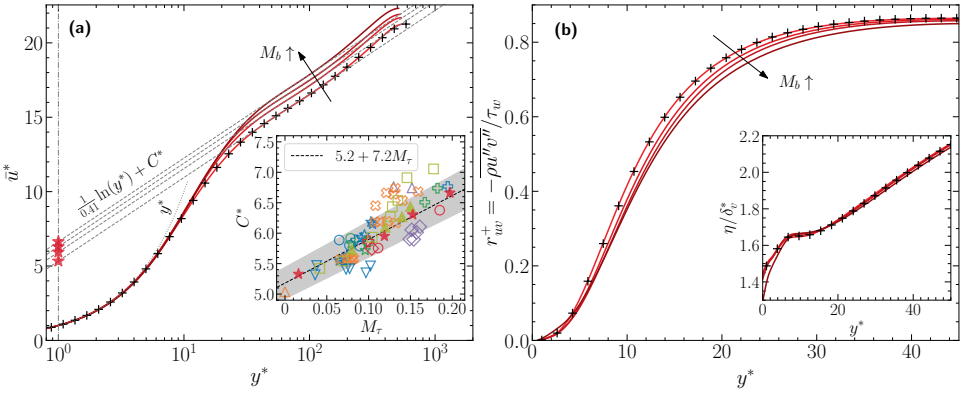

Figure 5.1: (a) Mean velocity profiles in constant-property (CP) compressible channel flows, after the semi-local transformation (Trettel and Larsson, 2016; Patel et al., 2016a) defined as $d\bar{u}^* = \left(1 - y/\delta_v^* d\delta_v^*/dy\right)\sqrt{\bar{\rho}/\rho_w}\, d\bar{u}^+$ (since property variations are absent in these cases, the transformed velocity is equivalent to $\bar{u}^+$). (Inset): Log-law constant C^* (5.6) as a function of M_τ. Symbols are as in table 2.3. The dashed line shows a fit for the constant-property cases, whereas the gray shaded area indicates an error bar of +/-5%. Note that low-Reynolds-number cases (i.e., the cases where the semi-local Reynolds number Re_τ^* falls below 300 anywhere in the domain) are excluded. (b) Turbulent shear stress for the constant-property compressible cases. (Inset): Kolmogorov length scale, scaled by the semi-local viscous length scale δ_v^*. The black symbols represent the incompressible case of Moser et al. (1999), in both (a) and (b).

an upward shift in the logarithmic portion of the mean velocity profiles attributable to intrinsic compressibility effects.

To determine whether the log-law shift observed in the semi-local transformation for high-speed flows (figure 1.5b) is also due to IC effects—similar to the CP cases—it is first necessary to quantify this shift and plot it as a function of a suitable parameter that appropriately characterizes these effects.

5.2.1. THE APPROPRIATE PARAMETER TO QUANTIFY IC EFFECTS

In chapter 4, by taking τ_w as the appropriate hydrodynamic scale of pressure, and $\bar{\rho}\bar{c}^2$ as the suitable thermodynamic scale, we found that the semi-local friction Mach number—defined as $M_\tau^* = u_\tau^*/\bar{c}$, with $\bar{c}$ being the local speed of sound—is an appropriate parameter to quantify IC effects. Moreover, by noting that the distribution of M_τ^* is approximately constant in the domain for both CP as well as variable-property ideal gas cases (figure 2.2), we assumed $M_\tau^* \approx M_\tau$. Finally, we substantiated these arguments by showing that IC effects on the wall-pressure r.m.s. and the peak of streamwise Reynolds stress accurately scale with M_τ.

Support for M_τ is also found in the literature. From dimensional analysis in the near-wall region of compressible boundary layers, Bradshaw (1977) deduced $u_\tau = \sqrt{\tau_w/\rho_w}$ to be the relevant velocity scale, and $c_w = \sqrt{\gamma R T_w}$ as the relevant sound speed, respectively. Thus, $M_\tau = u_\tau/c_w$ was identified as the most suitable Mach number, as also supported by Smits and Dussauge (2006). Moreover, Yu et al. (2022) observed that intrinsic compressibility effects on the wall-shear-stress and wall-pressure fluctuations accurately scale with M_τ.

5.2.2. QUANTIFYING THE LOG-LAW SHIFT

We quantify the log-law shift as

$$C^* = \frac{1}{y_2^* - y_1^*} \int_{y_1^*}^{y_2^*} \left(\bar{u}^* - \frac{1}{0.41} \ln y^* \right) dy^*, \tag{5.6}$$

where y_1^* and y_2^* determine the limits of the logarithmic region. We take $y_1^* \approx 50$ and y_2^* as the value corresponding to $y/h \approx 0.1$ or $y/\delta \approx 0.1$, where h is the channel half-height and δ is the boundary layer thickness. If y_2^* correponding to $y/\delta \approx 0.1$ (or $y/h \approx 0.1$) is less than 60, then we take $y_2^* \approx 70$ to obtain a sufficient window of integration.

The inset in figure 5.1(a) shows C^* as a function of the friction Mach number M_τ for the four CP cases, and for several compressible ideal gas channel flows and boundary layers available in the literature. The trend line in the inset of figure 5.1(a) is obtained by considering the CP cases only, hence it is a measure of the log-law shift due to intrinsic compressibility alone. Interestingly, the majority of the other cases follow the trend line, suggesting that the increase in the log-law intercept for those cases is also due to intrinsic compressibility effects. Deviations from the common trend can be attributed to effects other than those directly related to mean property variations (within the assumptions of the semi-local scaling theory) and intrinsic compressibility, as briefly discussed towards the end of this chapter (and also in chapter 8 and Appendix B). Note that non-negligible scatter is also observed in incompressible flows (Nagib and Chauhan, 2008), which suggests that the precise determination of the log-law constant is sensitive to numerical/experimental uncertainties.

As discussed in chapter 3, the log-law shift in the mean velocity profiles stems from a corresponding outward shift (or reduction) in the turbulent shear stress profiles. This outward shift for the CP cases is also shown here in figure 5.1(b). To account for this shift, we drop the universality assumption of the turbulent shear stress, made in Trettel and Larsson (2016) and Patel et al. (2016a), and derive a mean velocity transformation accounting for intrinsic compressibility effects.

5.3. DERIVATION OF THE MEAN VELOCITY TRANSFORMATION

In the inner layer of parallel (or quasi-parallel) shear flows, integration of the mean momentum equation implies that the sum of viscous and turbulent shear stresses is equal to the total shear stress, given as

$$\bar{\mu} \frac{d\tilde{u}}{dy} - \overline{\rho u'' v''} \approx \tau_{tot}, \tag{5.7}$$

where $\tau_{tot} \approx \tau_w$ in boundary layers and it varies linearly in channel flows. Note that terms due to viscosity fluctuations are neglected. Normalizing equation (5.7) by τ_w and using the definitions of u_τ^* and δ_ν^*, we get the non-dimensional form as

$$\underbrace{\frac{\delta_\nu^*}{u_\tau^*} \frac{d\tilde{u}}{dy}}_{d\tilde{u}^*/dy^*} + r_{uv}^+ \approx \tau_{tot}^+, \tag{5.8}$$

where $r_{uv}^+ = -\overline{\rho u'' v''}/\tau_w$ and $\tau_{tot}^+ = \tau_{tot}/\tau_w$. Next, following Trettel and Larsson (2016), we assume universality of the total shear stress and equate equation (5.8) with its

incompressible counterpart to get

$$\frac{d\bar{U}^+}{dY^+} + R^+_{uv} = \frac{\delta^*_v}{u^*_\tau}\frac{d\bar{u}}{dy} + r^+_{uv}, \tag{5.9}$$

where $\bar{U}^+ = \bar{U}/u_\tau$ and $Y^+ = Y/\delta_v$ denote the non-dimensional velocity and wall-normal coordinate of an incompressible flow, that constitute the universal law of the wall.

Introducing the definition of the eddy viscosity for incompressible flows (superscript 'i') as $\mu^i_t/\mu_w = R^+_{uv}/(d\bar{U}^+/dY^+)$, and similarly for compressible flows (superscript 'c') as $\mu^c_t/\bar{\mu} = r^+_{uv}/([\delta^*_v/u^*_\tau]d\bar{u}/dy)$, equation (5.9) can be written as

$$\left(1+\mu^i_t/\mu_w\right)\left(\frac{d\bar{U}^+}{dY^+}\right) = \left(1+\mu^c_t/\bar{\mu}\right)\left(\frac{\delta^*_v}{u^*_\tau}\frac{d\bar{u}}{dy}\right), \tag{5.10}$$

which upon rearrangement yields

$$\frac{d\bar{U}^+}{d\bar{u}^+} = \left(\frac{1+\mu^c_t/\bar{\mu}}{1+\mu^i_t/\mu_w}\right)\frac{\delta^*_v}{\delta_v}\frac{dY^+}{dy^+}\frac{u_\tau}{u^*_\tau}. \tag{5.11}$$

Equation (5.11) offers a very general eddy-viscosity-based framework for deriving compressibility transformations for wall-bounded flows that satisfy equation (5.7). This equation in dimensional form is similar to that proposed in Iyer et al. (2019), where it is employed to deduce an eddy viscosity model, provided a velocity transformation kernel is known (see also Yang and Lv (2018)).

In order to fully define the velocity transformation, a relationship between Y^+ and y^+ shall be established. Assuming that the turbulent shear stress is universal in the inner layer, Trettel and Larsson (2016) deduced that $Y^+ = (\delta_v/\delta^*_v)y^+ = y^*$. However, as seen in figure 5.1(b), the turbulent shear stress is not universal in the presence of intrinsic compressibility effects, hence the question of whether or not $Y^+ = y^*$ still holds has to be reassessed. Indeed, $Y/\delta_v = y/\delta^*_v$ implies that δ^*_v is the proper length scale for small-scale turbulence and viscous effects in compressible flows, just like δ_v in incompressible flows. This was first proposed by Huang et al. (1995) and later verified for a range of turbulence statistics by Patel et al. (2015). The inset of figure 5.1(b) shows the distribution of the Kolmogorov length scale (i.e., a measure of small turbulent scales) non-dimensionalized by δ^*_v (Patel et al., 2016a) for the four CP cases and the incompressible case of Moser et al. (1999) at a similar Reynolds number. The nearly universal distribution throughout the inner layer, despite non-universality of the turbulent shear stress, implies that δ^*_v is still an appropriate measure of small-scale turbulence, thereby supporting the validity of $Y^+ = y^*$ also in the presence of intrinsic compressibility effects.

Exploiting the coordinate transformation $Y^+ = y^*$, and using

$$dy^*/dy^+ = \left(1 - y^*\, d\delta^*_v/dy\right)\delta_v/\delta^*_v,$$

we obtain the final proposed velocity transformation kernel from equation (5.11) as

$$\frac{d\bar{U}^+}{d\bar{u}^+} = \underbrace{\left(\frac{1+\mu^c_t/\bar{\mu}}{1+\mu^i_t/\mu_w}\right)}_{3}\underbrace{\left(1 - \frac{y}{\delta^*_v}\frac{d\delta^*_v}{dy}\right)}_{2}\underbrace{\frac{u_\tau}{u^*_\tau}}_{1}. \tag{5.12}$$

Equation (5.12) embodies a sequence of velocity transformations, as outlined below:

- Factor 1 is the correction proposed by Van Driest (1951) to account for the change in the friction velocity scale from $u_\tau = \sqrt{\tau_w/\rho_w}$ to $u_\tau^* = \sqrt{\tau_w/\bar{\rho}}$. It can also be written as $\sqrt{\bar{\rho}/\rho_w}$.
- Factor 2 is the correction proposed in Trettel and Larsson (2016) and Patel et al. (2016a) to account for the change in the viscous length scale from δ_ν to δ_ν^*. Factors 1 and 2 combined form the semi-local transformation kernel (5.4). These factors account for the effects of mean property variations on the velocity transformation.
- Factor 3 is the proposed correction which accounts for additional physics beyond those captured by the semi-local transformation.

In order to obtain a closed form of the transformation, the eddy viscosities μ_t^i and μ_t^c must be prescribed. Out of the many possible eddy viscosity models, we consider the Johnson-King (JK) model (Johnson and King, 1985) to achieve an explicit expression of the transformation. The JK model is built on Van Driest's mixing-length arguments in the logarithmic region (Van Driest, 1951), with a damping function (Van Driest, 1956a) to reproduce the correct near-wall behaviour. The eddy viscosity is defined as $\mu_t^i = \sqrt{\tau_w \rho_w}\kappa Y[1-\exp(-Y^+/A^+)]^2$. The set of constants $\kappa = 0.41$, $A^+ = 17$ is commonly used (Iyer and Malik, 2019), and yields an incompressible log-law intercept 5.2. Similarly, for compressible flows, $\mu_t^c = \sqrt{\tau_w \bar{\rho}}\kappa y[1-\exp(-y^*/A^+)]^2$, with the damping function defined based on the the semi-local wall distance (y^*) to account for mean property variations (Patel et al., 2016b; Yang and Lv, 2018). As outlined previously, intrinsic compressibility effects modulate the near-wall damping of turbulence, causing the turbulent shear stress to shift outwards (figure 5.1b). Thus, we modify the damping constant to depend on M_τ, such that the compressible eddy viscosity model reads

$$\mu_t^c = \sqrt{\tau_w \bar{\rho}}\kappa y \underbrace{\left[1-\exp\left(\frac{-y^*}{A^+ + f(M_\tau)}\right)\right]^2}_{D(y^*,M_\tau)}. \tag{5.13}$$

The increase in the effective damping constant ($A^+ + f(M_\tau)$) in equation (5.13), implies that the eddy viscosity (and hence, turbulent shear stress) shifts outwards, with subsequent increase of the log-law intercept (C^*). In fact, it can be readily checked that C^* grows linearly with the damping constant. Since the log-law intercept also depends linearly on M_τ (see inset of figure 5.1a), we argue that the corrective term $f(M_\tau)$ should be linear. Here, we use $f(M_\tau) = 19.3\,M_\tau$ to reproduce the linear curve-fit presented in figure 5.1(a).

Writing eddy viscosities in the non-dimensional form as $\mu_t^i/\mu_w = \kappa Y^+ D(Y^+,0)$ and $\mu_t^c/\bar{\mu} = \kappa y^* D(y^*,M_\tau)$, and replacing Y^+ by y^* in μ_t^i/μ_w yields the final velocity transformation

$$\bar{U}^+ = \int_0^{\bar{u}^+} \left(\frac{1+\kappa y^* D(y^*,M_\tau)}{1+\kappa y^* D(y^*,0)}\right)\left(1-\frac{y}{\delta_\nu^*}\frac{d\delta_\nu^*}{dy}\right)\sqrt{\frac{\bar{\rho}}{\rho_w}}\,d\bar{u}^+. \tag{5.14}$$

5.4. RESULTS AND DISCUSSION

This transformation is tested and compared to the semi-local (or TL) and GFM transformations in figure 5.2 for 70 boundary layer and channel flow cases reported

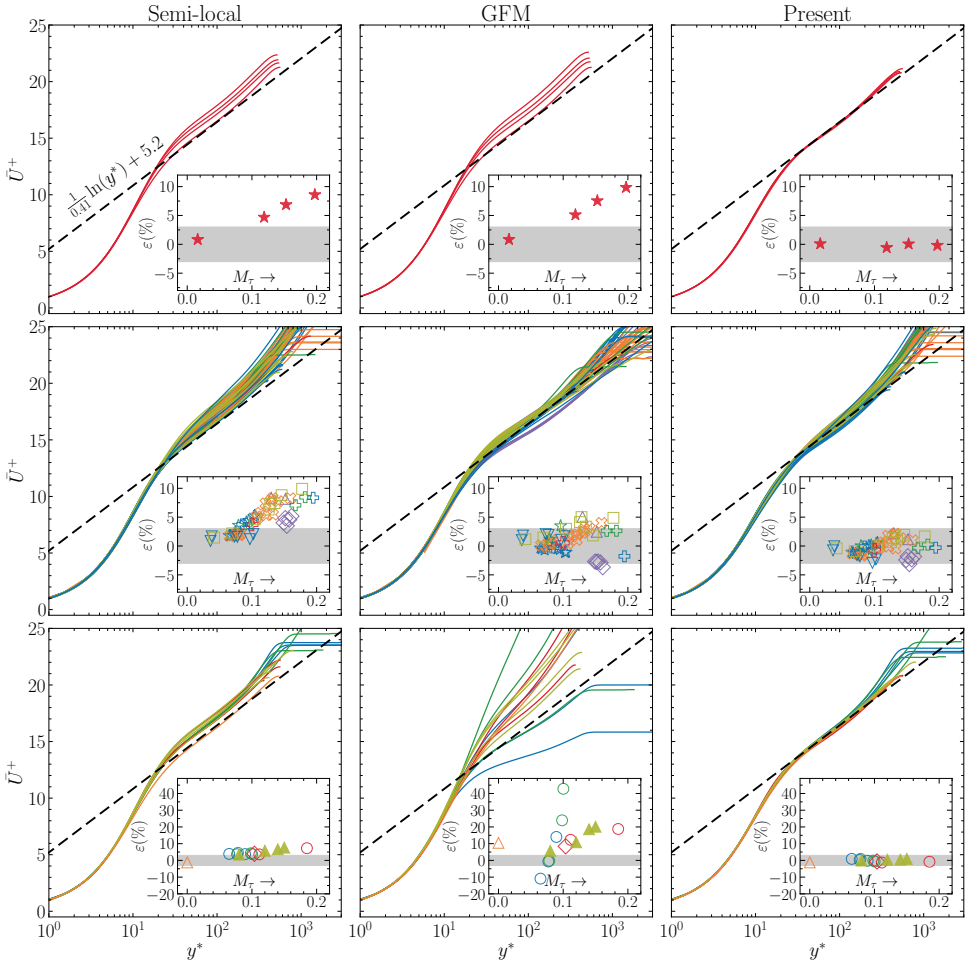

Figure 5.2: Assessment of the semi-local, GFM and proposed transformations for 65 ideal-gas and 5 non-ideal-fluid cases reported in table 2.3. Line colors correspond to the color of the symbols in table 2.3. The top row corresponds to the four 'CP' cases. The centre row represents the 'conventional', 'T_b-controlled', and 'BL-like' cases shown in table 2.3. The latter two types are combined with conventional cases since they have property profiles similar to conventional boundary layers, but in a channel flow setting. The last row represents the non-conventional cases, namely, the 'non-air-like', 'dense-gas', 'supercritical', and 'heat-source' cases in table 2.3. (Insets): Percent error (ε) in the velocity transformation computed with respect to the incompressible reference (Lee and Moser, 2015), as described in Griffin et al. (2021). Note that the insets in the third row have larger axis limits. Symbols are as in table 2.3. Shaded region indicates an error bar of +/-3%. As in figure 5.1, low-Reynolds-number cases are excluded.

in table 2.3. We compare the transformations for three broad groups of cases. The first row corresponds to the CP cases, where only intrinsic compressibility effects play an important role. The second row represents the conventional ideal-gas air-like cases, which includes 'conventional', 'T_b-controlled', and 'BL-like' case types reported in table 2.3. The latter two types are combined with conventional cases since they have property profiles similar to conventional boundary layers, but in a channel flow setting. The last row represents the non-conventional cases, namely, the 'non-air-like', 'dense-gas', 'supercritical', and 'heat-source' cases reported in table 2.3.

The three transformations are equivalent in the viscous sublayer for all types of cases. This equivalence occurs because the GFM transformation, through its blending function, reduces to the semi-local transformation in this region. Similarly, the current transformation naturally simplifies to the semi-local form near the wall, as $\mu_t \approx 0$ and factor 3 in equation (5.12) reduces to unity.

Let us now compare the transformations in the buffer and log layers. For the CP cases (first row), both the semi-local and GFM transformations remain ineffective, as they rely solely on mean property variations, which are approximately constant in these flows. In contrast, the proposed transformation successfully collapses the profiles—as expected—since it is tuned based on these cases.

For the conventional ideal-gas, air-like cases (second row), the log-law shift in the semi-local transformation is clearly evident. While the GFM transformation does not exhibit this selective upward shift, it still results in noticeable spread within the logarithmic region. The proposed transformation, on the other hand, effectively eliminates the log-law shift observed in the semi-local transformation, and demonstrates the least spread for the cases considered herein.

For the non-conventional cases (third row), the semi-local transformation shows a similar upward log-law shift as observed for the conventional cases above (second row). The GFM transformation, on the other hand, shows reduced accuracy for these type of flows. Among the three transformations, the proposed transformation offers a better collapse of the profiles for the non-conventional cases presented herein.

The possible reason why the GFM transformation works for ideal gas cases with air-like viscosity laws (second row), but fails for ideal gas cases with non-air-like viscosity laws and for non-ideal flows (third row), is explained as follows: Figure 5.3 (top row) plots $\epsilon^+/\bar{\mu}^+$, $P^\ddagger/\epsilon^+$ and their product as a function of y^* for the ideal gas air-like boundary layers of Cogo et al. (2023), covering free-stream Mach numbers from 2 to 6 (yellow lines). The black lines show the corresponding quantities for an incompressible boundary layer of Jiménez et al. (2010) at $Re_\tau \approx 450$. Contrary to the assumptions made by GFM, both the dissipation rate, $\epsilon^\ddagger = \epsilon^+/\bar{\mu}^+$ (top row; left), and the ratio $P^\ddagger/\epsilon^+$ (top row; centre), clearly vary with Mach number. However, their product depicts a much better collapse (top row; right). These observations suggest that the Mach-number-dependent variations in $\epsilon^+/\bar{\mu}^+$ and $P^\ddagger/\epsilon^+$ cancel each other out for ideal gas air-like flows, such that the mean shear, $S_{eq} = (P^\ddagger/\epsilon^+)(\epsilon^+/\bar{\mu}^+)(1/\overline{\rho u'' v''}^+)$, becomes a universal function of y^*, resulting in accurate transformed profiles. This balance appears to be disrupted in non-air-like or non-ideal (e.g., supercritical) flows, leading to a deterioration in accuracy.

It is still unclear why the quantities $\epsilon^+/\bar{\mu}^+$ and $P^\ddagger/\epsilon^+$ fail to collapse in figure 5.3 (top row). The quantity $\epsilon^+/\bar{\mu}^+$ was assumed to be universal in GFM's framework following the

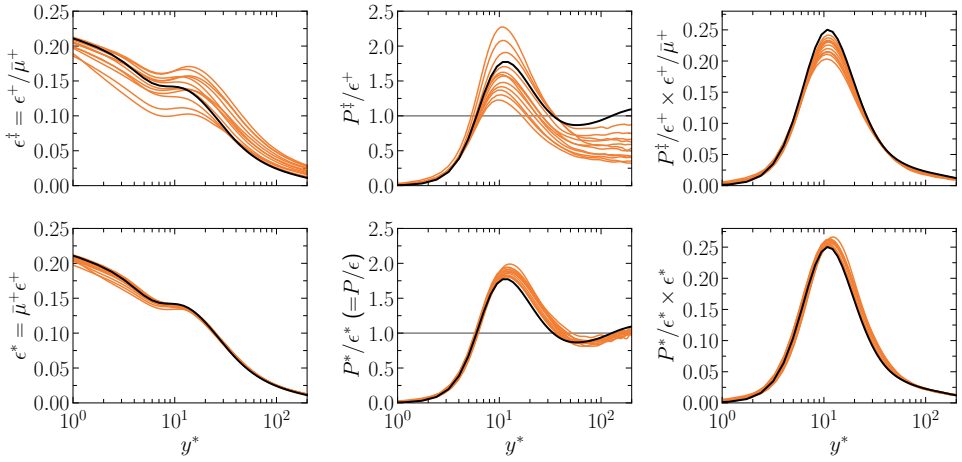

Figure 5.3: Top row: (left) TKE dissipation rate $\epsilon^+/\bar{\mu}^+$, (centre) the ratio $P^\ddagger/\epsilon^+$ and (right) their product, for the air-like ideal gas boundary layers of Cogo et al. (2023), with free-stream Mach numbers ranging from 2 to 6 (yellow lines); see table 2.3. Bottom row: the semi-locally consistent counterparts of the quantities plotted in the top row, namely, (left) $\epsilon^* = \bar{\mu}^+\epsilon^+$, (centre) the ratio P^*/ϵ^* (=P/ϵ) and (right) their product. The black lines indicate the corresponding quantities for the incompressible case from Jiménez et al. (2010), at a similar friction Reynolds number ($Re_\tau \approx 450$) as the compressible cases in Cogo et al. (2023).

work of Guarini et al. (2000); Lagha et al. (2011); Zhang et al. (2012)[2]. However, in those studies, this assumption was made only for adiabatic boundary layers, and as a function of y^+, not y^*. Extending the same to diabatic flows, by simply replacing y^+ with y^* may require further assessment—especially in the light of evidence that the semi-locally scaled dissipation rate, namely $\epsilon^* = \bar{\mu}^+\epsilon^+$, is a universal function of y^* in the log-layer (Patel et al., 2016a; Modesti and Pirozzoli, 2016; Zhang et al., 2018; Cogo et al., 2023)[3], rather than $\epsilon^+/\bar{\mu}^+$. Figure 5.3 also confirms this for the ideal-gas air-like boundary layers of Cogo et al. (2023); compare the top (GFM scaled) and bottom (semi-locally scaled) rows in the left column.

The quantity $P^\ddagger/\epsilon^+$ fails to be Mach-number-invariant because the production and dissipation in this ratio are scaled differently (one with a mix of classical and semi-local scales, and the other with classical scales). Different scalings imply that $P^\ddagger/\epsilon^+$ differs from the ratio constructed using dimensional quantities P/ϵ[4]. This implies that if $P^\ddagger/\epsilon^+$ is Mach-number-invariant, then the ratio P/ϵ must vary with Mach number, which violates the equilibrium assumption ($P/\epsilon \approx 1$). However, upon comparing the top and bottom rows in the centre column of figure 5.3, it becomes clear that it is P/ϵ, rather than $P^\ddagger/\epsilon^+$, that remains nearly Mach-number-invariant, upholding the equilibrium

[2]Zhang et al. (2012) made the assumption regarding the universality of $\epsilon^+/\bar{\mu}^+$, based on the collapse of vorticity r.m.s. reported in Guarini et al. (2000) and Lagha et al. (2011). The two are related as: $\epsilon^+/\bar{\mu}^+ \approx \overline{\omega_i'\omega_i'}^+$.

[3]In some of these studies, the semi-locally scaled vorticity r.m.s. is plotted, which, in principle, is similar to the dissipation rate.

[4]$P^\ddagger/\epsilon^+ \neq P/\epsilon$, unlike if the production and dissipation were scaled similarly, for instance, classically $P^+/\epsilon^+ = P/\epsilon$, or semi-locally $P^*/\epsilon^* = P/\epsilon$.

assumption in the log-layer.

Finally, note that for all the transformations, the spread is larger in the outer part of boundary layers and channels, which is arguably beyond their scope, all being focused on the inner, constant-stress layer.

Limitations of the proposed transformation.—Despite the improved accuracy, the proposed transformation is only as accurate as the assumptions made in its derivation. For instance, the transformation might be inaccurate for cases where equation (5.7) does not hold, such as in supercritical boundary layers where large density fluctuations induce a near-wall convective flux in the stress balance equation (Kawai, 2019). Also, we have assumed that variable-property effects are limited to factors 1 and 2 in equation (5.12), and that these effects do not contribute to the non-universality of the turbulent shear stress (factor 3 in equation 5.12). However, this is not always the case, as suggested by the scatter in the log-law intercept with respect to the fitted curve in figure 5.1(a), which is eventually reflected in the new transformation (see figure 5.2). We suspect cancellation between these unaccounted variable-property effects and intrinsic compressibility effects to be the reason why the semi-local transformation was found to be very accurate for ideal-gas compressible channel flows (Trettel and Larsson, 2016), but not for boundary layers. This hypothesis is further discussed in Appendix B. Incorporating these additional physics is the next step for future studies aimed at developing an even more general transformation. Lastly, it is important to note that for ideal gas cases, the semi-local friction Mach number (M_τ^*) is roughly constant in the wall-normal direction and is equal to M_τ (figure 2.2), however, for cases in which M_τ^* varies significantly in the domain, M_τ may not be the most suitable parameter.

5.5. IMPLICATIONS ON TURBULENCE MODELING

The eddy viscosity with modified damping function (equation 5.13) can be interpreted as a compressibility-corrected wall model for large eddy simulations (LES), which can be implemented in current codes by simply changing the damping function. Moreover, the modified eddy viscosity can be leveraged to improve the drag and heat transfer predictive theories as discussed in chapter 6. Last, the proposed transformation can also help developing Reynolds averaged Navier–Stokes (RANS) turbulence models sensitized to compressibility effects as discussed further in chapter 7.

5.6. SUMMARY

To summarize, the log-law shift observed in the semi-local transformation for the conventional cases (figure 1.5b) can be primarily attributed to the non-universality of the turbulent shear stress caused by intrinsic compressibility effects. We ascertain this based on our tailored constant-property compressible cases, in which the only dominant effect is due to intrinsic compressibility. Taking M_τ as the most suitable parameter to quantify these effects, we propose a new transformation that effectively removes the log-law shift. The proposed transformation accounts for the changes in friction velocity and viscous length scales due to variations in mean properties, and for intrinsic compressibility effects. Thus, it applies to a wide variety of cases.

In future, it would be interesting to analyse whether the transformation can be derived using an expansion series approach discussed in chapter 4.

6

ESTIMATING MEAN PROFILES AND FLUXES USING INNER/OUTER-LAYER SCALINGS

In this chapter, using a mixing-length eddy-viscosity formulation (equation 5.13) in the inner layer and Coles' law of the wake in the outer layer, we develop a methodology that predicts mean velocity and temperature profiles, as well as the skin-friction and heat transfer coefficients in zero-pressure-gradient high-speed boundary layers. While the eddy-viscosity is consistent with the transformation proposed in chapter 5, the Coles wake relation follows Van Driest scaling. The methodology is modular in the sense that it can be applied using other eddy-viscosity definitions and wake models, and it is also applicable to channel/pipe flows.

The contents of this chapter have been published as:
Hasan, A. M., Larsson, J., Pirozzoli, S., and Pecnik, R. (2024). Estimating mean profiles and fluxes in high-speed turbulent boundary layers using inner/outer-layer scalings. *AIAA Journal*, 62(2):848–853.

6.1. INTRODUCTION

Accurately predicting drag and heat transfer for compressible high-speed flows is of utmost importance for a range of engineering applications. A common approach is to use a compressible velocity scaling law (transformation), that inverse transforms the velocity profile of an incompressible flow, coupled with a temperature-velocity relation. Current methods (Huang et al., 1993; Kumar and Larsson, 2022) typically assume a single velocity scaling law, overlooking the different scaling characteristics of the inner and outer layers. In this chapter, we use distinct scalings for these two regions and model the velocity profile for compressible boundary layers using a classic eddy viscosity expression combined with a defect law. The inner-layer velocity profile is modeled using the mixing-length eddy viscosity presented in chapter 5, which incorporates variable-property effects through semi-local scaling, and accounts for intrinsic compressibility effects by adjusting the near-wall damping function. The outer-layer profile is modeled after Coles' law of the wake (Coles, 1956), scaled according to the Van Driest scaling. The result is an analytical expression for the mean shear valid in the entire boundary layer, which combined with the temperature-velocity relationship from Zhang et al. (2014), provides predictions of mean velocity and temperature profiles at high accuracy. Using these profiles, drag and heat-transfer coefficients are evaluated with an accuracy of +/-4% and +/-8%, respectively, for a wide range of zero-pressure-gradient compressible turbulent boundary layers up to Mach numbers of 14.

6.2. PROPOSED METHOD

The velocity profile of a turbulent boundary layer is composed of two parts: (1) the law of the wall in the inner layer, and (2) the velocity defect law in the outer layer. Using an eddy viscosity model for the inner layer and Coles' law of the wake for the outer layer, the mean shear for incompressible flows can be expressed as

$$\frac{d\bar{u}_{inc}}{dy} = \frac{u_\tau}{\delta_v}\frac{1}{1+\mu_t/\mu_w} + \frac{u_\tau}{\delta}\frac{\Pi}{\kappa}\pi\sin\left(\pi\frac{y}{\delta}\right), \tag{6.1}$$

where the first term on the right-hand side can be readily obtained by integrating the mean momentum equation (stress balance) of equilibrium flows, while the second term is the derivative of the Coles' wake function (Chauhan et al., 2007). Here, μ_t denotes the eddy viscosity, μ_w the viscosity at the wall, u_τ and δ_v the friction velocity and viscous length scales defined in equation (1.6), Π the Coles wake parameter, κ the von Kármán constant, y the wall-normal coordinate, and δ the boundary layer thickness. Modeling μ_t using simple inner-layer mixing-length models would lead to a linear profile close to the wall, developing into a logarithmic profile which extends to the outer layer where it is added to the wake component, as desired.

In compressible flows, the stress balance equation in the inner layer leads to the mean shear given by $d\bar{u}/dy = (u_\tau^*/\delta_v^*)/(1+\mu_t/\bar{\mu})$ (see chapter 5). Here, $\bar{\mu}$ is the mean viscosity, and u_τ^* and δ_v^* represent the semi-local friction velocity and viscous length scales defined in equation (1.12). For the wake region, following Van Driest's scaling, u_τ is replaced with u_τ^* to account for mean density variations, while maintaining the same outer-layer length scale, δ (Smits and Dussauge, 2006). With these changes, the mean

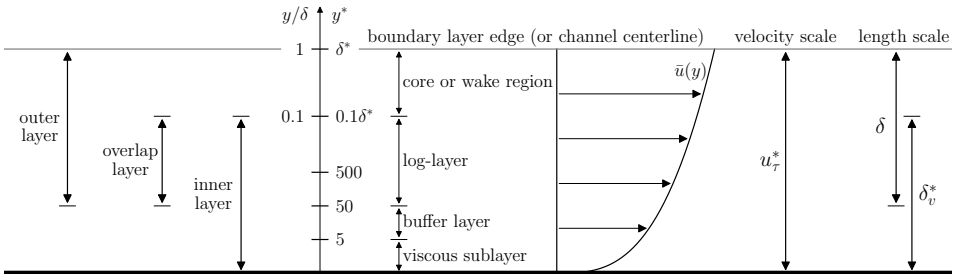

Figure 6.1: A schematic showing the different regions and the appropriate velocity and length scales in a compressible turbulent boundary layer (similar to figure 1.4, but for compressible flows). Here, $y^* = y/\delta_v^*$ and $\delta^* = \delta/\delta_v^*$, where y represents the wall-normal coordinate and δ is the boundary layer thickness. Note that both the y/δ and y^* axes are logarithmic.

shear for compressible flows reads

$$\frac{d\bar{u}}{dy} = \frac{u_\tau^*}{\delta_v^*}\frac{1}{1+\mu_t/\bar{\mu}} + \frac{u_\tau^*}{\delta}\frac{\Pi}{\kappa}\pi\sin\left(\pi\frac{y}{\delta}\right). \tag{6.2}$$

Now, modeling $\mu_t/\bar{\mu}$ based on the Johnson-King (JK) mixing-length eddy viscosity model (Johnson and King, 1985), corrected for variable property and intrinsic compressibility effects (equation 5.13), we get

$$\frac{d\bar{u}}{dy} = \frac{u_\tau^*}{\delta_v^*}\frac{1}{1+\kappa y^* D(y^*, M_\tau)} + \frac{u_\tau^*}{\delta}\frac{\Pi}{\kappa}\pi\sin\left(\pi\frac{y}{\delta}\right). \tag{6.3}$$

Equation (6.3) provides several useful insights. Analogous to an incompressible flow, the mean velocity in a compressible flow is controlled by two distinct length scales, δ_v^* and δ, characteristic of the inner and outer layers, respectively. The two layers are connected by a common velocity scale u_τ^* (the semi-local friction velocity), leading to a logarithmic law in the overlap region. These scales and their regions of validity are depicted schematically in figure 6.1.

Moreover, in the logarithmic layer and beyond, the first term on the right-hand side reduces to $\sqrt{\tau_w/\bar{\rho}}/(\kappa y)$ (where τ_w is the wall shear stress and $\bar{\rho}$ is the mean density), which is consistent with Van Driest's original arguments (Van Driest, 1951) . It is crucial to satisfy this condition, otherwise the logarithmic profile extending to the outer layer would not obey Van Driest's scaling, while the wake component to which it is added would. This condition is naturally satisfied here since our transformation, on which the eddy-viscosity is based, is consistent with the Van Driest transformation in the log-layer. One way to check this consistency is to compute the transformed diagnostic function $Y^+ d\bar{U}^+/dY^+$ and checking whether it is equal to $y^+ d\bar{U}_{VD}^+/dy^+$. Taking $Y^+ = y^*$, and $d\bar{U}^+$ from equation (5.14), one can readily verify this. However, other transformations, such as the ones proposed by Volpiani et al. (2020b) and Griffin et al. (2021), do not satisfy this property. Thus, implementation of the proposed method with those transformations may require additional steps as further discussed in section 6.3.

The near-wall damping function in equation (6.3) is given by

$$D(y^*, M_\tau) = \left[1 - \exp\left(\frac{-y^*}{A^+ + f(M_\tau)}\right)\right]^2, \tag{6.4}$$

where $M_\tau = u_\tau/\sqrt{\gamma R T_w}$ is the friction Mach number, with T_w as the wall temperature. The value of A^+ differs based on the choice of the von Kármán constant κ, such that the log-law intercept is reproduced for that κ (Nagib and Chauhan, 2008). With $\kappa = 0.41$, the value of $A^+ = 17$ gives a log-law intercept of 5.2 (Iyer and Malik, 2019), whereas, with $\kappa = 0.384$, $A^+ = 15.22$ gives a log-law intercept of 4.17. The additive term $f(M_\tau)$ accounts for intrinsic compressibility effects. In chapter 5, we proposed $f(M_\tau) = 19.3M_\tau$, which is independent of the chosen value of κ.

The second term on the right-hand side of equation (6.3) is the wake term accounting for mean density variations, where Coles' wake parameter Π depends on the Reynolds number, as discussed in the subsection below. It is important to note that Π also depends on pressure gradient (Coles, 1956), however, the focus of the current analysis is limited to zero-pressure-gradient turbulent boundary layers.

6.2.1. CHARACTERIZING LOW-REYNOLDS-NUMBER EFFECTS ON THE WAKE PARAMETER

For incompressible boundary layers, Coles' wake parameter is known to strongly depend on Re_θ at low Reynolds numbers (Coles, 1962; Fernholz and Finley, 1996; Cebeci and Smith, 1974). For compressible boundary layers, the ambiguity of the optimal Reynolds number definition poses a challenge to characterize the wake parameter. Fernholz and Finley (1980), mainly using experimental data at that time, observed that the momentum-thickness Reynolds number with viscosity at the wall ($Re_{\delta_2} = \rho_\infty u_\infty \theta/\mu_w$, where θ represents the momentum thickness, and the subscript '∞' signifies free-stream values) is the suitable definition to scale Π. On the other hand, Wenzel et al. (2018) observed that the wake parameter scales with Re_θ ($= \rho_\infty u_\infty \theta/\mu_\infty$) for their direct numerical simulations (DNS) at moderate Mach numbers ($M_\infty \leq 2.5$), consistent with the expectation that Π (being defined at the boundary layer edge) should scale with Reynolds number based on the free-stream properties (Smits and Dussauge, 2006; Cebeci and Smith, 1974). Yet, there is no clear consensus on which definition is relevant in scaling Π, especially for high-Mach-number flows where Re_{δ_2} and Re_θ are quite different from each other. Given the recent availability of hypersonic DNS, we revisit the question of which Reynolds number best describes the wake parameter.

First, we evaluate Π for several incompressible and compressible DNS cases from the literature and then report it as a function of different definitions of the Reynolds number, searching for the definition yielding the least spread of the data points. For incompressible flows, the wake strength can be determined as $\Pi = 0.5\kappa\left(\bar{U}^+(y=\delta) - (1/\kappa)\ln(\delta^+) - C\right)$, where C is the log-law intercept for the chosen κ. For compressible flows, the wake strength is based on the VD transformed velocity (Fernholz and Finley, 1980; Smits and Dussauge, 2006) as $\Pi = 0.5\kappa\left(\bar{U}^+_{vd}(y=\delta) - (\bar{U}^+_{vd})^{log}(y=\delta)\right)$, where $\bar{U}^+_{vd}$ is obtained from the DNS data. The reference log law $(\bar{U}^+_{vd})^{log}$, unlike for incompressible flows, cannot be computed as $(1/\kappa)\ln(y^+) + C_{vd}$, because C_{vd} is found to be non-universal for diabatic compressible boundary layers (Bradshaw, 1977; Trettel and Larsson, 2016); see also figure 1.5(a). Hence, $(\bar{U}^+_{vd})^{log}$ can be obtained either by fitting a logarithmic curve to $\bar{U}^+_{vd}$ (Fernholz and Finley, 1980), or by inverse transforming the incompressible law of the wall. Here, we follow the latter approach by using the compressibility transformation discussed in chapter 5.

The value of the von Kármán constant κ plays a crucial role in estimating Π. Spalart

(1988) noted that a strong consensus on κ is needed to accurately estimate Π. However, such a consensus is yet missing (Monkewitz and Nagib, 2023). Nagib and Chauhan (2008) showed that $\kappa = 0.384$ is a suitable choice for incompressible boundary layers, verified to be true also for channels (Lee and Moser, 2015) and pipes (Pirozzoli et al., 2021). However, due to historical reasons and wide acceptance of $\kappa = 0.41$, we will proceed with this value. The same procedure can straightforwardly be repeated with a different value of κ.

Figure 6.2 shows the wake parameter for 24 compressible and 19 incompressible boundary layer flows, as a function of (a) Re_{δ_2}, (b) Re_θ, (c) Re_{δ^*} ($= \rho_\infty u_\infty \delta^* / \mu_\infty$, where δ^* is the displacement thickness) and (d) $Re^*_{\tau_\infty}$ (i.e., the semi-local Reynolds number $Re^*_\tau = \bar{\rho} u^*_\tau \delta / \bar{\mu}$ computed using free-stream properties). The spread in the data points is found to be quite large for all the definitions, as Π is the difference of two relatively large quantities, namely $\bar{U}^+_{vd}$ and $(\bar{U}^+_{vd})^{log}$ at the boundary layer edge, as outlined above. Note that even incompressible boundary layers are not devoid of this scatter (Spalart, 1988; Fernholz and Finley, 1996). Figure 6.2(a) shows the presence of two distinct branches, hence Re_{δ_2} does not seem to be suitable to characterize Π, unlike reported in previous literature (Fernholz and Finley, 1980; Huang et al., 1993). Among the four definitions of Reynolds number, Re_θ seems to show the least spread, further confirming the conclusions in Wenzel et al. (2018). Figure 6.2(b) also reports several functional forms of $\Pi = f(Re_\theta)$. Use of the modified Kármán-Schoenherr friction formula (Nagib et al., 2007) for indirect evaluation of Π, does not show saturation at high Reynolds numbers as observed in Coles (1962) for incompressible flows. The Cebeci-Smith (hereafter CS) relation (Cebeci and Smith, 1974) underpredicts Π, but reproduces saturation at high Reynolds numbers. Wenzel et al. (2018) modified the CS relation with a higher saturation value of Π (0.66) and fit it to the DNS data of Schlatter et al. (2009) and Schlatter and Örlü (2010). Here, we propose a relation similar to that proposed by (Cebeci and Smith, 1974), but fitted to the more recent incompressible DNS data of Jiménez et al. (2010) and Sillero et al. (2013), in which particular care was exercised to guarantee that the numerical boundary layers are in a fully developed state. Those data support similar behavior as CS in the low-Re regime, but with a higher saturation value, resulting in the relation

$$\Pi = 0.69 \left[1 - \exp(-0.243\sqrt{z} - 0.15\, z)\right], \quad \text{where} \quad z = Re_\theta / 425 - 1. \tag{6.5}$$

We also note that some high-Reynolds-number cases have higher value of the wake parameter than that predicted by equation (6.5). This could be due to the previously noted high data scatter, or to inaccuracies arising from application of the Van Driest transformation to the wake velocity profile, or both. Regardless, these differences are tolerable for the scope of the present chapter, as the results are not highly sensitive to the precise value of the wake parameter (see section 6.3).

The inset in figure 6.2(b) compares the skin-friction curve computed using equation (6.5) with the modified Kármán-Schoenherr skin-friction formula (Nagib et al., 2007). The distance between the two curves is large at low Reynolds numbers, but less so at higher Reynolds numbers. As expected, the incompressible DNS data of Jiménez et al. (2010) and Sillero et al. (2013) follow the friction curve computed using equation (6.5).

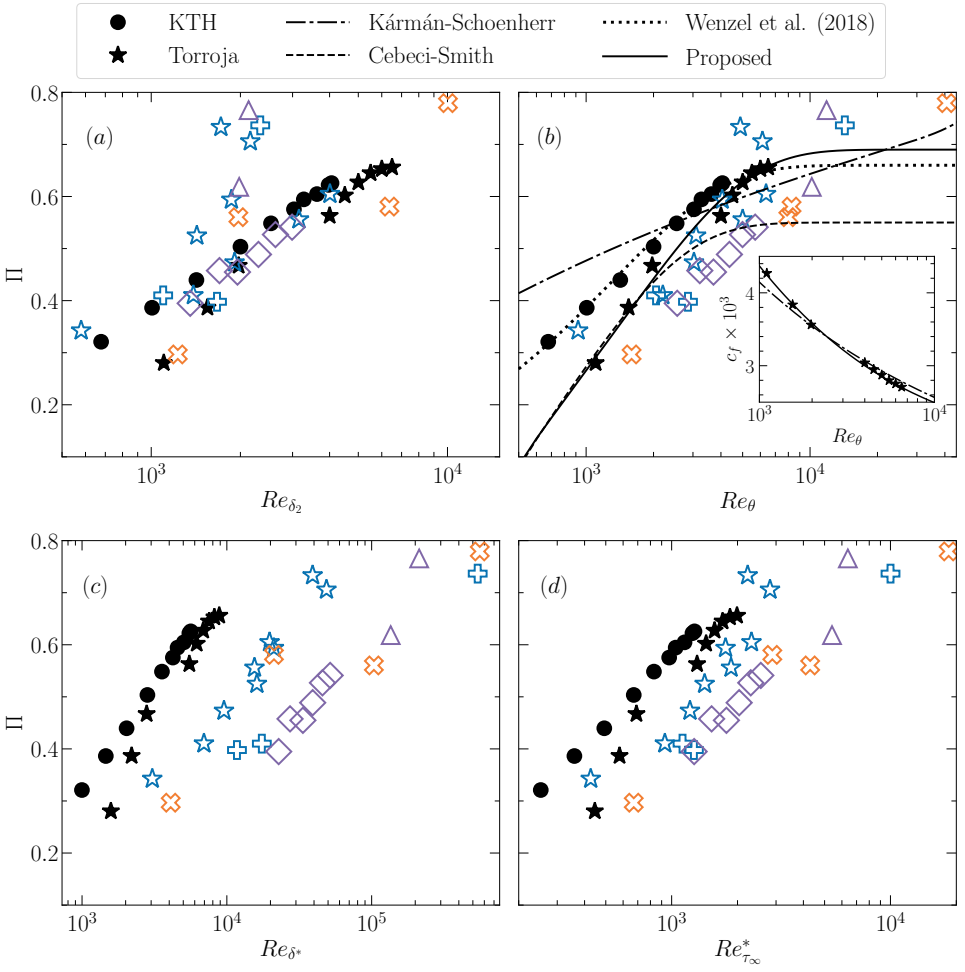

Figure 6.2: The wake parameter Π computed using the DNS data and plotted as a function of (a) Re_{δ_2} (b) Re_θ (c) Re_{δ^*} and (d) $Re^*_{\tau_\infty}$ for 19 incompressible (Schlatter et al., 2009; Schlatter and Örlü, 2010; Jiménez et al., 2010; Sillero et al., 2013) and 24 compressible (Zhang et al., 2018; Bernardini and Pirozzoli, 2011; Cogo et al., 2022; Ceci et al., 2022, A. Ceci, private communication) turbulent boundary layers reported in table 2.3.

6.2.2. IMPLEMENTATION OF THE PROPOSED METHOD

For convenience of implementation, equation (6.3) can also be expressed in terms of the dimensional quantities τ_w, $\bar{\mu}$ and $\bar{\rho}$ as

$$\frac{d\bar{u}}{dy} = \frac{\tau_w}{\bar{\mu} + \underbrace{\sqrt{\tau_w \bar{\rho}}\kappa y D(y^*, M_\tau)}_{\mu_t}} + \frac{\sqrt{\tau_w/\bar{\rho}}}{\delta}\frac{\Pi}{\kappa}\pi \sin\left(\pi\frac{y}{\delta}\right), \tag{6.6}$$

where μ_t is the dimensional form of the compressibility-corrected Johnson-King eddy viscosity model, which can be readily used in turbulence modeling, for instance, as a wall-model in large eddy simulations (LES).

Note that other eddy viscosity models can also be used in deriving the mean shear equation, for example, Prandtl's mixing-length model. The mean shear equation using Prandtl's mixing-length model is

$$\frac{d\bar{u}}{dy} = \frac{2\tau_w}{\bar{\mu} + \sqrt{\bar{\mu}^2 + [2\sqrt{\tau_w \bar{\rho}}\kappa y D(y^*, M_\tau)]^2}} + \frac{\sqrt{\tau_w/\bar{\rho}}}{\delta}\frac{\Pi}{\kappa}\pi \sin\left(\pi\frac{y}{\delta}\right), \tag{6.7}$$

where $D(y^*, M_\tau)$ is the damping function corrected for intrinsic compressibility effects as $D(y^*, M_\tau) = 1 - \exp\left(-y^*/(A^+ + 39M_\tau)\right)$, with $A^+ = 25.53$ (or 26) for $\kappa = 0.41$, and where the additive term $39M_\tau$ is obtained following similar steps as for the Johnson-King model (see chapter 5).

In this chapter, the results will be presented using equation (6.6). This equation covers the entire boundary layer, and it can be integrated in conjunction with a suitable temperature model such as the one proposed by Zhang et al. (2014), which is given as

$$\frac{\bar{T}}{T_w} = 1 + \frac{T_r - T_w}{T_w}\left[(1 - sPr)\left(\frac{\bar{u}}{u_\infty}\right)^2 + sPr\left(\frac{\bar{u}}{u_\infty}\right)\right] + \frac{T_\infty - T_r}{T_w}\left(\frac{\bar{u}}{u_\infty}\right)^2, \tag{6.8}$$

where $sPr = 0.8$, $T_r/T_\infty = 1 + 0.5r(\gamma - 1)M_\infty^2$, and $r = Pr^{1/3}$, with T_r denoting the adiabatic temperature, r the recovery factor and Pr the molecular Prandtl number. Moreover, a suitable viscosity law (e.g., power or Sutherland's law), and the ideal gas equation of state $\bar{\rho}/\rho_w = T_w/\bar{T}$ have to be used to compute mean viscosity and density profiles, respectively. The inputs that need to be provided are the Reynolds number (Re_θ), free-stream Mach number ($M_\infty = u_\infty/\sqrt{\gamma R T_\infty}$), wall cooling/heating parameter (T_w/T_r) and (optionally) the dimensional wall or free-stream temperature for Sutherland's law. It is important to note that equation (6.8), and all solver inputs are based on the quantities in the free-stream, and not at the boundary layer edge. For more insights on the solver, please refer to the source code available on GitHub (Pecnik and Hasan, 2023).

6.3. RESULTS

Figure 6.3 shows the predicted velocity and temperature profiles for a selection of high Mach number cases. As can be seen, the DNS and the predicted profiles are in good agreement, thus corroborating our methodology. The insets in figure 6.3 show the error in the predicted skin-friction and heat-transfer coefficients for 28 compressible cases from the literature. For most cases, the friction coefficient, $c_f = 2\tau_w/(\rho_\infty u_\infty^2)$, is

predicted with $+/-4\%$ accuracy, with a maximum error of -5.3%. The prediction of the heat-transfer coefficient, $c_h = q_w/(c_p\rho_\infty u_\infty(T_w - T_r))$, where q_w is the wall heat flux, shows a slightly larger error compared to c_f, potentially due to additional inaccuracies arising from the temperature-velocity relation. In most cases, c_h is predicted with $+/-8\%$ accuracy, with a maximum error of 10.3%.

To assess the sensitivity of the predictions with respect to the relation used for the wake parameter, we recomputed the results using our method, but instead of using equation (6.5) to estimate Π, we employed the relation proposed by Wenzel et al. (2018). The maximum error in the c_f prediction changed from -5.3% to -6.08%, with most of the cases within error bounds of $+/-5\%$. For the c_h prediction, there was an increase in the maximum error from 10.3% to 11.4%, with most of the cases within error bounds of $+/-8\%$.

The proposed method is modular as it can also be applied using other velocity transformations as building blocks (Griffin et al., 2021; Volpiani et al., 2020b). For instance, one can use an eddy viscosity derived from the GFM transformation in equation (6.2). One can also skip the intermediate step of deriving an eddy viscosity from a transformation and directly use inverse transformations to predict mean velocity profiles (Huang et al., 1993; Kumar and Larsson, 2022). However, in place of using a single transformation for the entire boundary layer, as done previously, we rather advocate the use of distinct transformations for the inner and outer layers. Considering the reference incompressible velocity profile as being made up of the sum of an inner part ($\bar{U}^+_{inn}$) and of a wake correction ($\bar{U}^+_{wake}$), we separately inverse transform the related velocity increments to yield

$$d\bar{u}^+ = \mathscr{T}^{-1}_{inn} d\bar{U}^+_{inn} + \mathscr{T}^{-1}_{out} d\bar{U}^+_{wake}, \tag{6.9}$$

where $\mathscr{T}_{inn}$ and $\mathscr{T}_{out}$ denote the inner- and outer-layer velocity transformation kernels, respectively.

The two approaches, i.e., the one adopted in section 6.2 and the one based on inverse transformations are equivalent as evident from the subsequent discussion. Starting from equation (6.9), and using the transformation kernel presented in chapter 5 for $\mathscr{T}_{inn}$ and the Van Driest (Van Driest, 1951) kernel for $\mathscr{T}_{out}$, we get

$$d\bar{u}^+ = f_3^{-1} f_2^{-1} f_1^{-1} d\bar{U}^+_{inn} + f_1^{-1} d\bar{U}^+_{wake}, \tag{6.10}$$

where the factors f_1, f_2, and f_3 are given by

$$f_1 = \sqrt{\frac{\bar{\rho}}{\rho_w}}, \quad f_2 = \left(1 - \frac{y}{\delta^*_v}\frac{d\delta^*_v}{dy}\right), \quad f_3 = \left(\frac{1+\kappa y^* D(y^*, M_\tau)}{1+\kappa Y^+ D(Y^+, 0)}\right), \tag{6.11}$$

and the damping function, $D(y^*, M_\tau)$, is as per equation (6.4). Here, Y denotes the wall-normal coordinate for the incompressible flow. In equation (6.10), $d\bar{U}^+_{inn}$ is modeled using the Johnson-King eddy viscosity model as $dY^+/[1+\kappa Y^+ D(Y^+, 0)]$, which after integration, recovers the incompressible law of the wall, and $d\bar{U}^+_{wake} = (\Pi/\kappa)\sin(\pi Y/\Delta)\pi\, d(Y/\Delta)$ is the derivative of the Coles' wake function, where Δ denotes δ_{99} of an incompressible flow. Inserting the expressions for $d\bar{U}^+_{inn}$, $d\bar{U}^+_{wake}$ in equation (6.10), we get

$$d\bar{u}^+ = f_3^{-1} f_2^{-1} f_1^{-1} \frac{dY^+}{1+\kappa Y^+ D(Y^+, 0)} + f_1^{-1} \frac{\Pi}{\kappa} \pi \sin\left(\pi \frac{Y}{\Delta}\right) d\left(\frac{Y}{\Delta}\right). \tag{6.12}$$

Similar to the use of distinct velocity transformations in the inner and outer layers, it is essential to employ separate coordinate transformations for these regions as well. In the inner layer, the transformation $Y^+ = y^*$, as discussed in chapter 5, is appropriate, whereas in the outer layer we use $Y/\Delta = y/\delta$. Now, using the inner- and outer-layer coordinate transformations, and using $dy^*/dy = f_2/\delta_v^*$, $u_\tau = u_\tau^* f_1$, we get the dimensional form of the mean-velocity gradient as in equation (6.3).

Before proceeding, we note that applying the inverse-transformation-based approach with the transformations of Volpiani et al. (2020b) and Griffin et al. (2021) requires a minor modification, so as to ensure that the logarithmic profile extending to the outer layer is consistent with Van Driest's scaling (as outlined in section 6.2). For these transformations, we modify equation (6.9) as follows:

$$\begin{aligned} Y^+ \leq 50: \quad d\tilde{u}^+ &= \mathscr{T}_{inn}^{-1} d\tilde{U}_{inn}^+ + \mathscr{T}_{vd}^{-1} d\tilde{U}_{wake}^+, \\ Y^+ > 50: \quad d\tilde{u}^+ &= \mathscr{T}_{vd}^{-1} d\tilde{U}_{inn}^+ + \mathscr{T}_{vd}^{-1} d\tilde{U}_{wake}^+, \end{aligned} \tag{6.13}$$

where $\mathscr{T}_{inn}$ and $\mathscr{T}_{vd}$ denote the inner-layer and Van Driest transformation kernels, respectively, and Y^+ is the transformed coordinate. The value of 50 is taken arbitrarily as a start of the logarithmic region.

Figure 6.4 compares c_f from the proposed approach with that from the modular approach of Kumar and Larsson (2022), both with different inner-layer transformations. Additionally, the figure includes results obtained with the method of Huang et al. (1993) using the VD transformation, and the widely recognized Van Driest II skin-friction formula (Van Driest, 1956b; Hopkins and Inouye, 1971). Figure 6.4 also shows the root-mean-square error, determined as

$$\text{RMS} = \sqrt{\frac{1}{N}\sum \varepsilon_{c_f}^2}, \tag{6.14}$$

where N is the total number of DNS cases considered.

The Van Driest II formula and the method of Huang et al. have similar RMS errors of about 6%[1], which is not surprising as both of them are built on Van Driest's mixing-length arguments. The errors are systematically positive for a majority of the cases, and increase with higher Mach number and stronger wall cooling. The source of this error mainly resides in the inaccuracy of the VD velocity transformation in the near-wall region for diabatic flows. To eliminate this shortcoming, Kumar and Larsson (2022) developed a modular methodology, which is quite accurate when the transformation of Volpiani et al. (2020b) is used, but is less accurate if other velocity transformations are implemented. This inaccuracy is because the outer-layer velocity profile is also inverse transformed according to the inner-layer transformation. In the current approach, the velocity profile is instead inverse transformed using two distinct transformations, which take into account the different scaling properties of the inner and outer layers, thus reducing the RMS error with respect to Kumar and Larsson's modular method for all the transformations tested herein. The error using the proposed approach with the semi-local (or TL) transformation is positive for all the cases, attributed to the log-law shift inherent in that transformation. This shift was effectively removed in our transformation (chapter 5), thereby yielding an RMS error of 2.66%, which is the lowest among all approaches.

[1]Huang et al.'s method with the more accurate temperature velocity relation in Zhang et al. (2014) leads to an RMS error of 12%, suggesting error cancellation while using the less accurate Walz's relation.

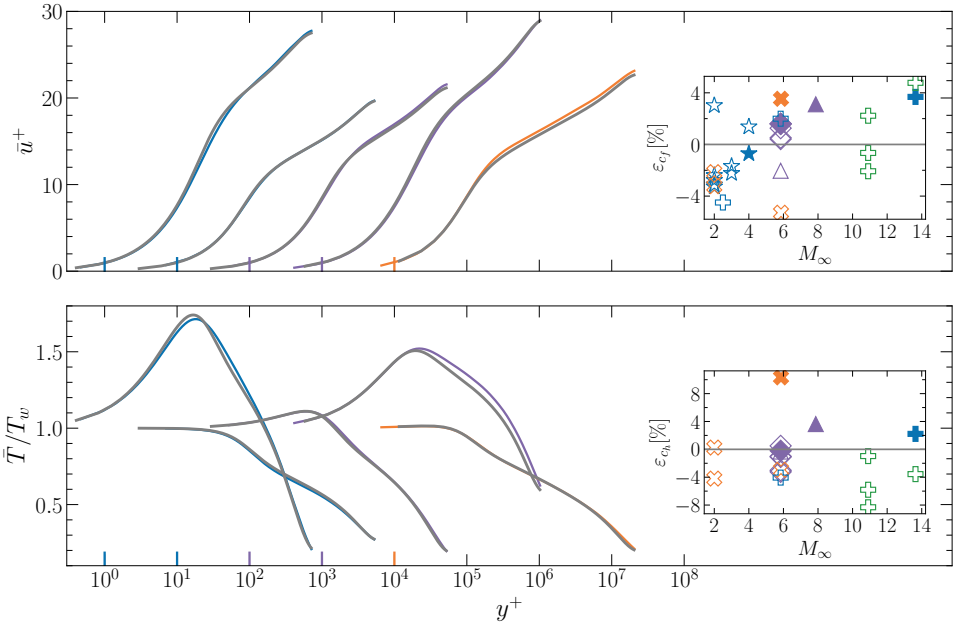

Figure 6.3: Predicted velocity (top) and temperature (bottom) profiles (solid grey lines) compared to DNS (solid colored lines) for the following cases reported in table 2.3: (left to right) $M_\infty = 13.64$, $T_w/T_r = 0.18$ (Zhang et al., 2018); $M_\infty = 4$, $T_w/T_r = 1$ (Bernardini and Pirozzoli, 2011); $M_\infty = 7.87$, $T_w/T_r = 0.48$ (A. Ceci, private communication); $M_\infty = 5.84$, $T_w/T_r = 0.25$ (Ceci et al., 2022); $M_\infty = 5.86$, $T_w/T_r = 0.76$ (Cogo et al., 2022). The line colors match the color of the symbols for the respective authors reported in table 2.3. For clarity, the velocity and temperature profiles for different cases are shifted by one decade along the abscissa. The colored vertical lines on the abscissa signify $y^+ = 10^0$ for each case, with their colors matching the corresponding cases. (Insets): Percent error in skin-friction (top) and heat-transfer (bottom) predictions for 26 compressible turbulent boundary layers listed in table 2.3 (Zhang et al., 2018; Bernardini and Pirozzoli, 2011; Huang et al., 2022; Cogo et al., 2022; Ceci et al., 2022, A. Ceci, private communication), as well as for two additional cases from Huang et al. (2022) that are not reported in table 2.3 due to unavailability of data files. The error is computed as $\varepsilon_{c_f} = (c_f - c_f^{DNS})/c_f^{DNS} \times 100$ and likewise for ε_{c_h}. Symbols are as in table 2.3. The filled symbols correspond to the cases whose velocity and temperature profiles are plotted.

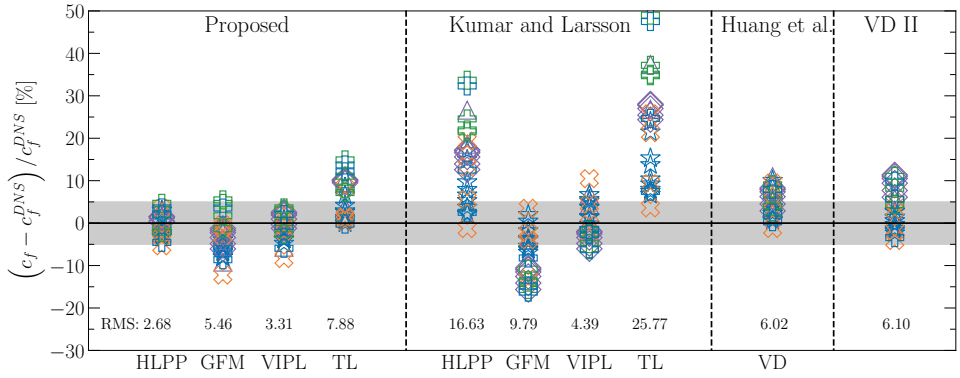

Figure 6.4: Error in skin-friction prediction using the proposed approach compared to different state-of-the-art approaches. The letters on the X-axis denote the velocity transformation used for that approach. HLPP, GFM, VIPL, TL, and VD stand for the transformations proposed in chapter 5, Griffin et al. (2021), Volpiani et al. (2020b), Trettel and Larsson (2016), and Van Driest (1951), respectively. The numbers are RMS values computed as outlined in the text. Symbols are as in table 2.3. The shaded region shows an error bar of +/-5%. Note that inputs for all the methods are based on properties in the free-stream instead of at the edge of the boundary layer.

6.4. SUMMARY

We have derived an expression for the mean-velocity gradient in high-speed boundary layers (equation 6.6) that uses distinct mean velocity scalings in the inner (chapter 5) and outer (Van Driest) layers, thus covering the entire boundary layer. The Coles' wake parameter in this expression is determined using an adjusted Cebeci and Smith relation (equation 6.5), with Re_θ found to be the most suitable parameter to characterize low-Reynolds-number effects on Π. This method allows remarkably accurate predictions of the mean velocity and temperature profiles, leading to estimates of the friction and heat-transfer coefficients which are within $+/-4\%$ and $+/-8\%$ of the DNS data, respectively. When compared with other skin-friction prediction methods in the literature, our approach yields the lowest RMS error of 2.66%.

The methodology presented here promises straightforward application to other classes of wall-bounded flows like channels and pipes, upon change of the temperature-velocity relation (e.g. Song et al., 2022), and using different values of the wake parameter Π (Nagib and Chauhan, 2008). Also, the method is modular in the sense that it can be used with other temperature models and equations of state.

7

COMPRESSIBILITY CORRECTIONS FOR TURBULENCE MODELS

In this chapter, we introduce a novel approach to derive compressibility corrections for Reynolds-averaged Navier-Stokes (RANS) models. Using this approach, we derive variable-property corrections for wall-bounded flows that take into account the distinct scaling characteristics of the inner and outer layers, extending the earlier work of Otero Rodriguez et al. (2018). We also propose modifying the eddy viscosity to account for changes in the near-wall damping of turbulence due to intrinsic compressibility effects. The resulting corrections are consistent with our velocity transformation (chapter 5) in the inner layer and the Van Driest velocity transformation in the outer layer. Furthermore, we address some important aspects related to the modeling of the energy equation, primarily focusing on the turbulent Prandtl number and the modeling of the source terms. Compared to the existing state-of-the-art compressibility corrections, the present corrections, combined with accurate modeling of the energy equation, lead to a significant improvement in the results for a wide range of turbulent boundary layers and channel flows.

The contents of this chapter have been published as:
Hasan, A. M., Elias, A. J., Menter, F., and Pecnik, R. (2025). Variable-property and intrinsic compressibility corrections for turbulence models using near-wall scaling theories. *Journal of Fluid Mechanics*, 1019:A8.

7.1. INTRODUCTION

Accurate modeling of turbulent compressible flows is crucial for a wide range of engineering applications. In particular, turbulence determines skin friction and heat transfer, and consequently the performance and efficiency of heat exchangers, aerospace vehicles, gas turbines, combustion processes, and high-speed propulsion systems. In order to capture the complex turbulence phenomena associated with these flows, standard turbulence models (developed for incompressible flows) must be modified. Such modifications are termed as 'compressibility corrections' in the literature.

The earliest compressibility corrections for compressible boundary layers were inspired from the turbulence modeling of shear layers. These corrections focus on incorporating direct intrinsic compressibility terms, such as pressure dilatation and dilatational dissipation, into the turbulent kinetic energy equation. For instance, Zeman (1990) proposed a dilatational dissipation model for high-speed free shear flows, which was later extended to wall-bounded flows by Zeman (1993). Although dilatational dissipation is typically negligible for wall-bounded flows (Huang et al., 1995; Zhang et al., 2018; Sciacovelli et al., 2024), applying Zeman's model still improves the results, as it adds just the right amount of extra dissipation to reduce the eddy viscosity, especially important in cooled-wall boundary layers (Rumsey, 2010). In other words, the improvement occurs for the wrong reasons and the model does not capture the correct physical mechanisms. This motivates the need for more physics-based compressibility corrections. To achieve this, it is important to first understand and characterize the underlying physics.

As outlined in chapter 1, compressibility effects in wall-bounded turbulent flows can be classified into two main branches. The first involves effects related to heat transfer, often referred to as variable-property effects. The second branch is associated with changes in fluid volume in response to changes in pressure, also termed intrinsic compressibility effects. While variable-property effects can be significant at any, or even at zero, Mach numbers, intrinsic compressibility effects become important only at high Mach numbers. Therefore, it is crucial that compressibility corrections are developed with a clear distinction of these mechanisms and that they remain consistent with the relevant physics—whether concerning heat transfer (variable-property effects) or intrinsic compressibility. This can be ensured by deriving separate compressibility corrections from scaling theories associated with these effects.

For flows at non-hypersonic Mach numbers, Morkovin's hypothesis suggests that intrinsic compressibility effects are small, and only mean property (density and viscosity) variations are important to describe the turbulence dynamics (Smits and Dussauge, 2006). Because of these variations in mean properties, the classical scaling framework—which advocates using conventional definitions of friction velocity and viscous length scales, with density and viscosity taken at the wall (see equation 1.6)—becomes inaccurate for developing scaling laws. This led to the development of the semi-local scaling framework (Van Driest, 1951; Morkovin, 1962; Huang et al., 1995; Coleman et al., 1995; Patel et al., 2015; Trettel and Larsson, 2016; Patel et al., 2016a), where the friction velocity and viscous length scales are defined using local density and viscosity, as

$$u_\tau^* = \sqrt{\frac{\tau_w}{\bar{\rho}}}, \quad \delta_\nu^* = \frac{\bar{\mu}}{\bar{\rho}\, u_\tau^*}, \tag{7.1}$$

with τ_w the wall shear stress, and $\bar{\rho}$ and $\bar{\mu}$ the mean local density and viscosity that vary in the wall-normal direction; see also chapter 1.

Several compressible scaling laws in literature are based on these modified scales. For instance, the popular Van Driest velocity transformation accounts for changes in the friction velocity scale as

$$\bar{U}^+_{VD} = \int_0^{\bar{u}^+} \sqrt{\frac{\bar{\rho}}{\rho_w}} d\bar{u}^+ = \int_0^{\bar{u}^+} \frac{u_\tau}{u^*_\tau} d\bar{u}^+, \tag{7.2}$$

where $\bar{u}^+ = \bar{u}/u_\tau$ represents the classically scaled mean velocity, with $u_\tau = \sqrt{\tau_w/\rho_w}$ the wall-based friction velocity scale. This transformation, when plotted as a function of $y^+ = y/\delta_\nu$ (where $\delta_\nu = \mu_w/(\rho_w u_\tau)$ represents the classical viscous length scale), leads to a collapse on to the incompressible law of the wall for adiabatic flows, however, its accuracy deteriorates for diabatic flows (figure 1.5a; see also Bradshaw, 1977; Huang and Coleman, 1994; Trettel and Larsson, 2016; Patel et al., 2016a; Griffin et al., 2021). This is because the Van Driest transformation does not account for changes in the viscous length scale, which can vary significantly in diabatic flows but remains nearly constant in adiabatic flows close to the wall.

Subsequently, Trettel and Larsson (2016) and Patel et al. (2016a) independently derived the semi-local velocity transformation, which is an extension to the Van Driest velocity transformation accounting for variations in the semi-local viscous length scale. This transformation (also known as the TL transformation) can be written as

$$\bar{u}^* = \bar{U}^+_{TL} = \int_0^{\bar{u}^+} \left(1 - \frac{y}{\delta^*_\nu}\frac{d\delta^*_\nu}{dy}\right) \frac{u_\tau}{u^*_\tau} d\bar{u}^+. \tag{7.3}$$

When plotted as a function of the semi-locally scaled wall-normal coordinate $y^* = y/\delta^*_\nu$, $\bar{u}^*$ collapses on to the incompressible law of the wall for low-Mach number (Patel et al., 2016a) and moderate-Mach number (Trettel and Larsson, 2016) channel flows. However, this transformation loses accuracy for high-Mach number boundary layers (figure 1.5b; see also Patel et al., 2016a; Trettel and Larsson, 2016; Griffin et al., 2021), where Morkovin's hypothesis fails and intrinsic compressibility effects can no longer be neglected.

At high Mach numbers, intrinsic compressibility effects modify the near-wall damping of turbulent shear stress, leading to an upward shift in the semi-locally transformed mean velocity profile (chapters 3 and 5). By adjusting the damping function of a mixing-length turbulence model, in chapter 5, we proposed an extension to the semi-local velocity transformation, given as

$$\bar{U}^+_{HLPP} = \int_0^{\bar{u}^+} \left(\frac{1+\kappa y^* D(y^*, M_\tau)}{1+\kappa y^* D(y^*, 0)}\right) \left(1 - \frac{y}{\delta^*_\nu}\frac{d\delta^*_\nu}{dy}\right) \frac{u_\tau}{u^*_\tau} d\bar{u}^+. \tag{7.4}$$

Here, the damping function is given as

$$D(y^*, M_\tau) = \left[1 - \exp\left(\frac{-y^*}{A^+ + f(M_\tau)}\right)\right]^2, \tag{7.5}$$

with $f(M_\tau) = 19.3 M_\tau$, where $M_\tau = u_\tau/c_w$ is the friction Mach number and c_w is the speed of sound based on wall properties. This transformation, when plotted as a function of

y^*, collapses on to the incompressible law of the wall for a wide variety of high- and low-speed turbulent flows including (but not limited to) adiabatic and cooled boundary layers, adiabatic and cooled channels, supercritical flows, and flows with non-air-like viscosity laws (figure 5.2).

These compressible scaling laws can provide guidelines for developing compressibility corrections for turbulence models. For instance, Huang et al. (1994) demonstrated that to achieve the correct slope of the Van Driest scaled mean velocity profile in the logarithmic layer, the model constants must be functions of the mean density gradients. Later, Catris and Aupoix (2000) argued that the density dependence of the model constants can be eliminated by modifying the turbulent diffusion term in the turbulence model equations. Consequently, they modified the diffusion terms of several turbulence models, and found that the correct slope of $1/\kappa$ in the Van Driest transformed mean velocity profile was obtained.

A formal approach to deriving compressibility corrections from scaling laws was provided by Pecnik and Patel (2017). They first scaled the mean momentum and continuity equations using u_τ^* as the velocity scale and channel half-height h as the length scale. From these, they derived a semi-locally scaled turbulence kinetic energy (TKE) equation and, by analogy, formulated a corresponding semi-locally scaled dissipation equation. By rewriting these equations in the dimensional form, Otero Rodriguez et al. (2018) analytically derived variable-property corrections for several turbulence models and noted that these corrections only modify the diffusion terms. Interestingly, this modification closely resembles the compressibility corrections proposed by Catris and Aupoix (2000). The key difference is that in Otero Rodriguez et al. (2018), the correction applies to the entire diffusion term (both molecular and turbulent), whereas in Catris and Aupoix (2000), only the turbulent diffusion is corrected. Additionally, the derivation in Otero Rodriguez et al. (2018) results in a slightly different form for the diffusion of turbulent kinetic energy. Despite these differences, both approaches yield very similar results.

The compressibility corrections of Catris and Aupoix (2000) and Otero Rodriguez et al. (2018) (hereafter abbreviated as 'CA/OPDP' based on the last names of the authors) both give results consistent with the Van Driest transformation, since they are essentially based on u_τ^* and h as the relevant velocity and length scales. However, this makes the CA/OPDP corrections valid only in the outer layer, as they do not account for variations in the viscous length scale δ_ν^* in the inner layer. Despite this limitation, the results obtained with the CA/OPDP corrections are still accurate, even for diabatic flows, where the viscous length scales can vary significantly. This is because the variations in the viscous length scale are taken into account differently. Specifically: in the k-ϵ model by using y^* instead of y^+ in the damping functions; in the Spalart-Allmaras model through the damping function f_{v1} that uses a semi-locally consistent parameter $\chi = \check{\nu}/\bar{\nu} = \check{\nu}/(u_\tau^* \delta_\nu^*)$; in the $v^2 - f$ model with the length scale L_t that switches from $k^{1.5}/\epsilon$ (where k is the TKE and ϵ is its dissipation rate) to the Kolmogorov length scale η in the vicinity of the wall which is proportional to δ_ν^* (Patel et al., 2016a). However, this indirect accounting of the variations in the viscous length scale is not robust, and would fail for turbulence models without damping functions, for instance, the k-ω SST model (Menter, 1993), as observed in Catris and Aupoix (2000) and Otero Rodriguez et al. (2018). Thus, compressibility corrections that account for viscous length scale variations directly in the

model equations are needed.

At high Mach numbers, corrections based solely on mean property variations are insufficient, as intrinsic compressibility effects also play an important role. These effects modify the near-wall damping of turbulent shear stress, causing it to shift outwards with increasing Mach number (see chapters 3 and 5). From a turbulence modeling standpoint, this implies that the eddy viscosity formulation needs to be augmented with a damping function which accounts for this outward shift in the turbulent shear stress as a function of Mach number. In fact, the velocity transformation derived in chapter 5 is based on such a modification of the damping function for a mixing-length model (equations 5.13 and 7.5). Similar modifications are also needed for other turbulence models.

In addition to the compressibility corrections discussed earlier, accurate modeling of the energy equation is essential for estimating thermophysical properties, such as density and viscosity, which are critical for solving the turbulence model equations accurately. There are two key aspects of the energy equation modeling: (1) accurate estimation of the eddy-conductivity (analogue of eddy viscosity) and (2) accurate modeling of the source terms. For high-speed flows, the eddy-conductivity is often estimated using a constant turbulent Prandtl number (Pr_t) of 0.9 (Wilcox et al., 2006). However, this constant-Pr_t assumption has been questioned in various recent papers, especially close to the wall (Huang et al., 2022; Griffin et al., 2023; Chen et al., 2024). The source terms, on the other hand, require modeling of the viscous and turbulent diffusion of the mean and turbulent kinetic energy. Using the direct numerical simulation (DNS) data of turbulent channel flows, Huang et al. (2023) argued that the viscous and turbulent diffusion of the TKE is negligible. On the contrary, using the DNS data of turbulent boundary layers, Cheng and Fu (2024) showed that only the third-order correlation (turbulent diffusion of TKE) is negligible, while the viscous diffusion term remains important.

In light of these points, the aim of this chapter is threefold: (1) to properly account for changes in the viscous length scale in the inner layer directly within the turbulence model equations, thereby enabling more accurate predictions in flows with heat transfer at low as well as high Mach numbers; (2) to further enhance the model by incorporating intrinsic compressibility effects, allowing for improved predictions for high Mach number flows; and (3) to correctly model the energy equation by including the viscous and turbulent diffusion of TKE, leading to better predictions of the temperature profile for high-speed turbulent boundary layers and channel flows. This chapter is written with a particular emphasis on the k-ω SST model (Menter, 1993). However, the proposed approach can be extended to other models such as the Spalart and Allmaras (1992) model (see section 7.9), k-ϵ models, and the $v^2 - f$ model (Durbin, 1991).

7.2. VARIABLE-PROPERTY CORRECTIONS

7.2.1. INNER LAYER

From several studies in the past decades (Morkovin, 1962; Coleman et al., 1995; Huang et al., 1995; Patel et al., 2015; Trettel and Larsson, 2016; Modesti and Pirozzoli, 2016; Patel et al., 2017; Zhang et al., 2018), it has been shown that turbulence quantities, when semi-locally scaled (i.e. using u_τ^* and δ_v^* as the relevant velocity and length scales, respectively), collapse well onto their respective incompressible counterparts when plotted as a function of the semi-local coordinate y^*. Some of these quantities, in

their classically and semi-locally scaled form are listed in table 7.1 ('Inner layer').

Similarly, we argue that if the individual variables collapse when semi-locally scaled, then their model equations written in the semi-locally scaled form must be analogous to those written in the classically scaled form for incompressible flows. Here, we enforce a strict analogy by replacing the individual variables in a classically scaled equation by their semi-locally scaled counterparts.

Let us start by writing the modelled turbulent kinetic energy equation in the inner layer of a canonical incompressible constant-property flow. Neglecting advection terms, the equation reduces to a simple balance between production, dissipation and diffusion of turbulent kinetic energy as

$$\mu_t \left(\frac{d\bar{u}}{dy}\right)^2 - \beta^\star \rho_w k\omega + \frac{d}{dy}\left[\left(\mu_w + \sigma_k \mu_t\right)\frac{dk}{dy}\right] = 0, \tag{7.6}$$

where μ_t is the eddy viscosity, $\bar{u}$ the mean velocity, k the turbulent kinetic energy, ω the specific dissipation rate, ρ_w, μ_w the density and viscosity at the wall, and $\beta^\star$, σ_k the SST model constants.

Rewriting this equation using the non-dimensional form of the variables, as given in table 7.1 ('Inner layer'), leads to

$$\mu_t^+ \left(\frac{d\bar{u}^+}{dy^+}\right)^2 - \beta^\star k^+\omega^+ + \frac{d}{dy^+}\left[\left(1 + \sigma_k \mu_t^+\right)\frac{dk^+}{dy^+}\right] = 0, \tag{7.7}$$

where the superscript '+' denotes the classical wall-based scaling. Now we replace all classically scaled variables with their semi-locally scaled counterparts (refer table 7.1), which gives

$$\mu_t^* \left(\frac{d\bar{u}^*}{dy^*}\right)^2 - \beta^\star k^*\omega^* + \frac{d}{dy^*}\left[\left(1 + \sigma_k \mu_t^*\right)\frac{dk^*}{dy^*}\right] = 0, \tag{7.8}$$

where the superscript '$*$' denotes semi-local scaling. Rewriting equation (7.8) using the dimensional form of the variables (see table 7.1), we get

$$\frac{\mu_t}{\bar{\mu}}\left(\frac{\delta_v^*}{u_\tau^*}\right)^2 \left(\frac{d\bar{u}}{dy}\right)^2 - \beta^\star \frac{k}{u_\tau^{*2}}\frac{\omega}{u_\tau^*/\delta_v^*} + \frac{d}{d(y/\delta_v^*)}\left[\left(1 + \sigma_k \frac{\mu_t}{\bar{\mu}}\right)\frac{d(k/u_\tau^{*2})}{d(y/\delta_v^*)}\right] = 0. \tag{7.9}$$

Using the definitions of u_τ^* and δ_v^* from equation (1.12), we get

$$\frac{\mu_t}{\bar{\mu}}\frac{\bar{\mu}^2}{\tau_w^2}\left(\frac{d\bar{u}}{dy}\right)^2 - \beta^\star \frac{\bar{\rho}}{\tau_w} k \frac{\bar{\mu}}{\tau_w}\omega + \frac{d}{d(y\sqrt{\tau_w\bar{\rho}}/\bar{\mu})}\left[\left(1 + \sigma_k \frac{\mu_t}{\bar{\mu}}\right)\frac{d(\bar{\rho}k/\tau_w)}{d(y\sqrt{\tau_w\bar{\rho}}/\bar{\mu})}\right] = 0. \tag{7.10}$$

Dividing the equation by $\bar{\mu}/\tau_w^2$ gives

$$\mu_t \left(\frac{d\bar{u}}{dy}\right)^2 - \beta^\star \bar{\rho} k\omega + \frac{1}{\bar{\mu}}\frac{d}{d(y\sqrt{\bar{\rho}}/\bar{\mu})}\left[\left(\bar{\mu} + \sigma_k \mu_t\right)\frac{1}{\bar{\mu}}\frac{d(\bar{\rho}k)}{d(y\sqrt{\bar{\rho}}/\bar{\mu})}\right] = 0. \tag{7.11}$$

Applying the chain rule to the diffusion term, we get

$$\mu_t \left(\frac{d\bar{u}}{dy}\right)^2 - \beta^\star \bar{\rho} k\omega + \frac{1}{\bar{\mu}}\frac{dy}{d(y\sqrt{\bar{\rho}}/\bar{\mu})}\frac{d}{dy}\left[\left(\bar{\mu} + \sigma_k \mu_t\right)\frac{1}{\bar{\mu}}\frac{dy}{d(y\sqrt{\bar{\rho}}/\bar{\mu})}\frac{d(\bar{\rho}k)}{dy}\right] = 0, \tag{7.12}$$

Quantity	Incompressible (classical)	Compressible (semi-local)
Inner layer		
Wall distance	$y^+ = y/\delta_\nu$	$y^* = y/\delta_\nu^*$
Mean shear	$d\bar{u}^+/dy^+ = (\delta_\nu/u_\tau)d\bar{u}/dy$	$d\bar{u}^*/dy^* = (\delta_\nu^*/u_\tau^*)d\bar{u}/dy$
TKE	$k^+ = k/u_\tau^2$	$k^* = k/u_\tau^{*2}$
Turb. diss.	$\epsilon^+ = \epsilon/({u_\tau}^3/\delta_\nu)$	$\epsilon^* = \epsilon/({u_\tau^*}^3/\delta_\nu^*)$
Spec. turb. diss.	$\omega^+ = \omega/(u_\tau/\delta_\nu)$	$\omega^* = \omega/(u_\tau^*/\delta_\nu^*)$
Eddy visc.	$\mu_t^+ = \mu_t/(\rho_w u_\tau \delta_\nu) = \mu_t/\mu_w$	$\mu_t^* = \mu_t/(\bar{\rho} u_\tau^* \delta_\nu^*) = \mu_t/\bar{\mu}$
Dyn. visc.	$\mu^+ = \mu_w/(\rho_w u_\tau \delta_\nu) = \mu_w/\mu_w = 1$	$\bar{\mu}^* = \bar{\mu}/(\bar{\rho} u_\tau^* \delta_\nu^*) = \bar{\mu}/\bar{\mu} = 1$
Outer layer		
Wall distance	$y^\oplus = y/\delta$	$y^\circledast = y/\delta$
Mean shear	$d\bar{u}^\oplus/dy^\oplus = (\delta/u_\tau)d\bar{u}/dy$	$d\bar{u}^\circledast/dy^\circledast = (\delta/u_\tau^*)d\bar{u}/dy$
TKE	$k^\oplus = k/u_\tau^2$	$k^\circledast = k/u_\tau^{*2}$
Turb. diss.	$\epsilon^\oplus = \epsilon/({u_\tau}^3/\delta)$	$\epsilon^\circledast = \epsilon/({u_\tau^*}^3/\delta)$
Spec. turb. diss.	$\omega^\oplus = \omega/(u_\tau/\delta)$	$\omega^\circledast = \omega/(u_\tau^*/\delta)$
Eddy visc.	$\mu_t^\oplus = \mu_t/(\rho_w u_\tau \delta) = (\mu_t/\mu_w)/Re_\tau$	$\mu_t^\circledast = \mu_t/(\bar{\rho} u_\tau^* \delta) = (\mu_t/\bar{\mu})/Re_\tau^*$
Dyn. visc.	$\mu^\oplus = \mu_w/(\rho_w u_\tau \delta) = 1/Re_\tau$	$\bar{\mu}^\circledast = \bar{\mu}/(\bar{\rho} u_\tau^* \delta) = 1/Re_\tau^*$

Table 7.1: An example of quantities that are classically (superscripts '+' and '$\oplus$' for the inner and outer layers, respectively) and semi-locally scaled (superscripts '$*$' and '$\circledast$' for the inner and outer layers, respectively). As indicated in chapter 1, classical scaling uses the length scale δ_ν in the inner layer, and δ in the outer layer, with the velocity scale u_τ in the entire boundary layer. Analogously, semi-local scaling uses δ_ν^* in the inner layer, and δ in the outer layer, with u_τ^* in the entire boundary layer; see chapter 6. $Re_\tau = \rho_w u_\tau \delta/\mu_w$ is the friction Reynolds number, and $Re_\tau^* = \bar{\rho} u_\tau^* \delta/\bar{\mu}$ is its semi-local counterpart (Foysi et al., 2004; Patel et al., 2015). k indicates the turbulent kinetic energy (TKE), ϵ the TKE dissipation rate (per unit mass), and ω the specific turbulent dissipation rate, defined as ϵ/k. Note that $\bar{u}^*$ in $d\bar{u}^*/dy^*$ represents the semi-locally transformed mean velocity, as defined in (7.3). Also note that $\bar{u}^\circledast$ in $d\bar{u}^\circledast/dy^\circledast$ represents the Van Driest transformed mean velocity, as defined in (7.2).

where $d(y\sqrt{\bar{\rho}}/\bar{\mu})/dy$ represents the stretching of the wall-normal coordinate due to variable density and viscosity. Note that y in $y\sqrt{\bar{\rho}}/\bar{\mu}$ corresponds to the distance from the closest wall. However, y represents this distance only when the origin of the y-axis is located on the wall. To make the equations invariant to the choice of the origin of y-axis, i.e., to ensure Galilean invariance, we propose to replace y with ℓ, where ℓ represents the distance from the closest wall.

Finally, introducing a stretching variable S_y, defined as

$$S_y = \left(\frac{d\left(\ell\sqrt{\bar{\rho}}/\bar{\mu}\right)}{dy} \right)^{-1} = \left(\frac{\sqrt{\bar{\rho}}}{\bar{\mu}} + \ell \frac{d\left(\sqrt{\bar{\rho}}/\bar{\mu}\right)}{dy} \right)^{-1}, \tag{7.13}$$

we get

$$\mu_t \left(\frac{d\bar{u}}{dy} \right)^2 - \beta^\star \bar{\rho} k\omega + \frac{S_y}{\bar{\mu}} \frac{d}{dy} \left[\left(\bar{\mu} + \sigma_k \mu_t \right) \frac{S_y}{\bar{\mu}} \frac{d(\bar{\rho}k)}{dy} \right] = 0. \tag{7.14}$$

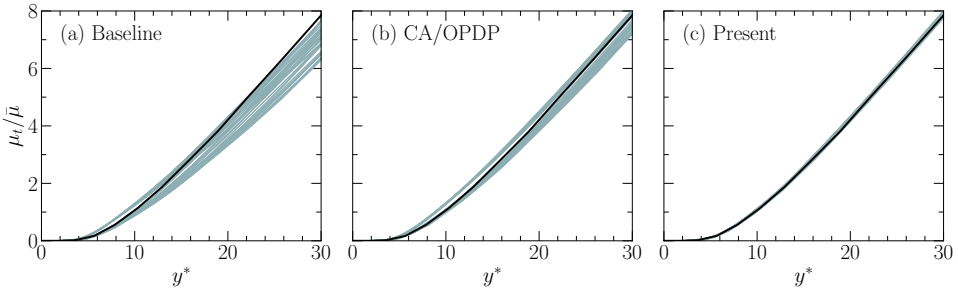

Figure 7.1: Wall-normal distributions of $\mu_t/\bar{\mu}$ computed using the k-ω SST model with (a) no corrections, (b) CA/OPDP corrections, and (c) present corrections for the zero-pressure-gradient turbulent boundary layers listed in table 2.3. The black lines represent the constant-property case of Sillero et al. (2013) at $Re_\tau = 1437$. For details about the implementation, refer section 7.6.

Comparing equation (7.14) with a standard TKE equation for compressible flows, one can note that the present compressibility corrections only modify the modeling of the diffusion term, just as in the CA/OPDP corrections. It is important to note that since we enforce a strict analogy, these corrections modify the modeling of the total diffusion term, not just the turbulent diffusion term.

For the ease of implementation in existing computational fluid dynamic solvers, these compressibility modifications can be reformulated in the form of a source term (Φ_k^{in}; where the superscript 'in' represents inner layer) as follows:

$$\mu_t\left(\frac{d\bar{u}}{dy}\right)^2 - \beta^\star\bar{\rho}k\omega + \frac{d}{dy}\left[\left(\bar{\mu}+\sigma_k\mu_t\right)\frac{dk}{dy}\right] + \Phi_k^{\text{in}} = 0, \tag{7.15}$$

where the other terms except Φ_k^{in} represent the standard TKE equation in the inner layer. Φ_k^{in} can then be written as

$$\Phi_k^{\text{in}} = \frac{S_y}{\bar{\mu}}\frac{d}{dy}\left[\left(\bar{\mu}+\sigma_k\mu_t\right)\frac{S_y}{\bar{\mu}}\frac{d(\bar{\rho}k)}{dy}\right] - \frac{d}{dy}\left[\left(\bar{\mu}+\sigma_k\mu_t\right)\frac{dk}{dy}\right]. \tag{7.16}$$

$\Phi_k^{\text{in}} = 0$ for cases with constant mean properties, while Φ_k^{in} is consistent with the CA/OPDP corrections for cases where δ_v^* remains uniform in the inner layer.

Repeating the same procedure for the ω model equation, we obtain

$$\Phi_\omega^{\text{in}} = \frac{\bar{\rho}S_y}{\bar{\mu}^2}\frac{d}{dy}\left[\left(\bar{\mu}+\sigma_\omega\mu_t\right)\frac{S_y}{\bar{\mu}}\frac{d(\bar{\mu}\omega)}{dy}\right] - \frac{d}{dy}\left[\left(\bar{\mu}+\sigma_\omega\mu_t\right)\frac{d\omega}{dy}\right]. \tag{7.17}$$

The standard k-ω SST model equations along with the source terms defined in equations (7.16) and (7.17) represent the proposed compressibility corrections in the inner layer.

Figure 7.1 shows $\mu_t/\bar{\mu}$ obtained with the k-ω SST model with (a) no corrections, with (b) CA/OPDP corrections, and with (c) the present corrections for numerous compressible turbulent boundary layers (represented by gray lines) from the literature (see section 7.6 for details on the implementation and table 2.3 for details on the cases). The black lines in the figure show an incompressible case of Sillero et al. (2013) at $Re_\tau = 1437$. The collapse on to a single curve in figure 7.1(c) clearly shows that the present corrections are consistent with the semi-local scaling framework.

7.2.2. OUTER LAYER

In the outer layer, the appropriate length scale is δ (boundary layer thickness; equivalent to h for channels) instead of δ_ν^*. Thus, the corrections discussed so far, which are based on δ_ν^*, are not valid there. To obtain valid compressibility corrections in the outer layer, one may follow the same approach as in the previous section, but using u_τ^* and δ as the relevant scales.

In the following, we derive the outer-layer corrections based on the logarithmic region. These corrections are then extended to the defect layer under the assumption that the advection terms remain unaffected by variable-property corrections. This approach was also employed in Catris and Aupoix (2000).

We start by writing the the modeled turbulent kinetic energy equation in the logarithmic region of a canonical incompressible constant-property flow as

$$\mu_t \left(\frac{d\bar{u}}{dy}\right)^2 - \beta^\star \rho_w k\omega + \frac{d}{dy}\left[\left(\mu_w + \sigma_k \mu_t\right)\frac{dk}{dy}\right] = 0. \tag{7.18}$$

(Note that we do not drop the diffusion term in the log region, since it may become relevant in the defect layer where the derived corrections will be extended. Also, the viscous diffusion term, despite being irrelevant in the outer layer is retained for the sake of completeness).

Rewriting this equation using the non-dimensional form of the variables, as given in table 7.1 ('Outer layer'), leads to

$$\mu_t^\oplus \left(\frac{d\bar{u}^\oplus}{dy^\oplus}\right)^2 - \beta^\star k^\oplus \omega^\oplus + \frac{d}{dy^\oplus}\left[\left(1 + \sigma_k \mu_t^\oplus\right)\frac{dk^\oplus}{dy^\oplus}\right] = 0, \tag{7.19}$$

where the superscript '$\oplus$' denotes the classical scaling in the outer layer. Now, following section 7.2.1, we replace all classically scaled variables with their semi-locally scaled counterparts (refer table 7.1), which gives

$$\mu_t^\circledast \left(\frac{d\bar{u}^\circledast}{dy^\circledast}\right)^2 - \beta^\star k^\circledast \omega^\circledast + \frac{d}{dy^\circledast}\left[\left(1 + \sigma_k \mu_t^\circledast\right)\frac{dk^\circledast}{dy^\circledast}\right] = 0, \tag{7.20}$$

where the superscript '$\circledast$' denotes semi-local scaling in the outer layer. Rewriting equation (7.20) using the dimensional form of the variables (see table 7.1), we get

$$\frac{\mu_t}{\bar{\rho} u_\tau^* \delta}\left(\frac{\delta}{u_\tau^*}\right)^2 \left(\frac{d\bar{u}}{dy}\right)^2 - \beta^\star \frac{k}{u_\tau^{*2}}\frac{\omega}{u_\tau^*/\delta} + \frac{d}{d(y/\delta)}\left[\left(\frac{\bar{\mu}}{\bar{\rho} u_\tau^* \delta} + \sigma_k \frac{\mu_t}{\bar{\rho} u_\tau^* \delta}\right)\frac{d(k/u_\tau^{*2})}{d(y/\delta)}\right] = 0. \tag{7.21}$$

Now, using the definition of u_τ^* from equation (1.12), we get

$$\frac{\mu_t}{\sqrt{\tau_w \bar{\rho}}}\frac{\delta}{\tau_w/\bar{\rho}}\left(\frac{d\bar{u}}{dy}\right)^2 - \beta^\star \frac{\bar{\rho}}{\tau_w} k \frac{\delta}{\sqrt{\tau_w/\bar{\rho}}}\omega + \frac{d}{d(y/\delta)}\left[\left(\frac{\bar{\mu}}{\sqrt{\tau_w \bar{\rho}}\delta} + \sigma_k \frac{\mu_t}{\sqrt{\tau_w \bar{\rho}}\delta}\right)\frac{d(\bar{\rho}k/\tau_w)}{d(y/\delta)}\right] = 0, \tag{7.22}$$

which when divided by $\sqrt{\bar{\rho}}\delta/\tau_w^{1.5}$ gives

$$\mu_t \left(\frac{d\bar{u}}{dy}\right)^2 - \beta^\star \bar{\rho} k\omega + \frac{1}{\sqrt{\bar{\rho}}}\frac{d}{dy}\left[\left(\bar{\mu} + \sigma_k \mu_t\right)\frac{1}{\sqrt{\bar{\rho}}}\frac{d(\bar{\rho}k)}{dy}\right] = 0. \tag{7.23}$$

Note that these corrections are identical to the ones proposed by Otero Rodriguez et al. (2018) for the entire boundary layer.

Now, as done in section 7.2.1, we express these corrections in the form of a source term as

$$\Phi_k^{\text{out}} = \frac{1}{\sqrt{\bar{\rho}}}\frac{\partial}{\partial y}\left[\left(\bar{\mu}+\sigma_k\mu_t\right)\frac{1}{\sqrt{\bar{\rho}}}\frac{\partial(\bar{\rho}k)}{\partial y}\right] - \frac{\partial}{\partial y}\left[\left(\bar{\mu}+\sigma_k\mu_t\right)\frac{\partial k}{\partial y}\right]. \tag{7.24}$$

Note that partial derivatives are used because derivatives in the wall-parallel directions are non-zero in the outer layer.

Repeating the same procedure for the ω equation, we get

$$\Phi_\omega^{\text{out}} = \frac{\partial}{\partial y}\left[\left(\bar{\mu}+\sigma_\omega\mu_t\right)\frac{1}{\sqrt{\bar{\rho}}}\frac{\partial(\sqrt{\bar{\rho}}\omega)}{\partial y}\right] - \frac{\partial}{\partial y}\left[\left(\bar{\mu}+\sigma_\omega\mu_t\right)\frac{\partial\omega}{\partial y}\right]. \tag{7.25}$$

These source terms are blended with their inner-layer counterparts and then used in the full k and ω transport equations as discussed in section 7.3.

Note that in the SST model, the transport equation for ω includes a cross-diffusion term, given by

$$CD_{k\omega} = 2(1-F_1)\frac{\bar{\rho}\sigma_{\omega 2}}{\omega}\frac{\partial k}{\partial y}\frac{\partial\omega}{\partial y}, \tag{7.26}$$

where F_1 is a blending function introduced by Menter (1993) to smoothly transition between the k-ω and k-ϵ models. This term is primarily active in the outer region of a boundary layer, where $F_1 \to 0$.

Previous studies (Catris and Aupoix, 2000; Otero Rodriguez et al., 2018) have employed the conventional form of this term (7.26) in their computations. However, we argue that because the cross-diffusion term originates from the diffusion term—and given that our proposed corrections target the diffusion term—it is necessary to modify this term for consistency.

Following the same approach as described earlier, the variable-property-corrected cross-diffusion term is given by

$$CD_{k\omega} = 2(1-F_1)\frac{\sigma_{\omega 2}}{\sqrt{\bar{\rho}}\omega}\frac{\partial\bar{\rho}k}{\partial y}\frac{\partial\sqrt{\bar{\rho}}\omega}{\partial y}. \tag{7.27}$$

Finally, as previously done, we express the corrections on the CD term in the form of a source term as

$$\Phi_{CD} = \underbrace{2(1-F_1)\frac{\sigma_{\omega 2}}{\sqrt{\bar{\rho}}\omega}\frac{\partial\bar{\rho}k}{\partial y}\frac{\partial\sqrt{\bar{\rho}}\omega}{\partial y}}_{\text{variable-property-corrected}} - \underbrace{2(1-F_1)\frac{\bar{\rho}\sigma_{\omega 2}}{\omega}\frac{\partial k}{\partial y}\frac{\partial\omega}{\partial y}}_{\text{conventional}}. \tag{7.28}$$

7.3. PROPOSED VARIABLE-PROPERTY CORRECTIONS FOR THE ENTIRE BOUNDARY LAYER

Implementing different corrections for the inner and outer layers requires switching between the two forms or blending them with suitable functions. This is essential to preserve the distinct scaling characteristics of these two regions, as demonstrated in chapter 6 using mixing-length models.

To obtain corrections valid in the entire boundary layer, we propose to blend the inner- (equations 7.16 & 7.17) and outer-layer (equations 7.24 & 7.25) forms using a suitable damping function $\mathscr{F}$ as

$$\Phi_k = \mathscr{F}\Phi_k^{\text{in}} + (1-\mathscr{F})\,\Phi_k^{\text{out}}, \tag{7.29}$$

$$\Phi_\omega = \mathscr{F}\Phi_\omega^{\text{in}} + (1-\mathscr{F})\,\Phi_\omega^{\text{out}}, \tag{7.30}$$

where $\mathscr{F}$ transitions from unity in the viscous sublayer to zero in the outer layer. In this chapter, we use SST model's F_1 as the appropriate blending function; however, other options could be more suitable, whose discussion is deferred to a future study.

With these corrections, the k and ω transport equations in an SST model are modified as:

$$\bar{\rho}\frac{Dk}{Dt} = \text{Conventional TKE terms} + \Phi_k, \tag{7.31}$$

$$\bar{\rho}\frac{D\omega}{Dt} = \text{Conventional } \omega \text{ terms} + \Phi_\omega + \Phi_{CD}. \tag{7.32}$$

Lastly, three important points are worth noting. First, only the wall-normal component of the diffusion term in equations (7.16), (7.17), (7.24) and (7.25) is modified; the wall-parallel components remain unchanged. This is because semi-local scaling, and thus the corrections derived from it, are concerned with variations only along the wall-normal direction. However, applying these corrections also in the wall-parallel directions should not influence the results, since mean property gradients along those directions are comparatively negligible. The formulation of the corrections in cases where the wall-normal direction does not align with the coordinate axis (for e.g. flow over an inclined wall) is discussed in Appendix C. Second, as expected, the proposed corrections vanish in the free-stream region, where the mean properties remain constant. Third, in free-shear flows, these corrections—especially the outer-layer ones—would have minimal impact, leading to little improvement over an uncorrected model (Aupoix, 2004). The inner-layer corrections are irrelevant in such flows due to negligible viscous effects.

7.4. INTRINSIC COMPRESSIBILITY CORRECTIONS

The semi-local scaling approach presented in the previous section accounts for effects associated with mean density and viscosity variations. However, at higher Mach numbers, in addition to variable property effects, intrinsic compressibility effects also play an important role. These compressibility effects modify the near-wall damping of turbulence, particularly in the buffer layer, resulting in an outward shift in the eddy viscosity profile, and an upward shift in the logarithmic portion of the semi-locally (or TL) transformed mean velocity profile (refer chapters 5 and 3).

To account for this outward shift in the eddy viscosity, in chapter 5, we modified the Van Driest damping function in a mixing length model (equations 5.13 and 7.5) as

$$\mu_t = \bar{\rho}u_\tau^*\kappa y D(y^*,0)\underbrace{\frac{D(y^*,M_\tau)}{D(y^*,0)}}_{D^{ic}}, \tag{7.33}$$

where $\bar{\rho} u_\tau^* \kappa y D(y^*, 0)$ is the semi-local eddy viscosity that accounts for mean property variations alone, and D^{ic} is the change in damping caused due to intrinsic compressibility effects. Note that D^{ic} is mainly active in the buffer layer and approaches unity in the log-layer and beyond.

Similarly, we propose for the SST model, to multiply the eddy viscosity with a damping function that captures the outward shift due to intrinsic compressibility effects as

$$\mu_t = \underbrace{\frac{a_1 \bar{\rho} k}{max(a_1 \omega, F_2 \Omega)}}_{\text{conventional } \mu_t} (D^{ic})_{\text{sst}}, \tag{7.34}$$

where the constant $a_1 = 0.31$, and $\Omega = d\bar{u}/dy$ for canonical flows (Menter, 1993). The damping function in this equation is defined as

$$(D^{ic})_{\text{sst}} = \frac{D(R_t, M_t)}{D(R_t, 0)}, \tag{7.35}$$

with

$$D(R_t, M_t) = \left[1 - \exp\left(\frac{-R_t}{K + f(M_t)}\right)\right]^2, \tag{7.36}$$

where $M_t = \sqrt{2k}/\bar{c}$ ($\bar{c}$ being the local speed of sound) is the turbulence Mach number, and $R_t = \bar{\rho} k/(\bar{\mu}\omega)$ is the turbulence Reynolds number. The constant K controls the region in which the damping function $(D^{ic})_{\text{sst}}$ is active (analogous to A^+ in equation 7.5). To apply the modifications mainly in the buffer layer, we choose $K = 3.5$.

The function $f(M_t)$ controls how the eddy viscosity decreases (or shifts outward) with increasing Mach number, analogous to the function $f(M_\tau)$ in equation (7.5). The first step in obtaining the function $f(M_t)$ is to determine the value of K in equation (7.36). We set $K = 3.5$ based on the value of R_t for the SST model at $y^* \approx 17$. The value $y^* = 17$ corresponds to A^+ in the mixing-length damping function, as described in equation (7.5).

Next, we treat $f(M_t)$ to be uniform in the domain (constant) and gradually increase its value from 0 in the denominator of equation (7.36). Simultaneously, we solve the inner-layer equations discussed in section 7.6.1, where the eddy viscosity formulation is multiplied with the damping function given in equation (7.36). For these calculations, we focus solely on the damping function and assume $\bar{T}/T_w = 1$ (no variable-property effects), meaning we do not solve the energy equation. Additionally, we assume a specific Reynolds number, $Re_\tau = 750$, and verify that the final form of $f(M_t)$ is not significantly influenced by the choice of Re_τ.

From the predicted velocity profiles, we compute the log-law intercept C and observe how it changes with variations in $f(M_t)$. For the SST model, the log-law intercept C is non-linearly related to $f(M_t)$ through the expression:

$$C - 5.2 = 12 f(M_t)^{1.3}. \tag{7.37}$$

It is known from chapter 5 that C is a linear function of the friction Mach number M_τ:

$$C - 5.2 = 7.18 M_\tau. \tag{7.38}$$

Combining equations (7.37) and (7.38), we obtain:

$$f(M_t)^{1.3} = \frac{7.18}{12} M_\tau. \tag{7.39}$$

Using DNS data from over 30 cases in the literature, we note that there exists a linear relationship between M_τ and the maximum value of M_t, given by $M_t^{max} \approx 3.33 M_\tau$ (not shown). Substituting this relationship into equation (7.39), we derive:

$$f(M_t)^{1.3} \approx \frac{7.18}{12 \times 3.33} M_t^{max},$$

which simplifies to:

$$f(M_t) \approx 0.27 \left(M_t^{max}\right)^{0.77}. \tag{7.40}$$

The constant 0.27 in equation (7.40) is based on the DNS-derived relationship between M_τ and M_t^{max}. However, the k-ω SST model predicts values of k, and hence, M_t^{max} that differ from those obtained from DNS. Moreover, M_t^{max} is a single value, whereas we seek a relationship that depends on the local M_t, which varies throughout the domain. To address these issues, we retain the functional form of equation (7.40) but replace M_t^{max} with the local M_t. We then adjust the constant 0.27 until the relationship $C - 5.2 = 7.18 M_\tau$ is accurately reproduced by the SST model. This process yields:

$$f(M_t) \approx 0.39 M_t^{0.77}. \tag{7.41}$$

The same approach can be used to formulate and tune $f(M_t)$ for other turbulence models.

7.5. MODELING THE ENERGY EQUATION

We now turn our attention to the accurate modeling of the energy equation, which provides the density, viscosity, and other thermo-physical properties essential for solving the turbulence model equations discussed in the previous sections.

The total energy equation in the inner layer of canonical wall-bounded flows can be written as

$$\frac{d}{dy}\left(-\tilde{q}_y - \bar{\rho}\widetilde{v''h''}\right) + \frac{d}{dy}\left(\tilde{u}\bar{\tau}_{xy} - \tilde{u}\bar{\rho}\widetilde{u''v''}\right) + \frac{d}{dy}\left(\overline{u_i''\tau_{ij}'} - \frac{1}{2}\bar{\rho}\widetilde{v''u_i''u_i''}\right) - \frac{d\bar{p}}{dx}\tilde{u} = 0, \tag{7.42}$$

where q_y is the molecular heat flux in the wall-normal direction, v the wall normal velocity, h the enthalpy, and τ_{ij} the viscous shear stress. The first term on the left hand side represents molecular and turbulent diffusion of enthalpy, the second term represents molecular and turbulent diffusion of mean kinetic energy, and the third term represents molecular and turbulent diffusion of turbulent kinetic energy. The last term represents the work done by the mean pressure gradient in the streamwise direction. For fully developed channel flows, $d\bar{p}/dx = -\tau_w/h$, and for zero-pressure-gradient boundary layers, $d\bar{p}/dx = 0$.

We can simplify the second term on the left hand side as

$$\frac{d}{dy}\left(\tilde{u}\bar{\tau}_{xy} - \tilde{u}\bar{\rho}\widetilde{u''v''}\right) = \tau_{tot}\frac{d\tilde{u}}{dy} + \tilde{u}\frac{d\tau_{tot}}{dy}, \tag{7.43}$$

where $\tau_{tot} = \bar{\tau}_{xy} - \bar{\rho}\widetilde{u''v''}$. For fully developed channel flows, we can write $d\tau_{tot}/dy = -\tau_w/h = d\bar{p}/dx$, and for ZPG boundary layers $d\tau_{tot}/dy = 0$ in the inner layer. Taking these simplifications into account, we get

$$\frac{d}{dy}\left(-\tilde{q}_y - \bar{\rho}\widetilde{v''h''}\right) + (\bar{\tau}_{xy} - \bar{\rho}\widetilde{u''v''})\frac{d\tilde{u}}{dy} + \frac{d}{dy}\left(\overline{u_i''\tau_{ij}'} - \frac{1}{2}\bar{\rho}\widetilde{v''u_i''u_i''}\right) = 0. \tag{7.44}$$

The terms in equation (7.44) are modeled as follows (Wilcox et al., 2006):

$$-\frac{d\bar{q}_y}{dy} = \frac{d}{dy}\left(\frac{\bar{\mu}c_p}{Pr}\frac{d\tilde{T}}{dy}\right), \quad -\frac{d\bar{\rho}\widetilde{v''h''}}{dy} = \frac{d}{dy}\left(\frac{\mu_t c_p}{Pr_t}\frac{d\tilde{T}}{dy}\right), \tag{7.45}$$

$$\tau_{xy}\frac{d\tilde{u}}{dy} = \bar{\mu}\left(\frac{d\tilde{u}}{dy}\right)^2, \quad -\bar{\rho}\widetilde{u''v''}\frac{d\tilde{u}}{dy} = \mu_t\left(\frac{d\tilde{u}}{dy}\right)^2, \tag{7.46}$$

where Pr_t is the turbulent Prandtl number. The last term on the left hand side in equation (7.44) represents the total diffusion of TKE, which is modeled as (see section 7.2.1, equation 7.14)

$$\frac{d}{dy}\left(\overline{u_i''\tau_{ij}'} - \frac{1}{2}\bar{\rho}\widetilde{v''u_i''u_i''}\right) = \frac{S_y}{\bar{\mu}}\frac{d}{dy}\left[\left(\bar{\mu}+\sigma_k\mu_t\right)\frac{S_y}{\bar{\mu}}\frac{d(\bar{\rho}k)}{dy}\right]. \tag{7.47}$$

With these modeled terms, equation (7.44) can be written as

$$\frac{d}{dy}\left(\left[\frac{\bar{\mu}c_p}{Pr}+\frac{\mu_t c_p}{Pr_t}\right]\frac{d\tilde{T}}{dy}\right) = -\left(\bar{\mu}+\mu_t\right)\left(\frac{d\tilde{u}}{dy}\right)^2 - \frac{S_y}{\bar{\mu}}\frac{d}{dy}\left[\left(\bar{\mu}+\sigma_k\mu_t\right)\frac{S_y}{\bar{\mu}}\frac{d(\bar{\rho}k)}{dy}\right]. \tag{7.48}$$

In the inner layer, the total diffusion of TKE (last term in equation 7.48) is balanced by its production and dissipation (see equation 7.14), such that

$$\frac{S_y}{\bar{\mu}}\frac{d}{dy}\left[\left(\bar{\mu}+\sigma_k\mu_t\right)\frac{S_y}{\bar{\mu}}\frac{d(\bar{\rho}k)}{dy}\right] = -\mu_t\left(\frac{d\tilde{u}}{dy}\right)^2 + \bar{\rho}\epsilon. \tag{7.49}$$

Using this relation to substitute the total diffusion of TKE in (7.48), we get

$$\frac{d}{dy}\left(\left[\frac{\bar{\mu}c_p}{Pr}+\frac{\mu_t c_p}{Pr_t}\right]\frac{d\tilde{T}}{dy}\right) = -\left(\bar{\mu}+\mu_t\right)\left(\frac{d\tilde{u}}{dy}\right)^2 + \mu_t\left(\frac{d\tilde{u}}{dy}\right)^2 - \bar{\rho}\epsilon, \tag{7.50}$$

which further simplifies to

$$\frac{d}{dy}\left(\left[\frac{\bar{\mu}c_p}{Pr}+\frac{\mu_t c_p}{Pr_t}\right]\frac{d\tilde{T}}{dy}\right) = \underbrace{-\bar{\mu}\left(\frac{d\tilde{u}}{dy}\right)^2 - \bar{\rho}\epsilon}_{\Phi_e}, \tag{7.51}$$

where Φ_e represents the source term in this equation.

Commonly, the TKE dissipation term in (7.51) is assumed to be equal to the production term in the entire domain, i.e., $\bar{\rho}\epsilon \approx \mu_t(d\tilde{u}/dy)^2$, thereby implying equilibrium (Larsson et al., 2016; Bose and Park, 2018; Huang et al., 2023). However, this assumption breaks down near the wall and is responsible for inaccuracies in predicting the temperature peak in high-speed, cooled-wall boundary layers (see section 7.7). This implies that accurate modeling of ϵ is essential for accurate temperature predictions.

Another possible source of error in the energy equation (7.51) is the turbulent Prandtl number, which is often assumed to be a constant and equal to 0.9 (Wilcox et al., 2006). However, it is well-known that for cooled-wall boundary layers Pr_t is not a constant but rather varies substantially in the near-wall region. Furthermore, at the location of the temperature peak, Pr_t is undefined (Griffin et al., 2023; Chen et al., 2024). In section 7.7, we will briefly analyse the sensitivity of our results with respect to different values of Pr_t.

7.6. IMPLEMENTATION

The proposed corrections primarily differ from the CA/OPDP corrections within the inner layer, while they remain identical in the outer layer. Consequently, for a meaningful comparison between the two approaches, it suffices to focus on solving the inner layer. This also allows us to gauge the effectiveness of the proposed inner-layer corrections without any potential influence from the outer layer.

In this section, we present the implementation of the proposed corrections for simple canonical flows that can be modeled as one-dimensional problems, such as the inner layer of zero-pressure-gradient (ZPG) boundary layers and fully developed channel flows. In these flows, mainly the effect of Φ_k^{in}, Φ_ω^{in}, and the damping function D_{sst}^{ic} is tested. Subsequently, in section 7.8, we test the full corrections, i.e., Φ_k^{in} and Φ_ω^{in} in the inner layer, blended with Φ_k^{out} and Φ_ω^{out} in the outer layer (equations 7.29 and 7.30), together with the damping function D_{sst}^{ic} and the correction for the cross-diffusion term Φ_{CD}.

7.6.1. ZERO-PRESSURE-GRADIENT BOUNDARY LAYERS

To solve the inner layer of boundary layers, we follow the methodology outlined in section 4.6.3 of Wilcox et al. (2006) for incompressible flows. This approach involves solving the integrated streamwise momentum equation, also known as the total stress balance equation, in conjunction with one-dimensional turbulence model equations to determine the inner-layer velocity profile in a turbulent boundary layer. In this work, we extend this framework to compressible flows.

For compressible boundary layers, the inner-layer velocity and temperature profiles are obtained by solving the integrated forms of the momentum and energy equations, given as

$$\begin{aligned} \frac{d\bar{u}}{dy} &= \frac{\tau_w}{\bar{\mu}+\mu_t}, \quad \text{and} \\ c_p\left(\frac{\bar{\mu}}{Pr}+\frac{\mu_t}{Pr_t}\right)\frac{d\bar{T}}{dy} &= -\frac{\mu_w c_p}{Pr}\left(\frac{d\bar{T}}{dy}\right)_w - \int_0^y \Phi_e\, dy, \end{aligned} \tag{7.52}$$

respectively. These equations are solved in a domain spanning from $y = 0$ to $y = 0.2\delta$, where $y = 0.2\delta$ is arbitrarily taken to be the edge of the inner layer. (Note that a higher value of the edge of the inner layer is chosen ($y/\delta = 0.2$) than that shown in figure 1.4 ($y/\delta = 0.1$), mainly because some of the cases tested in this chapter are at low Reynolds numbers, such that $y/\delta = 0.1$ would correspond to the buffer or just the start of the log-layer).

The dynamic viscosity $\bar{\mu}$ in (7.52) is computed using Sutherland's law, the mean density is obtained as $\bar{\rho}/\rho_w = T_w/\bar{T}$, and the Prandtl number Pr is equal to 0.72. The first term on the right-hand-side of the energy equation, scaled by wall-based quantities ($\rho_w u_\tau c_p T_w$), corresponds to the non-dimensional wall heat flux B_q.

The eddy viscosity μ_t in (7.52) is computed by solving the one-dimensional SST model (without advection terms), analogous to the one-dimensional k-ω model described in Wilcox et al. (2006) (see equation 4.184). This model is solved with the source terms Φ_k^{in} and Φ_ω^{in} described in equations (7.16) and (7.17), along with the standard eddy viscosity formulation being multiplied by $(D^{ic})_{\text{sst}}$ (7.35). The boundary conditions for the SST

model are defined as

$$\begin{aligned} k &= 0, \quad \omega = \frac{60\bar{\mu}}{\beta_1 \bar{\rho}(\Delta y)^2} \quad \text{at} \quad y = 0, \quad \text{and} \\ k &= \frac{u_\tau^{*2}}{\sqrt{\beta^\star}}, \quad \omega = \frac{u_\tau^*}{\sqrt{\beta^\star}\kappa y} \quad \text{at} \quad y = 0.2\delta, \end{aligned} \tag{7.53}$$

where Δy is the distance to the next grid point away from the wall. The first row of eq. (7.53) corresponds to the wall boundary condition described in Menter (1993), and the second row corresponds to the log-layer asymptotic solution for k and ω as described in Wilcox et al. (2006) (see equation 4.185), but adapted to compressible flows.

The turbulent Prandtl number Pr_t in (7.52) is assumed to be a constant and equal to 0.9. However, to show the sensitivity of the results with respect to the constant Pr_t assumption, we will also compute some of the results with Pr_t from DNS and then compare them with $Pr_t = 0.9$.

Lastly, the source term Φ_e in (7.52) was defined in equation (7.51) as

$$\Phi_e = \bar{\mu}(d\bar{u}/dy)^2 + \bar{\rho}\epsilon. \tag{7.54}$$

As discussed earlier, a common way to model the TKE dissipation rate is to assume it to be equal to the production term ($\bar{\rho}\epsilon = \mu_t(d\bar{u}/dy)^2$), such that the source term becomes

$$\Phi_{e,1} = \bar{\mu}(d\bar{u}/dy)^2 + \mu_t(d\bar{u}/dy)^2, \tag{7.55}$$

where '1' in the subscript corresponds to the first type of approximation that we will use in this chapter. This approximation is inaccurate near the wall, since close to the wall the production term tends to zero, whereas the dissipation term is finite and balances the total diffusion of TKE.

Therefore, we seek a more accurate representation of ϵ. One way is to use the TKE dissipation rate estimated by the model itself, which in the case of SST is equal to $\epsilon_{\text{sst}} = \beta^\star k\omega$. However, just like the production term, ϵ_{sst} also approaches zero at the wall, as $k \to 0$ while ω remains finite (see wall-boundary conditions in equation 7.53). Consequently, using ϵ from the SST model would yield results similar to those obtained with $\Phi_{e,1}$. To address this inherent limitation, we follow the approach of Rahman et al. (2012) and model the dissipation rate as

$$\epsilon_{\text{eff}} = \sqrt{\epsilon_{\text{sst}}^2 + \epsilon_w^2}, \tag{7.56}$$

where ϵ_w ensures non-zero dissipation rate at the wall, given by $\epsilon_w = 2A_\epsilon(\bar{\mu}/\bar{\rho})(d\bar{u}/dy)^2$, with $A_\epsilon = 0.09$ (Rahman et al., 2012), and where ϵ_{eff} represents the effective dissipation rate. With this, the second approximation of Φ_e that we will use in this chapter is given as

$$\Phi_{e,2} = \bar{\mu}(d\bar{u}/dy)^2 + \bar{\rho}\epsilon_{\text{eff}}. \tag{7.57}$$

We solve the equations listed above iteratively until convergence; see Hasan et al. (2024a) for more details on the solver.

7.6.2. FULLY DEVELOPED CHANNEL FLOWS

For channel flows, instead of solving only for the inner layer, we solve for the entire domain (spanning from $y = 0$ to $y = 2h$, h being the channel half-height). However, we do not switch to the outer-layer compressibility corrections, but consistently use the inner-layer corrections in the entire domain. This is because the velocity profile in the outer layer of channel flows closely follows the logarithmic profile of the inner layer, meaning the error introduced by not solving the outer layer with the correct corrections is minimal.

For fully developed channel flows, we solve the momentum and energy equations, given as

$$\frac{d}{dy}\left[\left(\bar{\mu}+\mu_t\right)\frac{d\bar{u}}{dy}\right] = -\frac{\tau_w}{h}, \qquad \frac{d}{dy}\left(\left[\frac{\bar{\mu}c_p}{Pr}+\frac{\mu_t c_p}{Pr_t}\right]\frac{d\bar{T}}{dy}\right) = -\Phi_e, \tag{7.58}$$

where $\bar{\mu}$ is computed using a power-law $(\bar{T}/T_w)^n$ with an exponent of 0.75 for high-Mach number flows and 0.7 for the low-Mach number cases. The mean density is computed as $\bar{\rho}/\rho_w = T_w/\bar{T}$, and the Prandtl number Pr is assumed to be a constant and equal to 0.72 for the high-Mach-number cases, and is defined as $Pr = (\bar{T}/T_w)^{0.7}$ for the low-Mach-number cases. The different choices for $\bar{\mu}$ and Pr are consistent with those used in the respective DNSs of these cases.

The eddy viscosity μ_t in (7.58) is obtained by solving the one-dimensional SST model with the proposed corrections (similar to ZPG boundary layers discussed above), along with the wall boundary conditions ($k = 0$ and $\omega = 60\bar{\mu}/[\beta_1\bar{\rho}(\Delta y)^2]$) imposed on the two walls located at $y = 0$ and $y = 2h$.

The turbulent Prandtl number (Pr_t) in equation (7.58) is assumed to be constant, with $Pr_t = 0.9$ for high-Mach-number channel flows, similar to ZPG boundary layers, and $Pr_t = 1$ for low-Mach-number flows. The higher value for the low-Mach-number cases is based on the results of Patel et al. (2017), where Pr_t is reported to be close to 1, or even slightly higher for these cases. This is likely due to the strong similarity between momentum and energy equations in these flows.

The source term Φ_e in (7.58) for high-Mach-number channel flows can be approximated as $\Phi_{e,1}$ or $\Phi_{e,2}$, similar to ZPG boundary layers. In contrast, for low-Mach-number flows, the dissipation of mean and turbulent kinetic energy does not contribute to the right-hand side of equation (7.58). This can be explained as follows: $\Phi_{e,1}$ (or $\Phi_{e,2}$) scales with $\rho_r\mathscr{U}^3/\mathscr{L}$, where ρ_r is a reference density scale, and $\mathscr{U}$ and $\mathscr{L}$ are relevant velocity and length scales, respectively. On the other hand, the left-hand side of the energy equation (7.58) scales with $\rho_r\mathscr{U}c_{p,r}T_r/\mathscr{L}$, where $c_{p,r}$ and T_r are reference scales for c_p and $\bar{T}$, respectively. The ratio of these scales corresponds to an Eckert number, defined as $\mathscr{U}^2/(c_{p,r}T_r)$ which is proportional to the square of the Mach number. For flows at low (or zero) Mach numbers, this ratio tends to zero which explains why $\Phi_{e,1}$ and $\Phi_{e,2}$ are ineffective in equation (7.58). Thus, in those flows, temperature and hence property variations are created by adding a user-defined heat source which is uniform in the domain. For the two low-Mach-number gas-like cases considered here, this external heat source is equal to $17.55(\mu_w c_p/Pr_w)T_w/h$ (Patel et al., 2015) and $75(\mu_w c_p/Pr_w)T_w/h$ (Pecnik and Patel, 2017).

All the equations described above are solved in their wall-scaled form. For more details on the solver, refer the jupyter notebook (Hasan et al., 2024a).

7.7. RESULTS

We now present the results obtained from our inner-layer compressibility corrections (equations 7.16, 7.17 and 7.35) and compare them with those obtained using the state-of-the-art CA/OPDP corrections (Catris and Aupoix, 2000; Pecnik and Patel, 2017; Otero Rodriguez et al., 2018), which correspond to the outer-layer corrections presented in equations (7.24) and (7.25). We also present results computed using the baseline model without any corrections.

These results are presented for 39 ZPG boundary layers and 11 channel flows described in table 2.3, and visually represented in figure 2.4. Note that for ZPG boundary layers, the results are presented only in the inner layer. For results covering the entire boundary layer, refer to section 7.8.

7.7.1. ZERO-PRESSURE-GRADIENT BOUNDARY LAYERS

Out of the 39 cases, five cases with increasing wall cooling are selected and their velocity and temperature profiles are shown in figure 7.2(a) and (b), respectively. The different line types correspond to the results obtained with different compressibility corrections and with different modeling approximations in the energy equation, as shown in the legend. They are summarized as follows. (1) The grey dotted lines correspond to the results obtained with the baseline SST model (without any compressibility corrections), along with $\Phi_{e,1}$ in the energy equation. (2) The grey short-dashed lines represent the results computed with the state-of-the-art CA/OPDP compressibility corrections, with $\Phi_{e,1}$ in the energy equation. (3) The grey long-dashed lines signify the results when the inner-layer corrections described in equations (7.16), (7.17) and (7.35) are used, along with $\Phi_{e,1}$ in the energy equation. (4) Finally, the solid grey lines depict the results obtained using the present inner-layer corrections, but with $\Phi_{e,2}$ in the energy equation. All of these results are computed with $Pr_t = 0.9$.

Let us first focus on the grey dotted lines. With increasing wall cooling (see cases from left to right), the velocity profiles computed using the baseline model shift downwards relative to the DNS (solid colored lines), while the temperature profiles are over-predicted.

When the CA/OPDP corrections are applied (see short-dashed lines), the results remain largely similar to the baseline model (also observed previously in Catris and Aupoix (2000); Rumsey (2010) and Otero Rodriguez et al. (2018)), with slight deterioration observed in some cases. To further improve the accuracy, it becomes important to account for the variations in the viscous length scale (δ_ν^*) in the inner layer. Moreover, the cases in figure 7.2 also correspond to higher Mach numbers, and thus, it also becomes important to account for intrinsic compressibility effects.

Upon applying the present corrections (see long-dashed lines), which account for δ_ν^* variations and intrinsic compressibility effects, the results for both velocity and temperature substantially improve with respect to the baseline and CA/OPDP corrections. However, the temperature profiles are still inaccurate compared to the DNS, mainly for the strongly-cooled cases.

This inaccuracy in the temperature profiles can be resolved by replacing $\Phi_{e,1}$ in the energy equation with $\Phi_{e,2}$ (grey solid lines). Clearly, the temperature profiles with $\Phi_{e,2}$ are more accurate, particularly in capturing the peak temperature. This highlights the importance of accurately estimating the source terms in the energy equation for accurate

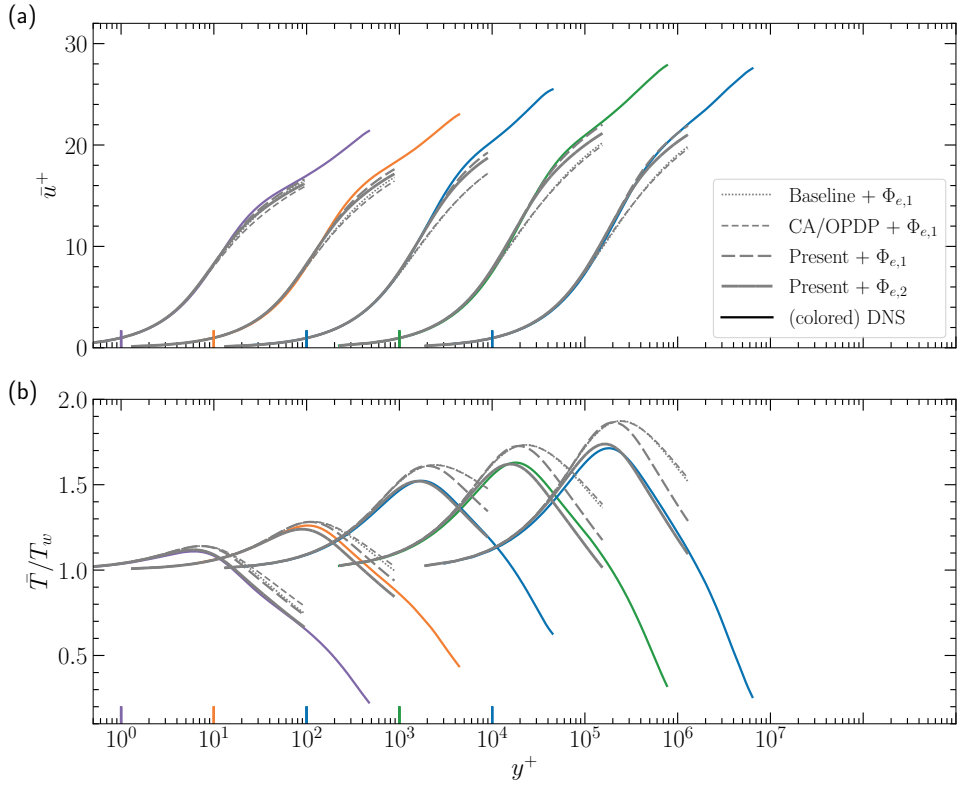

Figure 7.2: Computed mean velocity (a) and temperature (b) profiles compared to the DNS (colored solid lines) for the following boundary layers with increasing wall-cooling: (left to right) $M_\infty = 7.87$, $T_w/T_r = 0.48$ (A. Ceci, private communication); $M_\infty = 6$, $T_w/T_r = 0.35$ (Cogo et al., 2023); $M_\infty = 5.84$, $T_w/T_r = 0.25$ (Zhang et al., 2018); $M_\infty = 10.9$, $T_w/T_r = 0.2$ (Huang et al., 2022); $M_\infty = 13.64$, $T_w/T_r = 0.18$ (Zhang et al., 2018). The line colors match the color of the symbols for the respective authors reported in table 2.3. Refer to the legend for line types. 'Baseline' stands for the SST model without corrections, 'CA/OPDP' stands for the compressibility corrections proposed in Catris and Aupoix (2000); Pecnik and Patel (2017); Otero Rodriguez et al. (2018), 'Present' stands for the corrections proposed in this chapter (equations 7.16, 7.17 and 7.35). For clarity, the velocity and temperature profiles for different cases are shifted by one decade along the abscissa. The colored vertical lines on the abscissa signify $y^+ = 10^0$ for each case, with their colors matching the corresponding cases.

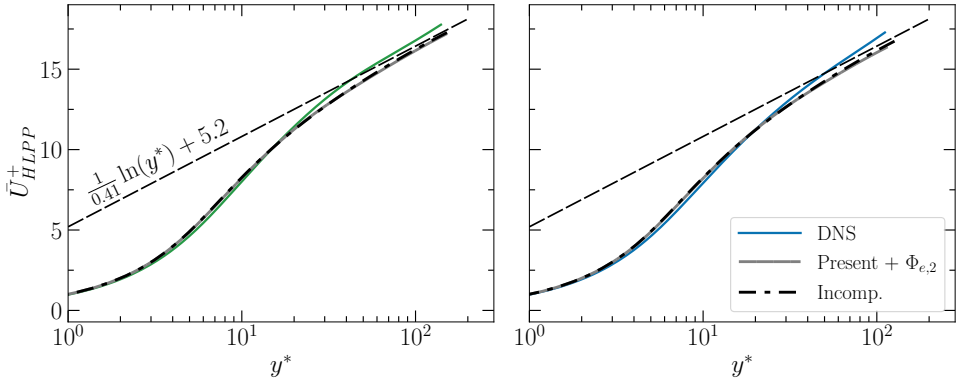

Figure 7.3: The HLPP-transformed (7.4) mean velocity profiles as a function of the semi-local coordinate y^*, for the (left) $M_\infty = 10.9$, $T_w/T_r = 0.2$ (Huang et al., 2022) and (right) $M_\infty = 13.64$, $T_w/T_r = 0.18$ (Zhang et al., 2018) cases described in table 2.3. These cases correspond to the fourth and fifth cases from left in figure 7.2. The colored lines correspond to DNS, whereas the grey solid lines correspond to that estimated from the SST model with the present corrections, along with $\Phi_{e,2}$ in the energy equation. The dash-dotted black lines correspond to that estimated from the SST model for an incompressible (constant-property) case at similar Re_τ as the respective compressible cases described above. Note that the DNS profiles are plotted only until $y/\delta = 0.2$ (edge of the inner layer) for clarity.

7

temperature estimations in high-speed boundary layers.

While the temperature profiles improve, the velocity profiles slightly deteriorate when $\Phi_{e,2}$ is used as the source term. This is explained as follows. The present corrections (equations 7.16, 7.17 and 7.35) make the SST model results consistent with the proposed transformation (7.4)—also termed as the 'HLPP' transformation. In other words, the velocity profiles estimated by the corrected model, upon HLPP transformation, would collapse on to the velocity profile estimated by the model for an incompressible flow. Figure 7.3 shows the HLPP-transformed profiles for the fourth and fifth cases (from left) in figure 7.2. Clearly, the solid grey lines that correspond to the corrected model collapse on to the black dash-dotted lines that represent the SST model prediction for incompressible flows. However, these lines are shifted downwards with respect to the DNS (depicted by solid colored lines). Such a downward-shifted model profile, when inverse transformed with accurate mean properties would result in $\bar{u}^+$ which is also under-predicted with respect to the DNS. This is what we observed in figure 7.2 for these cases (compare solid grey and colored lines). On the contrary, with $\Phi_{e,1}$, due to inaccurate temperature, and hence, property profiles, there are error cancellations which results in more accurate $\bar{u}^+$ observed in figure 7.2 (compare long-dashed grey and solid colored lines).

Next, we quantify the error in the velocity and temperature profiles in terms of the inner-layer edge values, namely

$$\varepsilon_\phi = \frac{\left|\phi_{y=0.2\delta} - \phi^{DNS}_{y=0.2\delta}\right|}{\phi^{DNS}_{y=0.2\delta}} \times 100, \tag{7.59}$$

where ϕ could either be $\bar{u}^+$ or $\bar{T}/T_w$. Such an error definition represents the integrated or cumulative error in solving equation (7.52) across the entire domain. In other words,

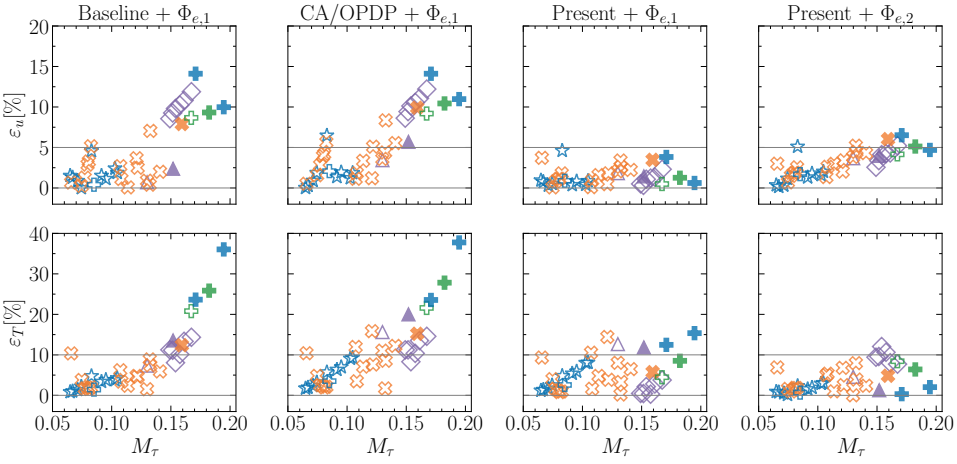

Figure 7.4: Percent error in velocity (top row) and temperature (bottom row) predictions for 39 compressible turbulent boundary layers from the literature as shown in table 2.3. The error is computed using equation (7.59). Symbols are as in table 2.3. The filled symbols correspond to the cases whose velocity and temperature profiles are plotted in figure 7.2. The gray horizontal lines in the inset indicate errors of 0% and 5% for velocity, and 0% and 10% for temperature.

it quantifies the overall accumulation of errors in key quantities such as μ_t, which is particularly relevant to the present study as our corrections directly impact μ_t.

Figure 7.4 presents the error in velocity and temperature for the 39 boundary layer cases listed in table 2.3. The titles of the subfigures correspond to various modeling corrections discussed earlier. With the baseline model (first column), consistent with the observations made in figure 7.2, the errors in both velocity and temperature are significantly high reaching approximately 15% and 40%, respectively. When the CA/OPDP corrections are applied (second column), these errors remain similar or even slightly increase in some cases.

With the implementation of the present inner-layer corrections (third column), the errors in both velocity and temperature reduce significantly, falling within approximately 5% and 15%, respectively. Finally, when the source term $\Phi_{e,1}$ is replaced with $\Phi_{e,2}$ (fourth column), the velocity errors slightly increase (as explained above), whereas the temperature errors improve across all cases except those of Ceci et al. (2022). This discrepancy may be due to minor inaccuracies in the wall-cooling parameter (B_q) for these cases, which serves as an input to the solver (Hasan et al., 2024a).

SENSITIVITY OF THE RESULTS TO Pr_t

The results discussed so far were obtained using a constant turbulent Prandtl number, $Pr_t = 0.9$, throughout the domain. In this section, we assess the sensitivity of the results to Pr_t by comparing temperature profiles computed with Pr_t from DNS to those obtained with $Pr_t = 0.9$. We continue using the present corrections, with $\Phi_{e,2}$ in the energy equation, and focus on the Mach 6 and 14 cases from Zhang et al. (2018) (third and fifth cases from the left in figure 7.2), as DNS data for Pr_t is available for them.

Figure 7.5 (top row) compares the DNS-based Pr_t (solid colored lines) with $Pr_t = 0.9$ (solid grey lines) for the Mach 6 (left) and Mach 14 (right) cases mentioned above.

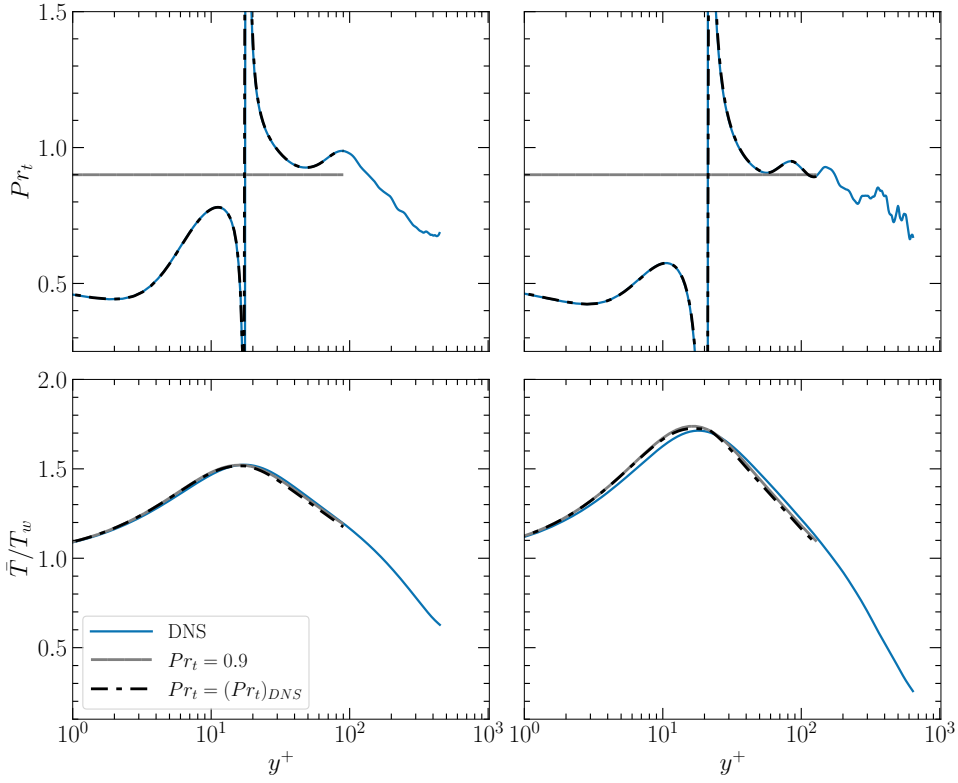

Figure 7.5: The turbulent Prandtl number (Pr_t; top row) and temperature profiles (bottom row) for the $M_\infty = 5.84$, $T_w/T_r = 0.25$ (left) and $M_\infty = 13.64$, $T_w/T_r = 0.18$ (right) cases of Zhang et al. (2018). These cases correspond to the third and fifth profiles in figure 7.2. The solid colored lines represent the Pr_t and $\bar{T}/T_w$ profiles extracted from the DNS. The solid grey lines correspond to the constant approximation $Pr_t = 0.9$ in the top row and the resulting temperature profiles computed using this approximation in the bottom row. Finally, the dash-dotted black lines depict the DNS-based Pr_t interpolated onto the solver's mesh in the top row, and the corresponding temperature results obtained using this interpolated profile in the bottom row.

The difference is significant in the near-wall region ($y^* < 15$), but the profiles converge further away from the wall. To incorporate this DNS-based Pr_t into our computations, we interpolate it onto the mesh used by our solver. The interpolated values closely match the DNS profiles, as seen from the dash-dotted black lines in figure 7.5 (top row).

Using these interpolated Pr_t values, we recompute the temperature profiles and present them in figure 7.5 (bottom row) with dash-dotted black lines. These results are nearly identical to those obtained with $Pr_t = 0.9$ (solid grey lines), suggesting that $Pr_t = 0.9$ is a reasonable approximation for the ideal-gas, air-like cases considered here.

The nearly identical results can be explained as follows. In the near-wall region, the molecular diffusion of energy dominates the turbulent diffusion. As a result, despite the significant mismatch between the DNS-based Pr_t and $Pr_t = 0.9$ in this region, the temperature profiles remain largely unaffected. Further away from the wall, where turbulent diffusion becomes significant, the DNS-based Pr_t closely aligns with $Pr_t = 0.9$, leading to similar temperature predictions. These findings contradict previous studies (Chen et al., 2024), which state that the near-wall variations in the turbulent Prandtl number are the primary cause of errors in temperature predictions for high-speed flows.

7.7.2. FULLY DEVELOPED CHANNEL FLOWS

Figure 7.6 shows the (a) mean velocity and (b) temperature profiles for two low-Mach (red) and two high-Mach-number turbulent channel flows (blue) described in the figure caption. The line types in the legend are similar to those discussed earlier for boundary layers, except that here $\Phi_{e,1}$ and $\Phi_{e,2}$ are only applicable to the high-Mach-number cases. For the low-Mach-number cases, the source term is a user-defined constant (see section 7.6).

Low-Mach-number cases – Let us first focus on the two low-Mach-number cases (first and second cases from the left). While using the baseline model (grey dotted lines), both the velocity and temperature profiles are under-predicted compared to the DNS.

Similar under-predictions are also observed when the CA/OPDP corrections are applied (see grey short-dashed lines). This inaccuracy originates from the fact that CA/OPDP corrections are based on Van Driest's scaling, which becomes inaccurate for strongly-cooled flows.

The grey long-dashed and the grey solid lines correspond to the results where the CA/OPDP corrections are replaced by the proposed variable-property corrections which account for variations in the viscous length scale (see equations 7.16 and 7.17). These lines are equivalent for the low-Mach-number cases, and thus, only the grey solid lines are visible. This is because the main difference between these lines is in the source term ($\Phi_{e,1}$ and $\Phi_{e,2}$). For the low-Mach cases, these source terms are zero, since the Mach number is zero.

Comparing the grey solid lines with the grey dotted and grey short-dashed lines, we note a substantial improvement for both velocity and temperature. This highlights the importance of accounting for viscous length scale variations in the model equations.

High-Mach-number cases – Next, we look at the last two cases from the left, corresponding to the compressible turbulent channel flows. Similar to the low-Mach-number cases, the velocity and temperature profiles are under-predicted while using the baseline model with no corrections (see grey dotted lines) as well as while using the CA/OPDP corrections (see grey short-dashed lines). The results improve when

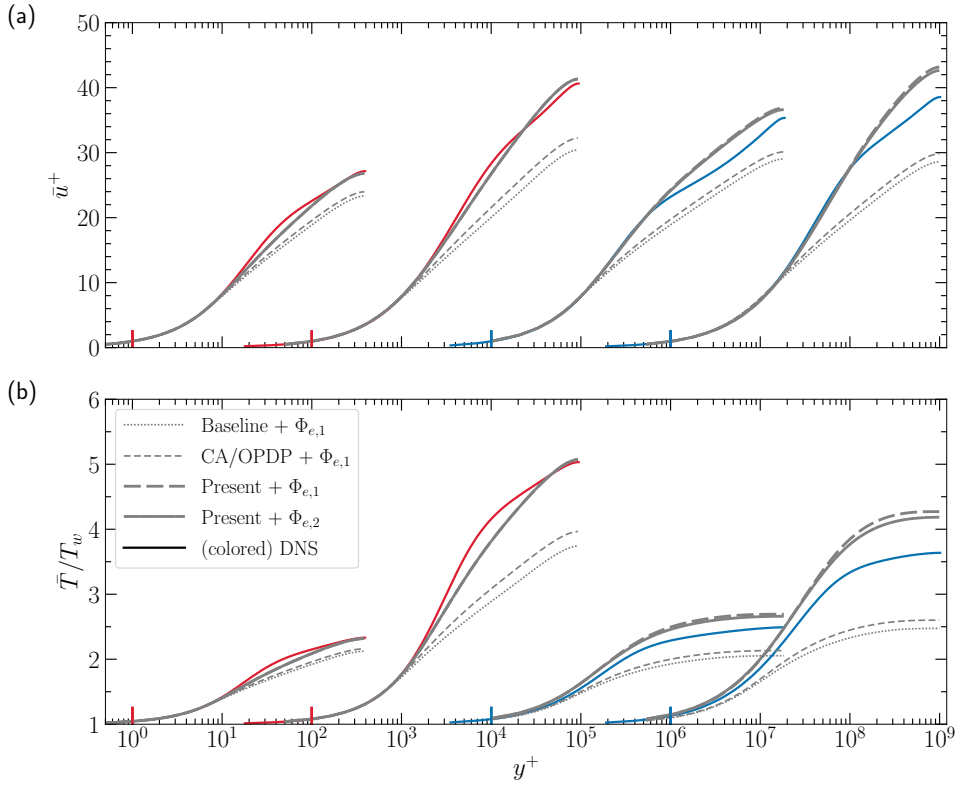

Figure 7.6: Computed mean velocity (a) and temperature (b) profiles compared to the DNS (colored solid lines) for the following turbulent channel flows: (left to right) $M_b = 0$, $Re_\tau = 395$ (gas-like case of Patel et al. (2015)); $M_b = 0$, $Re_\tau = 950$ (gas-like case of Pecnik and Patel (2017)); $M_b = 3$, $Re_\tau = 1876$ and $M_b = 4$, $Re_\tau = 1017$ (compressible cases of Trettel and Larsson (2016)). The line colors match the color of the symbols for the respective authors reported in table 2.3. The line types in the legend are explained in the caption of figure 7.2. Note that $\Phi_{e,1}$ and $\Phi_{e,2}$ only apply to the high-Mach number cases. For the low-Mach cases, the source term is a user-defined constant, as noted in section 7.6. For clarity, the velocity and temperature profiles for different cases are shifted by two decades along the abscissa. The colored vertical lines on the abscissa signify $y^+ = 10^0$ for each case, with their colors matching the corresponding cases.

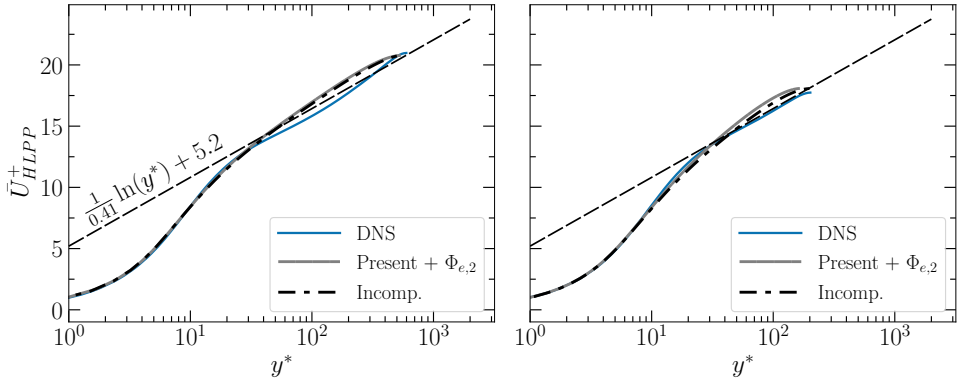

Figure 7.7: The HLPP-transformed (7.4) mean velocity profiles as a function of the semi-local coordinate y^*, for the (left) $M_b = 3$, $Re_\tau = 1876$ and (right) $M_b = 4$, $Re_\tau = 1017$ cases of Trettel and Larsson (2016) described in table 2.3. These cases correspond to the third and fourth cases from left in figure 7.6. The colored lines correspond to DNS, whereas the grey solid lines correspond to that estimated from the SST model with the present corrections, along with $\Phi_{e,2}$ in the energy equation. The dash-dotted black lines correspond to that estimated from the SST model for an incompressible (constant-property) case at similar $Re^*_{\tau_c}$ (semi-local Reynolds number computed using channel centreline properties as $Re^*_{\tau_c} = \bar{\rho}_c u^*_{\tau_c} h/\bar{\mu}_c$) as the respective compressible cases described above.

the proposed corrections are used, as indicated by grey long-dashed lines, however, the velocity and temperature profiles are now over-predicted compared to the DNS. Changing the source term in the energy equation from $\Phi_{e,1}$ to $\Phi_{e,2}$ (grey solid lines) leads to little improvement, with the over-prediction largely unchanged.

The possible reason for this over-prediction is discussed next. We have observed that HLPP-transformed DNS mean velocity profiles for compressible channel flows are shifted downwards in the logarithmic region compared to the incompressible law of the wall (see Appendix B). This trend is also observed in figure 7.7 for the Mach 3 case (left). However, for the Mach 4 case (right), such a downward shift is not evident, likely due to its low Reynolds number. (Specifically, the local Reynolds number in this case decreases from 1017 at the wall to below 250 at $y^* \approx 15$, continuing to drop further away from the wall).

On the other hand, the transformed profiles predicted by the SST model slightly overshoot relative to the law of the wall, especially in the logarithmic region and beyond ($y^* > 30$). As a result, these model profiles are consistently higher than the DNS in these regions, such that when inverse-transformed, the estimated $\bar{u}^+$ is also higher. The higher $\bar{u}^+$ directly influences the energy equation via the source terms $\Phi_{e,1}$ and $\Phi_{e,2}$, thereby leading to an over-prediction in temperature profiles. This, in turn, influences $\bar{u}^+$ through mean properties, further intensifying the over-prediction.

Interestingly, when we break this coupling between velocity and temperature by using temperature from the DNS in our computations, we observe that the over-prediction in $\bar{u}^+$ is significantly reduced (not shown) suggesting that the coupling between energy and momentum equations plays an important role in the higher $\bar{u}^+$ and $\bar{T}/T_w$ values.

Finally, we quantify the errors (ε_ϕ) in the computed velocity and temperature profiles using equation (7.59), but now ϕ is taken at the channel centreline ($\phi_{y=h}$).

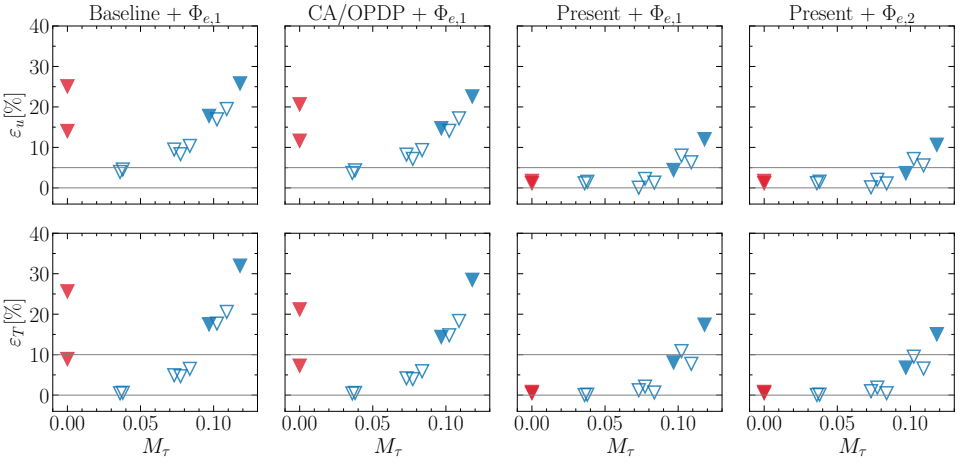

Figure 7.8: Percent error in velocity (top row) and temperature (bottom row) predictions for 11 turbulent channel flows from the literature as shown in table 2.3. The error is computed using equation (7.59). Symbols are as in table 2.3. The filled symbols correspond to the cases whose velocity and temperature profiles are plotted in figure 7.6. The gray horizontal lines in the inset indicate errors of 0% and 5% for velocity, and 0% and 10% for temperature.

7

Figure 7.6 shows the errors in the velocity profiles (ε_u) for two low-Mach-number and nine high-Mach-number channel flow cases listed in table 2.3. Like in figure 7.4, the titles of the subfigures correspond to various modeling corrections discussed earlier. The errors using the baseline model with no corrections (first column) and with the CA/OPDP corrections (second column) remain similar, with the errors for velocity and temperature reaching up to approximately 25% and 30%, respectively.

With our corrections (third and fourth columns), the errors in both velocity and temperature are significantly reduced, falling within approximately 10% and 15%, respectively. Furthermore, the errors remain similar for both $\Phi_{e,1}$ and $\Phi_{e,2}$, suggesting lower sensitivity of the channel flow results to the choice of the source term.

7.8. TESTING THE PROPOSED CORRECTIONS ON A FULL BOUNDARY LAYER

In the previous sections, we discussed the implementation and results for the inner layer of ZPG boundary layers and channel flows, that can be modeled using one-dimensional equations. However, it is so far unclear how the proposed corrections perform in a two-dimensional boundary layer simulation, where the outer layer is also solved for.

To address this point, we performed a flat plate boundary layer simulation for the $M_\infty = 10.9$, $T_w/T_r = 0.2$ case of Huang et al. (2022), using Ansys Fluent. The computational domain spans 1.5 m in the streamwise direction and 0.2 m in the wall-normal direction, discretized using a structured mesh consisting of 1600 cells along the streamwise direction and 300 cells in the wall-normal direction. The mesh is stretched in the wall-normal direction such that the first grid point lies within one viscous wall unit from the wall. With this mesh, we achieve a resolution of about

$\Delta x^+ \approx 97$ and $\Delta y^+_{\text{min}} \approx 0.014$ at the streamwise location whose profiles are shown in figure 7.9. This resolution is finer than that adopted in Danis and Durbin (2022) for the same case.

A velocity-inlet boundary condition is applied at the inlet, prescribing a constant streamwise velocity of 1778.4 m/s, pressure of 1966.1 Pa, and temperature of 64.4 K. At the wall, a no-slip boundary condition is imposed along with a constant wall temperature of 300 K. A pressure far-field boundary condition is specified at the top boundary, with the pressure and temperature set to 1966.1 Pa and 64.4 K, matching their respective values at the inlet. At the outlet, a pressure-outlet boundary condition is used, prescribing the pressure to be equal to the free-stream pressure, and the backflow temperature is set to 300 K. Note that the free-stream temperature specified in the DNS is 66.5 K; here, we slightly reduce this value to account for the temperature jump across the oblique shockwave originating from the leading-edge, such that the post-shock temperature is approximately 66.5 K. (The pressure also changes across the shockwave; however, the ratio of its post-shock value to the wall value remains unchanged. In contrast, because the wall temperature is fixed, the corresponding ratio for temperature is affected. This, in turn, alters the density ratio and ultimately influences the computed skin friction and heat transfer coefficients in figure 7.10.) With these boundary conditions, we perform the simulations using Fluent's density based solver. Further details on the simulation setup (for instance, the case file) can be found on our GitHub repository (Hasan et al., 2024a).

To implement the proposed corrections in Fluent, we use user-defined functions (UDFs). In these UDFs, we compute the source terms Φ_k, Φ_ω and Φ_{CD} and add them on the right-hand-side of the conventional SST model as indicated in equations (7.31) and (7.32). We also redefine the eddy-viscosity as in equation (7.34). The reader is referred to our GitHub repository (Hasan et al., 2024a) for more details on the UDFs used to generate the results shown below.

To obtain the mean temperature profile, we solve the full energy equation:

$$\begin{aligned}\frac{\partial\left[\bar{\rho}(e+\widetilde{u}_i\widetilde{u}_i+k)\right]}{\partial t}+\frac{\partial\left[\bar{\rho}\widetilde{u}_j(h+\widetilde{u}_i\widetilde{u}_i+k)\right]}{\partial x_j}=&\frac{\partial}{\partial x_j}\left[\left(\frac{\bar{\mu}c_p}{Pr}+\frac{\mu_t c_p}{Pr_t}\right)\frac{\partial\bar{T}}{\partial x_j}\right]+\\&\frac{\partial}{\partial x_j}\left[\widetilde{u}_i\left(2\left(\bar{\mu}+\mu_t\right)\widetilde{S}_{ij}\right)\right]+\\&\underbrace{\frac{\partial}{\partial x_j}\left[\left(\bar{\mu}+\sigma_k\mu_t\right)\frac{\partial k}{\partial x_j}\right]+\Phi_k}_{\text{variable-property-corrected (section 7.2.1)}}\quad,\end{aligned}\tag{7.60}$$

where e and h are the internal energy and enthalpy per unit mass, and S_{ij} is the strain rate tensor. (Refer to section 7.5 for a discussion on the energy equation in the inner layer.) Adding Φ_k to the conventional equation implies that the viscous and turbulent diffusion of TKE are modeled after accounting for variable property effects, consistent with the diffusion term in the TKE transport equation (see section 7.2.1).

Note that in Fluent, TKE is not included in the definition of total energy, and its diffusion does not appear in the energy equation. Therefore, to correctly solve equation (7.60), it is necessary to add the TKE transport term $\bar{\rho}\,Dk/Dt$ to the left-hand side of the energy equation and the TKE diffusion term to the right-hand side. We achieve this in Fluent by introducing a source term on the right-hand side of the energy

equation, equal to the TKE diffusion term minus $\bar{\rho}\,Dk/Dt$. This term is effectively equal to $-P_k + \bar{\rho}\epsilon$, where P_k denotes the production of TKE. For further details, refer to the UDF provided in Hasan et al. (2024a).

In the inner layer, equation (7.60) reduces to equation (7.48). Interestingly, with k taken from the SST model, solving equation (7.60) in the inner layer is equivalent to solving equation (7.52) with $\Phi_e = \bar{\mu}(d\bar{u}/dy)^2 + \bar{\rho}\epsilon_{\text{sst}}$. However, as discussed above equation (7.56), solving such an equation in the inner layer would lead to inaccuracies in predicting the mean temperature, since ϵ_{sst} tends to zero at the wall, instead of a non-zero value. Thus, there, we proposed replacing ϵ_{sst} with ϵ_{eff} (7.56), or in other words, we proposed adding a source term, namely, $\bar{\rho}\epsilon_{\text{eff}} - \bar{\rho}\epsilon_{\text{sst}}$ to $\bar{\mu}(d\bar{u}/dy)^2 + \bar{\rho}\epsilon_{\text{sst}}$, such that effectively we arrive at $\Phi_{e,2}$ (7.57).

In the same spirit, to include the effects of ϵ_w in the two-dimensional solver, one needs to add a source term equal to $\bar{\rho}\epsilon_{\text{eff}} - \bar{\rho}\epsilon_{\text{sst}}$ on the right-hand-side of equation (7.60). However, including such a source term does not lead to any improvement in the temperature profile (not shown), unlike what one would expect based on the one-dimensional results, where including the effects of ϵ_w improved the temperature profiles (see gray solid lines in figure 7.2b). This is explained as follows: In the one-dimensional solver (7.52), the wall heat flux (first term on the right hand side) is fixed and provided as a boundary condition. Thus, any increase in Φ_e resulting from adding the source term $\bar{\rho}\epsilon_{\text{eff}} - \bar{\rho}\epsilon_{\text{sst}}$ would directly reduce the conductive heat flux, thereby reducing the temperature peak. Contrastingly, in the two-dimensional solver, the wall temperature is fixed, and the heat flux is allowed to vary. Now, since the integral of the added source term from the wall to the free-stream at a particular streamwise location is non-zero, it directly results in higher wall heat flux, rather than a lower conductive flux close to the wall. Thus, the temperature profile does not improve. Providing an accurate source term using the SST model, without erroneously adding to the wall heat flux, still remains unclear. Nevertheless, here, we provide the results using equation (7.60), i.e., without accounting for the influence of ϵ_w.

Figure 7.9 shows the mean velocity (left) and temperature (right) profiles for the $M_\infty = 10.9$ case described above. These profiles are extracted from the streamwise location where the friction Reynolds number matches the DNS value, i.e., $Re_\tau \approx 774$. The solid colored lines represent the DNS profiles, while the dotted gray lines depict the predictions from the conventional SST model. The solid gray lines show the results obtained using the corrected SST model equations (7.31) and (7.32), along with the modified eddy viscosity (7.34). The solid black lines correspond to the results obtained after solving the one-dimensional equations with the present inner-layer corrections and with $\Phi_e = \bar{\mu}(d\bar{u}/dy)^2 + \bar{\rho}\epsilon_{\text{sst}}$ (see section 7.6.1). This Φ_e is consistent with equation (7.60) in the inner layer, as discussed earlier.

As seen in figure 7.9, including the proposed corrections significantly improves the velocity profile compared to the one obtained with the baseline SST model (compare the dotted and solid gray lines). This improvement mainly originates from the inner-layer corrections. We confirmed this by setting Φ_k^{out}, Φ_ω^{out} and Φ_{CD} equal to zero in our simulations, such that we solve the baseline model in the outer layer. The resulting profiles were similar to those obtained when the outer-layer corrections were included. In contrast to the velocity, the temperature profiles remain largely unchanged.

Figure 7.9 also shows that, in the inner layer, the velocity and temperature profiles

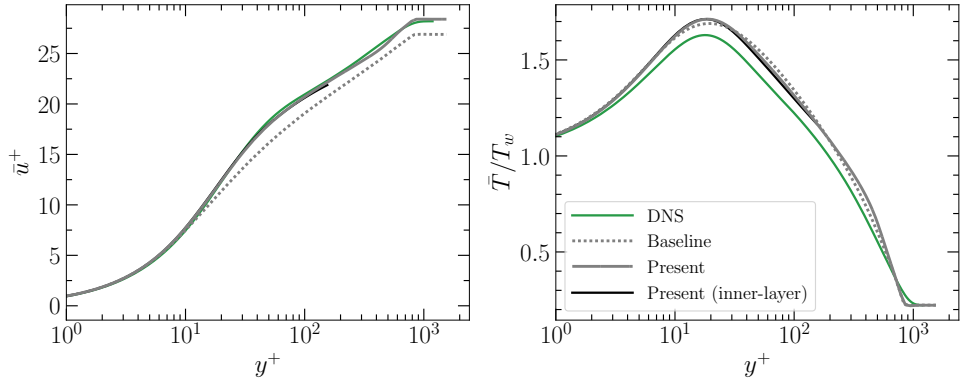

Figure 7.9: Computed full mean velocity (left) and temperature (right) profiles compared to the DNS (colored solid lines) for the following turbulent boundary layer: $M_\infty = 10.9$, $T_w/T_r = 0.2$ $Re_\tau = 774$ (Huang et al., 2022). Refer to the legend for line types. 'Baseline' represents the SST model without corrections, while 'Present' signifies the corrections proposed in this chapter (equations 7.29, 7.30, 7.28 and 7.35). Note that, in contrast with figure 7.2, where only the inner layer was solved, here both the baseline and present results are obtained by solving the entire boundary layer. Also note that these results are computed with (7.60) as the energy equation, except that for the baseline case $\Phi_k = 0$. The solid black lines correspond to the profiles obtained after solving the inner-layer equations (7.52) with $\Phi_e = \bar{\mu}(d\bar{u}/dy)^2 + \bar{\rho}\epsilon_{\text{sst}}$.

computed using Fluent (gray solid line) collapses well on to the respective profiles computed using the one-dimensional approach discussed earlier (black solid lines). Note that in Fluent, the molecular Prandtl number for air is close to 0.74, and the turbulent Prandtl number is assumed to be 0.85. Thus, to be consistent, the one-dimensional results are also computed with these Pr and Pr_t values.

Finally, in figure 7.10, we present the distribution of the skin-friction ($c_f = \tau_w/[0.5\rho_\infty U_\infty^2]$) and heat transfer ($c_h = q_w/[\rho_\infty U_\infty c_p(T_r - T_w)]$) coefficients along the plate, as a function of Re_τ. The filled symbols represent the DNS data of Huang et al. (2022), and the black vertical lines represent an error margin of +/-5%. Clearly, the c_f and c_h predictions obtained from the corrected SST model are closer to the DNS values than those obtained from the conventional model (compare the dotted and solid gray lines).

7.9. THE PROPOSED CORRECTIONS FOR THE SPALART-ALLMARAS (SA) MODEL

Before summarizing, we briefly report the variable-property and intrinsic compressibility corrections for the SA model (Spalart and Allmaras, 1992), and present only the main results for the inner layer of boundary layers.

Following the same approach as described in section 7.2.1 for the inner layer and in

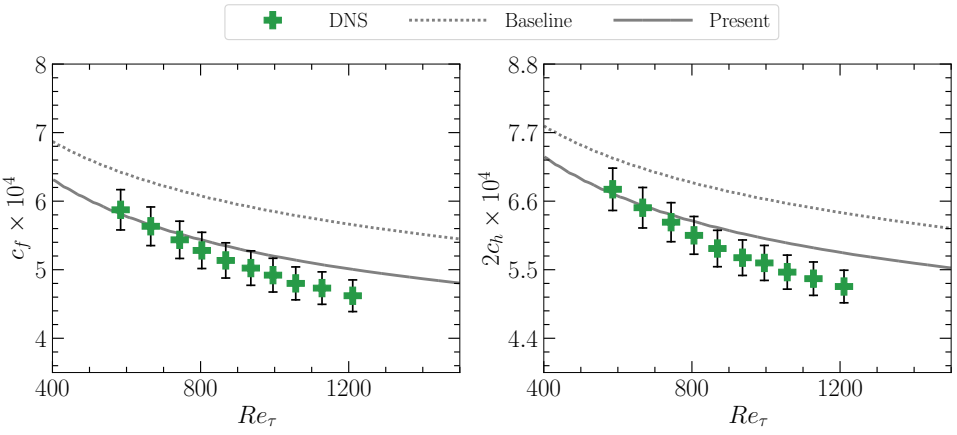

Figure 7.10: The skin-friction (left) and heat transfer coefficients (right) compared to the DNS (symbols) for the $M_\infty = 10.9$, $T_w/T_r = 0.2$ turbulent boundary layer of Huang et al. (2022). The dotted and solid gray lines correspond to the quantities obtained with the uncorrected and corrected SST models, respectively. The black vertical lines indicate an error margin of +/-5%. Note that in the right subfigure, the y-axis has been scaled by a factor of 1.1, corresponding to the assumed value of the ratio $2\,c_h/c_f$.

section 7.2.2 for the outer layer, but now applied to the SA model, we obtain

$$\Phi_{\check{\nu}}^{\text{in}} = \frac{c_{b2}}{c_{b3}}\left(\frac{S_y}{\sqrt{\bar{\rho}}}\frac{d(\bar{\rho}/\bar{\mu})\check{\nu}}{dy}\right)^2 - \frac{c_{b2}}{c_{b3}}\left(\frac{d\check{\nu}}{dy}\right)^2 + \frac{1}{c_{b3}}\frac{S_y}{\bar{\rho}}\frac{d}{dy}\left[\left(\frac{\bar{\mu}}{\bar{\rho}}+\check{\nu}\right)\frac{\bar{\rho}}{\bar{\mu}}S_y\frac{d(\bar{\rho}/\bar{\mu})\check{\nu}}{dy}\right] - \frac{1}{c_{b3}}\frac{d}{dy}\left[\left(\frac{\bar{\mu}}{\bar{\rho}}+\check{\nu}\right)\frac{d\check{\nu}}{dy}\right], \tag{7.61}$$

in the inner layer, and

$$\Phi_{\check{\nu}}^{\text{out}} = \frac{c_{b2}}{c_{b3}}\left(\frac{1}{\sqrt{\bar{\rho}}}\frac{d\sqrt{\bar{\rho}}\check{\nu}}{dy}\right)^2 - \frac{c_{b2}}{c_{b3}}\left(\frac{d\check{\nu}}{dy}\right)^2 + \frac{1}{c_{b3}}\frac{1}{\bar{\rho}}\frac{d}{dy}\left[\left(\frac{\bar{\mu}}{\bar{\rho}}+\check{\nu}\right)\sqrt{\bar{\rho}}\frac{d\sqrt{\bar{\rho}}\check{\nu}}{dy}\right] - \frac{1}{c_{b3}}\frac{d}{dy}\left[\left(\frac{\bar{\mu}}{\bar{\rho}}+\check{\nu}\right)\frac{d\check{\nu}}{dy}\right], \tag{7.62}$$

in the outer layer. $\Phi_{\check{\nu}}$ in these equations represents the source term that needs to be added to a conventional SA model for appropriate accounting of the variable-property effects, and c_{b2} and c_{b3} are the model constants. Note that the outer layer corrections are similar to the ones proposed in Catris and Aupoix (2000) and Otero Rodriguez et al. (2018). Also note that in these derivations we use $\check{\nu}^+ = \check{\nu}/(u_\tau \delta_v)$ and $\check{\nu}^* = \check{\nu}/(u_\tau^* \delta_v^*)$ in the inner layer, and $\check{\nu}^\oplus = \check{\nu}/(u_\tau \delta)$ and $\check{\nu}^\circledast = \check{\nu}/(u_\tau^* \delta)$ in the outer layer.

To account for intrinsic compressibility effects, similar to the SST model, we propose multiplying the eddy viscosity formulation with a damping function defined as

$$(D^{ic})_{\text{SA}} = \frac{D(R_t, M_t)}{D(R_t, 0)}, \tag{7.63}$$

with

$$D(R_t, M_t) = \left[1 - \exp\left(\frac{-R_t}{K + f(M_t)}\right)\right]^2, \tag{7.64}$$

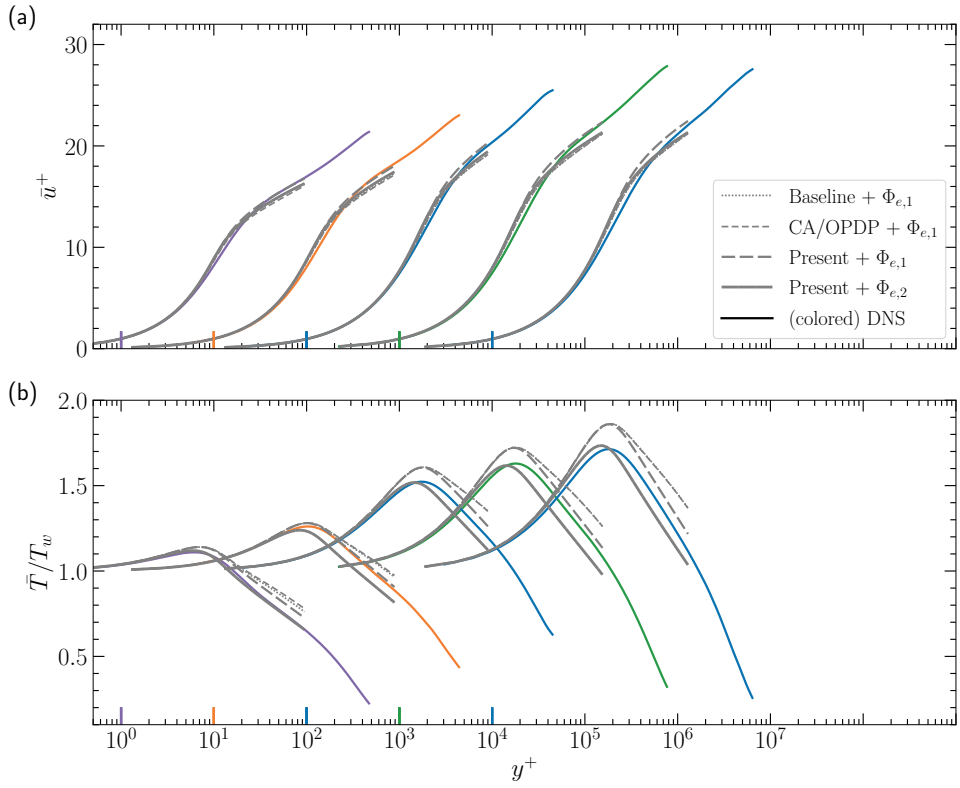

Figure 7.11: Computed mean velocity (a) and temperature (b) profiles compared to the DNS (colored solid lines) for the following boundary layers with increasing wall-cooling: (left to right) $M_\infty = 7.87$, $T_w/T_r = 0.48$ (A. Ceci, private communication); $M_\infty = 6$, $T_w/T_r = 0.35$ (Cogo et al., 2023); $M_\infty = 5.84$, $T_w/T_r = 0.25$ (Zhang et al., 2018); $M_\infty = 10.9$, $T_w/T_r = 0.2$ (Huang et al., 2022); $M_\infty = 13.64$, $T_w/T_r = 0.18$ (Zhang et al., 2018). Refer to the legend for line types. 'Baseline' stands for the SA model without corrections, 'CA/OPDP' stands for the compressibility corrections proposed in Catris and Aupoix (2000); Pecnik and Patel (2017); Otero Rodriguez et al. (2018), 'Present' stands for the corrections proposed in this chapter (equations 7.61 and 7.63). For clarity, the velocity and temperature profiles for different cases are shifted by one decade along the abscissa. The colored vertical lines on the abscissa signify $y^+ = 10^0$ for each case, with their colors matching the corresponding cases.

where $K = 7.5$, $f(M_t) = 7.3M_t$ (tuned following a similar procedure as described in section 7.4), $R_t = \check{\nu}/(\bar{\mu}/\bar{\rho})$, and $M_t = \sqrt{(1/0.3)\check{\nu} d\bar{u}/dy}/\bar{c}$ (Barone et al., 2024).

To depict the performance of the proposed corrections compared to the state-of-the-art approaches, we will present the results only for the inner layer of boundary layers. To obtain them we follow the implementation described in section 7.6.1 but now with μ_t obtained from the SA model. At the wall, we use $\check{\nu} = 0$, whereas at $y/\delta = 0.2$, we implement the mixing-length solution for $\check{\nu}$ as

$$\check{\nu} = u_\tau^* \kappa y \quad \text{at} \quad y = 0.2\delta. \tag{7.65}$$

Lastly, to produce results with a more accurate model for the source term ($\Phi_{e,2}$), we define the effective dissipation rate as in equation (7.56), but with ϵ_{SA} instead of ϵ_{sst}. To obtain the dissipation rate estimated by the SA model, we adapt the formulation proposed by Rahman et al. (2012), as

$$\epsilon_{\text{SA}} = \frac{(\mu_t d\bar{u}/dy)^2/a_1^2}{\bar{\mu} + \bar{\mu}_t/a_1^2}, \tag{7.66}$$

where $a_1 = 0.3$ is a constant which corresponds to the ratio of the turbulent shear stress and TKE in the log layer (Huang et al., 1994). As desired, ϵ_{SA} approaches $\mu_t(d\bar{u}/dy)^2$ in the logarithmic region and beyond. Refer the provided jupyter-notebook (Hasan et al., 2024a) for more details on the implementation of the SA model.

Figure 7.11 shows the (a) mean velocity and (b) temperature profiles for the five cases shown in figure 7.2. Different line types correspond to different modeling approximations, as discussed earlier in section 7.7.

Similar to the SST model, the results with the baseline model (without corrections) and those with the CA/OPDP (outer-layer, equation 7.62) corrections are nearly identical (compare the grey dotted and grey short-dashed lines; in some cases they overlap, making them difficult to distinguish). With these approaches, the mean velocity profiles are quite accurately estimated, whereas the temperature profiles are consistently over-estimated. The accuracy of $\bar{u}^+$ can be partially attributed to the semi-local consistency of the baseline model itself (see section 7.1). However, the high accuracy observed despite not accounting for intrinsic compressibility effects (7.63) is likely due to error cancellations resulting from the inaccuracies in the temperature profiles.

With the proposed corrections in equations (7.61) and (7.63) (long-dashed grey lines), both the temperature and velocity profiles show slight improvement, however, the temperature profiles remain over-estimated, particularly near the peak in strongly cooled boundary layers. The over-estimation of the peak temperature is eliminated, when $\Phi_{e,1}$ is replaced with $\Phi_{e,2}$ (solid grey lines). Despite this improvement, the temperature profiles with $\Phi_{e,2}$ appear to be shifted towards the wall compared to the DNS, resulting in an under-estimation beyond the peak location.

7.10. SUMMARY

We have presented a novel approach to derive compressibility corrections for turbulence models. Using this approach, we have derived variable-property corrections that take into account the different scaling characteristics of the inner and outer layers. In addition, we have formulated corrections that account for the change in near-wall

damping of turbulence due to intrinsic compressibility effects. We have also tested different approximations for the source terms in the energy equation, as well as the assumption of a constant turbulent Prandtl number (Pr_t). Our findings, based on the k-ω SST model, are summarized below.

The proposed corrections when compared with the baseline model (with no corrections) and with the state-of-the-art CA/OPDP corrections (Catris and Aupoix, 2000; Pecnik and Patel, 2017; Otero Rodriguez et al., 2018) produce significantly more accurate results for both turbulent boundary layers and channel flows.

In the context of temperature prediction, we highlighted the importance of accurately modeling the source term in the energy equation. When combined with the proposed compressibility corrections, these source terms substantially improve the accuracy of the peak temperature in cooled-wall turbulent boundary layers.

Another key factor in temperature prediction is the turbulent Prandtl number (Pr_t). By comparing two temperature profile predictions – one using a constant Pr_t of 0.9 and the other using a Pr_t distribution obtained from existing DNS data – we find the results to be nearly identical (tested for a $M_\infty = 6$ and $M_\infty = 14$ boundary layer). This suggests that a constant Pr_t of 0.9 is a reasonable approximation, contradicting previous studies that identify the inaccuracies in the turbulent Prandtl number to be the primary source of error.

Finally, we tested the proposed inner- and outer-layer corrections across the entire boundary layer using Ansys Fluent. Compared to the baseline model, the corrections significantly improve the accuracy of the mean velocity profile. However, the temperature profile remains largely unchanged. Moreover, the corrections also improve the accuracy of the predicted skin friction and heat transfer coefficients.

We recommend the following for future studies. (1) The formulation of the corrections in cases where the wall-normal direction does not align with the coordinate axis (see Appendix C) should be tested. (2) The performance of the proposed variable-property corrections should be tested in flows involving complex geometries, especially where the determination of the wall-normal direction is challenging (e.g. flows near corners). (3) Also, the efficacy of the damping function (7.35) in more complex flow configurations must be tested. (4) The possibility of adding an external heat source term to the full energy equation (7.60), without erroneously adding to the wall heat flux, must be explored. (5) Using the same approach as presented in this chapter for the SST model, the compressibility corrections for other turbulence models should be derived and tested. In section 7.9, we present and test the corrections for the Spalart-Allmaras (SA) model. (6) For the SA model, improved alternatives for the TKE dissipation rate are needed to achieve even more accurate temperature profile predictions. It should also be tested whether such alternatives could improve temperature predictions using mixing-length models, for example in wall-modeled large eddy simulations (WMLES). (7) The influence of including Φ_k in the energy equation (7.60) should be explored using a turbulence model which predicts non-zero TKE diffusion and dissipation values at the wall (e.g. v^2-f model (Durbin, 1991)).

8

CONCLUSION

In this thesis, we have devised four DNS cases of fully developed high-Mach-number channel flows with approximately constant mean properties (CP), whereby intrinsic compressibility effects are isolated. Based on these cases, we attempt to provide an explanation for the underlying mechanism through which intrinsic compressibility effects modulate the near-wall dynamics of turbulence. Building on this, we propose several scaling laws and turbulence model corrections which have been tested across a wide range of channel flow and boundary layer cases reported in the literature. Our key findings are as follows.

Part I: Theory

- The mean velocity profiles of the CP cases depict an upward log-law shift attributable to IC effects. This log-law shift can be primarily linked to an outward shift (or reduction) in the turbulent shear stress. This outward shift corresponds to a similar shift in the wall-normal Reynolds stress, as wall-normal motions drive momentum transport across mean shear, thereby generating turbulent shear stress. This shift in the wall-normal stress stems from reduced energy transfer from the streamwise to the other components, indicating **weakening of the quasi-streamwise vortices** that facilitate this transfer (Jeong et al., 1997) (chapter 3).

- To explain the weakening of quasi-streamwise vortices, we have decomposed the velocity field into solenoidal and dilatational parts and educed shear layers by applying conditional averaging (variable-interval space averaging) to the solenoidal field. We have noticed a streamwise phase shift between the buffer-layer sweeps and ejections that form shear layers, and the associated 'solenoidal' wall pressure. By invoking Taylor's hypothesis, this streamwise phase shift can be interpreted as a phase shift in time, such that regions of high positive (or negative) rate of change of wall pressure correspond to regions of high positive (or negative) wall-normal velocity, suggesting that the two are in-phase. Moreover, close to the wall, the high rate of change of solenoidal pressure leads to large dilatation values (also referred to as pseudo-sound dilatation) of opposite sign, such that they are out-of-phase. From these observations, it follows that the near-wall dilatation is essentially out-of-phase with respect to the wall-normal motions, or in other words, **the near-wall expansions and contractions of the fluid inherently oppose the buffer-layer sweeps and ejections**. Since these coherent motions are initiated by quasi-streamwise vortices, their opposition directly affects the evolution of those vortices, causing their weakening. This is schematically depicted in figure 3.13 (chapter 3).

- The remaining portion of dilatation (also referred to as the non-pseudo-sound component) does not play an important role in this opposition mechanism. Interestingly, the majority of the **travelling wave-packet-like structures**, recently discovered in the literature, are present in the non-pseudo-sound component of dilatation (chapter 3).

- The intrinsic-compressibility-induced outward shift in the turbulent shear stress is also responsible for **higher peak values of the streamwise Reynolds stress** in

compressible flows compared to incompressible flows (chapter 3).

Part II: Scaling laws and predictive models

- By expressing the streamwise Reynolds stress in the form of an expansion series in terms of M_τ, we proposed **a scaling relation for its peak value**. A similar scaling relation was also developed for the wall-pressure root-mean-square. In these relations, the leading order term accounts for Reynolds number and variable-property effects, and is modeled using incompressible relations but with an effective Reynolds number. For the peak streamwise intensity, the effective Reynolds number is the conventional friction Reynolds number, while for wall pressure, it is the semi-local friction Reynolds number defined using buffer-layer mean properties. Higher order terms capture intrinsic compressibility effects and are modeled as constant coefficients, calibrated based on the CP cases. These scaling relations demonstrate high accuracy, with predictions for the majority of the cases falling within a +/-10% error margin (chapter 4).

- The log-law shift observed in the semi-local transformation for high-speed flows is also caused by intrinsic compressibility effects. Taking friction Mach number M_τ as the most suitable parameter to quantify these effects, we propose **a transformation that effectively removes the log-law shift**. This transformation accounts for the changes in friction velocity and viscous length scales due to variations in mean properties, and for intrinsic compressibility effects. Thus, it applies to a wide variety of cases (chapter 5).

- We have derived an expression for the mean-velocity gradient in high-speed zero-pressure-gradient boundary layers that uses **distinct mean velocity scalings in the inner (proposed) and outer (Van Driest) layers**, thus covering the entire boundary layer. Using this expression we accurately predict mean velocity and temperature profiles, leading to estimation of the skin-friction and heat-transfer coefficients which are within $+/-4\%$ and $+/-8\%$ of the DNS data (chapter 6).

- We have presented a **novel approach to derive compressibility corrections** for RANS turbulence models, which are consistent with the proposed transformation in the inner layer and the Van Driest transformation in the outer layer. The proposed corrections produce significantly more accurate results for both turbulent boundary layers and channel flows, when compared to the state-of-the-art approaches (chapter 7).

- In the context of temperature predictions, we highlighted the importance of **accurately modeling the source term in the energy equation**. When combined with the proposed compressibility corrections, these source terms substantially improve the accuracy of the peak temperature in cooled-wall turbulent boundary layers (chapter 7).

- By comparing two temperature profile predictions – one using a constant turbulent Prandtl number Pr_t of 0.9 and the other using a Pr_t distribution obtained from existing DNS data – we find the results to be nearly identical. This suggests that a constant **turbulent Prandtl number of 0.9 is a reasonable approximation**,

contradicting previous studies that identify the inaccuracies in Pr_t to be the primary source of error (chapter 7).

8.1. FUTURE RECOMMENDATIONS

In the following, we list some recommendations for future work. We also discuss potential solutions where applicable.

8.1.1. COUPLING BETWEEN VARIABLE-PROPERTY AND IC EFFECTS

In chapter 4, we assumed the coupling between variable-property and intrinsic compressibility effects to be small while developing scaling laws for wall-pressure r.m.s. and the peak streamwise turbulence intensity. There, we calibrated the variable property contribution to the scaling laws using the low-Mach cases of Modesti and Pirozzoli (2024)—where IC effects are negligible—and the IC contribution using the CP cases—where variable-property effects are negligible. Then, assuming small coupling effects, we tested the developed scaling relations in flows where both of these effects were simultaneously present.

We followed a similar recipe in chapter 5, where we calibrated the increase in the log-law intercept with the friction Mach number using the CP cases (figure 5.1a), and then tested the calibration in flows where both variable-property and IC effects were present, assuming small coupling effects.

In high-Mach-number flows with strong heat transfer, these coupling effects may grow important, which should be tested in future studies. To isolate and study these effects, one can follow the approach suggested by Lele (1994), which involves contrasting a high-Mach-number simulation with a low-Mach-number counterpart that shares the same Reynolds number and mean property profiles as the high-Mach case. The algorithm described in section 2.2 can be utilised to simulate such a low-Mach-number flow.

8.1.2. COUPLING BETWEEN REYNOLDS NUMBER AND IC EFFECTS

In chapter 4, we also assumed the coupling between Reynolds number and intrinsic compressibility effects to be small while developing scaling laws for wall-pressure r.m.s. and the peak streamwise turbulence intensity. However, the cases that were used to verify this assumption were at low-to-moderate Reynolds numbers. Whether a similar assumption would hold at high Reynolds numbers is unknown. Moreover, how the opposition mechanism discussed in chapter 3 gets affected at high Reynolds numbers remains an open question. In future, simulations of constant-property high-Mach-number channel flows at a range of Reynolds numbers should be conducted to study any potential influences of Reynolds number on IC effects.

8.1.3. VARIABLE-PROPERTY EFFECTS BEYOND SEMI-LOCAL SCALING

Throughout this thesis, we adhered to semi-local scaling to account for variable-property effects, which advocates that these effects primarily influence the definiton of viscous length (δ_ν^*) and friction velocity (u_τ^*) scales (1.12). However, this framework implicitly assumes that the fractional change in u_τ^* and δ_ν^* across an eddy (or in other words, the fractional change in density and viscosity across an eddy) is negligible. A similar

assumption is implied under Morkovin's hypothesis (Bradshaw, 1977). To understand the implications when such fractional changes become important, we refer to the analysis in Pecnik and Patel (2017).

Those authors scaled the continuity and momentum equations using u_τ^* and outer-layer length scale h (channel half-height), and then consequently derived a semi-locally scaled TKE equation. That equation had terms analogous to an incompressible TKE equation, plus some additional terms that depend on the mean density gradient $d\bar{\rho}/dy$, which arose as a consequence of moving u_τ^* across wall-normal derivatives (d/dy). Particularly, those terms depend on the factor

$$d_y = \frac{h}{2\bar{\rho}}\frac{d\bar{\rho}}{dy},$$

which can be written in terms of u_τ^* as

$$d_y = -\frac{h}{u_\tau^*}\frac{du_\tau^*}{dy}.$$

Here, d_y can also be inferred as the fractional change of u_τ^* across an eddy of width h (outer-layer length scale).

In the inner layer, if one repeats the same analysis as Pecnik and Patel (2017) but using the inner-layer length scale δ_ν^*, instead of h (and neglecting advection terms), then one would arrive at a TKE equation that is analogous to incompressible flows, plus additional terms that depend on factors such as

$$\frac{y}{\delta_\nu^*}\frac{d\delta_\nu^*}{dy}, \qquad \frac{\delta_\nu^*}{u_\tau^*}\frac{du_\tau^*}{dy}.$$

The first factor signifies the fractional change in δ_ν^* across an eddy of width y[1], whereas the second term signifies the fractional change in u_τ^* across an eddy of width δ_ν^*. When the fractional changes in these quantities across eddies become important, the additional terms in the TKE equation that depend on them may also become important, thereby weakening the analogy between incompressible and compressible TKE equations in the inner layer (an assumption invoked in chapter 7). Such a breakdown of analogy between incompressible and compressible flows highlights a failure of semi-local scaling.

These effects that depend on the fractional changes of δ_ν^* and u_τ^* can become important in flows with very strong heat transfer at the walls (such as those at very high Mach numbers), or in non-ideal flows close to the Widom line, where the thermophysical properties change tremendously. In fact, some effects observed in moderately cooled flows can also be attributed to such fractional changes that are beyond the scope of semi-local scaling. For instance, the apparent spread in the log-law constant discussed in chapter 5 and in Appendix B, and the spread in the streamwise velocity peak reported in figure 4.1.

Future studies should focus on studying these effects in more detail, for instance, by analyzing the full semi-locally scaled TKE equation with the additional terms. Such an analysis may shed light on which parameter best describes such fractional-change effects, whose knowledge can then be accounted semi-empirically in the eddy-viscosity formulations to propose even better velocity transformations (see Appendix B).

[1]Note that this factor is also seen in the velocity transformation kernel (5.12).

8.1.4. EFFECT OF PRESSURE GRADIENT

Throughout this thesis, the focus has been on equilibrium flows, such as channel flows and zero-pressure-gradient boundary layers. However, certain aspects of the proposed scaling laws and turbulence models are expected to be influenced under non-equilibrium conditions. For instance, it is well-known from the literature that adverse pressure gradients strongly modify the wake region in incompressible flows (Coles, 1956; Monty et al., 2011). In the present context, this suggests that Π in equation (6.7) varies not only with the Reynolds number but also with the imposed pressure gradient.

In the future, it would be interesting to investigate other such influences of non-zero pressure gradients in compressible flows, for instance, the role of 'history effects' (Bobke et al., 2017; Chen et al., 2025).

Apart from these more general recommendations, we refer the reader to some specific recommendations provided in the summary section of chapters 3–7.

A

HELMHOLTZ DECOMPOSITION OF THE VELOCITY FIELD

The Helmholtz decomposition in compressible flows is the representation of the velocity field as the sum of divergence-free 'solenoidal' and curl-free 'dilatational' components. This is mathematically written as

$$u_i = u_i^s + u_i^d, \tag{A.1}$$

where superscripts 's' and 'd' stand for solenoidal and dilatational components. This equation is similar to equation (3.10) in the main text, the only difference being that there the decomposition was written explicitly for the fluctuating velocity field.

The dilatational component is computed as the gradient of a scalar potential ϕ, namely

$$u_i^d = \frac{\partial \phi}{\partial x_i}, \tag{A.2}$$

where ϕ is obtained by solving a Poisson equation as

$$\frac{\partial^2 \phi}{\partial x_j \partial x_j} = \frac{\partial u_i}{\partial x_i}. \tag{A.3}$$

Equation (A.3) is solved using a second-order accurate FFT-based Poisson solver (see Costa (2018) for example) with periodic boundary conditions in the streamwise and spanwise directions, and no-penetration boundary condition $\partial\phi/\partial y = 0$ (or $v^d = 0$) at the wall. Note that with these boundary conditions, no-slip is not satisfied at the wall, that is u^d and w^d are not equal to zero. While seemingly counter-intuitive at first glance, this is not unphysical, as pointed out in Sharma and Girimaji (2023).

Likewise, the solenoidal component can be obtained using the vorticity field as described in Yu et al. (2019) and Sharma and Girimaji (2023). However, here we will make use of the fact that the total velocity field is available from the direct numerical simulation. Thus, the solenoidal field is simply computed using equation (A.1) as

$$u_i^s = u_i - u_i^d. \tag{A.4}$$

B

UNACCOUNTED VARIABLE-PROPERTY EFFECTS ON THE MEAN VELOCITY PROFILES

Let us rewrite the transformation kernel derived in chapter 5 (equation 5.12) as

$$\frac{d\bar{U}^+}{d\bar{u}^+} = \underbrace{\left(\frac{1+\mu_t^c/\bar{\mu}}{1+\mu_t^i/\mu_w}\right)}_{3}\underbrace{\left(1-\frac{y}{\delta_v^*}\frac{d\delta_v^*}{dy}\right)}_{2}\underbrace{\frac{u_\tau}{u_\tau^*}}_{1}. \tag{B.1}$$

There, we assumed that variable-property effects are confined to factors 1 and 2 in equation (B.1), and that they do not influence the non-universality of the turbulent shear stress (i.e., factor 3 in equation B.1), which is attributed solely to IC effects. Based on this assumption, we modeled the non-universality of the eddy-viscosity in (B.1) only as a function of the friction Mach number M_τ as

$$\frac{d\bar{U}^+}{d\bar{u}^+} = \left(\frac{1+\kappa y^* D(y^*,M_\tau)}{1+\kappa y^* D(y^*,0)}\right)\left(1-\frac{y}{\delta_v^*}\frac{d\delta_v^*}{dy}\right)\frac{u_\tau}{u_\tau^*}, \tag{B.2}$$

where

$$D(y^*,M_\tau) = \left[1-\exp\left(\frac{-y^*}{A^+ + 19.3\,M_\tau}\right)\right]^2.$$

The validity of this assumption can be assessed from figure B.1, which shows the log-law constant resulting from the proposed transformation (referred to as 'HLPP' as in the literature) for the low-Mach-number variable-property cases of Modesti and Pirozzoli (2024) and the compressible channel flow cases of Trettel and Larsson (2016) (low-Reynolds-number cases are excluded); see table 2.3.

Let us first focus on the low-Mach-number cases, for which the friction Mach number is approximately zero, such that the proposed and the semi-local transformations are equivalent, i.e., factor $3 \approx 1$. As shown in figure B.1, the log-law constant for these cases is not universal; instead, it depicts a clear dependence on the temperature profile, particularly on the centreline-to-wall temperature ratio (T_c/T_w). This observation implies that factors 1 and 2 do not fully account for variable-property effects, and that the turbulent shear stress is non-universal even in flows where IC effects are absent. This influence of variable mean properties, not captured by factors 1 and 2, are referred to as 'unaccounted' variable property effects.

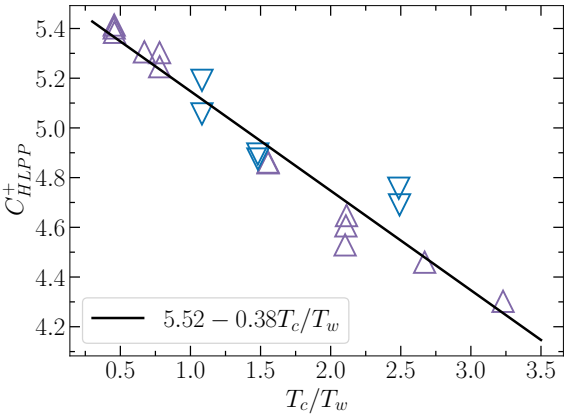

Figure B.1: The log-law constant resulting from the proposed transformation for the low-Mach-number variable-property channel flow cases of Modesti and Pirozzoli (2024) (triangles), and the compressible channel flow cases of Trettel and Larsson (2016) (inverted triangles). The computed constants are plotted as a function of the centreline-to-wall temperature ratio T_c/T_w. Note that low-Reynolds-number cases (i.e., the cases where the semi-local Reynolds number Re^*_τ falls below 300 anywhere in the domain) are excluded.

A similar trend with T_c/T_w is also observed for the compressible cases of Trettel and Larsson (2016). The fact that the these cases, upon accounting for intrinsic compressibility effects under the proposed transformation, also depict a similar trend as the low-Mach cases suggests that they are also affected by unaccounted variable-property effects. In fact, we hypothesize that the cancellation between these unaccounted effects—which induce a downward shift in the log-law constant—and IC effects—that cause an upward shift—is the reason why the semi-local transformation depcited a net zero shift in the log-law constant for those cases (see Trettel and Larsson (2016)).

In future, a more universal transformation would require that these unaccounted variable-property effects are somehow accounted for in the eddy-viscosity definition, for instance, by modifying the damping constant A^+ to be a function of a parameter that adequately gauges these effects. Note that T_c/T_w was used here primarily to show a trend for ideal gas air-like cases with monotonic temperature profiles. However, a better parameter which gauges these effects over a wide range of cases would be something that is defined in terms of the gradients of u^*_τ and δ^*_ν (see also the discussion in section 8.1.3).

C

FORMULATION OF THE COMPRESSIBILITY CORRECTIONS IN A GENERAL COORDINATE SYSTEM

In section 7.2, we derived the corrections for the case in which the wall-normal direction was aligned with the y-axis. For arbitrary wall orientations, the source terms must be modified. In such flows, we need to include the following source term in the inner layer:

$$\Phi_k^{\text{in}} = \frac{S_n}{\bar{\mu}} \frac{\partial}{\partial n} \left[\mu_{\text{eff}} \frac{S_n}{\bar{\mu}} \frac{\partial(\bar{\rho} k)}{\partial n} \right] - \frac{\partial}{\partial n} \left[\mu_{\text{eff}} \frac{\partial k}{\partial n} \right], \tag{C.1}$$

where n is the wall-normal coordinate and $\mu_{\text{eff}} = \bar{\mu} + \sigma_k \mu_t$, and where

$$S_n = \left(\frac{\partial \left(\ell \sqrt{\bar{\rho}} / \bar{\mu} \right)}{\partial n} \right)^{-1} = \left(\frac{\sqrt{\bar{\rho}}}{\bar{\mu}} + \ell \frac{\partial \left(\sqrt{\bar{\rho}} / \bar{\mu} \right)}{\partial n} \right)^{-1}. \tag{C.2}$$

To further simplify this term, we note that the conventional diffusion term is coordinate independent. For a two-dimensional system, this implies that

$$\frac{\partial}{\partial n} \left[\mu_{\text{eff}} \frac{\partial k}{\partial n} \right] + \frac{\partial}{\partial t} \left[\mu_{\text{eff}} \frac{\partial k}{\partial t} \right] = \frac{\partial}{\partial x} \left[\mu_{\text{eff}} \frac{\partial k}{\partial x} \right] + \frac{\partial}{\partial y} \left[\mu_{\text{eff}} \frac{\partial k}{\partial y} \right], \tag{C.3}$$

where t is the wall-parallel direction, and where x and y are the generic cartesian coordinates. Close to the wall, the diffusion term is mainly dominated by the wall-normal component. Thus, one could neglect the second term on the left-hand side to get

$$\frac{\partial}{\partial n} \left[\mu_{\text{eff}} \frac{\partial k}{\partial n} \right] \approx \frac{\partial}{\partial x_j} \left[\mu_{\text{eff}} \frac{\partial k}{\partial x_j} \right]. \tag{C.4}$$

Similarly, we can write

$$\frac{\partial}{\partial n} \left[\mu_{\text{eff}} \frac{S_n}{\bar{\mu}} \frac{\partial(\bar{\rho} k)}{\partial n} \right] \approx \frac{\partial}{\partial x_j} \left[\mu_{\text{eff}} \frac{S_n}{\bar{\mu}} \frac{\partial(\bar{\rho} k)}{\partial x_j} \right], \tag{C.5}$$

where $\mu_{\text{eff}} S_n / \bar{\mu}$ is the total diffusion coefficient, and $\bar{\rho} k$ is the diffused quantity.

Replacing the wall normal diffusion terms in equation (C.1) using equations (C.4) and (C.5), we get

$$\Phi_k^{\text{in}} = \frac{S_n}{\bar{\mu}} \frac{\partial}{\partial x_j} \left[\mu_{\text{eff}} \frac{S_n}{\bar{\mu}} \frac{\partial(\bar{\rho} k)}{\partial x_j} \right] - \frac{\partial}{\partial x_j} \left[\mu_{\text{eff}} \frac{\partial k}{\partial x_j} \right], \tag{C.6}$$

where S_n can be expressed using the general coordinate system as

$$S_n = \left(\frac{\sqrt{\bar{\rho}}}{\bar{\mu}} + \ell \, n_j \frac{\partial \left(\sqrt{\bar{\rho}} / \bar{\mu} \right)}{\partial x_j} \right)^{-1}, \tag{C.7}$$

where n_j represents a unit vector in the wall-normal direction. One could follow a similar approach to derive Φ_ω^{in}.

In the outer layer, we propose applying the corrections equivalently in all the directions. For instance,

$$\Phi_k^{\text{out}} = \frac{1}{\sqrt{\bar{\rho}}} \frac{\partial}{\partial x_j} \left[\mu_{\text{eff}} \frac{1}{\sqrt{\bar{\rho}}} \frac{\partial(\bar{\rho} k)}{\partial x_j} \right] - \frac{\partial}{\partial x_j} \left[\mu_{\text{eff}} \frac{\partial k}{\partial x_j} \right], \tag{C.8}$$

and similarly for Φ_ω^{out} and Φ_{CD}.

BIBLIOGRAPHY

Aupoix, B. (2004). Modelling of compressibility effects in mixing layers. *Journal of Turbulence*, 5(1):007.

Bai, T., Griffin, K. P., and Fu, L. (2022). Compressible velocity transformations for various noncanonical wall-bounded turbulent flows. *AIAA Journal*, pages 1–13.

Barone, M. F., Parish, E., and Jordan, C. (2024). Data-driven modifications to the spalart-allmaras turbulence model for supersonic and hypersonic boundary layers. In *AIAA SCITECH 2024 Forum*, page 0071.

Beresh, S. J., Henfling, J. F., Spillers, R. W., and Pruett, B. O. (2011). Fluctuating wall pressures measured beneath a supersonic turbulent boundary layer. *Physics of Fluids*, 23(7).

Bernardini, M., Modesti, D., Salvadore, F., and Pirozzoli, S. (2021). STREAmS: A high-fidelity accelerated solver for direct numerical simulation of compressible turbulent flows. *Computer Physics Communications*, 263:107906.

Bernardini, M. and Pirozzoli, S. (2011). Wall pressure fluctuations beneath supersonic turbulent boundary layers. *Physics of Fluids*, 23(8):085102.

Blackwelder, R. and Kaplan, R. (1976). On the wall structure of the turbulent boundary layer. *Journal of Fluid Mechanics*, 76(1):89–112.

Bobke, A., Vinuesa, R., Örlü, R., and Schlatter, P. (2017). History effects and near equilibrium in adverse-pressure-gradient turbulent boundary layers. *Journal of Fluid Mechanics*, 820:667–692.

Bose, S. T. and Park, G. I. (2018). Wall-modeled large-eddy simulation for complex turbulent flows. *Annual Review of Fluid Mechanics*, 50(1):535–561.

Bradshaw, P. (1967). 'inactive'motion and pressure fluctuations in turbulent boundary layers. *Journal of Fluid Mechanics*, 30(2):241–258.

Bradshaw, P. (1977). Compressible turbulent shear layers. *Annual Review of Fluid Mechanics*, 9(1):33–52.

Bradshaw, P. and Huang, G. P. (1995). The law of the wall in turbulent flow. *Proceedings of the Royal Society of London. Series A: Mathematical and Physical Sciences*, 451(1941):165–188.

Bradshaw, P. and Koh, Y. (1981). A note on Poisson's equation for pressure in a turbulent flow. *The Physics of Fluids*, 24(4):777–777.

Bull, M. (1996). Wall-pressure fluctuations beneath turbulent boundary layers: some reflections on forty years of research. *Journal of Sound and Vibration*, 190(3):299–315.

Candler, G. V. (2019). Rate effects in hypersonic flows. *Annual Review of Fluid Mechanics*, 51(1):379–402.

Catris, S. and Aupoix, B. (2000). Density corrections for turbulence models. *Aerospace Science and Technology*, 4(1):1–11.

Cebeci, T. and Smith, A. M. O. (1974). *Analysis of turbulent boundary layers*. Elsevier.

Ceci, A., Palumbo, A., Larsson, J., and Pirozzoli, S. (2022). Numerical tripping of high-speed turbulent boundary layers. *Theoretical and Computational Fluid Dynamics*, 36(6):865–886.

Chauhan, K., Nagib, H., and Monkewitz, P. (2007). On the composite logarithmic profile in zero pressure gradient turbulent boundary layers. In *45th AIAA Aerospace Sciences Meeting and Exhibit*, page 532.

Chen, P. E., Zhang, W., Wan, M., Yang, X. I., Shi, Y., and Chen, S. (2025). A log-layer analogy for fluid acceleration in the inner layer of wall-bounded turbulence with pressure gradients. *Journal of Fluid Mechanics*, 1010:A13.

Chen, X., Gan, J., and Fu, L. (2024). An improved Baldwin–Lomax algebraic wall model for high-speed canonical turbulent boundary layers using established scalings. *Journal of Fluid Mechanics*, 987:A7.

Chen, X. and Sreenivasan, K. R. (2021). Reynolds number scaling of the peak turbulence intensity in wall flows. *Journal of Fluid Mechanics*, 908:R3.

Chen, X. and Sreenivasan, K. R. (2022). Law of bounded dissipation and its consequences in turbulent wall flows. *Journal of Fluid Mechanics*, 933.

Cheng, C. and Fu, L. (2024). Mean temperature scalings in compressible wall turbulence. *Physical Review Fluids*, 9:054610.

Choi, H., Moin, P., and Kim, J. (1994). Active turbulence control for drag reduction in wall-bounded flows. *Journal of Fluid Mechanics*, 262:75–110.

Cogo, M., Baù, U., Chinappi, M., Bernardini, M., and Picano, F. (2023). Assessment of heat transfer and Mach number effects on high-speed turbulent boundary layers. *Journal of Fluid Mechanics*, 974:A10.

Cogo, M., Salvadore, F., Picano, F., and Bernardini, M. (2022). Direct numerical simulation of supersonic and hypersonic turbulent boundary layers at moderate-high Reynolds numbers and isothermal wall condition. *Journal of Fluid Mechanics*, 945:A30.

Coleman, G. N., Kim, J., and Moser, R. D. (1995). A numerical study of turbulent supersonic isothermal-wall channel flow. *Journal of Fluid Mechanics*, 305:159–183.

Coles, D. (1956). The law of the wake in the turbulent boundary layer. *Journal of Fluid Mechanics*, 1(2):191–226.

Coles, D. (1962). The turbulent boundary layer in a compressible fluid. Technical report, RAND Corp., R-403-PR.

Colonna, P., Casati, E., Trapp, C., Mathijssen, T., Larjola, J., Turunen-Saaresti, T., and Uusitalo, A. (2015). Organic Rankine cycle power systems: from the concept to current technology, applications, and an outlook to the future. *Journal of Engineering for Gas Turbines and Power*, 137(10):100801.

Costa, P. (2018). A FFT-based finite-difference solver for massively-parallel direct numerical simulations of turbulent flows. *Computers & Mathematics with Applications*, 76(8):1853–1862.

Danberg, J. E. (1964). *Characteristics of the turbulent boundary layer with heat and mass transfer at M= 6.7*. PhD thesis, Catholic University of America.

Danis, M. E. and Durbin, P. (2022). Compressibility correction to k-ω models for hypersonic turbulent boundary layers. *AIAA Journal*, 60(11):6225–6234.

Deshpande, R., Monty, J. P., and Marusic, I. (2021). Active and inactive components of the streamwise velocity in wall-bounded turbulence. *Journal of Fluid Mechanics*, 914:A5.

Duan, L., Beekman, I., and Martin, M. (2010). Direct numerical simulation of hypersonic turbulent boundary layers. Part 2. Effect of wall temperature. *Journal of Fluid Mechanics*, 655:419–445.

Duan, L., Beekman, I., and Martin, M. (2011). Direct numerical simulation of hypersonic turbulent boundary layers. Part 3. Effect of Mach number. *Journal of Fluid Mechanics*, 672:245–267.

Duan, L., Choudhari, M. M., and Zhang, C. (2016). Pressure fluctuations induced by a hypersonic turbulent boundary layer. *Journal of Fluid Mechanics*, 804:578–607.

Durbin, P. A. (1991). Near-wall turbulence closure modeling without "damping functions". *Theoretical and Computational Fluid Dynamics*, 3(1):1–13.

Edquist, K. T., Hollis, B. R., Dyakonov, A. A., Laub, B., Wright, M. J., Rivellini, T. P., Slimko, E. M., and Willcockson, W. H. (2007). Mars science laboratory entry capsule aerothermodynamics and thermal protection system. In *2007 IEEE Aerospace Conference*, pages 1–13. IEEE.

Fernholz, H. and Finley, P. (1996). The incompressible zero-pressure-gradient turbulent boundary layer: an assessment of the data. *Progress in Aerospace Sciences*, 32(4):245–311.

Fernholz, H.-H. and Finley, P. (1980). A critical commentary on mean flow data for two-dimensional compressible turbulent boundary layers. Technical report, AGARD-AG-253.

Foysi, H., Sarkar, S., and Friedrich, R. (2004). Compressibility effects and turbulence scalings in supersonic channel flow. *Journal of Fluid Mechanics*, 509:207–216.

Gatski, T. and Erlebacher, G. (2002). Numerical simulation of a spatially evolving supersonic turbulent boundary layer. Technical report.

Gatski, T. B. and Bonnet, J.-P. (2013). *Compressibility, turbulence and high speed flow*. Academic Press.

Gerolymos, G. and Vallet, I. (2023). Scaling of pressure fluctuations in compressible turbulent plane channel flow. *Journal of Fluid Mechanics*, 958:A19.

Goc, K. A., Lehmkuhl, O., Park, G. I., Bose, S. T., and Moin, P. (2021). Large eddy simulation of aircraft at affordable cost: a milestone in computational fluid dynamics. *Flow*, 1:E14.

Griffin, K. P., Fu, L., and Moin, P. (2021). Velocity transformation for compressible wall-bounded turbulent flows with and without heat transfer. *Proceedings of the National Academy of Sciences*, 118(34):e2111144118.

Griffin, K. P., Fu, L., and Moin, P. (2023). Near-wall model for compressible turbulent boundary layers based on an inverse velocity transformation. *Journal of Fluid Mechanics*, 970:A36.

Guarini, S. E., Moser, R. D., Shariff, K., and Wray, A. (2000). Direct numerical simulation of a supersonic turbulent boundary layer at Mach 2.5. *Journal of Fluid Mechanics*, 414:1–33.

Hasan, A. M., Costa, P., Larsson, J., and Pecnik, R. (2025a). Scaling of wall pressure and the streamwise turbulence intensity peak in compressible wall flows. *arXiv preprint no. 2505.07407*.

Hasan, A. M., Costa, P., Larsson, J., Pirozzoli, S., and Pecnik, R. (2025b). Intrinsic compressibility effects in near-wall turbulence. *Journal of Fluid Mechanics*, 1006:A14.

Hasan, A. M., Elias, A. J., Menter, F., and Pecnik, R. (2024a). Variable-property and intrinsic compressibility corrections for turbulence models using near-wall scaling theories. `https://github.com/Fluid-Dynamics-Of-Energy-Systems-Team/RANS_Scaling2024.git`.

Hasan, A. M., Elias, A. J., Menter, F., and Pecnik, R. (2025c). Variable-property and intrinsic compressibility corrections for turbulence models using near-wall scaling theories. *Journal of Fluid Mechanics*, 1019:A8.

Hasan, A. M., Larsson, J., Pirozzoli, S., and Pecnik, R. (2023). Incorporating intrinsic compressibility effects in velocity transformations for wall-bounded turbulent flows. *Physical Review Fluids*, 8(11):L112601.

Hasan, A. M., Larsson, J., Pirozzoli, S., and Pecnik, R. (2024b). Estimating mean profiles and fluxes in high-speed turbulent boundary layers using inner/outer-layer scalings. *AIAA Journal*, 62(2):848–853.

Hirai, R., Pecnik, R., and Kawai, S. (2021). Effects of the semi-local Reynolds number in scaling turbulent statistics for wall heated/cooled supersonic turbulent boundary layers. *Physical Review Fluids*, 6(12):124603.

Hopkins, E. J. and Inouye, M. (1971). An evaluation of theories for predicting turbulent skin friction and heat transfer on flat plates at supersonic and hypersonic Mach numbers. *AIAA Journal*, 9(6):993–1003.

Huang, J., Duan, L., and Choudhari, M. M. (2022). Direct numerical simulation of hypersonic turbulent boundary layers: effect of spatial evolution and Reynolds number. *Journal of Fluid Mechanics*, 937:A3.

Huang, P., Bradshaw, P., and Coakley, T. (1993). Skin friction and velocity profile family for compressible turbulent boundary layers. *AIAA Journal*, 31(9):1600–1604.

Huang, P., Bradshaw, P., and Coakley, T. (1994). Turbulence models for compressible boundary layers. *AIAA Journal*, 32(4):735–740.

Huang, P., Coleman, G., Spalart, P., and Yang, X. (2023). Velocity and temperature scalings leading to compressible laws of the wall. *Journal of Fluid Mechanics*, 977:A49.

Huang, P. and Coleman, G. N. (1994). Van Driest transformation and compressible wall-bounded flows. *AIAA Journal*, 32(10):2110–2113.

Huang, P. G., Coleman, G. N., and Bradshaw, P. (1995). Compressible turbulent channel flows: DNS results and modelling. *Journal of Fluid Mechanics*, 305:185–218.

Iyer, P. S. and Malik, M. R. (2019). Analysis of the equilibrium wall model for high-speed turbulent flows. *Physical Review Fluids*, 4(7):074604.

Iyer, P. S., Volpiani, P. S., Larsson, J., Pirozzoli, S., and Malik, M. R. (2019). A near-wall eddy viscosity for compressible turbulent flows based on velocity transformation with application to wall models. In *APS/DFD Annual Meeting*.

Jagannathan, S. and Donzis, D. A. (2016). Reynolds and Mach number scaling in solenoidally-forced compressible turbulence using high-resolution direct numerical simulations. *Journal of Fluid Mechanics*, 789:669–707.

Jenkins, D. R. (2000). *Hypersonics before the shuttle: A concise history of the X-15 research airplane*. Number 18. National Aeronautics and Space Administration.

Jeong, J., Hussain, F., Schoppa, W., and Kim, J. (1997). Coherent structures near the wall in a turbulent channel flow. *Journal of Fluid Mechanics*, 332:185–214.

Jiménez, J., Hoyas, S., Simens, M. P., and Mizuno, Y. (2010). Turbulent boundary layers and channels at moderate Reynolds numbers. *Journal of Fluid Mechanics*, 657:335–360.

Jiménez, J. and Pinelli, A. (1999). The autonomous cycle of near-wall turbulence. *Journal of Fluid Mechanics*, 389:335–359.

Johansson, A. V., Alfredsson, P. H., and Kim, J. (1991). Evolution and dynamics of shear-layer structures in near-wall turbulence. *Journal of Fluid Mechanics*, 224:579–599.

Johansson, A. V., Her, J.-Y., and Haritonidis, J. H. (1987). On the generation of high-amplitude wall-pressure peaks in turbulent boundary layers and spots. *Journal of Fluid Mechanics*, 175:119–142.

Johnson, D. A. and King, L. (1985). A mathematically simple turbulence closure model for attached and separated turbulent boundary layers. *AIAA Journal*, 23(11):1684–1692.

Kawai, S. (2019). Heated transcritical and unheated non-transcritical turbulent boundary layers at supercritical pressures. *Journal of Fluid Mechanics*, 865:563–601.

Kim, J. (1985). Turbulence structures associated with the bursting event. *The Physics of Fluids*, 28(1):52–58.

Kim, J. (1989). On the structure of pressure fluctuations in simulated turbulent channel flow. *Journal of Fluid Mechanics*, 205:421–451.

Kim, J. and Hussain, F. (1993). Propagation velocity of perturbations in turbulent channel flow. *Physics of Fluids A: Fluid Dynamics*, 5(3):695–706.

Kistler, A. and Chen, W. (1963). The fluctuating pressure field in a supersonic turbulent boundary layer. *Journal of Fluid Mechanics*, 16(1):41–64.

Kovasznay, L. S. (1953). Turbulence in supersonic flow. *Journal of the Aeronautical Sciences*, 20(10):657–674.

Kumar, V. and Larsson, J. (2022). Modular method for estimation of velocity and temperature profiles in high-speed boundary layers. *AIAA Journal*, 60(9):5165–5172.

Laganelli, A., Martellucci, A., and Shaw, L. (1983). Wall pressure fluctuations in attached boundary-layer flow. *AIAA Journal*, 21(4):495–502.

Lagha, M., Kim, J., Eldredge, J., and Zhong, X. (2011). A numerical study of compressible turbulent boundary layers. *Physics of Fluids*, 23(1).

Larsson, J., Kawai, S., Bodart, J., and Bermejo-Moreno, I. (2016). Large eddy simulation with modeled wall-stress: recent progress and future directions. *Mechanical Engineering Reviews*, 3(1):15–00418.

Larsson, J. and Pirozzoli, S. (2026). Wall-bounded compressible turbulent flows. In Larsson, J. and Zhong, X., editors, *Turbulence and Transition in Supersonic and Hypersonic Flows*. Elsevier. In press.

Lee, H., Helm, C., Martín, P. M., and Williams, O. J. (2023). Compressible boundary layer velocity transformation based on a generalized form of the total stress. *Physical Review Fluids*, 8(7):074604.

Lee, M. and Moser, R. D. (2015). Direct numerical simulation of turbulent channel flow up to $Re_\tau \approx 5200$. *Journal of Fluid Mechanics*, 774:395–415.

Lele, S. K. (1994). Compressibility effects on turbulence. *Annual Review of Fluid Mechanics*, 26(1):211–254.

Leyva, I. A. (2017). The relentless pursuit of hypersonic flight. *Physics Today*, 70(11):30–36.

Livescu, D. (2020). Turbulence with large thermal and compositional density variations. *Annual Review of Fluid Mechanics*, 52:309–341.

Lobb, R., Winkler, E., and Persh, J. (1955). NOL hypersonic tunnel No. 4, results 7: experimental investigation of turbulent boundary layers in hypersonic flow. Technical report, U.S. Naval Ordnance Laboratory, White Oak, Maryland.

Luhar, M., Sharma, A., and McKeon, B. (2014). On the structure and origin of pressure fluctuations in wall turbulence: predictions based on the resolvent analysis. *Journal of Fluid Mechanics*, 751:38–70.

Maeder, T., Adams, N. A., and Kleiser, L. (2001). Direct simulation of turbulent supersonic boundary layers by an extended temporal approach. *Journal of Fluid Mechanics*, 429:187–216.

Marusic, I., Baars, W. J., and Hutchins, N. (2017). Scaling of the streamwise turbulence intensity in the context of inner-outer interactions in wall turbulence. *Physical Review Fluids*, 2(10):100502.

Marusic, I., McKeon, B. J., Monkewitz, P. A., Nagib, H. M., Smits, A. J., and Sreenivasan, K. R. (2010). Wall-bounded turbulent flows at high Reynolds numbers: recent advances and key issues. *Physics of Fluids*, 22(6).

Menter, F. (1993). Zonal two equation k-w turbulence models for aerodynamic flows. In *23rd fluid dynamics, plasmadynamics, and lasers conference*, page 2906.

Modesti, D. and Pirozzoli, S. (2016). Reynolds and Mach number effects in compressible turbulent channel flow. *International Journal of Heat and Fluid Flow*, 59:33–49.

Modesti, D. and Pirozzoli, S. (2024). Friction and heat transfer in forced air convection with variable physical properties. *Journal of Fluid Mechanics*, 1001:A27.

Monkewitz, P. A. (2022). Asymptotics of streamwise Reynolds stress in wall turbulence. *Journal of Fluid Mechanics*, 931:A18.

Monkewitz, P. A. and Nagib, H. M. (2023). The hunt for the Kármán 'constant' revisited. *Journal of Fluid Mechanics*, 967:A15.

Monty, J. P., Harun, Z., and Marusic, I. (2011). A parametric study of adverse pressure gradient turbulent boundary layers. *International Journal of Heat and Fluid Flow*, 32(3):575–585.

Morinishi, Y., Tamano, S., and Nakabayashi, K. (2004). Direct numerical simulation of compressible turbulent channel flow between adiabatic and isothermal walls. *Journal of Fluid Mechanics*, 502:273.

Morkovin, M. V. (1962). Effects of compressibility on turbulent flows. *Mécanique de la Turbulence*, 367(380):26.

Moser, R. D., Kim, J., and Mansour, N. N. (1999). Direct numerical simulation of turbulent channel flow up to $\mathrm{Re}_\tau = 590$. *Physics of Fluids*, 11(4):943–945.

Nagib, H. M. and Chauhan, K. A. (2008). Variations of von Kármán coefficient in canonical flows. *Physics of Fluids*, 20(10):101518.

Nagib, H. M., Chauhan, K. A., and Monkewitz, P. A. (2007). Approach to an asymptotic state for zero pressure gradient turbulent boundary layers. *Philosophical Transactions of the Royal Society A: Mathematical, Physical and Engineering Sciences*, 365(1852):755–770.

Otero Rodriguez, G., Smit, S. H., and Pecnik, R. (2021). Three-dimensional unsteady stator-rotor interactions in high-expansion organic Rankine cycle turbines. *Energy*, 217:119339.

Otero Rodriguez, G. J., Patel, A., Diez Sanhueza, R., and Pecnik, R. (2018). Turbulence modelling for flows with strong variations in thermo-physical properties. *International Journal of Heat and Fluid Flow*, 73.

Panton, R. L., Lee, M., and Moser, R. D. (2017). Correlation of pressure fluctuations in turbulent wall layers. *Physical Review Fluids*, 2(9):094604.

Patel, A., Boersma, B. J., and Pecnik, R. (2016a). The influence of near-wall density and viscosity gradients on turbulence in channel flows. *Journal of Fluid Mechanics*, 809:793–820.

Patel, A., Boersma, B. J., and Pecnik, R. (2017). Scalar statistics in variable property turbulent channel flows. *Physical Review Fluids*, 2(8):084604.

Patel, A., Pecnik, R., Peeters, J., Hickel, S., and Moghadam, M. (2016b). Turbulence modulation by variable density and viscosity. In *Proceedings of the Summer Program*, page 213.

Patel, A., Peeters, J. W. R., Boersma, B. J., and Pecnik, R. (2015). Semi-local scaling and turbulence modulation in variable property turbulent channel flows. *Physics of Fluids*, 27(9):095101.

Pecnik, R. and Hasan, A. M. (2023). Drag and heat transfer estimation. `https://github.com/Fluid-Dynamics-Of-Energy-Systems-Team/DragandHeatTransferEstimation.git`.

Pecnik, R. and Hasan, A. M. (2026). Turbulence modeling. In Larsson, J. and Zhong, X., editors, *Turbulence and Transition in Supersonic and Hypersonic Flows*. Elsevier. In press.

Pecnik, R. and Patel, A. (2017). Scaling and modelling of turbulence in variable property channel flows. *Journal of Fluid Mechanics*, 823.

Pirozzoli, S. (2024). On the streamwise velocity variance in the near-wall region of turbulent flows. *Journal of Fluid Mechanics*, 989:A5.

Pirozzoli, S., Grasso, F., and Gatski, T. (2004). Direct numerical simulation and analysis of a spatially evolving supersonic turbulent boundary layer at M= 2.25. *Physics of Fluids*, 16(3):530–545.

Pirozzoli, S., Romero, J., Fatica, M., Verzicco, R., and Orlandi, P. (2021). One-point statistics for turbulent pipe flow up to $Re_\tau \approx 6000$. *Journal of Fluid Mechanics*, 926.

Pope, S. B. (2001). Turbulent flows.

Rahman, M. M., Wallin, S., and Siikonen, T. (2012). Exploring k and ϵ with R–equation model using elliptic relaxation function. *Flow, Turbulence and Combustion*, 89(1):121–148.

Ristorcelli, J. (1997). A pseudo-sound constitutive relationship for the dilatational covariances in compressible turbulence. *Journal of Fluid Mechanics*, 347:37–70.

Ritos, K., Drikakis, D., and Kokkinakis, I. (2019). Acoustic loading beneath hypersonic transitional and turbulent boundary layers. *Journal of Sound and Vibration*, 441:50–62.

Rumsey, C. L. (2010). Compressibility considerations for k-ω turbulence models in hypersonic boundary-layer applications. *Journal of Spacecraft and Rockets*, 47(1):11–20.

Samie, M., Marusic, I., Hutchins, N., Fu, M., Fan, Y., Hultmark, M., and Smits, A. (2018). Fully resolved measurements of turbulent boundary layer flows up to $Re_\tau = 20000$. *Journal of Fluid Mechanics*, 851:391–415.

Schlatter, P. and Örlü, R. (2010). Assessment of direct numerical simulation data of turbulent boundary layers. *Journal of Fluid Mechanics*, 659:116–126.

Schlatter, P., Örlü, R., Li, Q., Brethouwer, G., Fransson, J. H., Johansson, A. V., Alfredsson, P. H., and Henningson, D. S. (2009). Turbulent boundary layers up to Re_θ= 2500 studied through simulation and experiment. *Physics of Fluids*, 21(5):051702.

Sciacovelli, L., Cannici, A., Passiatore, D., and Cinnella, P. (2024). A priori tests of turbulence models for compressible flows. *International Journal of Numerical Methods for Heat & Fluid Flow*, 34(7):2808–2831.

Sciacovelli, L., Cinnella, P., and Gloerfelt, X. (2017). Direct numerical simulations of supersonic turbulent channel flows of dense gases. *Journal of Fluid Mechanics*, 821:153–199.

Sharma, B. and Girimaji, S. S. (2023). Effect of flow–thermodynamics interactions on the stability of compressible boundary layers: insights from Helmholtz decomposition. *Journal of Fluid Mechanics*, 962:A18.

Sillero, J. A., Jiménez, J., and Moser, R. D. (2013). One-point statistics for turbulent wall-bounded flows at Reynolds numbers up to $\delta^+ = 2000$. *Physics of Fluids*, 25(10):105102.

Smits, A. J. and Dussauge, J.-P. (2006). *Turbulent shear layers in supersonic flow*. Springer Science & Business Media.

Smits, A. J., Hultmark, M., Lee, M., Pirozzoli, S., and Wu, X. (2021). Reynolds stress scaling in the near-wall region of wall-bounded flows. *Journal of Fluid Mechanics*, 926.

Song, Y., Zhang, P., Liu, Y., and Xia, Z. (2022). Central mean temperature scaling in compressible turbulent channel flows with symmetric isothermal boundaries. *Physical Review Fluids*, 7(4):044606.

Spalart, P. and Allmaras, S. (1992). A one-equation turbulence model for aerodynamic flows. In *30th Aerospace Sciences Meeting and Exhibit*, page 439.

Spalart, P. R. (1988). Direct simulation of a turbulent boundary layer up to R_θ= 1410. *Journal of Fluid Mechanics*, 187:61–98.

Spina, E. F., Smits, A. J., and Robinson, S. K. (1994). The physics of supersonic turbulent boundary layers. *Annual Review of Fluid Mechanics*, 26(1):287–319.

Tang, J., Zhao, Z., Wan, Z.-H., and Liu, N.-S. (2020). On the near-wall structures and statistics of fluctuating pressure in compressible turbulent channel flows. *Physics of Fluids*, 32(11):115121.

Tennekes, H. and Lumley, J. L. (1972). A first course in turbulence.

Toki, T., Teramoto, S., and Okamoto, K. (2020). Velocity and temperature profiles in turbulent channel flow at supercritical pressure. *Journal of Propulsion and Power*, 36(1):3–13.

Townsend, A. (1961). Equilibrium layers and wall turbulence. *Journal of Fluid Mechanics*, 11(1):97–120.

Trettel, A. and Larsson, J. (2016). Mean velocity scaling for compressible wall turbulence with heat transfer. *Physics of Fluids*, 28(2):026102.

Trettel, A. J. (2019). *Transformations for variable-property turbulent boundary layers*. PhD thesis, UCLA.

Van Driest, E. R. (1951). Turbulent boundary layer in compressible fluids. *Journal of the Aeronautical Sciences*, 18(3):145–160.

Van Driest, E. R. (1956a). On turbulent flow near a wall. *Journal of the Aeronautical Sciences*, 23(11):1007–1011.

Van Driest, E. R. (1956b). *The problem of aerodynamic heating*. Institute of the Aeronautical Sciences.

Volpiani, P. S., Bernardini, M., and Larsson, J. (2020a). Effects of a nonadiabatic wall on hypersonic shock/boundary-layer interactions. *Physical Review Fluids*, 5(1):014602.

Volpiani, P. S., Iyer, P. S., Pirozzoli, S., and Larsson, J. (2020b). Data-driven compressibility transformation for turbulent wall layers. *Physical Review Fluids*, 5(5):052602.

Wan, Z.-H., Sun, D.-J., Lu, X.-Y., et al. (2024). The intrinsic scaling relation between pressure fluctuations and Mach number in compressible turbulent boundary layers. *Journal of Fluid Mechanics*, 993:A2.

Wang, J., Gotoh, T., and Watanabe, T. (2017). Spectra and statistics in compressible isotropic turbulence. *Physical Review Fluids*, 2(1):013403.

Wenzel, C., Gibis, T., and Kloker, M. (2022). About the influences of compressibility, heat transfer and pressure gradients in compressible turbulent boundary layers. *Journal of Fluid Mechanics*, 930:A1.

Wenzel, C., Selent, B., Kloker, M., and Rist, U. (2018). DNS of compressible turbulent boundary layers and assessment of data/scaling-law quality. *Journal of Fluid Mechanics*, 842:428–468.

Wilcox, D. C. et al. (2006). *Turbulence modeling for CFD*, volume 2. DCW Industries La Canada, CA.

Wu, Y. and Christensen, K. T. (2006). Population trends of spanwise vortices in wall turbulence. *Journal of Fluid Mechanics*, 568:55–76.

Yang, X. I. and Lv, Y. (2018). A semi-locally scaled eddy viscosity formulation for LES wall models and flows at high speeds. *Theoretical and Computational Fluid Dynamics*, 32(5):617–627.

Yu, M., Liu, P., Fu, Y., Tang, Z., and Yuan, X. (2022). Wall shear stress, pressure, and heat flux fluctuations in compressible wall-bounded turbulence, part I: One-point statistics. *Physics of Fluids*, 34(6):065139.

Yu, M. and Xu, C.-X. (2021). Compressibility effects on hypersonic turbulent channel flow with cold walls. *Physics of Fluids*, 33(7):075106.

Yu, M., Xu, C.-X., and Pirozzoli, S. (2019). Genuine compressibility effects in wall-bounded turbulence. *Physical Review Fluids*, 4(12):123402.

Yu, M., Xu, C.-X., and Pirozzoli, S. (2020). Compressibility effects on pressure fluctuation in compressible turbulent channel flows. *Physical Review Fluids*, 5(11):113401.

Yu, M., Zhou, Z., Dong, S., Yuan, X., and Xu, C. (2024). On the generation of near-wall dilatational motions in hypersonic turbulent boundary layers. *Journal of Fluid Mechanics*, 984:A44.

Zeman, O. (1990). Dilatation dissipation: the concept and application in modeling compressible mixing layers. *Physics of Fluids A: Fluid Dynamics*, 2(2):178–188.

Zeman, O. (1993). A new model for super/hypersonic turbulent boundary layers. In *31st Aerospace Sciences Meeting*, page 897.

Zhang, C., Duan, L., and Choudhari, M. M. (2017). Effect of wall cooling on boundary-layer-induced pressure fluctuations at Mach 6. *Journal of Fluid Mechanics*, 822:5–30.

Zhang, C., Duan, L., and Choudhari, M. M. (2018). Direct numerical simulation database for supersonic and hypersonic turbulent boundary layers. *AIAA Journal*, 56(11):4297–4311.

Zhang, P.-J.-Y., Wan, Z.-H., Liu, N.-S., Sun, D.-J., and Lu, X.-Y. (2022). Wall-cooling effects on pressure fluctuations in compressible turbulent boundary layers from subsonic to hypersonic regimes. *Journal of Fluid Mechanics*, 946:A14.

Zhang, Y.-S., Bi, W.-T., Hussain, F., Li, X.-L., and She, Z.-S. (2012). Mach-number-invariant mean-velocity profile of compressible turbulent boundary layers. *Physical Review Letters*, 109(5):054502.

Zhang, Y.-S., Bi, W.-T., Hussain, F., and She, Z.-S. (2014). A generalized Reynolds analogy for compressible wall-bounded turbulent flows. *Journal of Fluid Mechanics*, 739:392–420.

ACKNOWLEDGEMENTS

This thesis would not have been possible without the support, guidance, encouragement, and affection of all those around me. I begin by expressing my deepest gratitude to my promotor, **prof. dr. Rene Pecnik**. Words cannot do justice to the impact he has had on me as a researcher. One of our very first interactions—a two-hour discussion about potential Master-thesis topics—already left a lasting impression. The passion with which he explained each idea convinced me that this was the place I wanted to be. Since then, every meeting has been an intense scientific discussion, with his insightful comments proving invaluable to this research. Rene has remained approachable and supportive throughout this journey, whether the matter was related to research or life, even outside working hours. I am especially grateful for the freedom he gave me in steering the direction of this thesis, and for never dismissing my ideas, however unusual they might have seemed. Lastly, I thank him for enabling the productive collaborations we have had with researchers from other universities and industries.

My sincere thanks also go to my copromotor, **dr. Pedro Costa**, for his constant support at every hurdle I faced. His concise and effective comments during our meetings substantially improved the quality of this work. He has been a comforting presence, always radiating positivity. Although my own brother was far away from the Netherlands, Pedro often filled that role for me, guiding me with the encouragement and mentorship of an elder brother throughout this journey.

I gratefully acknowledge the contributions of **prof. dr. Johan Larsson** and **prof. dr. Sergio Pirozzoli**. Their expertise and the valuable insights they shared during our biweekly meetings have greatly strengthened the research presented here. I am also thankful to **dr. Alex José Elias** and **dr. Florian Menter** (yes, the man behind the SST model) for the fruitful collaboration on RANS modeling of compressible flows. The industrial perspective they brought was an invaluable learning experience. I would also like to thank the members of the dissertation committee for their efforts in evaluating this work.

I truly appreciate the company of my colleagues and friends from our research group. The core (ERC) group—**Pietro Carlo Boldini**, **dr. Benjamin Bugeat**, **dr. Marko Draskic**, **Sanath Kottursheттar** and **dr. Ryo Hirai**—with whom I have had many enlightening discussions, certainly helped shape this thesis in many ways. Pietro's discipline, Marko's perseverance, Ben's clarity, Sanath's directness, and Ryo's kindness have been truly inspiring to witness. I am grateful to **Teja Donepudi** for our informal conversations—from tennis to football, Bollywood to Tollywood—which always helped me blow off some steam on intense workdays. Although I interacted less with **dr. Giandomenico Lupo**, his elder-brother-like presence has always comforted me. I also thank **Max Knoop** for our numerous discussions on wall-bounded turbulence. Beyond the core group, I am fortunate to have had great interactions with colleagues from the Process & Energy department: **dr. Jurriaan Peeters**, **dr. Simone Silvestri**, **Stephan Smit**, **dr. Baptiste Hardy**, **dr. Rafael Diez**, **Atharv Naik**, **Darshan Raju**, **Shrinjay Sharma**,

Jelle Lagerweij, **dr. Heng Li**, **dr. An Zhao**, **Suriya Kumar**, **dr. Shahid Khan**, **Bartu Fazla**, **Vignesh Murugesan**, **Mammad Norouzi**, **Shaina Blitt**, **Tarun Hegde**, **Anna Pavan**, **Sowmya Kumar**, **Abhirath Anand**, and **Jesse Reijtenbagh**.

Life in the Netherlands was made joyful and full of memories thanks to **Fulin**, **K.v.A.**, **Kunal**, **Madhura**, **Aditya**, **Tarunay**, **Mahima**, and **Bilal**. To my childhood and early adulthood friends—**Jay**, **Vraj**, **Alan**, **Aman**, **Sagar**, **Kunal**, **Asim**, **Umair**, **Sadique**, **Kuldeep**, and many others—thank you for always being just a call away.

Above all, I owe everything to my family—**Dad**, **Mom**, **Bhai**, **Bhabhi**, **Mami**, **Mamu**, **Ajab**, and **Ammar**. This thesis would certainly not have been possible without their constant support. My **father**, who did not have the privilege of higher education, always ensured that I had everything I needed to study as much as I wished. When I said I wanted to pursue a Ph.D., he immediately agreed and asked, "How much will the tuition fees be?" Now that this journey is nearing its end, I hope he is watching from above and is proud of what he has made possible for us. My **brother**, too, has been a constant pillar of support, making sure I had everything I needed to continue my work, even while living thousands of miles away.

Finally, and most importantly, all praise be to God for bestowing upon me the unwavering support, patience, strength and guidance needed to accomplish this dissertation.

CURRICULUM VITÆ

Asif Manzoor Hasan was born in Mumbai, India, on 22 October 1995. In 2013, he joined Sardar Patel College of Engineering (SPCE, Mumbai) to pursue a Bachelor's degree in Mechanical Engineering, and graduated with distinction in 2017. In the same year, he appeared for the Graduate Aptitude Test in Engineering (GATE) and secured an **All India Rank 1** in Mechanical Engineering. Based on this score, he was selected as an Engineering Officer at Indian Oil Corporation Limited, where he worked from September 2017 to July 2019 at the petroleum storage terminal in Mangalore.

In August 2019, he moved to the Netherlands to pursue a Master's degree at Delft University of Technology. He graduated *cum laude* in June 2021, and his Master's thesis on "Thermal turbulence in variable property channel flows" was awarded the Best Master's Thesis award in Mechanical Engineering by the Royal Holland Society of Sciences and Humanities. During his Bachelor's and Master's studies, he also received several scholarships.

Since July 2021, he has been a Ph.D. researcher under the supervision of prof. dr. Rene Pecnik and dr. Pedro Costa. During this time, he has published articles in peer-reviewed journals, with his first paper on velocity transformations receiving an Editors' Suggestion. He has also presented his work at national and international conferences and delivered an invited talk at the Center for Turbulence Research, Stanford University.

LIST OF PUBLICATIONS

JOURNAL PUBLICATIONS

[1] **Hasan, A. M.**, Larsson, J., Pirozzoli, S., and Pecnik, R. (2023). Incorporating intrinsic compressibility effects in velocity transformations for wall-bounded turbulent flows. *Physical Review Fluids*, 8(11):L112601.

[2] **Hasan, A. M.**, Larsson, J., Pirozzoli, S., and Pecnik, R. (2024). Estimating mean profiles and fluxes in high-speed turbulent boundary layers using inner/outer-layer scalings. *AIAA Journal*, 62(2):848–853.

[3] Bugeat, B., Boldini, P. C., **Hasan, A. M.**, and Pecnik, R. (2024). Instability in strongly stratified plane Couette flow with application to supercritical fluids. *Journal of Fluid Mechanics*, 984:A31.

[4] **Hasan, A. M.**, Costa, P., Larsson, J., Pirozzoli, S., and Pecnik, R. (2025). Intrinsic compressibility effects in near-wall turbulence. *Journal of Fluid Mechanics*, 1006:A14.

[5] **Hasan, A. M.**, Elias, A. J., Menter, F., and Pecnik, R. (2025). Variable-property and intrinsic compressibility corrections for turbulence models using near-wall scaling theories. *Journal of Fluid Mechanics*, 1019:A8.

[6] **Hasan, A. M.**, Costa, P., Larsson, J., and Pecnik, R. (2025). Scaling of wall pressure and the streamwise turbulence intensity peak in compressible wall flows. Under review in *Journal of Fluid Mechanics*.

BOOK CHAPTERS

[1] Pecnik, R., and **Hasan, A. M.** (2026). Turbulence modeling. In Larsson, J. and Zhong, X. (eds.), *Turbulence and Transition in Supersonic and Hypersonic Flows*. Elsevier. In press.

CONFERENCE PUBLICATIONS AND PRESENTATIONS

[1] **Hasan, A. M.**, Larsson, J., Pirozzoli, S., and Pecnik, R. (2022). How accurate is Morkovin's hypothesis for supersonic wall-bounded turbulent flows? 75th Annual Meeting of the Division of Fluid Dynamics, American Physical Society, Indianapolis, Indiana, USA.

[2] **Hasan, A. M.**, Larsson, J., Pirozzoli, S., and Pecnik, R. (2023). Intrinsic compressibility effects in wall-bounded turbulent flows – understanding the physical mechanism. 18th European Turbulence Conference, Valencia, Spain.

[3] **Hasan, A. M.**, Larsson, J., Pirozzoli, S., and Pecnik, R. (2023). Incorporating intrinsic compressibility effects in velocity transformations for wall-bounded turbulent

flows. 76th Annual Meeting of the Division of Fluid Dynamics, American Physical Society, Washington, DC, USA.

[4] **Hasan, A. M.**, Costa, P., Larsson, J., Pirozzoli, S., and Pecnik, R. (2024). Intrinsic compressibility effects in near-wall turbulence. Burgers Symposium, Lunteren, The Netherlands.

[5] **Hasan, A. M.**, Larsson, J., Pirozzoli, S., and Pecnik, R. (2024). Estimating mean profiles and fluxes in high-speed turbulent boundary layers using inner/outer-layer transformations. In *Proceedings of the Thirteenth International Symposium on Turbulence and Shear Flow Phenomena*, Montreal, Canada.

[6] **Hasan, A. M.**, Costa, P., Larsson, J., Pirozzoli, S., and Pecnik, R. (2024). Intrinsic compressibility effects in near-wall turbulence. 1st European Fluid Dynamics Conference, Aachen, Germany.

[7] **Hasan, A. M.**, Costa, P., Larsson, J., Pirozzoli, S., and Pecnik, R. (2024). Intrinsic compressibility effects in near-wall turbulence. 77th Annual Meeting of the Division of Fluid Dynamics, American Physical Society, Salt Lake City, Utah, USA.

INVITED TALKS

[1] **Hasan, A. M.** (2024). Intrinsic compressibility effects in near-wall turbulence. Center for Turbulence Research, Stanford University, California, USA.

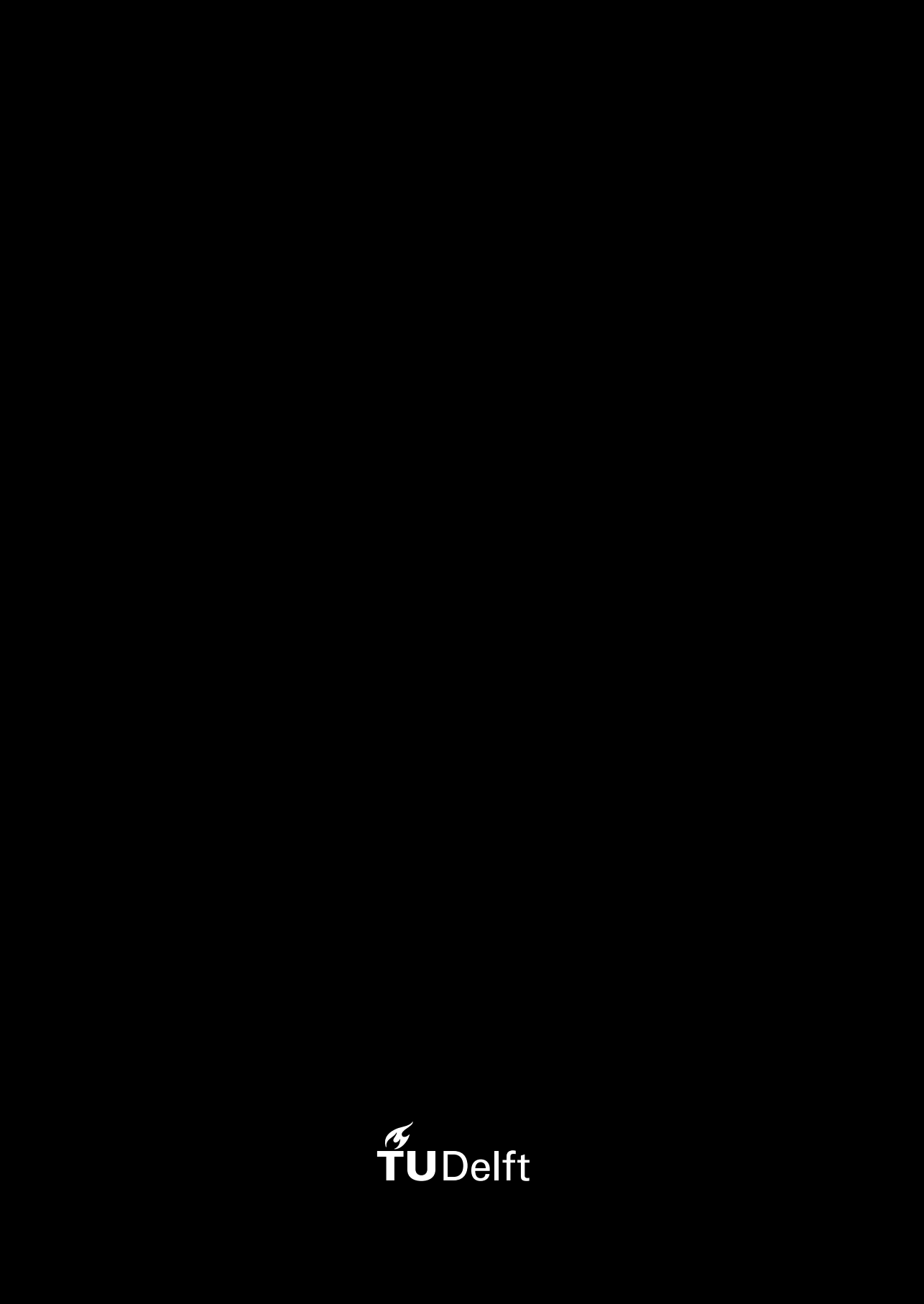
TUDelft